The old and the new: mouse models for evaluating the therapeutic margin of radiation in lung cancer



CRUK/MRC Oxford Institute for Radiation Oncology
Department of Oncology
University of Oxford

Luiza Helena Madia Lourenço
Hertford College, University of Oxford

Thesis submitted for the degree of Doctor of Philosophy in Radiobiology
Trinity Term, 2017

The old and the new: mouse models for evaluating the therapeutic margin of radiation in lung cancer

Luiza Helena Madia Lourenço
Hertford College, University of Oxford
Thesis submitted for the degree of Doctor of Philosophy in Radiobiology - Trinity Term, 2017

Abstract

Background: Radiotherapy is widely used in the treatment of lung cancer, with both curative and palliative intent according to the stage of the disease. The tumour control potential of radiotherapy is limited by the induction of side effects; in the case of thoracic radiotherapy (tRTX), common side effects are oesophagitis, pneumonitis and pulmonary fibrosis. The main challenges in the field are, therefore, to find ways to increase tumour killing and/or decrease normal tissue toxicity, to improve the therapeutic margin of radiation. **Aims:** Firstly, to characterise selected early and late tissue responses in a mouse model of tRTX. Secondly, to investigate approaches to improve the therapeutic margin of tRTX by modulating the inflammatory response or the DNA damage response (DDR). **Methods:** To evaluate normal tissue responses, we used tRTX of C57BL6 mice, a well-established preclinical model of radiation-induced pulmonary fibrosis. In parallel, human lung cancer cells were grown as subcutaneous xenografts in immune compromised nude mice, and used to evaluate anti-tumour responses. A/J mice bearing urethane-induced lung tumours were used to evaluate normal and tumour lung tissue responses simultaneously. Immunohistochemistry, western blotting and non-invasive imaging were used to assess treatment responses. **Results:** Acute and transient local (neutrophil lung infiltration) and systemic (plasma levels of pro-inflammatory cytokines) inflammatory/immune responses were induced by tRTX. Thoracic radiation induced DNA double-strand breaks in lung tissue, a proportion of which were persistent. Fractionation schedules of tRTX led to pneumonitis and pulmonary fibrosis. Knock-out of myeloperoxidase activity was associated with decreased early and late normal tissue responses to tRTX. In separate mouse models, we observed that DDR inhibitors effectively radiosensitised xenograft tumours, but differentially affected thoracic normal tissues. PARP inhibition in combination with tRTX lead to oesophagitis whereas ATM inhibition increased radiation-induced lung damage. Using the A/J strain, we simultaneously evaluated normal and tumour lung tissues responses to tRTX, establishing a novel mouse model for the study of therapeutic index. In the A/J model, ATM inhibition in combination with tRTX showed significant anti-tumour activity, but was also associated with increased late normal tissue effects. **Conclusions:** Myeloperoxidase contributes to early inflammatory responses and late effects induced by tRTX. DDR inhibitors have similar tumour responses but differential normal tissue responses when combined to tRTX. A newly established A/J mouse model has the potential to have a significant impact on studies evaluating the therapeutic index of novel therapies in combination with thoracic radiation by allowing for the simultaneous assessment of normal and tumour lung tissues in the context of a fully functional immune system.

Acknowledgements

Firstly, I would like to thank my supervisor Andy Ryan for all the amazing support during these 4 years - not only for the scientific support with experiments and the thesis, but for all the career and life chats too.

I would also like to thank all the staff of the Department of Oncology, especially the BMS and Imaging Core for the incredible support given for the in vivo work. A big ‘thank you’ to current and previous Ryan lab members: Agnes, Agata, Yanyan, Amalina, Fiona, Yasmin, Sam, Anika, Sivan, Aoife, and especially John for the help with this thesis and with the animal work.

Also, this work has only been possible with the financial support of my home country, Brazil, through the CNPq - Science Without Borders scholarship program.

I am grateful to God for caringly putting the most amazing people in my life during this last 4 years. I simply cannot imagine getting to the end of this degree without the help of my friends, old and new. All the messages and phone calls from Brazil from Ana Luiza, Amanda, Mariana, Mari and Renata have always helped me to keep going. A most special ‘thank you’ to my dearest Oxford friends, Neele, Sophie, Greg, Flavia, Mikołaj, Deborah, Mary-Ann, Jen, Joe and Marcella, who were there for me whenever I needed the support or the company. Also, thank you to my beloved friends from Hertford MCR: Laura, Mustak, Andy, Frankie, Rory Nolan, Naomi, Bas, Joey, Rory Hill and Mike.

Finally, I would like to thank my parents and family from Brazil, for making more than 5000 miles feel just like one heartbeat away.

Contents

1. Introduction 14

2. Methods 31

2.1. Reagents 31

2.2. In vivo studies 35

2.3. Cytokine profiling 47

2.4. Immunohistochemistry 48

2.5. Haematoxylin & eosin staining 53

2.6. Masson's trichrome staining 54

2.7. Fibrosis scoring 55

2.8. Protein extraction from lungs 57

2.9. Hydroxyproline assay 58

2.10. Western blotting 59

2.11. Cell culture 61

2.12. Myeloperoxidase incubation 61

2.13. Luminol-based MPO activity assay 62

2.14. CELLROX® assay 63

2.15. Comet assay 63

2.16. Immunofluorescence 65

2.17. Clonogenic survival 66

2.18. Statistical analysis 67

3. Characterisation of the early and late normal lung responses of C57BL/6J mice to thoracic irradiation 68

3.1. Introduction 68

3.2. Whole-thorax irradiation induces an acute and transient peak of inflammation and long-lived DNA damage in the lung 72

3.3. Weight loss and abnormal breathing are sensitive indicators of late toxicity induced by whole-thorax irradiation 76

3.4. Discussion 84

4. Impaired inflammation is associated with reduced adverse effects of whole-thorax irradiation in C57BL/6J mice 92

4.1. Introduction 92

4.2. MPO promotes oxidative stress but does not induce DNA damage in lung cells in vitro 97

4.3. MPO knock-out mice showed reduced neutrophil recruitment, altered pro-inflammatory cytokines in plasma and reduced DNA damage after irradiation 101

4.4. Discussion 107

5. The impact of targeting the DNA damage response induced by whole-thorax irradiation in C57BL/6J mice 112

5.1. Introduction 112

5.2. DNA damage response inhibitors show differential normal tissue effects in combination with radiation 122

5.3. The differential impact of targeting radiation-induced DNA damage in tumours compared to normal tissue: the need for a new model 129

5.4. Discussion 131

6. A mouse model for simultaneously evaluating the effect of new therapies in combination with radiation on lung damage and tumour response 139

6.1. Introduction 139

6.2. Radiation induced weight loss and collagen accumulation in the lungs of A/J mice 145

6.3. Normal and tumour tissues show differential DNA repair kinetics 153

6.4. Radiation treatment decreased tumour burden in urethane-treated A/J mice 157

6.5. Discussion 158

7. The value of using a therapeutic index model: evaluation of ATM inhibition in combination with radiation as a treatment for lung cancer 165

7.1. Introduction 165

7.2. ATM inhibition impacts early inflammation induced by thoracic radiation in A/J mice 167

7.3. ATM inhibition impacted early DNA damage response induced by thoracic radiation on normal and tumour lung tissue in A/J mice 169

7.4. ATM inhibition in combination with radiation led to weight loss, pulmonary haemorrhage and impairment of alveolar structure in A/J mice 175

7.5. ATM inhibition radiosensitised urethane-induced lung tumours 180

7.6. Discussion 181

8. General discussion and conclusion 186

9. References 193

10. Appendix 215

Final word count: approximately 40000

List of Figures

Figure 1.1. DNA damage generated by the direct interaction with radiation tracks. 18
Figure 1.2. DNA strand break repair pathways. 20
Figure 1.3. Radiation-induced pulmonary fibrosis. 24
Figure 1.4. Radiological changes following stereotactic ablative radiotherapy (SABR). 26
Figure 1.5. The development of radiation-induced pulmonary fibrosis. 30
Figure 2.1. Fractionated irradiation schedules. 37
Figure 2.2. Mouse positioning and shielding during irradiation. 38
Figure 2.3. Experimental design for pharmacodynamic analysis of ATM and ATR inhibitors in Calu6 xenograft tumours. 40
Figure 2.4. ATM and ATR inhibitors efficiently inhibited their targets. 41
Figure 2.5. Schedule for drug administration in combination with fractionated irradiation. ... 42
Figure 2.6. Number of lung tumours detected in A/J mice injected with urethane. 44
Figure 2.7. Example of nuclear staining analysis using the ImageScope Software. 52
Figure 2.8. Guidelines for fibrosis scoring. 56
Figure 3.1. Median survival time according to radiation dose exposure to the whole lungs of mice, non-human primates, and humans. 70
Figure 3.2. Experimental design for evaluation of early effects of whole-thorax irradiation.. 73
Figure 3.3. Whole-thorax irradiation induced systemic signalling of inflammation and immune cell recruitment to the lung. 74
Figure 3.4. Whole-thorax radiation induced long-lived DNA damage in the lung. 76
Figure 3.5. Experimental design for evaluation of late effects of whole-thorax radiation. 77
Figure 3.6. A total of 25 Gy given in fractionated doses to the whole-thorax induced severe lung damage and premature sacrifice in C57BL/6J mice. 79
Figure 3.7. Whole-thorax 20 Gy and 22.5 Gy irradiation induced weight loss and increased lethality in C57BL/6J mice. 80
Figure 3.8. Total doses of 22.5 Gy and 20 Gy to the whole-thorax induced mild pulmonary fibrosis in C57BL/6J mice. 82
Figure 3.9. Total dose of 22.5 Gy and 20 Gy given to the whole-thorax did not lead to detectable accumulation of collagen I and III in C57BL/6J mice. 84

Figure 3.10. Persistent damage leading to chronic inflammation and late lung damage. 88
Figure 4.1. Myeloperoxidase-induced lung damage hypothesis. 96
Figure 4.2. Myeloperoxidase (MPO) was internalised by lung cells in vitro and remained active after internalisation. 98
Figure 4.3. Internalised myeloperoxidase (MPO) led to increased levels of reactive oxygen species in human lung cells in vitro..... 99
Figure 4.4. Myeloperoxidase (MPO) did not induce significant DNA damage in lung cells in vitro..... 100
Figure 4.5. Myeloperoxidase (MPO) did not affect clonogenic capacity of lung cells in vitro. 100
Figure 4.6. Experimental design for evaluation of early effects of whole-thorax radiation in myeloperoxidase (MPO) knock-out mice. 101
Figure 4.7. MPO knock-out mice showed altered radiation-induced inflammation and decreased neutrophil recruitment to the lung. 103
Figure 4.8. MPO absence reduces radiation-induced DNA damage response in the lung cells. 104
Figure 4.9. Myeloperoxidase knock-out (MPO KO) mice receiving 25 Gy of whole-thorax irradiation showed less lung damage compared to myeloperoxidase wild-type (MPO WT) mice. 106
Figure 4.10. MPO contribution to radiation-induced chronic inflammation and late lung damage..... 111
Figure 5.1. The rational for targeting DNA damage repair pathways in cancer treatment. ... 113
Figure 5.2. ATM signalling upon DNA double strand break..... 116
Figure 5.3. ATR activation..... 118
Figure 5.4. PARP activation..... 120
Figure 5.5. Experimental design for evaluation of the impact of ATM, ATR and PARP inhibitors on the late effects of whole-thorax radiation..... 122
Figure 5.6. PARP inhibition in combination with whole-thorax radiation induced weight loss in C57BL/6J mice..... 124
Figure 5.7. PARP inhibition in combination with whole-thorax irradiation induced oesophagitis and dermatitis in C57BL/6J mice. 126

Figure 5.8. ATM inhibition in combination with whole-thorax irradiation induced increased levels of hydroxyproline and accumulation of collagen III in C57BL/6J mice. 128
Figure 5.9. Experimental design for evaluating the impact of ATM, ATR or PARP inhibition on the radiation response of Calu6 xenograft tumours. 130
Figure 5.10. ATM, ATR or PARP inhibition radiosensitised Calu6 xenograft tumours. 131
Figure 5.11. The impact of ATM inhibition on the normal lung tissue response to radiation. 137
Figure 6.1. Urethane metabolisation. 141
Figure 6.2. Urethane-induced lung tumours. 143
Figure 6.3. Experimental design for preliminary evaluation of late effects of whole-thorax radiation in A/J mice. 146
Figure 6.4. Whole-thorax irradiation led to increased collagen I and III in the lungs of A/J mice. 147
Figure 6.5. Experimental design for evaluation of late effects of whole-thorax irradiation in A/J mice. 148
Figure 6.6. Whole-thorax irradiation induced body weight loss in A/J mice. Two out of 10 mice in the irradiated group (IR) showed weight loss. 149
Figure 6.7. Whole-thorax radiation led to increased fibrosis score and collagen III accumulation in the lungs of A/J mice. 150
Figure 6.8. Whole-thorax radiation induced foamy macrophage infiltrate and fibrosis in the lung of A/J mice. 152
Figure 6.9. Experimental design for evaluation of early DNA damage induced by whole-thorax radiation in A/J mice. 154
Figure 6.10. Normal and tumour lung tissues showed differential kinetics of γH2AX resolution after whole-thorax radiation. 155
Figure 6.11. Normal and tumour lung tissues showed differential 53BP1 foci resolution after whole-thorax radiation. 156
Figure 6.12. Experimental design for evaluation of whole-thorax radiation effect on urethane-induced lung tumours. 157
Figure 6.13. Whole-thorax radiation decreased the number of urethane-induced lung tumours. 158

Figure 7.1. Experimental design for evaluation of early effects of whole-thorax irradiation and ATM inhibitor in A/J mice. 167
Figure 7.2. ATM inhibition impacted whole-thorax irradiation-induced systemic inflammation and neutrophil recruitment to the lung of A/J mice. 168
Figure 7.3. Differential normal and tumour lung tissue responses positivity for pKAP1 (ser824) with or without treatment with ATM inhibitor before whole-thorax irradiation. 170
Figure 7.4. Differential normal and tumour lung tissue responses positivity for γH2AX with or without treatment with ATM inhibitor before whole-thorax irradiation. 171
Figure 7.5. Differential normal and tumour lung tissue responses positivity for 53BP1 foci with or without treatment with ATM inhibitor before whole-thorax irradiation. 172
Figure 7.6. ATM inhibition showed differential impact on the radiation-induced DNA damage response of normal and tumour lung tissue. 174
Figure 7.7. Experimental design for evaluation of ATM inhibition on whole-thorax irradiation-induced late effects in A/J mice. 175
Figure 7.8. ATM inhibition in combination with whole-thorax irradiation induced body weight loss in A/J mice. 176
Figure 7.9. Inhibition of ATM in combination with whole-thorax irradiation did not lead to further increase in fibrosis in the lungs of A/J mice. 177
Figure 7.10. ATM inhibition in combination with whole-thorax irradiation did not lead to a further increase in the levels of collagen I, collagen III or hydroxyproline in the lungs of A/J mice. 179
Figure 7.11. ATM inhibition radiosensitised urethane-induced lung tumours. 180
Figure 8.1. Therapeutic strategies for treating radiation-induced pulmonary fibrosis. 190

List of Tables

Table 1.1. NSCLC stage at diagnosis and 5-year survival rates in the UK. 15
Table 1.2. NSCLC treatment options according to stage. 17
Table 2.1. Reagents. 31
Table 2.2. Description of irradiation schedules. 37
Table 2.3. Drug compounds used for in vivo experiments. 39
Table 2.4. Antibodies used for immunohistochemistry. 50
Table 2.5. Masson's trichrome staining steps and reagent details. 54
Table 2.6. Antibodies used for Western blotting. 60
Table 2.7. Antibodies used for immunofluorescence. 66
Table 4.1. Myeloperoxidase (MPO) knock-out was associated with decreased adverse effects (AE) in mice receiving fractionated whole-thorax irradiation. 105
Table 5.1. Overview of inhibitors tested and the normal tissue effects of combination with whole-thorax radiation in C57BL/6J mice. 123

Abbreviations

53BP1: tumour protein p53 binding protein 1
AE: adverse event
AEII: alveolar type II cell
Akt1: Protein kinase B
ALK: anaplastic lymphoma kinase
A-T: Ataxia-telangiectasia
ATM: Ataxia-telangiectasia mutated
ATR: Ataxia-telangiectasia and Rad3-related
ATRIP: ATR interacting protein
BED: biologically effective dose
BER: base excision repair
BRCA1/2: breast cancer type 1/2 susceptibility protein
CDC25A: cell division cycle 25
CDK1: cyclin dependent kinase 1
CHK1: checkpoint kinase 1
CHK2: checkpoint kinase 2
CT: computerised tomography
CXCR: C-X-C motif chemokine receptors
CYP2E1: cytochrome P450 2E1
DAB: 3,3'-Diaminobenzidine
DAMP: Damage-associated molecular patterns
DDR: DNA damage response
DNA: deoxyribonucleic acid
DNA-PK: DNA-dependent protein kinase
DSB: double strand break
EC: ethyl carbamate
EGFR: epidermal growth factor receptor
ETAA1: Ewing's tumor-associated antigen 1
FDA: Food and Drug Administration
H2AX: histone H2AX
HO-1: heme oxygenase 1
HOCl: hypochlorous acid
HR: homologous recombination
i.p.: intraperitoneal
IL-1: interleukin-1
IL-6: interleukin-6
IL-8: interleukin-8
iNOS: Inducible nitric oxide synthase
IR: irradiation
KC: Keratinocyte chemoattractant
Kras2: Kirsten rat sarcoma viral oncogene homolog 2
Las: lung adenoma susceptibility
LET: linear energy transfer
Ly6: lymphocyte antigen 6

MPO: myeloperoxidase
MRE11: meiotic recombination 11
MRI: magnetic resonance imaging
MRN: Protein complex including Mre11, Rad50 and Nbs1
mRNA: messenger ribonucleic acid
NAD: Nicotinamide adenine dinucleotide
NADPH: reduced nicotinamide adenine dinucleotide phosphate
NBS1: nibrin 1
NER: nucleotide excision repair
NF-κB: nuclear factor κB
NHEJ: non-homologous end joining
NHP: non-human primate
NSCLC: non-small cell lung cancer
p.o.: *per os*, orally
p53: tumour protein 53
PARP: poly(ADP-ribose)-polymerase
Pas: pulmonary adenoma susceptibility
PD1: programmed cell death protein 1
PD-L1: programmed cell death protein ligand 1
PET: positron emission tomography
PIKK: phosphatidylinositol 3-kinase-related kinase
RAD50: radiation sensitivity abnormal 50
RAD51: radiation sensitivity abnormal 51
Rb1: retinoblastoma 1
ROS: reactive oxygen species
RPA: replication protein A
SABR: stereotactic ablative radiotherapy
SASP: senescence-associated secretory phenotype
SCLC: small cell lung cancer
SD: standard deviation
SEM: standard error of the mean
SNV: single nucleotide variation
SSB: single strand-break
ssDNA: single-stranded DNA
STING: stimulator of interferon genes
TGF- β: Transforming growth factor β
TLR: Toll-like receptor
TOPBP1: topoisomerase (DNA) II Binding Protein 1
tRTX: thoracic radiotherapy
UHBI: upper half body irradiation
V20: radiation dose received by 20 % of lung volume
VC: vinyl carbamate
VCO: vinyl carbamate epoxide
WTI**:** whole thorax irradiation

1. Introduction

Lung cancer is the most common type of cancer worldwide (13%) and is responsible for 19.4% of cancer-related deaths (Ferlay et al., 2015). The overall survival for this malignancy is poor – in the UK, only 32% of patients survive for more than 1 year after diagnosis (Cancer Research UK, 2014c). The disease is divided in two main histological subtypes: small cell lung cancer (SCLC) and non-small cell lung cancer (NSCLC). The latter accounts for 85% of lung cancer cases of which 40% are adenocarcinomas, 25-30% are squamous cell carcinomas and 10-15% are large cell carcinomas (Wood, Pernemalm, Crosbie, & Whetton, 2015). Although SCLC patients are virtually all smokers, and the great majority of NSCLC cases are smoking-related, lung cancer in never-smoker patients may account for up to 25% of all cases of lung cancer, with a varied geographic distribution, and for 300 000 deaths every year (Parkin, Bray, Ferlay, & Pisani, 2005).

Currently, NSCLC patients are diagnosed by bronchoscopy and imaging techniques such as chest X-rays, computerised tomography (CT) or positron emission tomography (PET). Patients with a positive diagnosis will then be staged according to the size of the tumour(s), involvement of lymph nodes and presence of metastasis in distant organs. To date, most NSCLC patients are diagnosed with stage IV disease, in which case one year survival rates are 15% for men and 19% for women in the UK (Cancer Research UK, 2014b). This data illustrates the need for improving both early stage diagnosis and treatment options for advanced disease. Table 1.1 summarises the survival rates per stage at diagnosis in the UK.

Table 1.1. NSCLC stage at diagnosis and 5-year survival rates in the UK.

Stage	General description [1]	Stage at first diagnosis in England (%) [2]	5-year survival rate in the UK (%) [3]
I	Tumour of 5 cm or less without evidence of invasion	15	35
II	Any tumour size as long as not invading major extra-lung structures; involvement of ipsilateral/intrapulmonary lymph nodes	7	21
III	Any tumour size; involvement of contralateral lymph nodes, no distant metastasis	19	6
IV	Presence of distant metastasis	48	N/A [4]
unknown	-	10	6

[1] for more a detailed description, refer to Supplementary Table 1 and Supplementary Table 2.
[2] from (Cancer Research UK, 2014a).
[3] from (Cancer Research UK, 2014b).
[4] Stage IV survival could not be calculated at five years due to the small number of people surviving more than two years.

Based on the stage of the disease, NSCLC patients will receive a treatment plan designed, ideally, by a multi-disciplinary team (Table 1.2). Usually, patients with stage I or II disease will undergo surgery alone, with the possible addition of radiotherapy in those cases where positive margins are present post-surgery. For inoperable stage I and II disease, radical radiotherapy is the usual treatment option, given as conventional fractionation (total of 60 to 70 Gy given in fractions totalising 10 Gy per week), accelerated fractionation (total of 60 to 70 Gy given in fractions totalising more than 10 Gy per week) or stereotactic ablative radiotherapy (SABR; up to 5 fractions ranging from 7.5 to 20 Gy). Patients with operable stage IIIA disease have similar treatment options (i.e., are given follow-up radiotherapy only when presenting positive margins

post-surgery); nevertheless, in the case of inoperable patients, radiotherapy will be offered and patients may also receive concurrent chemotherapy. Locally advanced stage IIIB patients, in contrast, are usually treated with palliative intent, and according to their performance status, will be offered radiotherapy or chemotherapy monotherapies, or concurrent/sequential chemoradiotherapy. Patients with metastatic stage IV disease will usually receive platinum-based chemotherapy, and if the tumour tests positive for mutations in EGFR or ALK, they may also be offered an appropriate targeted therapy (e.g. gefitinib or crizotinib). Patients with stage IV disease may also receive additional palliative radiotherapy. From Table 1.2, it is noticeable that radiotherapy is a treatment modality used throughout all stages of the disease, and therefore the development of strategies to increase its therapeutic potential are encouraged.

Table 1.2. NSCLC treatment options according to stage. Patient management estimates are in red. Modified from (London Cancer, 2013).

Stage	Decision 1	Decision 2	Therapy
Stage I	Surgery 80%	Complete resection	No radiotherapy
		Positive margins	Radical radiotherapy
	No surgery – inoperable 20%		Radical radiotherapy
Stage II	Surgery 80%	Complete resection	No radiotherapy
		Positive margins	Radical radiotherapy
	No surgery – inoperable 20%		Radical radiotherapy
Stage IIIA	Surgery 10 %	N0-1	No radiotherapy
		Positive margin or ≥ N2	Radical radiotherapy
	No surgery 90%		Radical radiotherapy Concurrent chemoradiotherapy Palliative radiotherapy
Stage IIIB	Good performance status 50%		Palliative radiotherapy Concurrent chemoradiotherapy
	Poor performance status 50%		Palliative chemotherapy Palliative radiotherapy
Stage IV	Focal symptoms 50%		Palliative chemotherapy Targeted therapy Palliative radiotherapy
	No focal symptoms 50%		No radiotherapy

Radiotherapy is used as an anti-cancer treatment primarily due to its cell killing potential. Highly energised photons interact with the tissue in the field of radiation and oxidise molecules such as DNA, lipids, proteins and water. The interaction with water molecules leads to the formation of reactive oxygen species (ROS) that will then have the potential to interact with

other molecules and indirectly amplify the damage caused by radiation. The most lethal of those interactions (both though direct or indirect interaction) is radiation-induced DNA damage, especially DNA double strand breaks (DNA DSBs) (Santivasi & Xia, 2014; Willers, Dahm-Daphi, & Powell, 2004). Direct interaction of radiation with DNA can lead to base or nucleotide structure alteration or strand breaks. Importantly, clustered damage along the track of radiation can lead to the formation of DNA DSBs (Figure 1.1). However, with low linear energy transfer (LET) radiation such as photons, the oxidative damage is mostly at single sites in the form of base/nucleotide damage (Nikjoo, O'Neill, Wilson, & Goodhead, 2001; J. F. Ward, 1988).

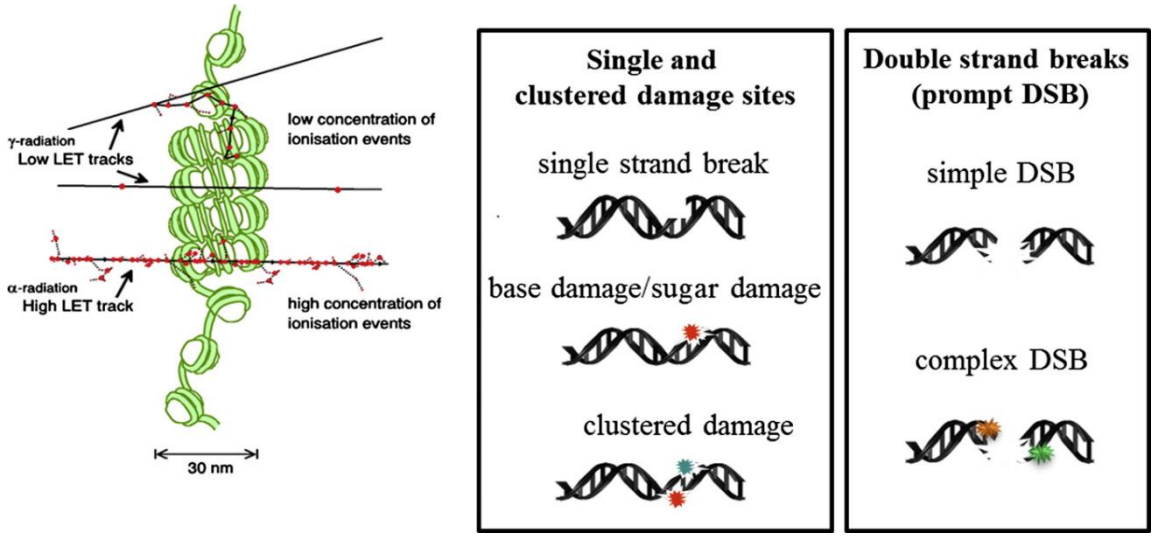


Figure 1.1. DNA damage generated by the direct interaction with radiation tracks. Single and double strand breaks can be induced, as well as nucleotide structural alteration. LET: linear energy transfer. DSB: double strand break. SSB: single strand break. Reproduced from (Lomax, Folkes, & O'Neill, 2013).

According to the type of DNA damage and the cell cycle phase, an appropriate DNA damage repair pathway will be initiated. In short, base/nucleotide damage will be repaired through base excision repair (BER) or nucleotide excision repair (NER), single strand breaks (SSBs) will be mostly repaired by BER, and double strand breaks (DSBs) will be repaired through homologous

recombination (HR) or non-homologous end joining (NHEJ) (Figure 1.2). BER and HR are considered to be error-free pathways as the complementary strand or sister chromatid are used as templates; NHEJ, in contrast, is considered error-prone as it usually involves loss of genetic material. HR requires close proximity of a sister chromatid; therefore, it does not occur during G0/G1 cell cycle phases or in unreplicated DNA in S phase. The outcomes once DDR is activated are recovery (repair), senescence or cell death. Of note, the killing potential of radiotherapy is not restricted to tumour cells, and can also affect normal tissue cells, but is thought to be higher in cancer cells as they have impaired DNA repair pathways (S. P. Jackson & Bartek, 2009). Not surprisingly, modulation of DNA damage response has been investigated as an approach to potentiate the cell killing effect of radiation, as already shown preclinically and more recently culminating in phase I clinical trials (O'Connor, 2015). This will be further discussed in Chapter 5.

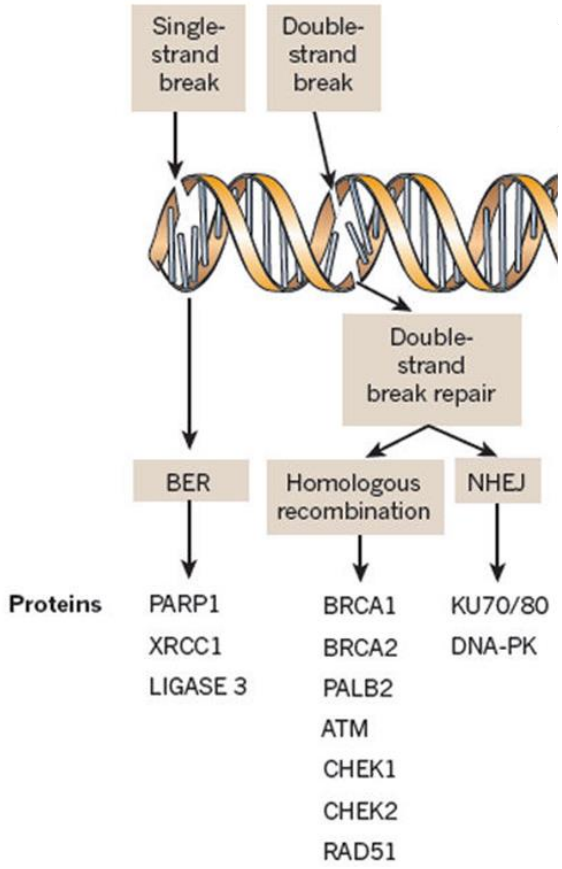


Figure 1.2. DNA strand break repair pathways. Upon single strand break, usually the base excision repair (BER) pathway will be activated, whilst upon double strand break, homologous recombination or non-homologous end joining (NHEJ) will be initiated. Selected proteins involved in those pathways are listed. Reproduced from (Lord & Ashworth, 2012).

Besides the initiation of DDR upon radiation treatment, cellular damage leads to the production of 'damage-associated molecular patterns' or DAMPs, which are recognised by Toll-like receptors (TLRs), among others, present in resident immune cells, such as alveolar macrophages in the lung. In turn, activated macrophages will produce and secrete a range of pro-inflammatory cytokines that lead to the recruitment of other immune cells and the establishment of acute inflammation. For instance, in a model of inflammatory kidney disease, stimulated alveolar macrophages have been reported to produce keratinocyte chemoattractant (KC), a pro-inflammatory cytokine known to act as a chemoattract for neutrophils. This happens through

the binding of KC to neutrophil receptors (C-X-C motif chemokine receptor 2, CXCR2), which leads to priming and extravasation of neutrophils from the blood stream to the site of damage (Altmann et al., 2012). Another cytokine produced by activated macrophages is interleukin 6 (IL-6), which is reported to contribute to the 'emergency' production of neutrophils in the bone marrow (Kishimoto, Akira, Narazaki, & Taga, 1995; Walker et al., 2008).

Radiation has also been reported to induce inflammation by direct regulation of inflammation-related genes, interaction with the cell membrane, activation of receptor tyrosine kinases and induction of cytokine production (Multhoff & Radons, 2012). Also, DDR proteins have been linked to the activation of the immune system through the stimulator of interferon genes (STING) signalling and other mechanisms, such as induction of nuclear factor kappa B (NF-κB) dependent transcription (Nakad & Schumacher, 2016). Additionally, a link between senescence and inflammation has been explored recently through the induction of a senescence-associated secretory phenotype (SASP), upon which cells secrete cytokines and stimulate immune response, representing another mechanisms that could link radiation and immune system activation (Coppé, Desprez, Krtolica, & Campisi, 2010).

Not surprisingly, approaches looking at improving radiation-induced tumour cell killing have explored the interaction between radiation and the tumour microenvironment (Schaue & Mcbride, 2015). For instance, tumours are known to have hypoxic regions in which cells are highly radioresistant. Therefore, drugs that selectively target radioresistant hypoxic cells, such as tirapazamine via the production of free radicals and subsequent DNA damage, have been studied, although none has yet been approved for clinical practice (Begg, Stewart, & Vens, 2011). Modulation of the immune system is also currently being explored to increase the tumour killing potential of radiotherapy. For instance, modulating the survival of T-cells by the

use of anti- programmed death 1 (PD1) and anti-programmed death ligand 1 (PD-L1) antibodies in combination with radiation has shown promising preclinical results and is now being evaluated in several clinical trials (Weichselbaum, Liang, Deng, & Fu, 2017). In support of this approach, recently, the anti–PD-L1 antibody durvalumab, showed marked improvements in progression-free survival in patients with inoperable stage III NSCLC compared to placebo when administered after chemoradiotherapy in a phase 3 clinical trial (Antonia et al., 2017).

As mentioned before, radiation not only leads to tumour cell killing, but also affects the normal tissue. Radiotherapy-associated side effects are usually divided in early (or acute, within days or weeks after treatment) and late (or long-term, within a month or years after treatment). Normal tissues have a pool of cells with replicative potential believed to act as tissue stem cells. It is believed that radiation can kill those tissue stem cells, thereby limiting the renewal capacity of normal tissues. This is the most widely accepted explanation for the early side effects of radiotherapy, as tissues with rapid turnover are affected shortly after radiotherapy treatment. This rationale could also explain in part the late effects as a 'delayed' response of tissues with a long turnover time, but it is not completely satisfactory as the late effects usually not only represent defective function of tissues due to loss of cell viability, but are also associated with exacerbated tissue remodelling. Therefore, it has been proposed that the late effects of radiation especially could be linked to the activation of immune response (Bentzen, 2006).

The main acute side effects associated with thoracic radiotherapy (mostly used for lung, breast and oesophageal cancer) are skin and oesophageal toxicity, whereas cardiac toxicity, pneumonitis and pulmonary fibrosis develop as late side effects (Baker & Fairchild, 2016; Carver et al., 2007). Early side effects (dermatitis and oesophagitis) have the highest incidence but are usually reversible and not life-threatening. The clinical management of those side effects

consists of careful planning of radiotherapy to avoid irradiation of as much normal tissue as possible and, upon onset, patients receive palliative care with topical creams, nutritional support and analgesics (Bolderston et al., 2006; Harris et al., 2012; Werner-Wasik, Yorke, Deasy, Nam, & Marks, 2010). Pneumonitis, defined as lung inflammation, usually develops within 3 months after radiotherapy treatment, and patients presenting with pneumonitis are usually treated palliatively with corticosteroids. Pulmonary fibrosis, on the other hand, usually takes at least 6 months to develop (but can occur as late as several years after treatment) and is defined as the accumulation of extracellular matrix in the lung tissue and, to date, there is no approved therapy for this life-threatening side effect (Sekine et al., 2006).

Numerous reviews have synthesised the current knowledge on the mechanisms of radiation-induced lung toxicity but despite the large amount of research, the underlying mechanisms are yet to be completely revealed (Cappuccini et al., 2011; Ghafoori, Marks, Vujaskovic, & Kelsey, 2008; Graves, Siddiqui, Anscher, & Movsas, 2010; Kainthola et al., 2017; Tsoutsou & Koukourakis, 2006). The general understanding is that initial damage triggers an acute stimulation of the immune system that develops into chronic inflammation (transient pneumonitis phase), culminating in excess deposition of extracellular matrix and impaired lung function (establishment of irreversible fibrosis) (Figure 1.3). Over the years, several contributors to this process have been described and studied, especially cytokines, believed to be responsible for the systemic and prolonged effects of thoracic radiation (Rubin, Johnston, Williams, McDonald, & Finkelstein, 1995). Of note is the role of different cellular components in this response, such as immune cells, endothelial cells, alveolar cells and stromal cells (Almeida et al., 2013; Andersson-Sjöland, Karlsson, & Rydell-Törmänen, 2016; Citrin et al., 2013; Rock et al., 2011).

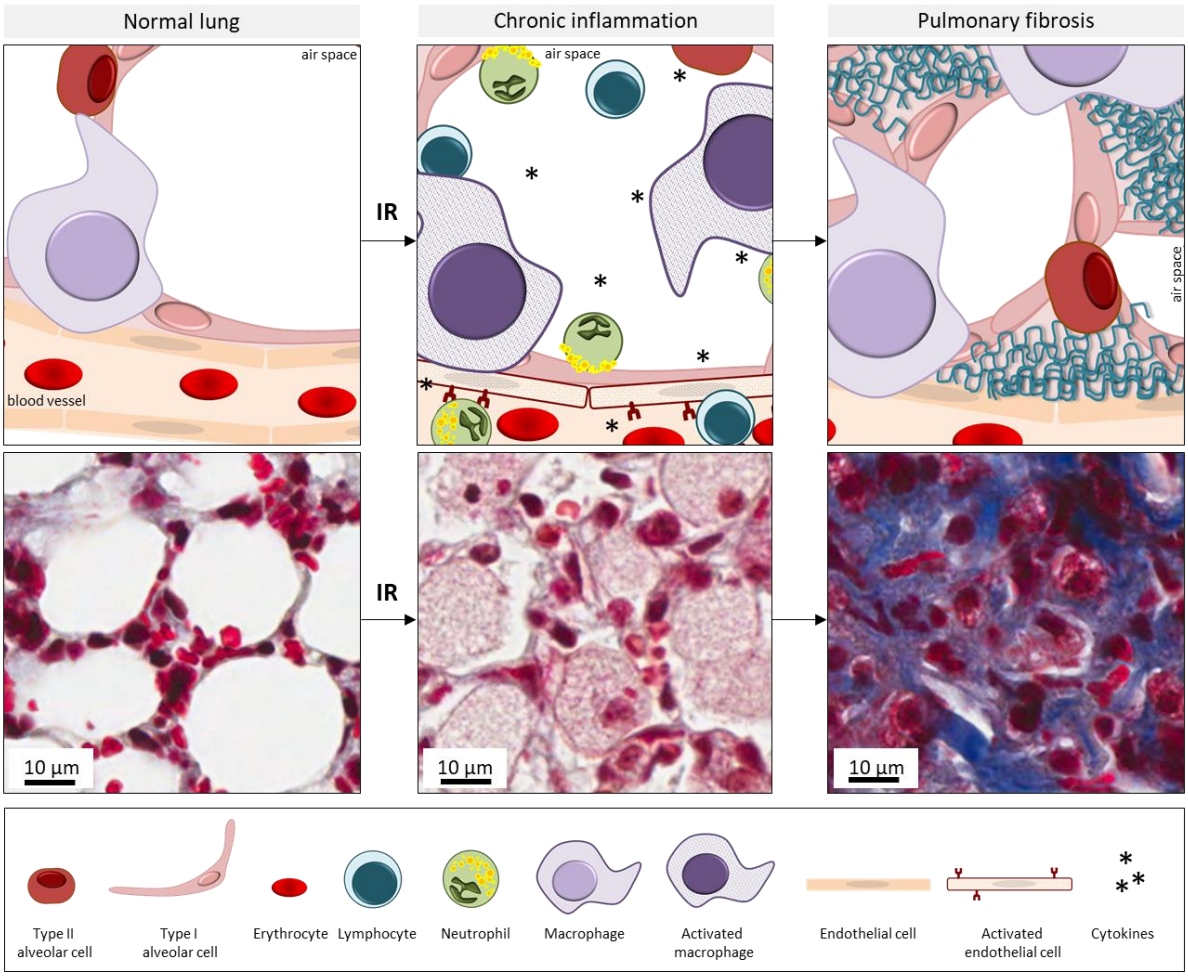


Figure 1.3. Radiation-induced pulmonary fibrosis. The top panel shows a schematic of the events following lung irradiation (IR). Radiation leads to the activation of the immune system and recruitment of immune cells to the lung. Upon treatment with radiation, activated macrophages accumulate in the lung tissue (~15 weeks post-irradiation). Chronic inflammation can take place through a mechanism that is still unknown and culminate in over-scaring of lung tissue (fibrosis). Collagen (in blue) accumulation leads to reduction of alveolar space. In the bottom panel, examples of Masson's trichrome stained mouse lung samples from the present work are shown.

Pneumonitis can be asymptomatic for weeks (referred to as 'latent period'), and the incidence of symptomatic pneumonitis ranges between 5-15% of patients (Abid, Malhotra, & Perry, 2001). Nevertheless, using more sensitive diagnosing techniques, the incidence can reach 43% of patients receiving thoracic radiotherapy (Movsas, Raffin, Epstein, & Link, 1997). Pneumonitis generally occurs 1-3 months after radiotherapy and is characterised by protein

leakage into the alveolar space, alveolar septa thickening, oedema, capillary alterations and immune cell infiltration (Tsoutsou & Koukourakis, 2006). Importantly, a clinical report showed that the incidence and grade of pneumonitis are significantly related to the volume of the lung receiving 20 Gy (V20); for instance, the two patients (of 71 patients in total) in the reported study that developed fatal pneumonitis had a mean V20 of 35% (Tsujino et al., 2003). Of note, the current London Cancer guidelines for lung irradiation determines that the V20 should reach a maximum of 35% but preferably less than 30% (London Cancer, 2013).

Pulmonary fibrosis can develop in up to 10-15% of patients who have received lung irradiation (Mazeron et al., 2010). The radiation dose plays an important role in the prevalence of fibrosis (Palma, van Sornsen de Koste, Verbakel, Vincent, & Senan, 2011), and a study showed that 99% of patients receiving a SABR regimen to treat lung tumours developed mild to moderated radiological changes in the irradiated lung areas within 36 months after treatment, with effects progressing even 2 years post-treatment (Figure 1.4) (Dahele, Palma, Lagerwaard, Slotman, & Senan, 2011). Therefore, dose escalation should be considered carefully, especially now that meta-analysis of randomised clinical trials have been published showing that higher radiation doses can lead to longer survival in lung cancer patients, even though the onset of normal tissue toxicity was not evaluated in the mentioned study (Ramroth et al., 2016).

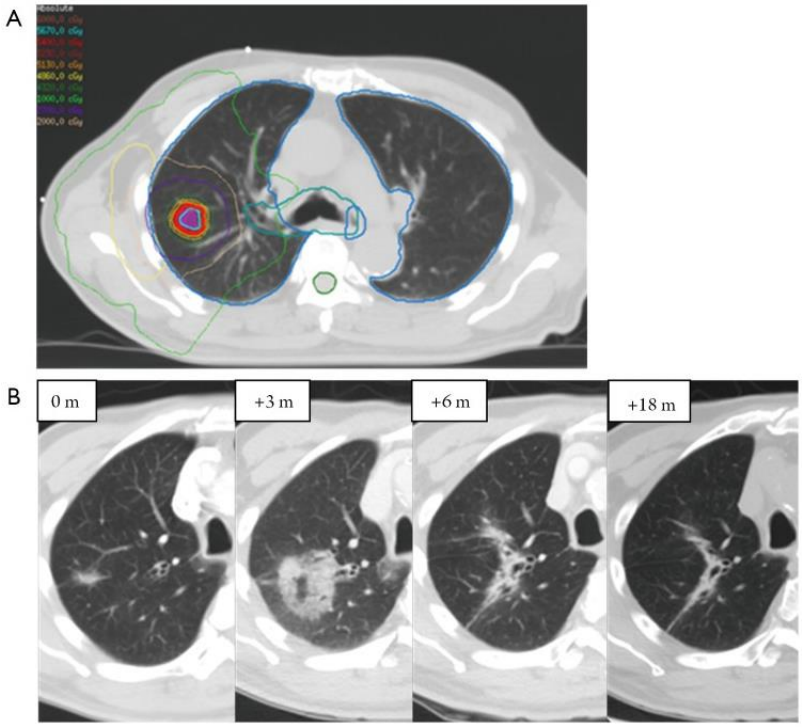


Figure 1.4. Radiological changes following stereotactic ablative radiotherapy (SABR). This lung adenocarcinoma patient received 54 Gy in 3 fractions with the above treatment plan (A). Radiological changes are seen (B) where 0 m indicates the pre-treatment lesion measuring 2.0 cm. At 3 months post-SABR, further enlargement of a ground-glass semi-solid opacity and at 6 months there is interval reduction in size and a decrease in ground-glass opacity, with ongoing reduction in size by 18 months. Reproduced from (Mattonen, Huang, Ward, Senan, & Palma, 2014).

The incidence of radiation-induced side effects has decreased in the past decades with the development of more sophisticated radiation planning techniques, dose adjustment, fractionation schemes and adjuvant treatments (Fenwick et al., 2009). For instance, the use of techniques such as intensity-modulated radiotherapy (IMRT) has been shown to decrease the dose delivery to normal tissues at risk in the treatment of lung cancer (Christodoulou, Bayman, McCloskey, Rowbottom, & Faivre-Finn, 2014). In addition, the use of imaging to guide radiation delivery has made it possible to escalate doses given to the tumours. However, normal tissue damage still represents a problem in the clinic, especially in the treatment of centrally

localised tumours when avoiding sensitive normal tissue is even more challenging (Tekatli et al., 2016; Tekatli, Senan, Dahele, Slotman, & Verbakel, 2015).

It has been shown that quality of life is a good prognostic factor for long term survival in locally advanced lung cancer patients, therefore decreasing radiation-induced lung damage is paramount to increase survival (Movsas et al., 2009). Several therapeutic approaches to overcome radiation-induced pneumonitis and fibrosis have been investigated in preclinical models and in the clinic. The most common approaches include targeting free radical production, inflammatory cell recruitment, cytokines and growth factors, as recently reviewed in (Deng et al., 2017; Rajan Radha & Chandrasekharan, 2017). As mentioned previously, the management of patients with radiation-induced lung damage is often by the use of corticosteroids, but not only this is purely a palliative approach, it has been shown that the pathology often recurs after therapy withdrawal (Otani, Nishiyama, Ito, Kawaguchi, & Inaji, 2014).

Despite all the effort, the only radioprotector approved to date (for radiotherapy in head and neck cancer patients) is amifostine. This prodrug becomes activated once dephosphorylated by alkaline phosphatases. The main mechanism that accounts for the role of amifostine as a radioprotector is its ability as an oxygen scavenger once activated. Importantly, due to low pH, tumour cells do not activate amifostine to the same extent as normal cells, which means amifostine is a selective radioprotector (Kouvaris, Kouloulias, & Vlahos, 2007). Nevertheless, in a large randomised phase III clinical trial it did not prove to be radioprotective when given prior to lung radiotherapy and a meta-analysis of 16 clinical trials also questioned its efficacy (Devine & Marignol, 2016; Movsas et al., 2005).

Another approach to decrease normal tissue toxicity of radiotherapy is the use of fractionated schedules of radiation. In addition to sparing of normal tissue, it has been proposed that fractionation can increase tumour cell killing due to the '5 Rs' of radiotherapy, namely repair, reoxygenation, repopulation, redistribution in cell cycle and radiosensitivity (Good & Harrington, 2013). Therefore, the use of fractionated schedules can increase the therapeutic index i.e. promote tumour control while avoiding normal tissue toxicity (Marcu, 2010; Shibamoto, Miyakawa, Otsuka, & Iwata, 2016). Recently, a debate around the ideal fractionation scheme has been raised. A meta-analysis of data from 12 clinical trials showed that patients with non-metastatic NSCLC derived a significant overall benefit from accelerated hyperfractionated radiotherapy (for instance, 40 fractions of 1.5 Gy twice daily) compared to conventional fractionation but that was accompanied by increased acute oesophageal toxicity (Mauguen et al., 2012). In contrast, reports on the use of hypofractionation have indicated that it is an effective option for the treatment of centrally localised tumours, reducing the onset of toxicity when compared to conventional SABR (Baker, Dahele, Lagerwaard, & Senan, 2016; Barriger et al., 2012; Haseltine et al., 2016; Tekatli et al., 2016; Timmerman et al., 2003, 2006).

Considering the longstanding issue of normal tissue toxicity induced by radiation and combination treatments, experimental models have been used to study radiation-induced normal tissue responses preclinically. A comprehensive review recently published by Dabjan et. al. looking at 538 papers from 1970 to 2015 showed the mouse was the predominant species used (65%), followed by rats (25%), dogs and swine (3%), rabbits (2%), and non-human primates (1%). The most commonly used mouse strain in the recent years has been C57BL/6J, followed by CBA, C3H and Balb-c. Also, among the studies using mice, 83% used whole thorax irradiation, 11% whole body irradiation, 1% upper half body irradiation and 5% localised

regional lung irradiation. The diversity of irradiated field and fractionation schemes makes it challenging to correlate results from different studies and to translate preclinical data into information that would be useful in the treatment of patients (Dabjan et al., 2016).

Several issues have been raised when trying to translate preclinical findings to the bedside. In humans, following thoracic radiation, patients can develop pneumonitis, pulmonary fibrosis, both or neither. In contrast, probably because laboratory animals are inbred and therefore have homogeneous genetic background within the same strain, there are strains known to be either pneumonitis- or fibrosis-prone, as opposed to presenting a mixed phenotype. For instance, C57BL/6J mice are fibrosis-prone and C3H and CBA mice are pneumonitis-prone. Nevertheless, similarities are found in the responses of humans and mice, such as the impact of the volume of irradiated lung, dose and fractionation schedules in the late effects observed. Other issues concerning preclinical models of radiation-induced lung damage have also been raised by Dabjan et. al., such as the duration of the 'latent period', the impact of sex and the direct attribution of thoracic radiation lethality to pulmonary fibrosis. Therefore, it is challenging to identify one mouse model as the most predictable of human response (Dabjan et al., 2016).

Considering the current knowledge regarding normal tissue responses to radiation, we hypothesised that pulmonary fibrosis is observed when the initial acute inflammatory response is not resolved and develops to chronic inflammation. This would exacerbate the tissue remodelling signalling and lead to pulmonary fibrosis (Figure 1.5). Therefore, any approach under investigation to improve radiotherapy anti-tumour effect should ideally be tested for its modulation of normal tissues as well. Failure to do so before reaching the clinic could lead to decreased quality of life and therefore would not be beneficial to patients.

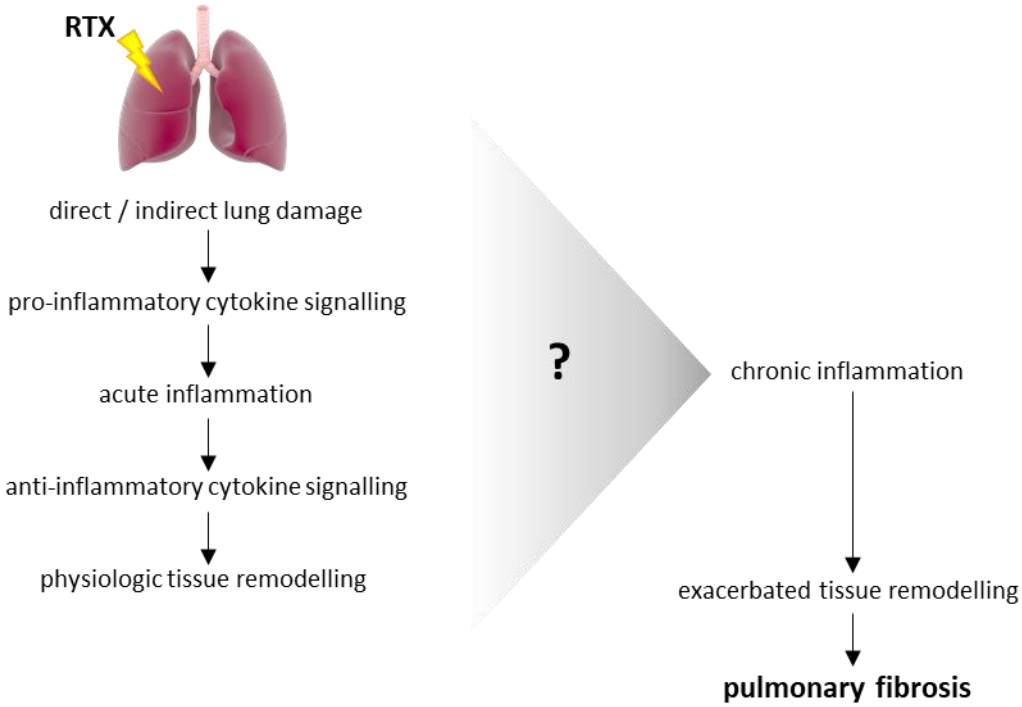


Figure 1.5. The development of radiation-induced pulmonary fibrosis. Upon radiation, the immune system is activated and when this response is not resolved, chronic inflammation leads to pathological signalling for tissue remodelling culminating with fibrosis. The mechanisms of transition from acute to chronic inflammation in this disease are not yet understood.

Therefore, the general aims of this work are to: (i) characterise the early and late response of normal lung cells to radiation, (ii) investigate approaches to decrease radiation-induced normal tissue damage through modulation of the inflammatory response, (iii) assess the impact of modulation of DDR in combination with radiation on normal tissue responses and (iv) establish a mouse model with the potential to assess the therapeutic index of novel approaches combined with thoracic radiotherapy. The specific aims as wells as more detailed background are presented at the beginning of each result chapter.

2. Methods

2.1.Reagents

A list of the providers and catalogue numbers of reagents used in the experiments described in this thesis is provided in Table 2.1. Manufactures of equipment used in this work were indicated throughout this chapter.

Table 2.1. Reagents.

Reagent	Company	Catalogue number
Acetic Acid	BDH Chemicals	100012K
Agarose (low melting point)	Bio-Rad	161-3111
Amersham ECL Prime Western Blotting Detection Reagent	GE Healthcare Life Sciences	RPN2232
Antisedan	Orion Pharma	-
Bovine serum albumin	Sigma-Aldrich	B4287
Citroclear	TCS Biosciences	HC5005
Criterion™ TGX gels	Bio-Rad	5671085
Crystal violet	Merck	1.15940.0025
Dimethylacetamide	Sigma-Aldrich	ARK2190

Dimethylsulfoxide (DMSO)	Thermo Scientific	85190
Dormitor	Orion Pharma	-
DPX mountant for histology	Sigma-Aldrich	06522
Dulbecco modified Eagle medium plus F-12 medium	Life Technologies	12634-010
EDTA	BDH Chemicals	4438882G
ECL™ Prime Western Blotting Detection Reagent	GE	RPN2236
Elite ABC kit (Rat IgG)	Vectastain	PK-6104
Ethanol	Fisher Chemicals	E/0665DF/17
Eosin	Sigma-Aldrich	HT110132
Foetal bovine serum	Sigma-Aldrich	F7524
Formalin (10 % neutral buffered)	Sigma-Aldrich	HT501128
GlutaMAX	Life Technologies	35050-038
Glycerol	VWR	24388260
Goat serum	Millipore	S26-100ML
Haematoxylin (Harris')	VWR	351945S
Hoechst	Sigma-Aldrich	H6024
Hydrochloric acid	VWR	20252.290
Hydrogen peroxide 30% (100 volumes)	Fisher Chemical	H/1750/15
Hydroxyproline	Sigma-Aldrich	H54409

Ketaset	Orion Pharma	-
Kolliphor HS 15	Sigma-Aldrich	42966
Lithium carbonate	Scientific Laboratory Supplies	CHE2354
Magnesium sulphate	Scientific Laboratory Supplies	CHE2456
Masson's trichrome kit	Sigma-Aldrich	HT10132
Matrigel	Corning	356234
Methanol	Sigma-Aldrich	32213
Menadione	Supelco	47775
Mini-PROTEAN® Precast gels	Bio-Rad	4561086
Mouse CXCL1/KC Quantikine ELISA Kit	R&D Systems	MKC00B
Mouse IL-6 Quantikine ELISA Kit	R&D Systems	M6000B
Mouse TGF-β1 Quantikine ELISA Kit	R&D Systems	MB100B
Myeloperoxidase	Sigma-Aldrich	M6908
Nitrocellulose membrane (0.45 µm pores)	Bio-Rad	162-0115
NP-40 (Igepal)	Sigma-Aldrich	I3021
Paraffin (Histoplast)	Thermo Scientific	6774060
Paraformaldehyde	BDH Chemicals	28794.295

Penicillin-streptomycin	Life Technologies	15070-063
Pentobarbitone sodium (Pentoject®)	Animalcare Ltd.	-
Phosphate-buffered saline (PBS)	Sigma-Aldrich	94417
Poly(ethylene glycol)	Sigma-Aldrich	91893
Ponceau S solution	Sigma-Aldrich	P7170
Protease inhibitor	Roche	11697498001
REAL EnVision Detection System HRP/DAB, Rb/Mo	Dako	K406511
Sample buffer, Laemmli 2x concentrated	Sigma-Aldrich	S3401
Sodium bicarbonate	Corning	61-065-RO
Sodium chloride (NaCl)	BDH Chemicals	443824T
Sodium citrate (pre-prepared tubes)	Starsted	41.1350.005
Sodium dodecylsulphate (SDS)	Applichem	A0676,0500
Sodium fluoride (NaF)	Sigma-Aldrich	450022
Sodium hydroxide (NaOH)	BDH Chemicals	28244.262
Sodium orthovanadate (Na_3VO_4)	Sigma-Aldrich	450243-10G
SYBR Gold	Life Technologies	S11494
Running buffer (10x)	Bio-Rad	1610732
Transfer buffer (10x)	Bio-Rad	1610734
Tris-base;	Calbiochem	648310
Tris-HCl	Promega	H5121

Triton X-100	BDH Chemicals	437002A
Trypsin-EDTA (0.25%)	Life Technologies	25200-056
TWEEN 20	Sigma-Aldrich	P1379
Urethane	Sigma-Aldrich	U2857
Xylene	Sigma-Aldrich	534056

2.2.In vivo studies

All in vivo studies were performed according to national guidelines under a project license issued by the UK Home Office under the UK Animals (Scientific Procedures) Act of 1986 which was approved by a local animal welfare ethical review committee.

2.2.1. Mouse strains

Four mouse strains were used in this project: C57BL/6J, B6.129X1-Mpo$^{tm1Lus/J}$, A/J and CD1 nude. Mice were purchased from Charles Rivers Laboratories (UK), Jackson Laboratories (USA), Envigo (UK) and Charles Rivers Laboratories (UK), respectively. Experiments were performed with female mice (unless otherwise specified) at 4-7 days post-delivery and when mice were 6-10 weeks old. A pair of B6.129X1-Mpo$^{tm1Lus/J}$ was purchased and used for breeding. This strain was originated by the Lusis group from RW4 embryonic cells (129/SvJ

strain) transfected with a myeloperoxidase (MPO) targeting vector. Mice with mutated allele of MPO were bred to C57BL/6J (Brennan et al., 2001). The mutated MPO allele contains a premature stop codon, leading to absence of MPO protein. Breeding was performed in house to expand the cohort of mice and hereafter these mice will be referred to as MPO knock-out (MPO KO). As suggested by the Jackson Laboratories, we used C57BL/6J as the control strain for our experiments, which will be referred to as MPO wild-type (MPO WT).

2.2.2. Irradiation

Mice were anaesthetised by intra peritoneal (i.p.) injection of 100 µL of a mixed solution at final concentration of 100 µg/ml Dormitor® and 8 mg/ml Ketaset® in saline. Within 5-10 minutes mice were fully anaesthetised and then were place inside the irradiator (Gulmay Medical RS320). Lead shields were used to cover the animals leaving only the thorax exposed (approximately 1 cm x 2 cm) or the tumour exposed in the case of xenograft studies. X-rays were delivered at a rate of 1.82 Gy/min. Radiation was given at 300 kV and 10 mA, for 1 min and 23 sec (2.5 Gy), 2 min and 45 sec (5 Gy) or 5 min and 30 sec (10 Gy). Mice were then injected with 100 µL of Antisedan® (i.p.) at a final concentration of 200 µg/mL in saline and kept in an acclimatised rack at 37 °C for approximately 30 minutes until they were fully recovered from anaesthesia. Animals treated with fractionated radiation schedules were given 2 days to recover between treatments (Figure 2.1). Fractionated schedules were given as described in Table 2.2. In each result chapter, a simplified schematic for the experimental design

will be displayed, but the schedule below was always performed, allowing for 2 days break between irradiation doses.

Schedule	Treatment (day)												
	1	2	3	4	5	6	7	8	9	10	11	12	13
4 x 5 Gy	X			X			X			X			
4 x 5 Gy + 2.5 Gy	X			X			X			X			X
5 x 5 Gy	X			X			X			X			X

Figure 2.1. Fractionated irradiation schedules. Mice were irradiated on the indicated days (X), leaving two days break for recovery between irradiation doses.

Table 2.2. Description of irradiation schedules.

Total dose (Gy)	Fractionation scheme	Equivalent in single dose (Gy)*	Biologically Effective Dose (Gy)*
20	4 x 5 Gy	11.4	48.6
22.5	4 x 5 Gy + 1 x 2.5 Gy	12.2	54.6
25	5 x 5 Gy	12.9	60.7

* obtained from http://www.nempconsulting.com/widgets/bed.php, considering lung $\alpha/\beta=3.5$.

For whole-thorax irradiation, mice were positioned as depicted in Figure 2.2 A, where an area of 2 cm x 2 cm colocalised with the thorax was exposed to irradiation (limited by the bottom of the bone externum and the top of the mouse's neck). As for irradiation of xenograft tumours, mice were positioned as depicted in Figure 2.2 B.

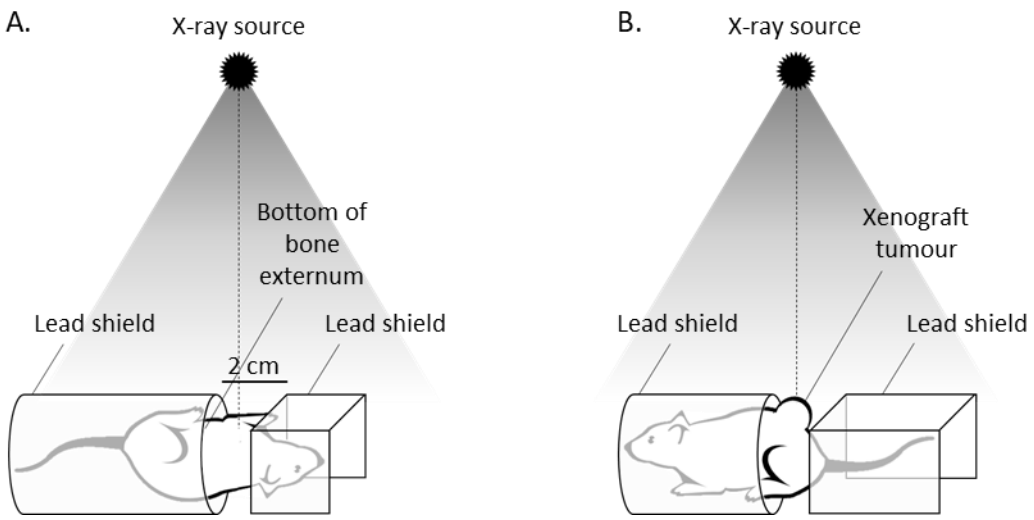


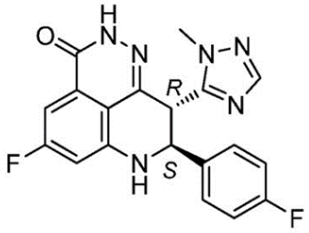
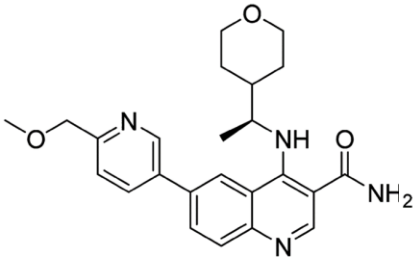
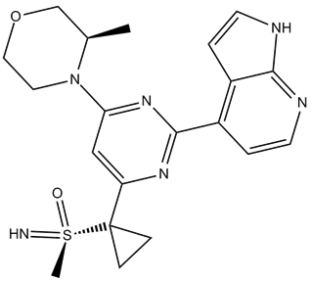
Figure 2.2. Mouse positioning and shielding during irradiation. Whole-thorax irradiation was performed by shielding of the head (above neck) and bottom body (below the externum bone), leaving 2 cm space between the shields to expose the thorax (A). For xenograft tumour irradiation, the area containing the tumour was exposed and the rest of the body was protected by lead shields (B).

2.2.3. Drugs and vehicles

The drug compounds used for in vivo experiments are listed in Table 2.3. AZ31 (ATM inhibitor) and AZD6738 (ATR inhibitor) were kindly provided by AstraZeneca. BMN673 (PARP inhibitor) was purchased from SELLECK. AZ31 was weighed and resuspended in DMSO and then in 20% captisol. The solution was gently mixed and once clear, it was diluted in distilled water to obtain the final desired concentration of vehicle and drug. A similar procedure was performed for AZD6738, which was weighed and resuspended in DMSO and then in 80% poly(ethylene glycol). The solution was gently mixed and once clear, it was further diluted in distilled water to obtain the final desired concentration of vehicle and drug. BMN673 was resuspended in dimethylacetamide and then diluted in 6% Kolliphor. Solutions were prepared fresh every week and were kept at 4°C between in vivo administrations. Mice were treated with

100 µl of treatment solution per10g of body weight by oral gavage (*per os*, p.o.) using plastic feeding tubes (Instech, FTP-20-38) connected to 1 mL syringes (Terumo, GS572).

Table 2.3. Drug compounds used for in vivo experiments.

Compound / Structure	Dose (mg/kg)	Vehicle	Reference
BMN673 (PARP inhibitor) 	0.33	10 % dimethylacetamide 6% Kolliphor HS 15 (in PBS)	(Shen et al., 2013)
AZ31 (ATM inhibitor) 	50	2.5% DMSO 10 % captisol (in distilled water)	(Degorce et al., 2016)
AZD6738 (ATR inhibitor) 	50	2.5% DMSO 40% poly(ethylene glycol) (in distilled water)	(Vendetti et al., 2015)

The dose of BMN673 used was based on the literature - it has been shown that 0.33 mg/kg shows antitumor activity in vivo in xenograft models of tumours carrying defects in DNA repair (BRCA mutations or PTEN deficiency). AZ31 and AZD673 doses were determined by a pharmacodynamic experiment with Calu6 xenografts. As described in section 2.3.4, tumour cells were injected subcutaneously in the back of CD1 nude mice and once tumours were established (100 mm^3 volume), mice were given a single dose of compound (50 mg/ml). One hour later, tumours were irradiated with a single dose of 10 Gy and mice were sacrificed at 2 h or 24 h after irradiation (Figure 2.3).

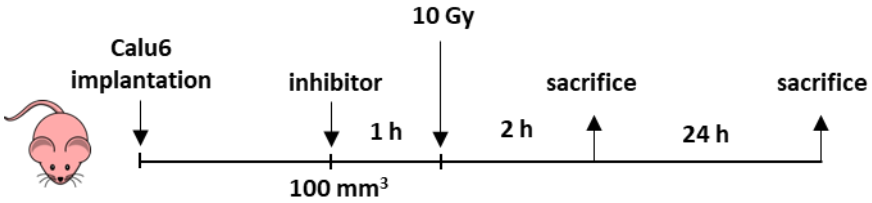


Figure 2.3. Experimental design for pharmacodynamic analysis of ATM and ATR inhibitors in Calu6 xenograft tumours. Calu6 cells ($5x10^6$) were subcutaneously injected in the back of CD1 nude mice. Once tumours reached 100 mm^3, mice were given 50 mg/kg of inhibitor orally (n=3 per group). One hour after treatment, tumours were locally irradiated (10 Gy) and sacrificed 2 h or 24 h later. Tumours were collected and fixed in formalin for further histological analysis.

To determine the effect of drugs on target activity, tumours were collected and fixed as described in section 2.3.5 and histochemistry was performed as described in section 2.4. ATM activity was measured by pKAP1 positivity and ATR activity was measured by pan-nuclear γH2AX positivity. Quantification of pKAP1-positive cells was performed using automated software as described in section 2.4.5 and quantification of pan-nuclear γH2AX was performed manually in 4 randomly selected fields of 240 µm x 160 µm per sample. We observed a decrease in the number of pKAP1-postive cells at 2 h post-irradiation in the group treated with 50 mg/kg

of AZ31 compared to the group that received radiation plus vehicle (Figure 2.4. A). At 24 h post-irradiation, both groups treated with IR + vehicle and IR + ATM inhibitor did not show detectable levels of pKAP1 staining. In addition, we observed an increase in the number of pan-nuclear γH2AX-postive cells at 24 h post-irradiation in the group treated with 50 mg/kg of AZD6738 compared to the group that received radiation plus vehicle (Figure 2.4. B). At 2 h post-irradiation, the same effect was observed (11 ± 8.6 % pan-nuclear γH2AX positive cells in the IR + ATRi group).

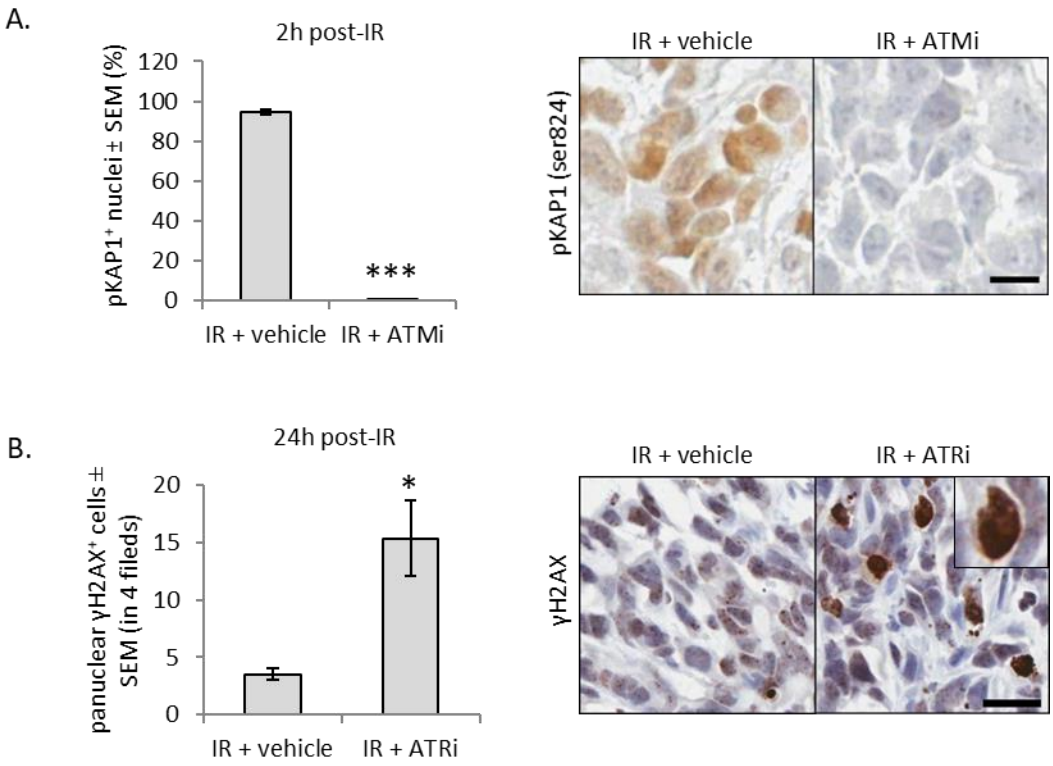


Figure 2.4. ATM and ATR inhibitors efficiently inhibited their targets. The group treated with ATM inhibitor in combination with radiation (IR + ATMi) showed decreased number of nuclei positive for pKAP1 (ser824) in comparison to IR + vehicle group as assessed by immunohistochemistry on tumours collected 2 h after radiation (A, IR: radiation). The number of pan-nuclear γH2AX-positive cells increased in the group treated with ATR inhibitor in combination with radiation (IR + ATRi) compared to IR + vehicle group as assessed by immunohistochemistry on tumours collected 24 h after radiation (B). Graph bars represent the average in the group (n=3 per group) and error bars represent the SEM; *p<0.05 and ***p<0.0005 compared to IR + vehicle group (t-test, one-tailed distribution, two-sample equal variance). Scale bars represent 10 µm (A) and 25 µm (B), inset image shows one individual cell with pan-nuclear γH2AX staining.

For experiments using combination of drug treatment with fractionated irradiation, drug treatment was given 1 h before and 24 h after each irradiation dose, allowing for 2 days break between irradiation doses (Figure 2.5). In each result chapter, a simplified schematic for the experimental design will be displayed, but the schedule below was always performed, allowing for 2 days break between irradiation doses.

Schedule	Treatment (day)													
	1	2	3	4	5	6	7	8	9	10	11	12	13	14
4 x 5 Gy	0X	0		0X	0		0X	0		0X	0			
5 x 5 Gy	0X	0		0X	0		0X	0		0X	0		0X	0

Figure 2.5. Schedule for drug administration in combination with fractionated irradiation. Mice were irradiated on days indicated by 'X' and treated with drug on days indicated by '0', allowing two days break for recovery between irradiation doses.

2.2.4. Establishment of subcutaneous xenograft tumours

We used Calu6 cells cultured as described in section 2.11 to establish xenograft tumours. A mixture of Calu6 cells resuspended in Advanced DMEM/ F12 (FBS and antibiotic free) and matrigel (in a proportion of 1:1) was prepared in advance and kept on ice. CD1 mice were anaesthetised with isoflurane (4% in air/oxygen for induction and 2-3% for maintenance; oxygen was supplied at a rate of 1-2 L/min). Once under anaesthesia, mice were injected subcutaneously in the back (approximately 1 cm above the base of the tail) with 100 µL of the mixture of cells and matrigel, such as each animal was inoculated with 5×10^6 cells. Anaesthesia was withdrawn and animals fully recovered. Experiments were performed once tumours

reached a volume of 100 mm^3, which was calculated using calliper measurements and applying the following formula:

$$\text{Volume } (mm^3) = ½ \times [\text{length (mm)} \times \text{width (mm)} \times \text{height (mm)}]$$

Mice were sacrificed at the appropriate time point according to the experimental design, once tumours reached 400 mm^3 or at 42 days post drug treatment, whichever happened first. Tumours were collected and fixed as described in section 2.4.5.

2.2.5. Induction of lung tumours with urethane

Female A/J mice (6-8 weeks old) were i.p. injected with 10 µL/ 10 mg body weight of freshly prepared solution of 10 % (w/v) urethane diluted in PBS. Urethane injection induced anaesthesia, and mice were kept on a warm pad (37 °C) until full recovery. A pilot experiment performed by Yanyan Jiang showed that at 6 and 12 weeks it was possible to detect tumours in the lung of A/J mice by histology (Figure 2.6). Therefore, for the experiments where the objective was to evaluate tumours early after irradiation, induction was planned to happen at 12 weeks before irradiation. In contrast, when tumour evaluation was happening only months post-irradiation, induction of tumours was planned 8 weeks before irradiation.

Mouse ID	Time post-injection	Tumours/lung
A1	6 weeks	1
A2	6 weeks	0
A3	6 weeks	1
A4	12 weeks	0
A5	12 weeks	1
A6	12 weeks	0
A7	24 weeks	2
A8	24 weeks	4
A9	24 weeks	3

Figure 2.6. Number of lung tumours detected in A/J mice injected with urethane. H&E slices were used to quantify tumours present at 6, 12 and 24 weeks in 3 animals per group.

2.2.6. Sacrifice, sample harvesting and processing

Mice were sacrificed with an i.p. injection of 200 µL of 200 mg/kg sodium pentobarbitone. Left lungs or xenograft tumours were collected and fixed in > 10 volumes of 4% paraformaldehyde or 10 % neutral buffered formalin for 24 h at 4°C and then transferred to 70% ethanol. Within 14 days of harvesting, lung samples or xenograft tumours were processed by an automated Tissue Processor (Leica, TP1050) through an ethanol series (70%, 80%, 80%, 95%, 100%, 100%), followed by xylene (3 baths) and then paraffin (3 baths). Samples were then embedded in paraffin blocks. Right lungs were fresh frozen in dry ice. Cardiac puncture was performed and 200 µL of blood was incubated in prepared tube containing 130 µL of 0.106 mol/L sodium citrate for 10 minutes at room temperature. Tubes were then kept on ice until centrifugation (10 minutes at 1500 g at room temperature). Plasma was collected and stored at -80 °C. In the experiment described at chapter 5.2, oesophagi were also collected following the 'swiss-roll technique' and fixed as described for the left lung (Moolenbeek & Ruitenberg, 1981).

2.2.7. Welfare end-points

Mice were observed daily for general welfare. Animals were weighed at least twice per week. Three specific adverse clinical signs were of particular note during the in vivo studies and required certain mice to be sacrificed as described in section 2.2.6. These adverse events were (i) more than 10% body weight loss for at least 2 consecutive days, or greater than 15% body weight loss on any individual day, or (ii) breathing impairment (persistent coughing or shallow breathing) or (iii) skin desquamation without signs of resolution within 48 h. Adverse events happening within 3 months of radiation treatment will be referred to as 'early effects' and adverse events happening after 3 months post-radiation will be referred to as 'late effects'.

2.2.8. Computer tomography scanning

Mice were anaesthetised as described in section 2.4.2. and placed in Small Animal Radiation Research Platform (SARRP) (Xstrahl Ltd., UK). Cone beam computed tomography (CT) images were acquired using 50kVp X-rays, with 720 projections taken at uniform intervals as the stage was rotated through 360° in a total scan time of 127 seconds. CT images were reconstructed using a modified Feldkamp-Davis-Kress reconstruction algorithm into 0.16 mm isotropic voxels. Imaging was performed by Staff in the Imaging Core of the Department of Oncology (University of Oxford, UK).

2.2.9. Magnetic Resonance Imaging (MRI)

MR imaging was performed by the Imaging Core at the University of Oxford. Mice were anaesthetised using isoflurane in air/oxygen (as described in section 2.2.4) before imaging and kept under maintenance anaesthesia during the imaging process. MRI was performed on a 4.7 T, 310 mm horizontal bore Varian Nuclear Magnetic Resonance Spectrometer (VNMRS) preclinical imaging system equipped with a 120 mm bore gradient insert capable of 400 mTesla/m in all three axes (Varian Inc, CA). Radiofrequency (RF) transmission and reception was performed with a 30 mm long, 25 mm quadrature birdcage coil (Rapid Biomedical GmbH, Germany). Balanced steady-state free precession (SSFP) scans were acquired with repetition time (TR): 2.684 ms, echo time: (TE) 1.342 ms, flip angle (FA): 20°, field of view (FOV): 48×24×24 mm3, matrix: 256×96×96 and RF hard pulse duration 16 μs. Prospective cardio-respiratory gating was performed with acquisition of 8 phase encode lines per cardiac R-wave and centric out ordering to align data acquisition to within a 25 ms window starting at the R-wave. Data were acquired with and without phase alternation of the RF transmitter and receiver. A maximum intensity projection (MIP) of the two data sets was performed to minimise banding artefacts in the final image.

Analysis of MR images was performed using the software ITK-SNAP ((Yushkevich et al., 2006)). The lungs were identified by automatic segmentation and tumours by manual segmentation. Afterwards, a 3D reconstruction of the segmented areas was obtained, and total tumour burden was calculated.

2.2.10. Plethysmography

To access lung function, we performed plethysmography using equipment developed by the Boris Vojnovic group and approved by the UK Home Office. The machine is composed of sealed chambers equipped with small electret-type microphone capsules which measure pressure changes derived from animal breathing. Mice were placed individually in the chambers and pressure change recording was started once breathing rates were normalised (approximately 2 minutes after animals were placed in the chamber). The software captured the 'breaths per minute' data for every second. The graphs on Figure 3.6 and Figure 4.9 show the average of data recorded during 180 seconds after the breathing pattern was normalised.

2.3. Cytokine profiling

To evaluate the plasma levels of cytokines, post whole-thorax irradiation, we used Quantikine® ELISA kits (R&D Systems). Enzyme-Linked Immunosorbent Assays (ELISAs) rely on the ability of antibodies to specifically recognise antigens. For ELISA experiments described in this work, plasma samples obtained as described in section 2.1.3 were assayed following the kit provider instructions. In short, plates containing immobilised antibodies for mouse IL-6 and KC were activated by the addition of assay diluent (provided in the kit). Samples or standard curve controls were then added in duplicate to the plate and incubated for 2 h at room temperature.

This step allows for the binding of the antigen by the antibodies immobilised on the plates. Then, plates were inverted to empty the wells and five washes were performed with the wash buffer provided to eliminate sample components that were not recognised by the plate antibodies. The conjugate reagent (containing specific antibodies that bind to antigen already bound by the antibody attached to the plate, generating an antigen 'sandwiched' between two antibodies, one bound to the plate, and the other conjugated to peroxidise enzyme) was added, incubated for 2 h and again 5 washes were performed. After that, a peroxidise substrate solution was added to the plate and incubated for 30 minutes in the dark and then a stop solution was added, all according to the manufacturer's instructions. The absorbance values at 450 nm and 540 nm were determined (POLARstar Omega spectrophotometer, BMG Labtech) and the 540 nm values subtracted from the 450 nm values. A standard curve was obtained, and the equation derived from this standard curve was used to calculate the concentration of IL-6 or KC in the experimental samples (Supplementary Figure 1).

2.4. Immunohistochemistry

Immunohistochemistry is a technique used to identify specific antigens in experimental samples by the specific binding of antibodies. Antigen retrieval (to break cross-links introduced by formaldehyde during the fixation process) is usually carried out on fixed samples to 'unmask' antigens. A primary antibody recognises the antigen of interest and then a secondary antibody is used to detect the primary antibody. The secondary antibody is usually linked to an enzyme that is then used to interact with a substrate to produce a chromogen that can then be detected

and quantified. In this work, immunohistochemistry was used to assess DNA damage induction and neutrophil recruitment to lung samples upon whole-thorax irradiation.

2.3.1. Deparaffinisation and antigen retrieval

Fixed lungs embedded in paraffin blocks were cut into 5 µm sections using a Leica RM2125 microtome, floated on water and then placed on charged slides (ThermoFisher Scientific, J3800AMNZ) and dried overnight in a 37 °C incubator. Slides were deparaffinised by two 3-minute-long immersions in Citroclear (HD Supplies, UK) and were then rehydrated in a series of decreasing concentrations of ethanol (3 minutes each: 100%, 100%, 70% and 50%). Antigen retrieval was performed in citrate buffer (10 mM citric acid, 0.05% TWEEN 20, pH 6) at 120 °C for 2 minutes in a Decloaker Chamber (Biocare Medical). Slides were left in the citrate buffer and allowed to cool down for 20 minutes. According to the origin of the primary antibody used (Table 2.4), one of two immunedetection kits was used, as described below.

Table 2.4. Antibodies used for immunohistochemistry.

Antigen	Company (catalogue number)	Concentration	Host	Incubation
53BP1	Cell Signalling (4937)	1:100	Rabbit	ON 4C
γH2AX	Millipore (05-636)	1:1000	Mouse	1 h RT
pKAP1 (ser824)	Bethyl (A300-767A)	1:5000	Rabbit	ON 4C
Ly6B	AbD Serotec (MCA771GA)	1:2000	Rat	1 h RT
Ly6C/G	Life Technologies (RM3000)	1:500	Rat	ON 4C

2.3.2. Detection of mouse and rabbit antibodies

For mouse and rabbit primary antibodies, the EnVision™ + Dual Link System-HRP/DAB (Dako, K406511) was used. After antigen retrieval, slides were washed in PBS for 3 minutes and then blocked with Mouse on Mouse Blocking Reagent (Vector Laboratories, MKB-2213) diluted in PBS at 1:25 for 1 h at room temperature. Slides were then washed in PBS for 3 minutes and incubated with the blocking reagent provided in the kit for 15 minutes at room temperature. Slides were washed in PBS and incubated with primary antibody diluted in antibody diluent (Abcam, ab64211) according to conditions described in Table 2.4. After primary antibody incubation, slides were washed with PBS-0.05%TWEEN 20 (PBS-T) for 3 minutes and the with PBS for another 3 minutes. Slides were then incubated with the polymer reagent provided in the kit for 20 minutes at room temperature. Slides were then washed in PBS-T for 3 minutes followed by a 3-minute wash with PBS.

2.3.3. Detection of rat antibodies

To detect primary antibodies raised in rat, we used the Elite ABC kit Rat IgG (Vectastain, PK-6104) according to manufacturer's instructions. After antigen retrieval, slides were washed in PBS for 3 minutes and then incubated with 3% hydrogen peroxide for 15 minutes at room temperature. Next, slides were washed in PBS for 3 minutes and then incubated with 5% rabbit serum provided in the kit for 1 h at room temperature. Slides were then washed in PBS for 3 minutes and then incubated with primary antibodies (dilution and incubation times as described in Table 2.4). After antibody incubation, slides were washed in PBS-T for 3 minutes and in PBS for another 3 minutes. Slides were then incubated with the secondary antibody provided in the kit diluted to 0.5% in 1.5% rabbit serum for 30 minutes at room temperature. After incubation, slides were washed twice in PBS for 3 minutes. Then, slides were incubated in a solution of PBS containing 2% of reagent A and 2% of reagent B (both reagents were provided in the kit) for 30 minutes at room temperature. Slides were then washed twice in PBS for 3 minutes.

2.3.4. Chromogenic development, counterstaining and mounting

Detection was then performed by incubation with 3,3'-diaminobenzidine (DAB) diluted in DAB substrate (provided in the Dako kit) for 2-5 minutes at room temperature until positive cells could be observed in a light microscope. Slides were then washed in running tap water for 5 minutes. Counterstaining was performed by immersing slides on aqueous Gill’s Haematoxylin

solution (Sigma-Aldrich, GHS132) for 30 seconds. Excess staining was washed off in running tap water for 3 minutes. After washing, slides were dehydrated by immersion in a series of ethanol baths (50%, 70%, 100% and 100%) and xylene (2 baths of 100%). After dehydration, slides were mounted using DPX mountant and left overnight to dry at room temperature.

2.3.5. Analysis

Once slides were dry, they were scanned using the Aperio ScanScope CS digital slide scanner (20X objective with doubler inserted) and analysed using ImageScope Software (v11.2.0.780). Within this software, the 'Nuclear Staining' algorithm was used. This detects the haematoxylin stained nuclei (total number of nuclei) and the DAB stained-nuclei (positive nuclei), which were used for calculating the percent of positive nuclei (Figure 2.7).

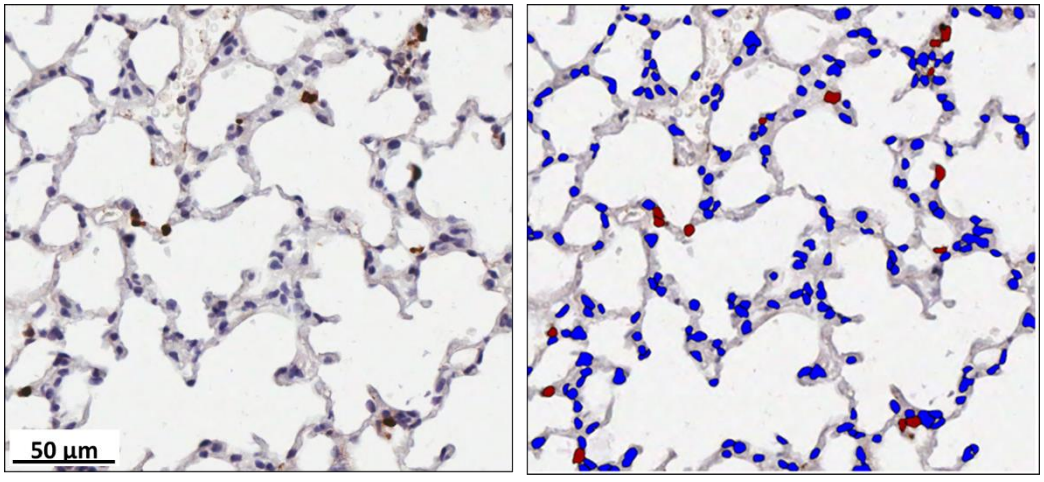


Figure 2.7. Example of nuclear staining analysis using the ImageScope Software. The image to the left shows the original image of a lung stained for Ly6B (brown nuclei). To the right, the algorithm recognised the cell nuclei, labelling the DAB-negative in blue and the DAB-positive in red.

2.5. Haematoxylin & eosin staining

Haematoxylin and eosin (H&E) staining is a simple protocol used to visualise evident structural and morphological characteristics of tissue samples. It is based on the ability of haematoxylin to stain acidic structures (such as the DNA) and eosin's ability to stain basic molecules (abundant in the cytoplasm of cells). We used H&E in lung samples to perform tumour count and in oesophageal samples to evaluate inflammatory changes. Formalin-fixed lung or oesophagi embedded in paraffin blocks were cut in 5 µm sections using a Leica RM2125 microtome, placed on charged slides (ThermoFisher Scientific, J3800AMNZ) and allowed to dry overnight at 37 °C. Slides were deparaffinised by two 3-minute immersions in Citroclear (HD Supplies, UK) and were then rehydrated in a series of decreasing concentrations of ethanol (3 minutes each: 100%, 100%, 70% and 50%). Slides were then immersed in Harris' haematoxylin for 5 minutes and then excess staining was washed off in running tap water for 3 minutes. Differentiation and blueing were performed by immersing slides in a series of acidic alcohol (1% hydrochloric acid in 70% ethanol in distilled water), Scott's tap water (42 mM of sodium bicarbonate, 166 mM of magnesium sulphate in distilled water), 0.5% lithium carbonate (in distilled water). Slides were rinsed in distilled water between the abovementioned baths. The next step was dehydration of samples in a series of 50%, 70% and 90% ethanol, followed by eosin staining (15 seconds). Excess eosin staining was removed by two washes in 90% ethanol. Slides were then further dehydrated in two washes of 100% ethanol and two washes of xylene and mounted using DPX mountant. Once dry, slides were scanned using the Aperio ScanScope CS digital slide scanner (20x objective with image doubler).

2.6. Masson's trichrome staining

To evaluate collagen content in lung samples, we used the well-established Masson's trichrome staining protocol. This protocol visualises collagen fibres stained by aniline blue. Also, nuclei are stained dark red or black by iron haematoxylin and cell cytoplasm is stained in red by scarlet fuchsin. Bouin's solution is used as a mordant to intensify dye staining. To perform Masson's trichrome staining, slides are deparaffinised as described in section 2.4.1 and then stained using a Masson's trichrome staining kit following the steps described in Table 2.5, as suggested by the kit manufacturer.

Table 2.5. Masson's trichrome staining steps and reagent details.

Step	Company	Catalogue number	Time
Bouin's Solution	Sigma	HT10132	overnight
Wash in distilled water	-	-	-
Weigert's Iron Haematoxylin solution	Sigma	HT10-79	5 minutes
Wash in distilled water	-	-	-
Biebrich Scarlet-Acid Fuchsin	Sigma	HT15-1	5 minutes
Wash in distilled water	-	-	-
Phosphomolybdic/Phosphotungstic solution	Sigma	HT15-2	15 minutes
Aniline Blue Solution	Sigma	HT15-4	5 minutes
Wash in distilled water	-	-	-
1% acetic acid solution	BDH Chemicals	100012K	3 minutes
Wash in distilled water	-	-	-

Following the last wash, slides were dehydrated and mounted as described in section 2.4.4. Slides were then scanned using the Aperio ScanScope CS digital slide scanner (20x magnification).

2.7. Fibrosis scoring

Scoring of lung samples stained by Masson's trichrome was performed following the modified Ashcroft scale proposed by the Bewig group (Hübner et al., 2008). A single central lung slice was evaluated per animal. In the 20x magnification scan image of the whole slice, 5 fields of 880 µm x 480 µm were randomly selected and scored from 0-1 according to the guidelines shown in Figure 2.8

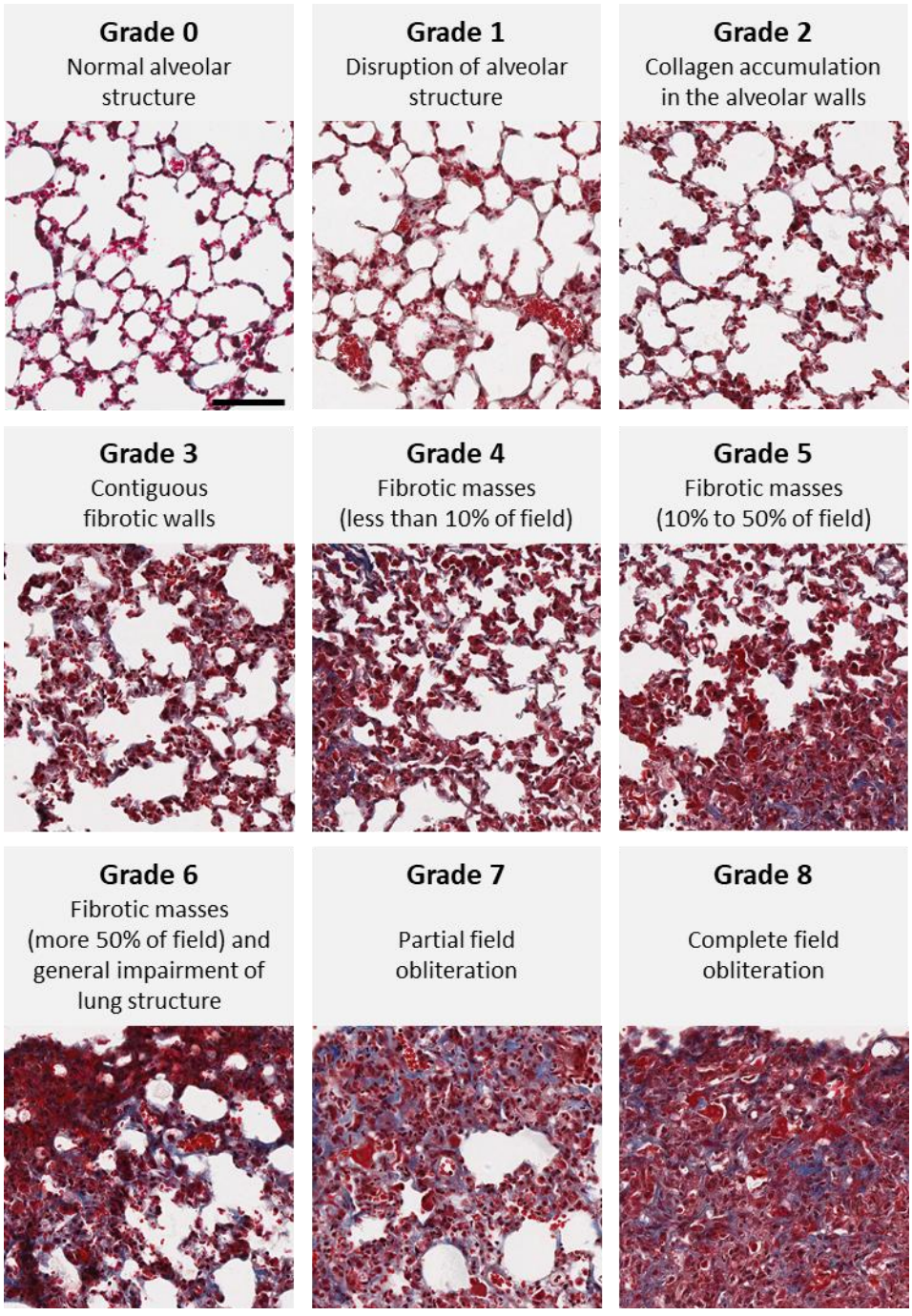


Figure 2.8. Guidelines for fibrosis scoring. Examples of lung samples stained with Masson's trichrome. Scale bar represents 80 μm and all images have the same magnification.

The average of 5 fields was used as the fibrosis score of one animal sample. Graphs presented in this work represent the average of all the animals in the respective experimental group, as detailed in each figure legend.

2.8. Protein extraction from lungs

The right lungs obtained from the in vivo experiments were snap frozen and subsequent protein extraction was performed to evaluate the accumulation of collagen directly by western blot or indirectly using the hydroxyproline assay. Frozen lungs were weighted and placed it in a screw cap tube. Cold lysis buffer (20 mM Tris pH 7.5, 137 mM NaCl, 50 mM NaF, 10 % glycerol, 1% NP-40, 0.1% SDS, 1mM Na_3VO_4 and 1 tablet of protease inhibitor/25mL of buffer) was added to the tube, in a ratio of 1 volume of tissue to 2 volumes of buffer (i.e. for 50 mg of tissue, 100 uL of lysis buffer was added). One 5 mm stainless steel bead (Qiagen, 69989) was added per tube and tubes were transferred to a TissueLyser LT (Qiagen, 85600). Disruption was performed at 50 Hz for 3 minutes. The content of the tube was then transferred to a 1.5 mL tube and sonicated in a Bioruptor® Plus (Diagenode) for 5 cycles of 20 seconds (10 seconds off between cycles). After that, samples were centrifuged for 20 minutes at 16100 g at 4°C. Supernatants were transferred to a new tube and stored at -20°C.

2.9. Hydroxyproline assay

Collagen content can be indirectly evaluated by the quantification of the hydroxyproline content present in a sample. Hydroxyproline is a modification of proline residues that is exclusively present in collagen molecules and therefore can be used to indirectly assess the collagen content. Based on the technique described by Reddy and Enwemeka, we developed an adapted hydroxyproline assay protocol to evaluate lung lysates extracted as described in section 2.7 instead of the whole lung as proposed in the original reference (Kesava Reddy & Enwemeka, 1996). Acetate-citrate buffer (0.88 M sodium acetate trihydrate, 0.24 M citric acid, 1.2 % acetic acid, 0.85 M sodium hydroxide, pH 6.5) and chloramine T reagent (0.056 M chloramine T, 10 % n-propanol, in acetate-citrate buffer) were prepared the day before the assay was performed. Thirty microliters of lysate were mixed with 20 µL of 5 M NaCl in O-ring screw-capped high temperature polypropylene tubes (StarLab, E1420 2641) and then incubated at 120 °C in a heating block for 20 minutes. Tubes were then centrifuged briefly to collect lid condensation. At room temperature, 450 µL of chloramine T reagent was added to each tube and incubated for 25 minutes. After this step, 500 µL of freshly prepared Ehrlich's reagent (1 M p-dimethylaminobenzaldehyde in 2:1 volumes of n-propanol to perchloric acid) was added to each tube, tubes were inverted gently to mix content and incubated for 20 minutes in a 65 °C water bath. Tubes were then centrifuged briefly to collect lid condensation. One hundred microliters of the content of each tube was pipetted in duplicates into a flat-bottom 96-well plate (Corning, 3997) and the absorbance was read at 550 nm in a POLARstar Omega spectrophotometer (BMG Labtech). A standard curve was prepared with 30 µL of a series of hydroxyproline solutions (0.50, 0.75, 1.00, 1.25, 1.50, 1.75, 2.0 µg/µL of hydroxyproline in distilled water), processed

alongside with the lung lysates. For the final analysis, a standard curve was obtained based on the absorbance values obtained for the standard samples, and the equation derived from this curve was used to calculate the concentration of hydroxyproline in the experimental samples. Graphs represent the hydroxyproline content of lung samples in comparison with the average of control samples (unirradiated mice).

2.10. Western blotting

Western blotting (immunoblotting) is a technique used to detect specific antigens contained in complex mixtures, usually, cell or tissue lysates. Proteins are separated in a polyacrylamide gel, based on their size, and are subsequently transferred to a membrane where they are immobilised. These membranes are incubated with antibodies that bind to and detect the antigens of interest. In this work, lung lysates obtained as described in section 2.6 were used to perform Western Blots. For the blots shown in Figure 5.8 and Figure 6.4 one microliter of lung lysate/sample was used and for the other blots 0.25% of the total lysate volume/sample was used. Samples were mixed in a 1:1 volume/volume proportion with Laemmli sample buffer (2x concentrate) and incubated at room temperature for 10 minutes. Samples were then loaded into wells of pre-cast 4-15% polyacrylamide gradient gels (Mini-PROTEAN® Precast gels or Criterion™ TGX gels, BioRad). In an appropriate tank containing running buffer (25 mM Tris, 192 mM glycine, 0.1% SDS, pH 8.3, made from 10x concentrate, BioRad), electric current was applied to Mini-PROTEAN® Precast gels or Criterion™ TGX gels at 250 V for 30 minutes or 150 V for 1 h, respectively. After electrophoresis, the gel and a nitrocellulose membrane were placed in a tank

containing transfer buffer (25 mM Tris, 192 mM glycine, pH 8.3, supplemented with 20% methanol) and proteins were transferred to the membrane at constant voltage: 150 V for 1 h or 90 V for 2 h for Mini-PROTEAN® Precast gels or Criterion™ TGX gels, respectively. To check the quality of protein lysates and protein separation and transfer, membranes were incubated with Ponceau S solution for 1-3 minutes and then washed in PBS. Membranes were blocked in a mixture of 1:1 of Odyssey® Blocking Buffer (LI-COR) and PBS. Antibodies were diluted in a mixture of 1:1 of Odyssey® Blocking Buffer (LI-COR) and PBS containing 0.1% TWEEN 20 as described in Table 2.6.

Table 2.6. Antibodies used for Western blotting.

Antigen	Company	Catalogue number	Host	Concentration
Primary antibodies				
Collagen I	Abcam	ab34710	Rabbit	1:1000
Collagen III	Abcam	ab7778	Rabbit	1:1000
PPIB	Abcam	ab16045	Rabbit	1:2000
Secondary antibodies				
Mouse IgG (H + L) conjugated to IRDye® 680RD	LI-COR Biosciences	926-68070	Goat	1:5000
Rabbit IgG (H + L) conjugated to IRDye® 800CW	LI-COR Biosciences	926-32211	Goat	1:5000

After antibody incubations, membranes were washed 3 x 5 minutes in PBS containing 0.1% TWEEN 20. Membranes were then placed in the Odyssey® Infrared Imaging System (LI-COR Biosciences), and fluorescent bands were detected. Quantification of bands were performed in

Image J (as described in https://imagej.nih.gov/ij/docs/menus/analyze.html#gels) and graphs throughout this work represent the relative pixel intensity of bands from irradiated samples compared to the control (unirradiated mouse).

2.11. Cell culture

Human lung cancer cell lines, A549 (lung carcinoma) and Calu-6 (anaplastic carcinoma) were purchased from American Type Culture Collection and a human bronchoepithelial cell line NBE1 was kindly provided by Professor P. Rabbitts. Cell lines were maintained in advanced Dulbecco modified Eagle medium plus F-12 medium supplemented with 5% foetal bovine serum, 2 mM GlutaMAX, and 50 U/mL penicillin / 50 µg/mL streptomycin (hereafter referred to as complete media). Cells were cultured at 37°C in a humidified environment containing 5.0% CO_2. At around 90% confluency, cells were passaged using 0.25% Trypsin-EDTA. Once passaged 10 times, a new batch of cells was thawed and cultured. A stock of cells was kept in liquid N_2 in complete media supplemented with 10% dimethyl sulfoxide.

2.12. Myeloperoxidase incubation

Myeloperoxidase (MPO) incubation was performed to simulate in culture the interaction of lung cells with MPO secreted by neutrophils recruited to irradiated tissues. Cells were seeded one day before incubation with MPO (cell number and plates used are described below according

to the experiment performed). Media was aspirated, cells were washed in sterile PBS, and DMEM/F12 media supplemented with 0.5% foetal bovine serum and 10 nM MPO was added to cells. Plates were returned to the incubator for 30 minutes. For experimental groups labelled as control or '0 nM MPO', fresh complete media without MPO was added. Cells were then processed as described below according to the assay performed.

2.13. Luminol-based MPO activity assay

As MPO is a peroxidase, we developed an assay to evaluate MPO activity. Based on the known use of luminol as a substrate to measure peroxidase activity, we used this principle to detect MPO activity. In 96-well plates (Corning, 3997), 3000 cells (A549 or NBE1) were seeded in triplicate one day before experiment. MPO incubation was performed as described in section 2.11, but instead of fresh media, after the PBS wash, 50 µL of Amersham ECL Prime Western Blotting Detection Reagent was added to each well. Four minutes afterwards, the luminescence signal was read from the top of the plates in a POLARstar Omega spectrophotometer (BMG Labtech). The graph in Figure 4.2 is representative of two independent experiments and shows the average of luminescence values in the triplicates for each experimental group.

2.14. CELLROX® assay

MPO activity is known to generate reactive oxygen species (ROS). Therefore, we used the CELLROX® assay to evaluate the induction of ROS upon MPO interaction with lung cells in vitro. Eight thousand cells were seeded in 96-well plates (Corning, 3997) one day before MPO incubation (performed as described in section 2.11). Menadione (50 µM) was used as a positive control. After MPO or menadione incubation, CELLROX reagent was added at a final concentration of 5 µM. Plates were placed back in the incubator for 30 minutes and imaged using an Eclipse TE2000 fluorescence microscope (Nikon). Three independent experiments were performed and images from one representative experiment were quantified using ImageJ. Sixteen-bit images were used for quantification, in which 4-pixel windows were placed at the centre of each cell nucleus (35 nuclei per image were analysed and 5 readouts of background areas were also quantified) to obtain the pixel value. The mean pixel value of the 5 background images was subtracted from the individual nuclei values and the final values were used to calculate the mean pixel value of each image. Two images were analysed per experimental group.

2.15. Comet assay

DNA damage can be directly and indirectly evaluated by several techniques. In this work, we used the alkaline comet assay to directly evaluate the induction of DNA strand breaks. This assay is based on the migration of DNA molecules when exposed to an electric field and further

staining and visualisation of these molecules. Broken DNA molecules are expected to migrate more freely towards the positive pole of the field, forming a comet tail. The intact, high molecular weight unbroken DNA remains in the nucleus and forms the 'head' of the comet, and the extent of damage is calculated as a proportion of tail and head DNA. To evaluate the induction of DNA breaks upon MPO interaction, cells (10^5 per well) were seeded in 12-well plates (Corning, 3512) two days before MPO incubation (performed as described in section 2.11). After incubation, cells were trypsinised, resuspended in PBS and kept on ice. As a positive control, trypsinised cells were irradiated (5 Gy). Cells in PBS were mixed to a proportion of 1:4 with a solution of 1% low melting point agarose (in PBS) kept at 37°C. This cell suspension was then added to glass slides pre-coated with agarose. Slides were left for 1-2 minutes to allow the agarose to solidify and were then immersed in lysis buffer (2.5 M NaCl/ 100 mM EDTA/ 10 mM Tris-base; pH 10) for 1-2 h at 4°C. Slides were rinsed with electrophoresis buffer (300 mM NaOH/ 1 mM EDTA; pH 13) and placed in an electrophoresis tank filled with ice-cold electrophoresis buffer for 30 minutes. Electrophoresis was conducted at 300 mA and 25 V for 25 minutes. Slides were neutralized by 3 washes of 10 minutes using neutralization buffer (0.5 M Tris-HCL; pH 8), followed by 2 washes of 5 minutes with distilled H_2O (pH 8). Slides were allowed to dry overnight than were rehydrated in distilled H_2O (pH 8) for 1-2 h at room temperature in the dark. Staining with SYBR Gold (1:10000 in distilled H_2O pH 8) was performed for 30 minutes in the dark, followed by 2 washes with distilled H_2O (pH 8). Slides were allowed to dry and were analysed using Komet 5.5 software (495 nm for excitation). Two slides were prepared for each experimental group and fifty cells were analysed per slide. Three independent experiments were performed and the data from one representative experiment is shown in Figure 4.4 A.

2.16. Immunofluorescence

Similarly to immunohistochemistry, immunofluorescence relies on the detection of antigens by antibodies on structure-preserved samples. Secondary antibodies are detected by the measuring the fluorescence of specific fluorophores (e.g. Alexa fluor dyes) that conjugated to the secondary antibodies. Immunofluorescence has the potential for greater sensitivity and resolution than immunohistochemistry. For MPO immunofluorescence, eight thousand cells were seeded into 96-well plates (Corning, 3997) one day before MPO incubation (performed as described in section 2.11). After incubation, media was aspirated and cells were fixed in 3% paraformaldehyde for 10 minutes. Cells were then washed twice with PBS and blocked with a solution of 0.1% Triton X-100, 1% bovine serum albumin and 1% goat serum (in PBS) for 1 h at room temperature. Blocking buffer was removed and cells were incubated with primary antibodies diluted in 1% bovine serum albumin and 1% goat serum (in PBS) overnight at 4°C. Cells were washed 3 times with PBS and incubated with secondary antibodies diluted in 1% bovine serum albumin and 10 mg/mL Hoechst 33258 (in PBS) for 1 h at room temperature in the dark. Primary and secondary antibodies details are described in Table 2.7. Cells were again washed in PBS (3 times) and imaged. The images presented in Figure 4.2 A are representative of 2 independent experiments in which images were acquired using the 63x objective with a confocal microscope (Zeiss LSM 710). For γH2AX and 53BP1 foci experiments, an INCell Analyzer 1000 automated epifluorescence microscope (GE Healthcare UK Ltd) was used to acquire images and its associated software was used to quantify foci. Data shown in Figure 4.4 B is representative from two independent experiments (each experimental group in triplicates).

Table 2.7. Antibodies used for immunofluorescence.

Antigen	Company	Catalogue number	Host	Concentration
Primary antibodies				
53BP1	NEB	4937	Rabbit	1:800
γH2AX	Millipore	05-636	Mouse	1:1500
α-tubulin	Sigma-Aldrich	T6074	Mouse	1:5000
MPO	Thermo Scientific	RB-373-A0	Rabbit	1:100
Secondary antibodies				
Anti-mouse IgG conjugated to Alexa488	Invitrogen	A11001	Goat	1:1200
Anti-rabbit IgG conjugated to Alexa555	Invitrogen	A21428	Goat	1:1200

2.17. Clonogenic survival

The clonogenic survival assay is used to evaluate the relative ability of individual cells to form colonies of at least 50 cells with and without various treatments. To evaluate clonogenic survival of lung cells upon MPO interaction in vitro, 300 cells/well were plated in 6-well plates (Corning, 3506), and were left in the incubator for 24 h to adhere before being exposed MPO (as described in section 2.11). Plates were returned to the incubator and colonies were allowed to form over 2-3 weeks. Colonies were then fixed and stained with a solution containing 0.5% [w/v] crystal violet, 5% acetic acid and 75% methanol in distilled water. Colonies with ≥50 cells were manually counted in 3 wells/experimental group. The graph presented in Figure 4.5 shows the

data from one of 3 representative experiments and bars represent the average of the number of colonies counted in the triplicate of each experimental group.

2.18. Statistical analysis

Values are expressed as average ± standard error of the mean (SEM) unless stated otherwise. For experiments in which groups presented an $n<3$ no statistical analysis were performed. Values were assumed to be normally distributed, but no testing for normality was conducted. Using Excel 1026 (Microsoft Office), Student's t-tests were performed. The specific group comparisons are specified in each figure legend. No correction for multiple tests were applied. Also, according to the design of each experiment, two or one-way tests were performed, as specified in the figure legends.

3. Characterisation of the early and late normal lung responses of C57BL/6J mice to thoracic irradiation

3.1. Introduction

A recent comprehensive review by Dabjan et al. identified C57BL/6J mice as the most commonly used preclinical model for the study of radiation-induced pulmonary fibrosis (Dabjan et al., 2016). This strain is fibrosis-prone, presenting low levels of pneumonitis and showing signs of lung damage at late time points post-irradiation, varying from weeks to months according to the dose used and the volume of irradiated lung. The early effects of thoracic irradiation have also been studied in C57BL/6J mice. Notably, increased levels of pro-inflammatory cytokines in the lung tissue and in the plasma have been reported, as well as induction of DNA damage (Ao et al., 2009; Rübe et al., 2010a). Nevertheless, to our knowledge, detailed time-courses of those two early effects of radiation have not been studied following whole-thorax radiation. Therefore, the first aim of this chapter was to characterise the effect of whole-thorax irradiation from 15 minutes to 28 days post-treatment in the lungs of C57BL/6J mice.

One of the most challenging aspects of radiation-induced normal lung tissue reported in the literature is the heterogeneity of doses and irradiated fields used in the published studies. There are several reports on single doses (varying from 5 to 90 Gy) and different delivery methods, allowing for irradiation of small lung areas up to whole-thorax irradiation. Also, researchers have not always reported survival time and rarely disclosed the extent of damage, usually

presenting only histological images of small areas of the lung. In addition, most published papers used single doses even though single dose irradiation is not usually used in the clinic. Another confounding factor is the inconsistency of the use of males and females, as sex was shown to play a role in the observed responses, female C57BL/6J mice being more sensitive to radiation and presenting a shorter latency period before the development of symptoms (Travis et al., 2011).

For instance, a study reporting the use of a single dose of 90 Gy given to a 3 mm^2 of lung area showed the induction of a highly obstructed lesion within 2 weeks post-irradiation, with no reported data for survival (Jin et al., 2017). In the same paper, a 20 Gy dose given to the whole thorax induced lung damage within 3 months and mice were followed until 12 months post-irradiation. In another paper, a single dose of 17 Gy given to the left lung induced lung damage within 8 weeks post-irradiation and mice were followed until 23 weeks post-irradiation (Pan et al., 2017). Another group showed that a single dose of 5 Gy given to the whole-thorax did not lead to histological differences at 30 weeks post-irradiation (Citrin et al., 2013). Dabjan et. al. combined together the data from several reports that used single doses of whole-thorax irradiation for several mouse strains and non-human primates and data from patients receiving upper whole-body irradiation to produce an useful graph illustrating median survival time versus radiation dose (Figure 3.1). Importantly, this graph shows the disconnect between the doses used in the clinic and in mouse experiments, and also suggests that the C57BL6 strain is more resistant to whole-thorax irradiation than humans (Dabjan et al., 2016).

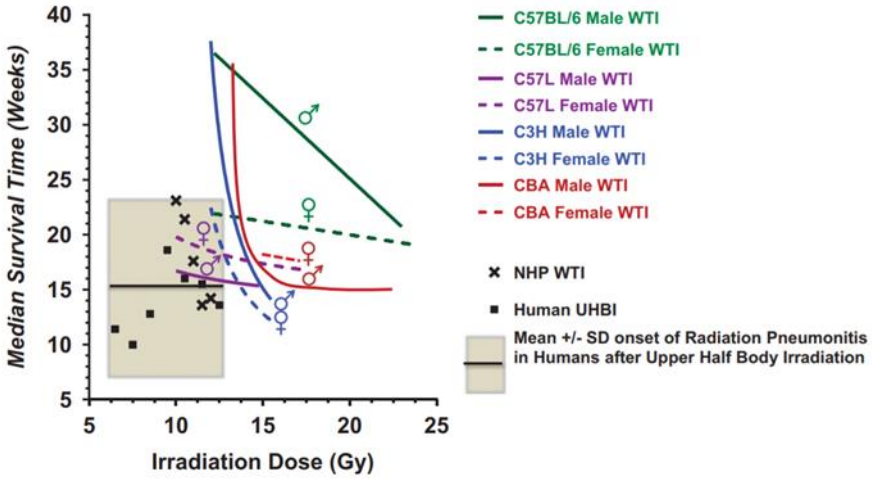


Figure 3.1. Median survival time according to radiation dose exposure to the whole lungs of mice, non-human primates, and humans. Upper half body irradiation (UHBI), non-human primates (NHP), whole-thorax irradiation (WTI). Reproduced from (Dabjan et al., 2016).

Despite all the preclinical data available on single doses of radiation given to the thorax, in the clinic cancer patients will generally receive fractionated schedules of radiation (Supplementary Table 3). For instance, according to a recently published meta-analysis of trials performed before 2006, non-conventional fractionation schedules (accelerated or hyperfractionated) led to an absolute benefit of 2.5% in 5-year overall survival, probably due to shorter overall treatment time (Mauguen et al., 2012). In addition, hypofractionation has been recommended for patients receiving sequential chemoradiotherapy (chemotherapy followed by radiotherapy) or radiotherapy alone for stage III disease (Postmus et al., 2017). For inoperable early stage disease patients, when SABR is not available or in the case of centrally localised tumours, hypofractionated doses are recommended over hyperfractionation following results from a meta-analysis study and a phase II clinical trial (Cheung et al., 2014; Mauguen et al., 2012).

Therefore, according to these clinical guidelines, the need for research on the effects of fractionated schedules using intermediate dose/fraction (2-5 Gy) is evident. The effect of

different fractionation schedules given to the normal lung tissue has been studied is the past, but there is a lack of recent studies in the literature exploring the underlying biological mechanisms (Hornsey, Kutsutanl, & Field, 1975; Travis, Thames, Watkins, & Kiss, 1987). Work on mice from the LAF1 strain showed decreased radiation-induced damage to lung cells when increasing the number of fractions. The authors showed that when standardising the comparison on total dose, the schedule of 1 dose/week was more toxic than daily or 2 doses/day schedules. No difference was observed between the daily and 2 doses/day schedules (Penney, Sieman, Rubin, & Maltby, 1994). Unfortunately, despite being the most used strain to study radiation-induced lung damage, C57BL/6J mice have only been used in two papers looking at fractionated schedules of irradiation (Chung et al., 2016; Citrin et al., 2013). In the most recent, the authors described the damage caused by 5 x 6 Gy given to the whole-thorax as multiple sub-pleural fibrotic foci within 16 weeks post-irradiation (Chung et al., 2016). In contrast, many papers have explored the effect of fractionation to the non-tumour cell components of tumours [reviewed in (Hellevik & Martinez-Zubiaurre, 2014)]. Therefore, our second aim was to investigate the late responses of C57BL/6J mice normal lung tissue to fractionated doses of radiation.

The third aim of this chapter was to evaluate different methods for the assessment of lung damage. In the literature, the most commonly reported methods are hydroxyproline assay (surrogate of collagen) and Masson's trichrome staining (collage is stained blue). As opposed to the histological analysis using Masson's trichrome, the hydroxyproline assay is a measure of total lung collagen, therefore it gives an average accumulation of collagen in the whole organ, which can be useful as some doses of radiation induce focal fibrotic lesions that could be missed by histology, as only a slice is being analysed. In addition, some groups also report in vivo

imaging techniques, such as computed tomography (CT) or magnetic resonance imaging (MRI), and breathing rates. Those methodologies are not often used, probably because they require the use of special equipment that is not widely available in research centres. Here we speculate how useful the different methodologies are according to our findings.

In this chapter, we characterised both early and late effects of whole-thorax irradiation on C57BL/6J mice. Early biological effects were evaluated following a single dose of radiation, whilst multiple fractions were used to reach a clinically relevant dose that induced late biological and toxic effects. The aims of this chapter were (i) to characterise the early effects of radiation that could be related to late effects, (ii) to determine a schedule and dose of fractionated radiation to be used during this work and (iii) to evaluate methods of toxicity assessment.

3.2. Whole-thorax irradiation induces an acute and transient peak of inflammation and long-lived DNA damage in the lung

To characterise the initial response of normal lung tissue to radiation, we irradiated mice with a single dose of 10 Gy given to the whole-thorax and collected blood and lungs at several time-points after radiation, ranging from 15 minutes to 28 days, in two independent experiments (Figure 3.2).

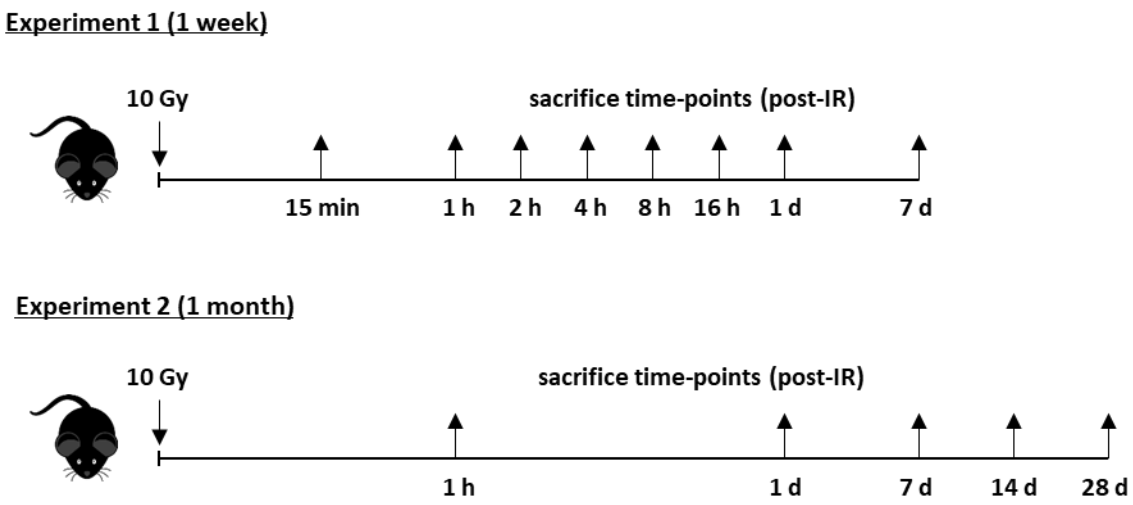


Figure 3.2. Experimental design for evaluation of early effects of whole-thorax irradiation. Two independent experiments were performed to evaluate the early effects of whole-thorax irradiation. C57BL/6J mice were given a single dose of 10 Gy to the whole-thorax and sacrificed at 15 minutes, 1 h, 2 h, 4 h, 8 h, 16 h, 1 d and 7 days after radiation (n=2 per time-point). In the second experiment, the same treatment was given and mice were sacrificed at 1 h, 1 d, 7 d, 14 d and 28 d post-IR (n=3 per time-point). Left lungs were fixed in formalin for further histological analysis and blood was collected for plasma extraction.

We first investigated if whole-thorax irradiation led to systemic effects detectable by changes to the plasma levels of two pro-inflammatory cytokines that have been reported to be related to lung toxicity: KC and IL-6, related to the recruitment and production of neutrophils, respectively. ELISA of plasma samples showed an acute and transient increase in the levels of both KC and IL-6, peaking at 2 h after treatment (Figure 3.3. A and B). At 14 and 28 days post-irradiation, the levels of KC and IL-6 were back to unirradiated control levels (213.6 ± 137.6 and 152.8 ± 108.1 pg/ml for KC and below detection level, i.e. 1.8 pg/mL, for IL-6, respectively).

The increase of pro-inflammatory cytokines in the blood suggested that immune cells could be activated and released from the bone marrow in response to whole-thorax irradiation. Therefore,

we evaluated the number of neutrophils present in the lung after radiation by immunohistochemistry. It was observed that neutrophils (Ly6B-positive cells) were recruited to the lungs in an acute and transient fashion, consistent with the changes observed for cytokines (Figure 3.3. C and D).

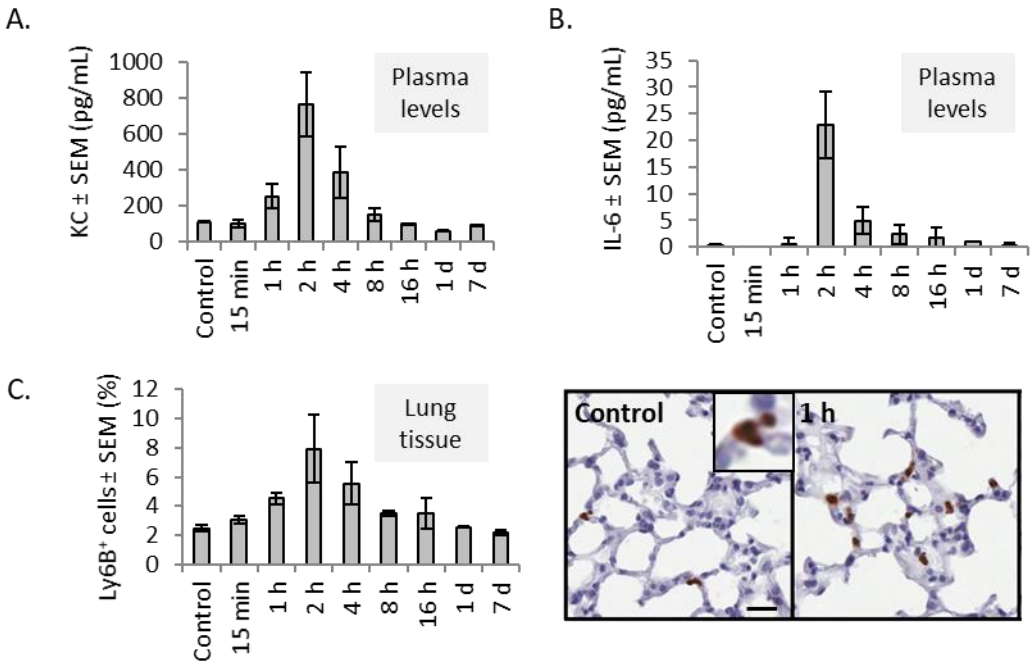


Figure 3.3. Whole-thorax irradiation induced systemic signalling of inflammation and immune cell recruitment to the lung. Plasma levels of KC (A) and IL-6 (B) were increased at 2 h after radiation as assessed by ELISA. Neutrophil count in the lung was increased at 15 minutes to 8 h after radiation as assessed by immunohistochemistry (C, Ly6B - marker for neutrophils). Graph bars represent the average in the group (n=2 per group) and error bars represent the SEM. Scale bars represent 15 µm; inset image is 4x enlarged.

Besides inflammation, we evaluated the DNA damage response in the lung following radiation. We performed γH2AX immunohistochemistry as a surrogate for DNA damage. Histone H2AX is phosphorylated on the serine residue 139 at sites of DNA DSBs (Valdiglesias, Giunta, Fenech, Neri, & Bonassi, 2013) and commonly referred to as γH2AX. It was observed that at 15 minutes after radiation 42.19 ± 7.59 % of lung cells were positive for γH2AX (Figure 3.4.

A). At 24 h after radiation, the number of positive cells dropped to 26.74 ± 9.52 % and at 7 days a further drop was observed (7.70 ± 0.59 %). The number of positive cells was then maintained to similar levels at 14 and 28 days (6.75 ± 1.45 and 6.72 ± 2.82, respectively; Figure 3.4. B). These data suggest that DNA DSB repair in lung cells occurs primarily within the first day after radiation but unrepaired DNA DSBs persist for weeks, in contrast to the acute and transient increase in cytokine plasma levels.

To confirm that persistent γH2AX staining represented DNA DSBs (and not i.e. apoptotic cells), the presence of tumour protein p53 binding protein 1 (53BP1) foci was assessed as an alternative marker of DNA DSBs. In contrast to γH2AX, 53BP1 is constitutively present in the cell nucleus. Upon damage, 53BP1 is activated and recruited to the DNA strand break, forming foci. Therefore, we quantified '53BP1 foci-positive cells' as a measure of cells with unrepaired DNA DSBs. Interestingly, at 7, 14 and 28 days post-irradiation it was possible to identify a significant fraction of 53BP1 foci-positive lung cells compared to unirradiated mice, which were interpreted as persistent unresolved DNA DSBs (Figure 3.4. C and D).

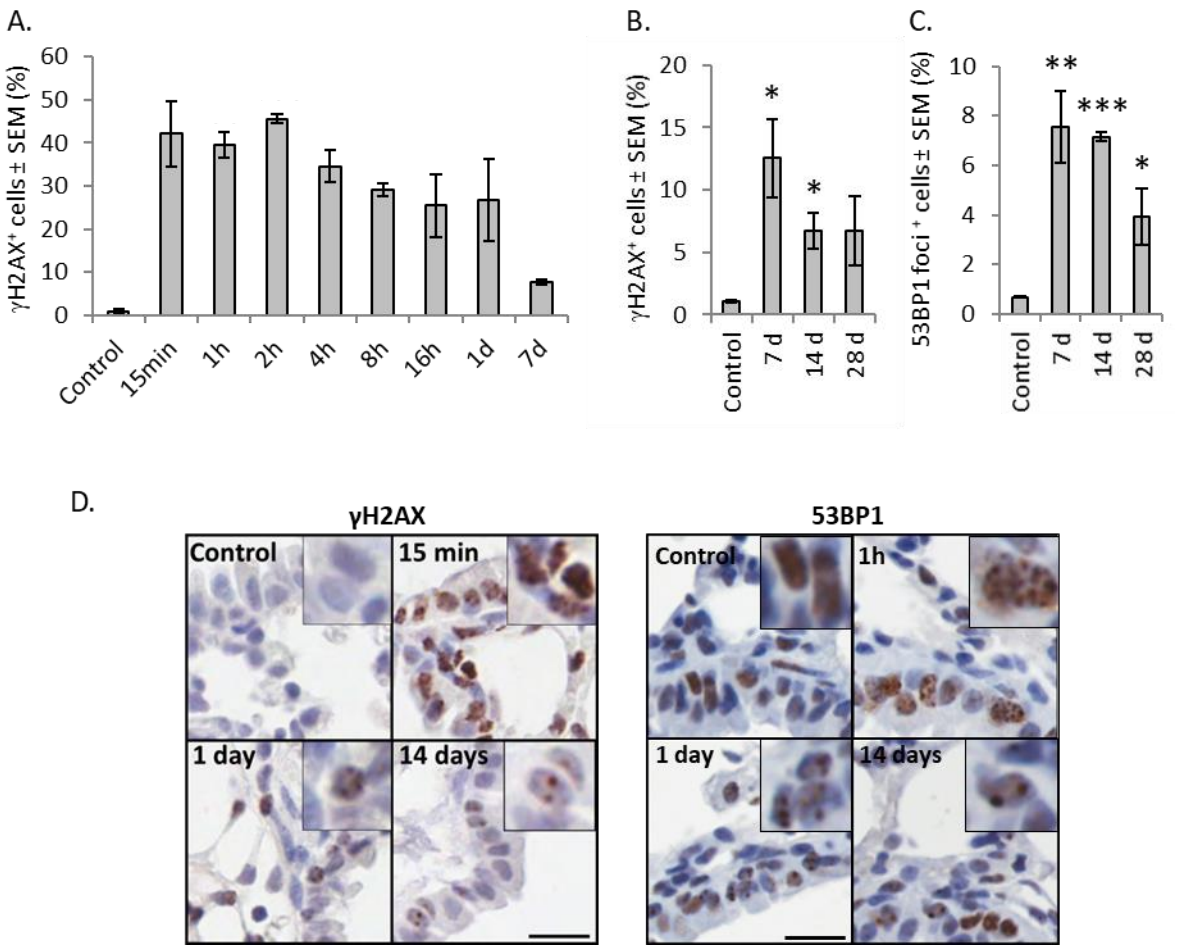


Figure 3.4. Whole-thorax radiation induced long-lived DNA damage in the lung. γH2AX-positive cell count in the lung increased as soon as 15 minutes after radiation as assessed by immunohistochemistry (A). The number of γH2AX-positive cells is still higher than control as long as 14 days after radiation (B) and the number of 53BP1 foci-positive cells is higher than unirradiated controls at 7, 14 and 28 days post-IR (C). γH2AX and 53BP1 foci-positive cells in the lung can be observed from 15 minutes to 14 days after radiation (D). Graph bars represent the average in the group (n=2 per group) and error bars represent the SEM; *$p<0.05$ and ***$p<0.0005$ compared to control group (t-test, one-tailed distribution, two sample equal variance). Scale bars represent 15 μm; insets images are 2x enlarged.

3.3. Weight loss and abnormal breathing are sensitive indicators of late toxicity induced by whole-thorax irradiation

Previous experiments in our laboratory following C57BL/6J mice six months after receiving a single whole-thorax dose of 10 Gy (biological effective dose 38.6 Gy) showed that this dose

induced mild accumulation of collagen and thickening of the alveolar walls but not fibrotic lesions or respiratory distress. Following this, we tested treatment options with higher biological effective doses (BED) and fractionated schedules to better emulate clinical schedules. Three different schedules were tested, given in multiples doses of 5 or 2.5 Gy to the whole-thorax of C57BL/6J mice, which were then monitored for 27 weeks for body weight loss and changes to breathing patterns (Figure 3.5).

A.



B.

Total dose (Gy)	Fractionation	BED (Gy)	Sacrifice (weeks)
25	5 x 5 Gy	60.7	18*
22.5	4 x 5 Gy + 1 x 2.5 Gy	54.6	27
20	4 x 5 Gy	48.6	27

Figure 3.5. Experimental design for evaluation of late effects of whole-thorax radiation. C57BL/6J mice were given multiple 5 Gy doses in different fractionation schedules to the whole-thorax and sacrifice was planned at 27 weeks after radiation (A). Details of fractionation schemes, biological effective dose (BED) and actual time post-irradiation until sacrifice; * mice receiving 25 Gy were sacrificed at 18 weeks after irradiation due to development of adverse clinical signs (B). Left lungs were fixed in formalin for further histological analysis, right lungs were fresh frozen and blood was collected for plasma extraction. IR: irradiation; n=5 per group.

At 17 weeks post-irradiation, 1 out of 5 mice receiving a total of 25 Gy showed accelerated respiration and shallow breathing. This animal (LL43) was sacrificed and had lungs and blood collected for further investigation. The other 4 mice in this treatment group (LL41, LL42, LL44, LL45) were assessed using unrestrained plethysmography, showing significantly increased breathing rate compared to untreated controls (Figure 3.6. A). One week later (18 weeks post-

irradiation), LL44 showed altered breathing and more than 10 % body weight loss in relation to its maximum body weight and therefore was also sacrificed.

Due to the development of adverse effects in this treatment group, asymptomatic mice LL42 and LL45 were imaged by computed tomography (CT). The scan images revealed areas of attenuation in the lung (Figure 3.6. B, white arrows), which could be due to increased cellularity, fluid accumulation or collagen deposition in the alveoli. Due to the imaging results, the 3 asymptomatic mice irradiated with 25 Gy and two unirradiated controls were also sacrificed at the end of week 18 post-irradiation.

Left lungs were processed for histology and stained with Masson's trichrome, which allows for the visualisation of collagen fibres (stained blue). The lungs of the symptomatic mice showed distinct histologies - LL43 had substantial accumulation of collagen with areas of complete air space obliteration whereas LL44 presented with collagen accumulation throughout the lung and thickening of alveolar walls but no large fibrotic lesions (Figure 3.6. C). The 2 symptomatic mice showed the highest fibrosis score within the group and the average fibrosis score of treated mice was increased when compared to untreated mice (Figure 3.6. D).

To complement the fibrosis scoring performed in a single slice of the left lung, we measured the collagen content in protein lysates obtained from fresh frozen whole right lungs. Collagen contains hydroxyproline, a modification of proline residues, which is necessary for the interaction between collagen molecules. This modified residue is only present in collagen molecules and therefore is considered a surrogate measure of collagen content. Unexpectedly, no difference was observed in the levels of hydroxyproline between untreated and irradiated animals (Figure 3.6. E).

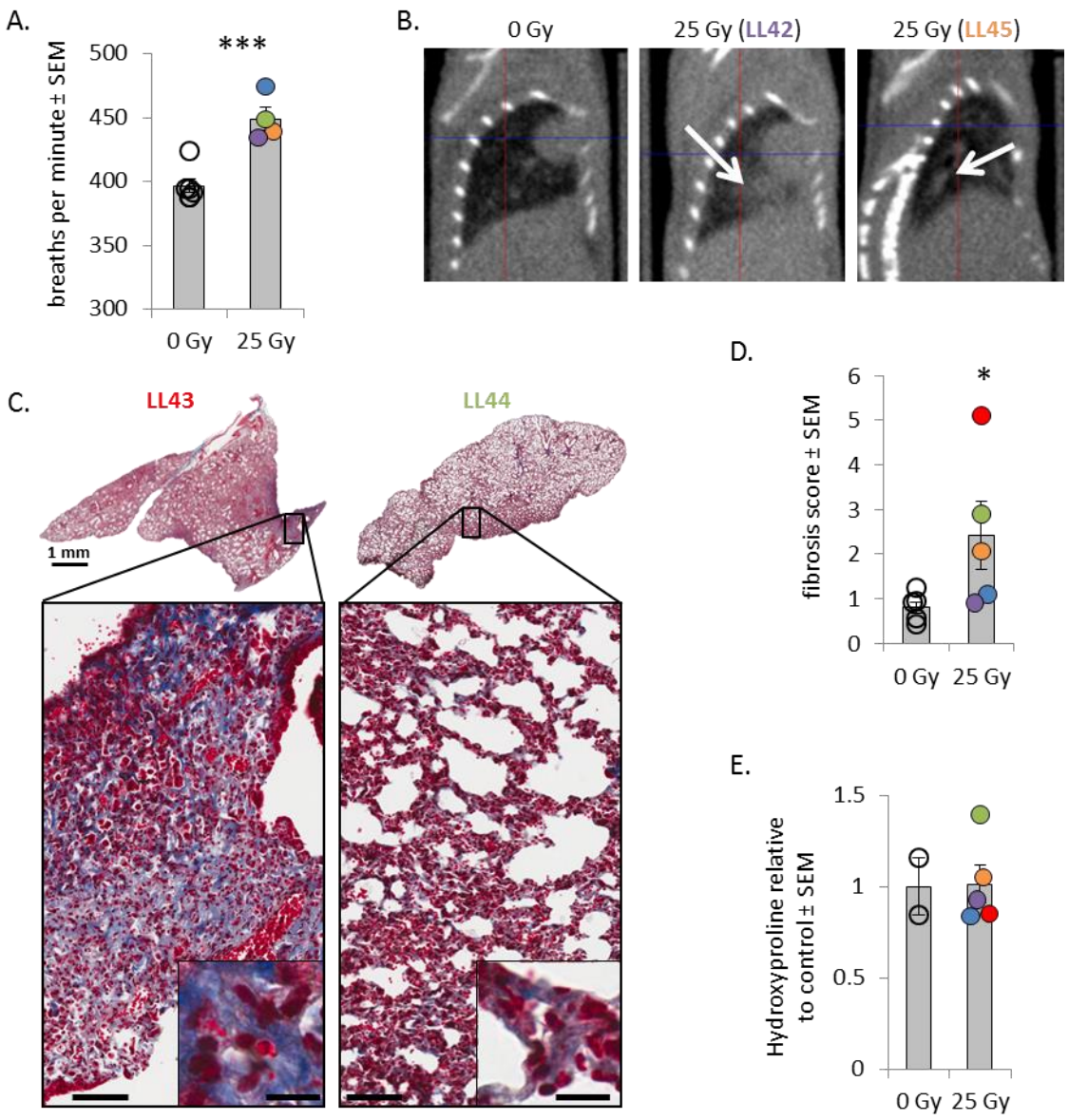


Figure 3.6. A total of 25 Gy given in fractionated doses to the whole-thorax induced severe lung damage and premature sacrifice in C57BL/6J mice. At 18 weeks post-irradiation, treated mice showed increased respiration rate compared to controls as evaluated by unrestrained plethysmography (A). In addition, CT scan of the thorax of irradiated mice showed lung attenuation (arrow), indicating lung damage (B). Masson's trichrome staining revealed collagen accumulation in the irradiated lungs (C). Scoring of those images by a modified Ashcroft scale showed increased fibrosis in treated animals (D). No increase in hydroxyproline levels was observed (E). Graph bars represent the average in the group (in control group of graphs A and D: n=2 sacrificed at 18 weeks post-irradiation and n=3 sacrificed at 27 weeks post-irradiation; in control group of graph E: n=2 sacrificed at 18 weeks post-irradiation), error bars represent the SEM and circles represent individual animals. Symptomatic mice: LL43 (red) and LL44 (green). Asymptomatic mice: LL41 (blue), LL42 (purple) and LL45 (orange). *p<0.05 and ***p<0.0005 compared to control group (t-test, one-tailed distribution, two sample equal variance). Large inset scale bars represent 100 µm, small inset scale bars represent 15 µm.

Mice treated with total doses of 20 and 22.5 Gy were followed until 27 weeks post-irradiation as planned. At week 26, one mouse treated with 20 Gy showed weight loss and was sacrificed (LL25). The remaining mice in the 20 Gy group did not show weight loss and were monitored until the final week of experiment. A few days before the end of experiment, one mouse in the 22.5 Gy group presenting with less than 10 % weight loss was found dead (LL37). Post-mortem examination showed pleural effusion. From the remaining 4 mice treated with 22.5 Gy, 2 showed mild weight loss (less than 10 %) at week 26 and were kept alive until the end of experiment (Figure 3.7).

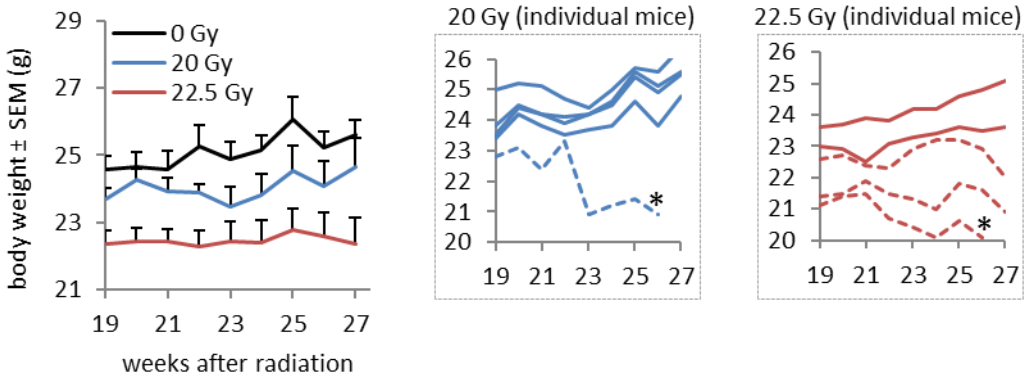


Figure 3.7. Whole-thorax 20 Gy and 22.5 Gy irradiation induced weight loss and increased lethality in C57BL/6J mice. Stars (*) indicate mice sacrificed before the end of experiment. One out of 5 mice treated with 20 Gy and 3 out of 5 mice treated with 22.5 Gy showed weight loss within the last weeks of the experiment. Left graph shows the groups weight averages; middle and right graphs show individual animal weights; dashed lines indicate animals with more than 10 % weight loss. 0 Gy: n=3, 20 Gy: n=5, 22.5 Gy: n=5.

Masson's trichrome staining showed that both 20 and 22.5 Gy treatment induced the development of focal fibrotic lesions at the lung surface and an increased fibrosis score (Figure 3.8 A and B). There was no clear association between early sacrifice due to weight loss and fibrosis score i.e. mice presenting more than 10 % body weight loss (LL25, blue triangle; and LL37, purple diamond) did not show fibrosis score higher than the respective group averages.

Hydroxyproline levels were not significantly altered when comparing the averages of irradiated and unirradiated mice; nevertheless, mouse LL37 (treated with 22.5 Gy and found dead) showed the highest level of hydroxyproline (Figure 3.8. C).

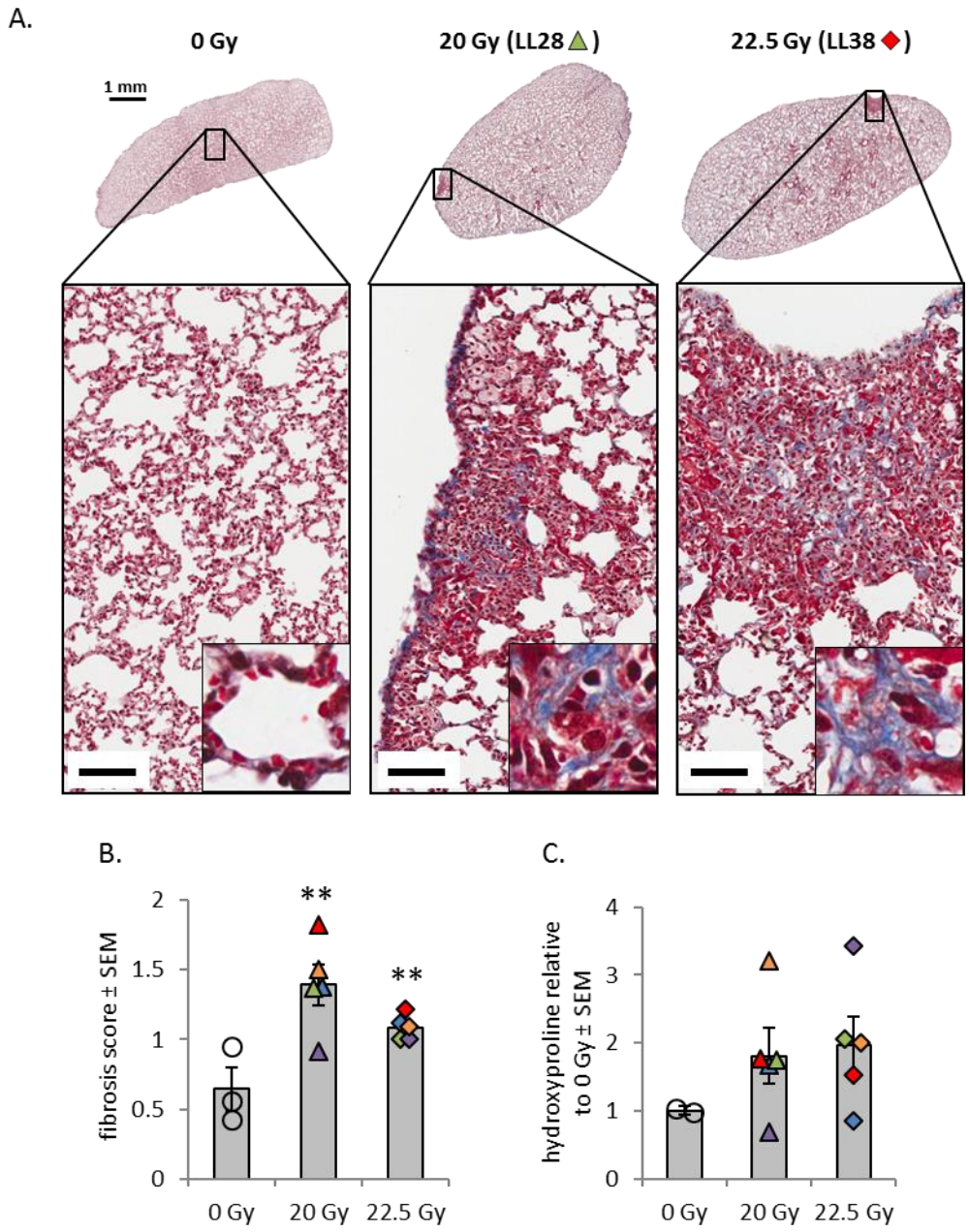


Figure 3.8. Total doses of 22.5 Gy and 20 Gy to the whole-thorax induced mild pulmonary fibrosis in C57BL/6J mice. The two schedules induced focal fibrotic lesions as assessed by Masson's trichrome staining (A) and showed increased lung fibrosis (B). Neither 20 or 22.5 Gy led to increased levels of hydroxyproline (C). Graph bars represent the average in the group and error bars represent the SEM. Circles represent unirradiated mice (0 Gy; n=3). Triangles represent mice receiving 20 Gy (n=5): LL25 (blue), LL26 (purple), LL27 (red), LL28 (green) and LL29 (orange). Diamonds represent mice receiving 22.5 Gy (n=5): LL36 (blue), LL37 (purple), LL38 (red), LL39 (green) and LL40 (orange). **$p<0.005$ compared to 0 Gy group (t-test, one-tailed distribution, two sample equal variance). Scale bars represent 100 µm and inset images are 6.5x enlarged.

The lung contains normal tissue structures enriched in collagen, such as bronchi, bronchioles and blood vessels, responsible for the basal levels of hydroxyproline in the lung. As hydroxyproline is present in all types of collagen, collagen molecules accumulated in the fibrotic lesions could be missed in the background amount of collagen present in the lung when hydroxyproline levels are quantified. To overcome this issue, protein levels of the fibrosis-related collagen types (collagen I and III) were quantified by western blot analysis. No increase in collagen protein levels was observed in irradiated mice compared to unirradiated controls. Nevertheless, the 2 symptomatic mice (LL25 and LL37) did show the highest levels of both types of collagen (Figure 3.9).

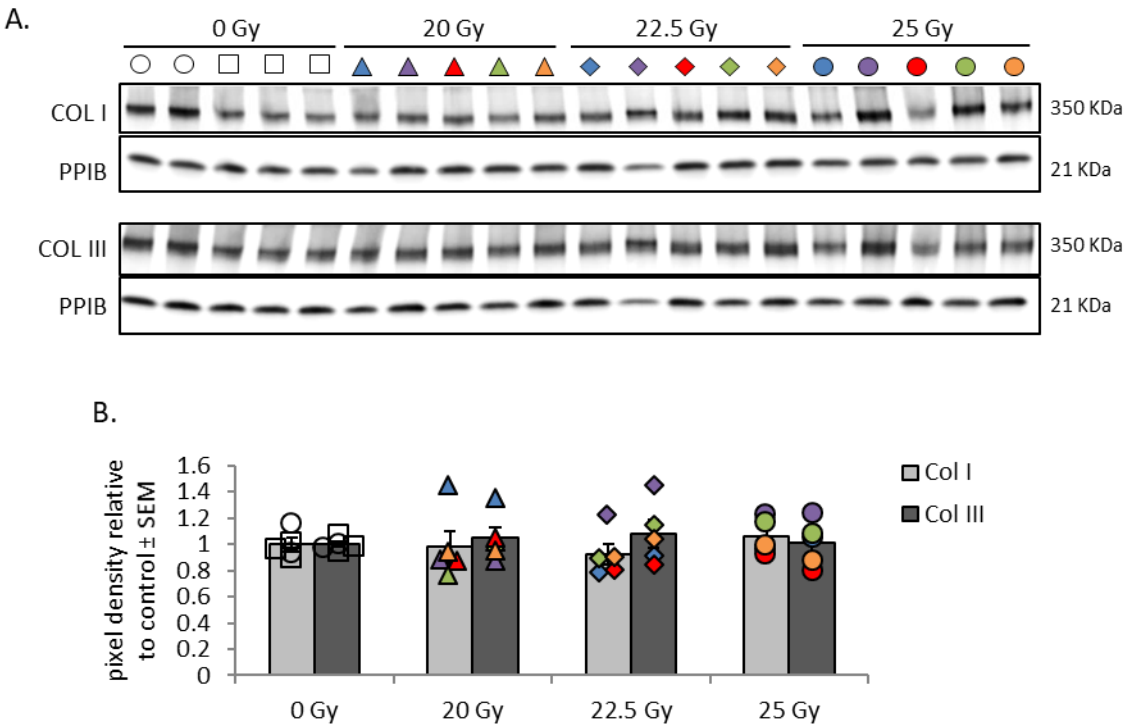


Figure 3.9. Total dose of 22.5 Gy and 20 Gy given to the whole-thorax did not lead to detectable accumulation of collagen I and III in C57BL/6J mice. Collagen I and III were measured by western blot analysis of lung protein extracts, and showed no increase in irradiated lungs compared to unirradiated lungs (A, individual animal extracts were loaded into each well and PPIB was used as loading control; B, blot quantification relative to loading control and respective unirradiated controls average). Graph bars represent the average in the group and error bars represent the SEM. Open circles (n=2): 18 weeks post mock irradiation. Open squares (n=3): 27 weeks post mock irradiation. Triangles represent mice receiving 20 Gy (n=5): LL25 (blue), LL26 (purple), LL27 (red), LL28 (green) and LL29 (orange). Diamonds represent mice receiving 22.5 Gy (n=5): LL36 (blue), LL37 (purple), LL38 (red), LL39 (green) and LL40 (orange). Coloured circles represent mice receiving 25 Gy: LL41 (blue), LL42 (purple), LL43 (red), LL44 (green) and LL45 (orange).

3.4. Discussion

Thoracic radiation is known to induce toxicity in patients and the mechanisms behind it have been extensively studied. Pneumonitis is the main cause of death by thoracic radiation and lethal cases of pulmonary fibrosis have also been reported (Marks et al., 2003; V. Mehta, 2005). Many mechanisms have been proposed to explain the molecular development of these side effects, including early inflammation, increased oxidative stress, DNA damage and senescence (Deng

et al., 2017; Ding, Li, San, & Sun, 2014; Marnett, 2000; Muñoz-Espín & Serrano, 2014; Williams et al., 1667; Yarnold & Vozenin Brotons, 2010). In this chapter, we evaluated the early induction of inflammation and DNA damage as well as the late lung damage that is present in C57BL/6J mice following whole-thorax irradiation.

Plasma levels of pro-inflammatory cytokines were increased in the first hours upon whole-thorax irradiation and were then decreased within the first month post-treatment, similarly to what has been observed by others (Ao et al., 2009). Interestingly, reports on the correlation between increased cytokines plasma levels and lung toxicity in patients disagreed on the predictive potential of cytokine profiling (Hartsell et al., 2007; Rübe et al., 2008; Siva et al., 2014; Stenmark et al., 2017; S. Wang et al., 2017). This may be due to cytokines being also produced by tumours, making it difficult to distinguish if the cytokines measured were in fact induced by radiation. As there are no tumours in the C57BL/6J model used in this work, we can be confident that the changes in cytokine levels are due to radiation and therefore use them to monitor tissue responses to radiation.

The induction of cytokines upon radiation consists of a complex network of several components that have been reported to be up and down regulated at different time-points post-irradiation (Di Maggio et al., 2015; Jeong et al., 2016; Kainthola et al., 2017; Schaue, Kachikwu, & McBride, 2012). Studies using 12 or 12.5 Gy doses of thoracic radiation have shown that the mRNA levels of some pro-inflammatory cytokines (such as TGF-β, IL-1α and IL-1β) raised in a biphasic fashion in the lung tissue exposed to radiation, showing an early peak in the first few days post-irradiation and a second peak several weeks post-irradiation (Rubin, Johnston, Williams, McDonald, & Finkelstein, 1995; Ruebe et al., 2004). These findings indicate that the regulation of the inflammatory response is not restricted to the initial damage directly caused by radiation.

In addition, the induction of the second peak of cytokines may be more localised to the irradiated tissues, as we could not detect a late peak in the plasma levels of TGF- β in plasma samples collected several weeks post-irradiation (4-26 weeks, Supplementary Figure 2). The cause for this secondary induction of inflammation has not been completely elucidated, but it has been suggested that it is related to systemic effects of radiation such as the observed induction of oxidative stress and senescence in tissues outside the field of radiation (Chinnadurai et al., 2011; Citrin et al., 2013; Y. Zhang, Zhang, Rabbani, Jackson, & Vujaskovic, 2012). In conclusion, monitoring of cytokines changes following radiation seems to be a valuable tool to study radiation-induced lung toxicity, although its interpretation is challenging due to the complexity of such response.

We also assessed the induction and repair of DNA damage upon radiation in normal lung tissue. We observed that a significant portion of lung cells was positive for DNA DSB markers γH2AX and 53BP1 foci at 7 and 14 days post-irradiation. Similarly, another study using an 18 Gy single dose, showed that a larger fraction of lung cells was positive for γH2AX foci at 7 days and 8 weeks post-irradiation when compared to unirradiated controls (Kunwar & Haston, 2015). In contrast, in another study where low doses were used (2 Gy single dose and 5 x 2 Gy), the average number of γH2AX foci per lung cell is virtually back to basal levels within 48 h post-irradiation (Rübe et al., 2010a). One possible explanation for this difference is that the amount of DNA damage is dependent on the radiation dose given to the lung. Additionally, the authors of the low dose study quantified the average of γH2AX foci per cell as opposed to the fraction of cells positive for γH2AX foci. Therefore, they might have overlooked a significant percentage of cells carrying residual DNA breaks. Our data shows that DNA DSB repair in the irradiated lung can take longer than anticipated from in vitro data (Beucher et al., 2009). This

finding should be considered in the treatment of lung cancer patients in the clinic, for example, when planning treatments that target DNA repair pathways in combination with radiotherapy.

Interestingly, the two acute effects of radiation described above - inflammation and DNA damage – are proposed to be correlated in a cyclic manner (Pálmai-Pallag & Bachrati, 2014). In short, DNA damage induces inflammation, which in turn leads to increased oxidative stress which has the potential to cause extra DNA damage. This interplay has been proposed to be an underlying mechanism for the systemic effects of radiation, in which tissues outside the field of radiation are affected by treatment (Formenti & Demaria, 2009; Rödel, Frey, Multhoff, & Gaipl, 2015; Siva et al., 2016). Another hypothesis relies on intercellular communication as the mechanism responsible for 'spreading damage signal' to unirradiated cells (Klammer, Mladenov, Li, & Iliakis, 2015). Interestingly, one could propose that even though the above mechanisms are not fully understood, they could explain how radiation treatment causes toxicity several months later. Alternatively, it has been reported that retention of γH2AX foci is related to loss of cell viability, which could explain the late effects due to delayed cell death (Banáth, MacPhail, & Olive, 2004; Olive, 2011). Even though the underlying mechanism is not yet apparent, it is possible that the remaining damaged cells may contribute for the radiation-induced late toxicity, possibly by maintaining a pro-inflammatory signalling leading to chronic inflammation (Figure 3.10).

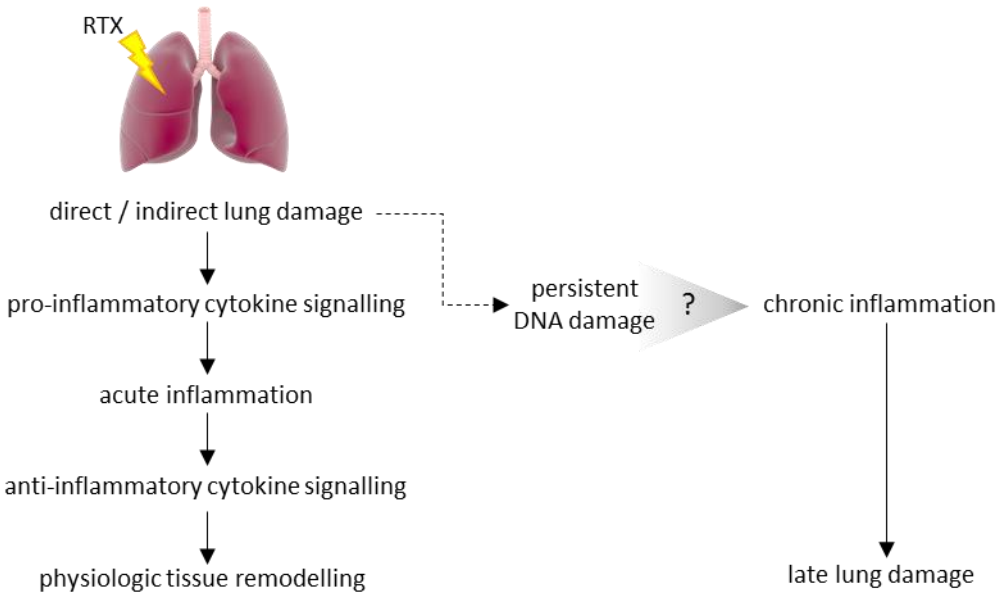


Figure 3.10. Persistent damage leading to chronic inflammation and late lung damage. We observed that unrepaired DNA breaks persist for at least 14 days post-irradiation and, therefore, we hypothesised that cells bearing unrepaired DNA breaks could be contributing to the maintenance of chronic inflammation.

We also explored the late effects of radiation, determining dose schedules that induced differential levels of lung toxicity and therefore would be suitable for further experimentation. Similarly to others, we found that high grade fibrosis (score greater than 2) was induced by the 25 Gy treatment (Citrin et al., 2013). We also observed pleural effusion in the 2 symptomatic mice, which has been proposed to be a consequence of decreased lymph node function (Cui et al., 2014). Despite being considered a confounding factor in the study of lung damage by Jackson et. al., pleural effusions have been observed in patients receiving thoracic radiotherapy and therefore could be clinically relevant (Chotirmall, Low, Murphy, & O'Neill, 2008; Halpenny et al., 2015; I. L. Jackson, Vujaskovic, & Down, 2010; Morrone, Gama e Silva Volpe, Dourado, Mitre, & Coletta, 1993; Rodríguez-García, Fraile, Moreno, Sánchez-Corral, & Peñalver, 1991; Shirai et al., 2011; Van Renterghem & Pauwels, 1995). Even though general welfare was not affected in all mice in the group, asymptomatic mice showed increased

breathing rate by plethysmography and lung abnormalities by in vivo imaging. Therefore, we concluded that the use of a fractionation schedule of a total dose of 25 Gy could be appropriate to test potential mitigators of radiation-induced toxicity. Due to the level of lung damage induced by this treatment, the impact on late effects could be readily assessed by lung function, weight loss and fibrosis scoring.

The lower doses tested (20 and 22.5 Gy) induced low grade pulmonary fibrosis and were mostly well tolerated. As mentioned previously, there is a lack of published literature using fractionated doses in preclinical models of normal tissue responses to radiation. Nevertheless, the fractionated radiation doses used in this work induced comparable late term effects to single doses of similar biologically effective dose (Elizabeth L. Travis et al., 2011). One animal treated with 22.5 Gy was found dead and we interpreted this event as a borderline toxicity that could not be detected by weight loss or abnormal breathing. Of note is the steep curve response observed, with 2.5 Gy escalation between the schedules causing considerable differential side effects. This is in line with what is observed for humans and non-human primates (Dabjan et al., 2016; Garofalo et al., 2014). Considering the risk of sudden death following the 22.5 Gy in this model and the mild induction of fibrosis following 20 Gy, we chose the latter as the preferred fractionation schedule to test combination therapies that have the potential of increasing radiation-induced late toxicity.

In the literature, lethality following thoracic radiation in C57BL/6J mice has been commonly attributed to the development of pulmonary fibrosis. Interestingly, as reported by Dabjan et. al. (2016) this assumption does not rely on strong scientific evidence. Here, we showed that in animals treated with a high dose of radiation (25 Gy) there was a clear association between fibrosis scoring and lethality, but the same was not observed for animals receiving 22.5 Gy. In

addition, the lowest dose used (20 Gy) did not induce high grade fibrosis or early lethality. Also, fibrosis scoring was performed in a single slice of the lung, which might have been misrepresentative of the overall organ pathology (more than one slice per lung should be evaluated for a more accurate measurement of fibrosis). Therefore, we could suggest that high grade fibrosis can lead to lethality but when low levels of fibrosis have developed other pathologies are also likely to be contributing to lethality.

In the clinic, CT scan is the gold standard method for diagnosis of lung fibrosis. To overcome the challenge of distinguishing tumours from lung damage, the use of magnetic resonance imaging in combination with polarised gas has been proposed (Huang et al., 2012; Roos, McAdams, Kaushik, & Driehuys, 2015). Preclinically, the challenge of using imaging techniques in experimental models is achieving enough resolution to differentiate among the potential causes of lung attenuation in small animals. Another methodology used in the clinic are lung function tests (Marks, Fan, Clough, Mun, 2000). We showed that 2 mice treated with 25 Gy showed lung attenuation and increased breathing rate but did not show weight loss, evident respiratory distress or high-grade fibrosis. We concluded that the changes detected by imaging and plethysmography are probably related to side effects other than pulmonary fibrosis such as pneumonitis or pleural effusion. Therefore, we used CT scan and plethysmography as complementary methods for the evaluation of lung damage but not as definitive methods for deciding on sacrifice or evaluation of pulmonary fibrosis.

Quantification of hydroxyproline and collagen I and III protein levels were also technically challenging although valuable as a complement to the fibrosis scoring. As the quantification is performed on the protein lysate obtained from frozen lungs, it accounts for the whole tissue in contrast to the fibrosis score that is obtained from a single lung slice. Nevertheless, the presence

of hard fibrotic lesions or even normal structures like bronchi, bronchioles and the trachea could interfere in the amount of protein extracted – especially in lungs with high grade fibrosis - and therefore may interfere in the final quantification. Another possible explanation for this lack of increase in collagen in the whole lung (especially in the case of high levels of fibrosis) could be the atrophy induced by radiation due to hypovascularisation as observed by others (Collins, Johanson, McCullough, Jones, & Waugh, 1978; Law, 1985; Law, Hornsey, & Field, 1976).

Considering the above, we determined the main end-point for toxicity induced by thoracic radiation as survival time - animals being sacrificed when showing > 10 % weight loss or respiratory distress such as shallow breathing - and, additionally, pulmonary fibrosis quantification by a modified version of Ashcroft scoring. Even though a single slice per lung was scored and fibrosis presented as focal lesions, other generalised abnormalities such as thickening of alveolar walls and extent of collagen deposition contribute to make this an appropriate measure of lung damage (Hübner et al., 2008). Nevertheless, other organs in the field of irradiation that were not assessed in this work (such as the heart) might also have contributed for toxicity and weight loss, potentially explaining the difficulty in associating our findings and decreased survival.

In conclusion, taking the early and late radiation-induced effects showed in this chapter, we hypothesised that early inflammation and DNA damage could be potential targets for modulating late radiation-induced toxicity. In chapter 4, we tested the role of myeloperoxidase, a neutrophil protein, in this response. Next, in chapter 5, we assessed the impact of combining DNA damage response modulators with radiation on late effects.

4. Impaired inflammation is associated with reduced adverse effects of whole-thorax irradiation in C57BL/6J mice

4.1. Introduction

In the previous chapter, increased pro-inflammatory cytokine plasma levels, neutrophil recruitment and DNA damage induction in the lung tissue were described as early effects of thoracic radiation in C57BL/6J mice. Considering the role of KC and IL-6 in the recruitment and maturation of neutrophils and the known cytotoxic effect of this innate immune system cell component, our aim in this chapter was to evaluate the role of neutrophil myeloperoxidase in the early and late responses of normal lung tissue to whole-thorax irradiation (Pojda & Tsuboi, 1990; X. W. Zhang, Liu, Wang, & Thorlacius, 2001).

As discussed before, radiation induces direct and indirect cell damage. Possible cellular outcomes upon radiation include: damage repair and survival, cell death and senescence. Damaged lung cells (alveolar cells, pericytes, endothelial cells, macrophages, fibroblasts) produce DAMPs and/or cytokines (G. Y. Chen & Nuñez, 2010). Of note is the effect of radiation on the endothelium, which becomes activated and express selectin ligands that are recognised by circulating neutrophils (Y. Wang, Boerma, & Zhou, 2016). This initial step of neutrophil activation is referred to as priming (Condliffe, Kitchen, & Chilvers, 1998). Upon attachment to the blood vessel wall, primed neutrophils roll along the endothelium towards the gradient of chemokines immobilised on the surface of endothelial cells (Massena et al., 2010; McDonald et al., 2010). Gradients of hydrogen peroxide are also known to be chemoattractant for

neutrophils (Klyubin, Kirpichnikova, & Gamaley, 1996). Then, neutrophil receptors interact with integrins on the surface of endothelial cells and extravasate into the damaged tissue.

The second step in neutrophil activation is the exocytosis of granules. Neutrophils have at least four types of granules: primary granules, secondary granules, tertiary granules and secretory vesicles (Lacy, 2006). Of interest within this work are the primary granules, which contain the most toxic molecules, such as myeloperoxidase (MPO), elastase, cathepsins, and defensins. Not only are the contents of the four types of granules different from each other, but so is the order of their release during neutrophil degranulation. Secretory vesicles are released first, followed by tertiary granules, secondary granules and lastly primary granules (Bentwood & Henson, 1980). The hierarchy of granule release has been shown to be responsive to increasing intracellular concentrations of Ca^{+}, in addition to many other mediators (Sengeløv, Kjeldsen, & Borregaard, 1993). Interestingly, exocytosis of primary granules specifically has been proposed to be regulated by the interaction of IL-8 and its receptor CXCR1 (Barlic et al., 2000).

In this work, we focused on MPO, a peroxidase enzyme abundantly present in neutrophils, that consists of up to 5% of their cellular content. MPO is also present - although in much lower levels - in monocytes. Of note is the interaction of MPO with hydrogen peroxide and chloride (and in a lower extent other halides and pseudohalides), leading to the generation of hypochlorous acid (HOCl), a potent microbicidal agent (Klebanoff, 2005). HOCl toxicity relies on its ability to interact with DNA, proteins and lipids, leading to nitration and halogenation of those molecules as well as formation of crosslinks. Therefore, HOCl activity does not specifically target pathogens (E Malle, Furtmüller, Sattler, & Obinger, 2007). Not surprisingly, neutrophils and especially MPO have been linked to several diseases mostly related to acute and chronic inflammation such as acute respiratory distress syndrome, atherosclerosis,

Parkinson's disease, kidney disease and ischemia reperfusion (D.-K. Choi et al., 2005; Hasegawa, Malle, Farhood, & Jaeschke, 2005; Ernst Malle et al., 2000; Sugamata et al., 2012).

Importantly, when neutrophil degranulation is happening, another a process called neutrophil respiratory burst takes place. This term refers to the increased consumption of oxygen by neutrophils, due to the activity of reduced nicotinamide adenine dinucleotide phosphate (NADPH)-oxidase and superoxide dismutase, which leads to the production of superoxide anion and hydrogen peroxide (Babior, 2000; Dahlgren & Karlsson, 1999; McCord & Fridovich, 1969). Therefore, the respiratory burst produces chemical species that are the substrate of enzymes contained in the primary granules. For instance, when released into the extracellular space, MPO interacts with hydrogen peroxide produced by the respiratory burst generating HOCl, which leads to killing of extracellular pathogens and normal tissue damage, as described above (Klebanoff, 2005). In addition, inducible nitric oxide synthases (iNOS) are also present in neutrophils, leading to the production of reactive nitrogen species (Weinberg et al., 1995). Finally, all the reactive species produced within the respiratory burst can react among each other and generate a myriads of oxidants, that will contribute to the oxidative stress promoted by the activation of neutrophils (Knaapen, Gu, Borm, & Schooten, 2006). Of note is the hydroxyl radical, that directly interacts with DNA (Lloyd, Hanna, & Mason, 1997).

By mechanisms not yet completely understood, the immune response is then switched to an anti-inflammatory mode. Acute inflammation resolution then takes place orchestrated by a complex anti-inflammatory cytokine network that limits neutrophil infiltration and promotes clearance of apoptotic cells (Serhan, 2010). The wound repair and tissue remodelling phases then take place – which has been classically described to be related mainly to alternatively-activated macrophages and fibroblasts. Nevertheless, during the last decade neutrophils have

been shown to also be involved in these phases of the immune response (Cauwe, Martens, Proost, & Opdenakker, 2009; Fournier & Parkos, 2012; Gong & Koh, 2010). These findings suggest that therapeutic approaches using neutrophil depletion can potentially have more implications than previously anticipated.

Interestingly, there is a debate whether the lung is a physiological neutrophil pool (such as the liver, spleen and bone marrow); with some authors arguing that technical artefacts might have activated neutrophils in the first place leading to wrong conclusions (Hogg & Doerschuk, 1995; Peters, 1998). Nevertheless, recent studies using intravital microscopy have shown that indeed a large number of neutrophils accumulate in the lung, which is believed to be sustained by the fact that neutrophils are bigger than the pulmonary capillaries therefore they need to undergo cytoskeletal changes to be able to traffic through the lung (Kreisel et al., 2010; Summers et al., 2010). In addition, the lung has been proposed to serve as a de-priming site for neutrophils, highlighting the intricate interplay between neutrophil activity and the lung tissue (Summers et al., 2014).

Considering the role of MPO in other inflammatory diseases, we hypothesised that MPO-generated oxidative damage could be enhancing the known damaging effects of radiation in the normal lung tissue. Potentially, this would lead to prolonged activation of the immune system in response to increased cellular damage, culminating with the establishment of chronic inflammation and worsening the level of radiation-induced pulmonary fibrosis (Figure 4.1). To test this hypothesis, in this chapter we explored the interaction between MPO and lung cells *in vitro*, as well as the early and late responses of wild-type and knock-out MPO (WT MPO and KO MPO) mice to whole-thorax irradiation.

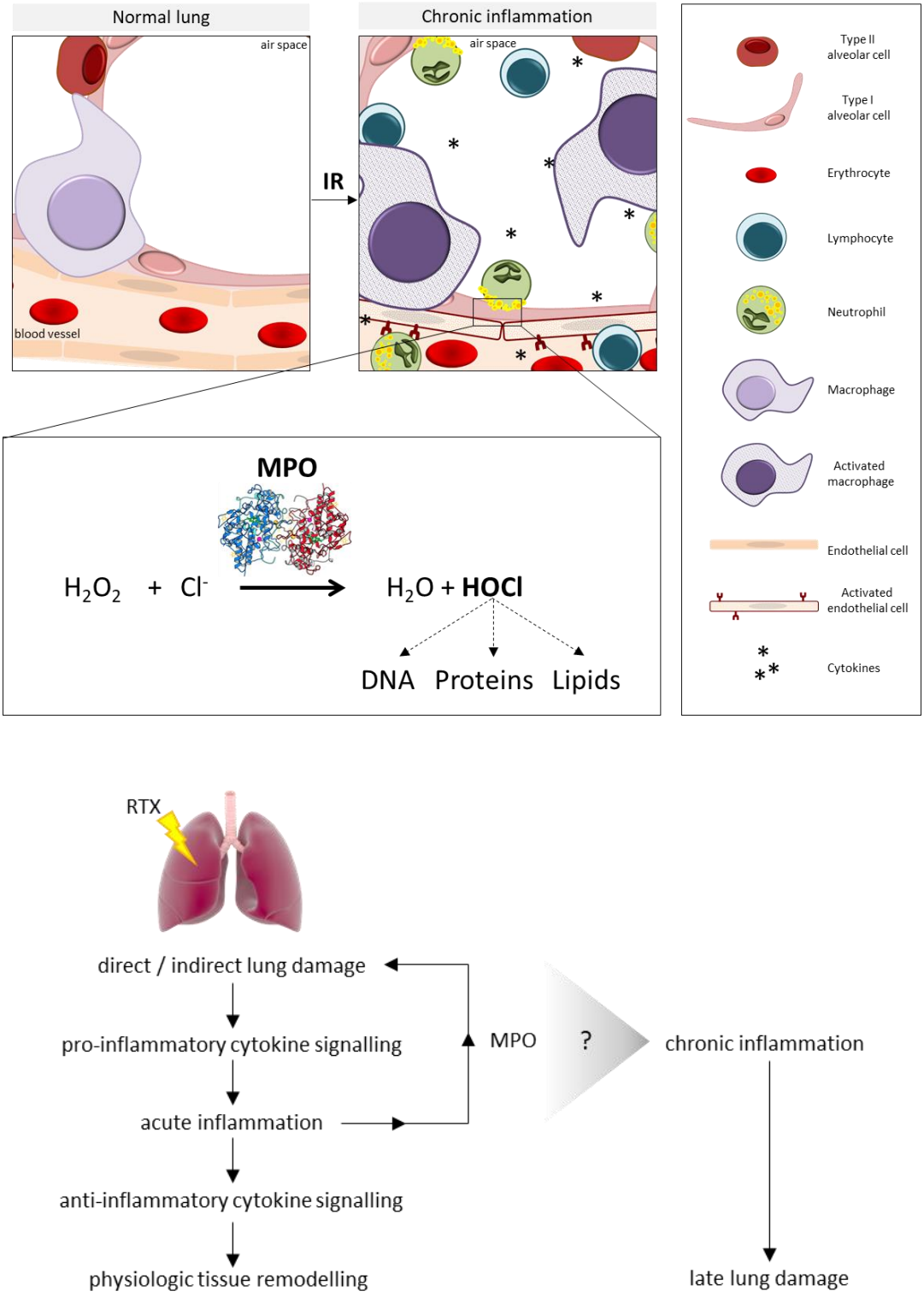


Figure 4.1. Myeloperoxidase-induced lung damage hypothesis. Upon radiation (IR), lung cells are damaged and neutrophils are recruited to the lung. Neutrophil myeloperoxidase (MPO) is released in the lung tissue, leading to production of hypochlorous acid (HOCl), which interacts and damages DNA, protein and lipids. MPO structure was reproduced from (Fiedler, Davey, & Fenna, 2000).

4.2. MPO promotes oxidative stress but does not induce DNA damage in lung cells *in vitro*

To assess if MPO interacts with lung cells, we incubated A549 (human lung adenocarcinoma cell line) or NBE1 (an immortalised human bronchoepithelial cell line) cells with MPO for 30 minutes and then processed the cells to detect MPO uptake by immunofluorescence. MPO was internalised by both cell lines, showing vesicular-like accumulation throughout the cytoplasm. To confirm MPO enzyme activity, we developed a luminol-based assay and verified that the internalised MPO was still active in both cell lines (Figure 4.2).

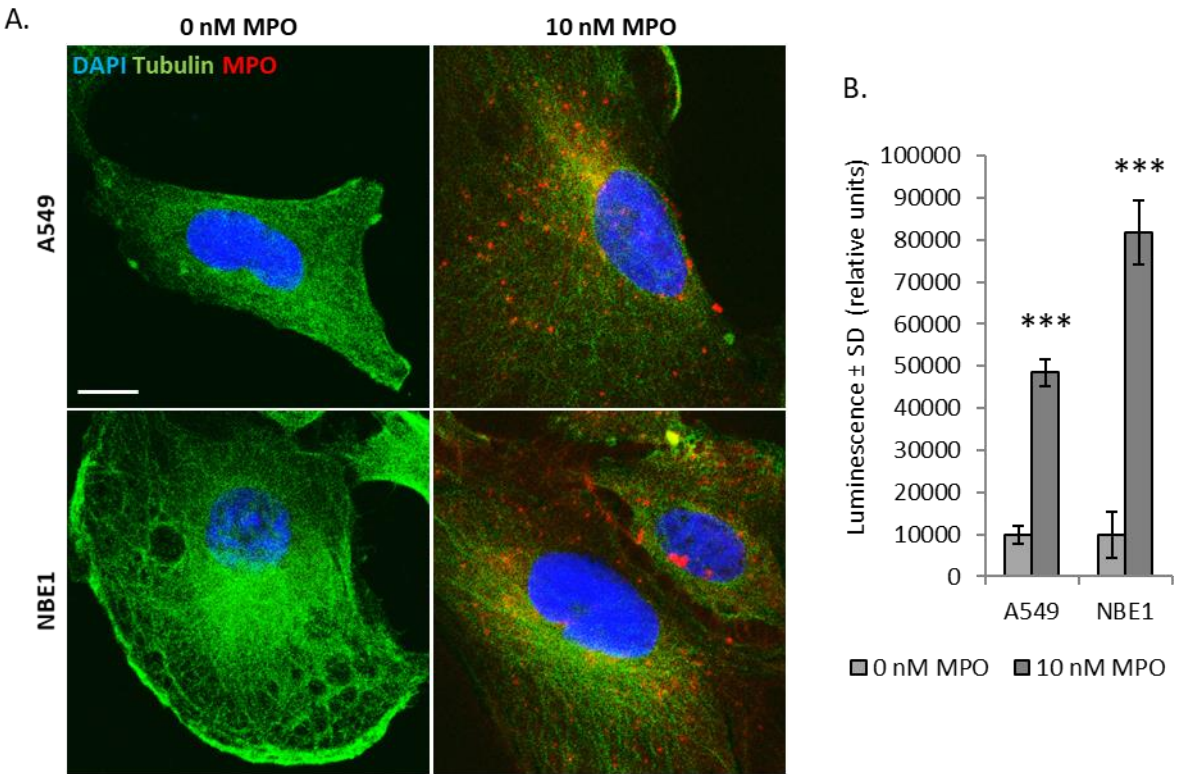


Figure 4.2. Myeloperoxidase (MPO) was internalised by lung cells *in vitro* and remained active after internalisation. Media containing MPO (10 nM) was added to human lung adenocarcinoma cells (A549) or immortalised human bronchoepithelial cells (NBE1) for 30 minutes. Cells were washed, fixed and processed for immunofluorescence. Confocal images showed internalisation of MPO by both cell lines (A; blue: DAPI, green: tubulin, red: MPO). A luminescence assay showed that MPO is active after being internalised (B). Graph bars represent the average in the group (n=3 per group) and error bars represent the SD; ***$p<0.0005$ compared to the respective 0 nM MPO group (t-test, two-tailed distribution, two-sample equal variance). Scale bar represents 20 µm.

Considering its role in generating oxidising species, we performed the CELLROX® assay and observed that both A549 and NBE1 cells incubated with MPO showed a higher level of ROS when compared to controls (Figure 4.3).

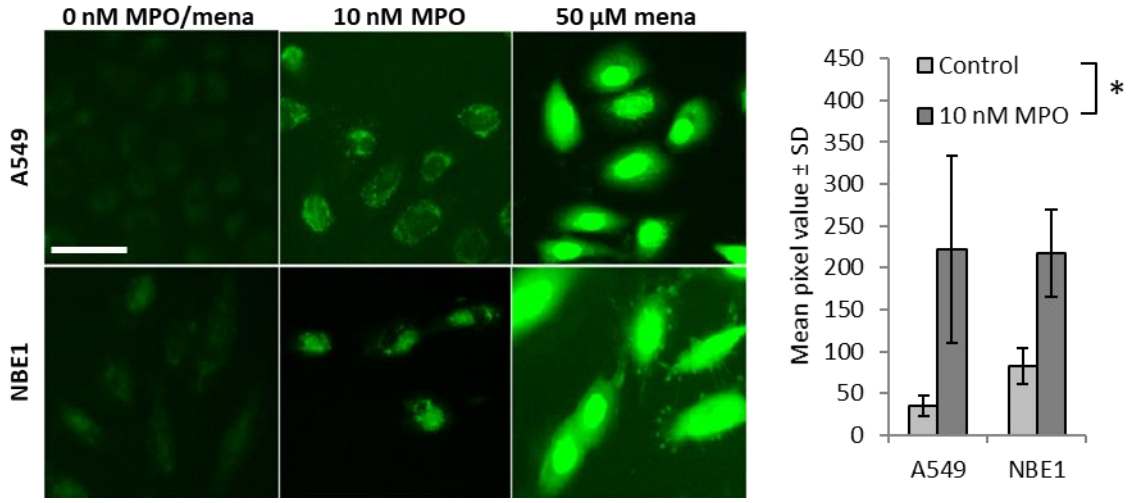


Figure 4.3. Internalised myeloperoxidase (MPO) led to increased levels of reactive oxygen species in human lung cells in vitro. MPO (10 nM) in media was added to A549 or NBE1 cells for 30 minutes and then CELLROX® reagent was added. Cells were imaged in a fluorescence microscope 30 minutes after the addition of CELLROX® dye which becomes fluorescent (green channel) upon oxidation. Graph bars represent the average of 2 replicate wells per group (mean fluorescence value per pixel was calculated for 35 cells per well). Error bars represent the SD; *$p<0.05$ comparing controls to cells incubated with MPO (t-test, two-tailed distribution, two sample equal variance). Menadione (mena, 50 µM) was used as a positive control for oxidation. Scale bar represents 50 µm.

To evaluate if MPO exposure would lead to the generation of DNA damage, we incubated NBE1 and A549 cells with MPO and performed an alkaline comet assay to measure DNA strand breaks, but we did not see an increase in DNA breaks, based on the percent of fluorescence in the comet tail relative to the comet head (Figure 4.4. A). In addition, the number of γH2AX and 53BP1 foci measured by immunofluorescence was no different in cells incubated with MPO compared to controls (Figure 4.4. B), indicating that internalised MPO did not lead to induction of detectable single or double DNA strand breaks.

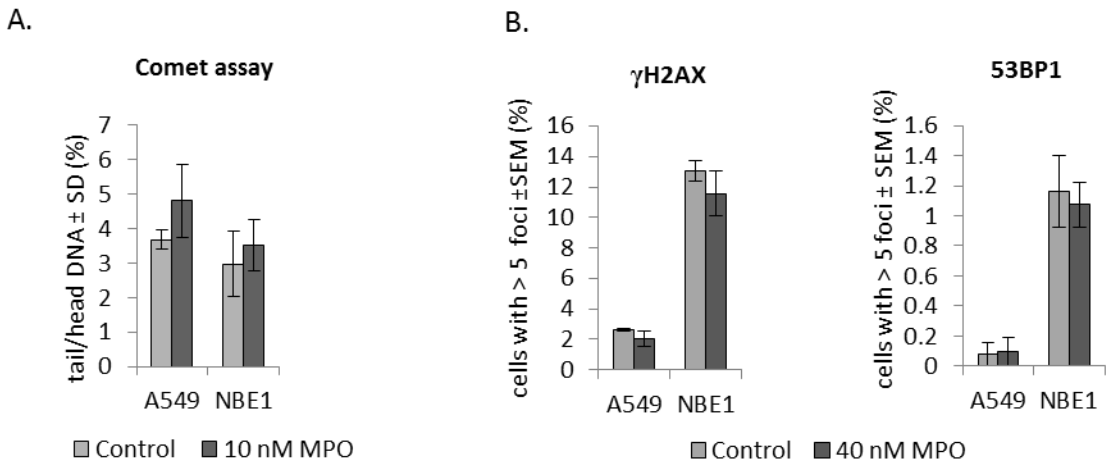


Figure 4.4. Myeloperoxidase (MPO) did not induce significant DNA damage in lung cells *in vitro*. MPO (10 or 40 nM) was added to A549 (human lung adenocarcinoma) or NBE1 (immortalised human bronchoepithelial) cells for 30 minutes. Alkaline comet assays were performed and showed no induction of DNA breaks upon incubation with MPO (A). Alternatively, cells were fixed, and processed for γH2AX or 53BP1 immunofluorescence and then imaged with a fluorescence microscope, but there was no increase in γH2AX or 53BP1 foci upon MPO incubation (B). Graph bars represent the average in the group (n=2 per group for A and n=3 per group for B) and error bars represent the SD or SEM, as stated.

As oxidative stress can also damage proteins and lipids leading to decreased cell viability, we tested whether clonogenic survival of A549 and NBE1 cells was affected by incubation with MPO, but no effect was observed (Figure 4.5).

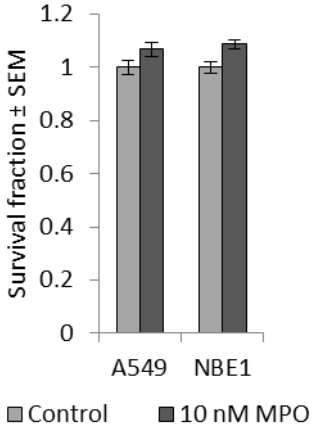


Figure 4.5. Myeloperoxidase (MPO) did not affect clonogenic capacity of lung cells *in vitro*. MPO (10 nM) containing media was added to A549 (human lung adenocarcinoma) and NBE1 (human normal bronchoepithelial) cells for 30 minutes, washed off and cells were provided with fresh media. Plates were placed back in the incubator for 2 weeks to allow for colony forming. No decrease in the surviving fraction upon incubation with MPO was observed. Graph bars represent the average in the group (n=6 per group) and error bars represent the SEM.

4.3. MPO knock-out mice showed reduced neutrophil recruitment, altered pro-inflammatory cytokines in plasma and reduced DNA damage after irradiation

To evaluate the interplay of MPO and radiation *in vivo*, MPO wild-type (MPO WT) and knock-out (MPO KO) C57BL/6J mice were given a single dose of radiation (10 Gy) to the whole-thorax and then sacrificed at several time-points after radiation, ranging from 15 minutes to 28 days, in two independent experiments (Figure 4.6). MPO WT data presented in this chapter was reproduced from chapter 3 to facilitate the comparison between the responses in the two mouse strains.

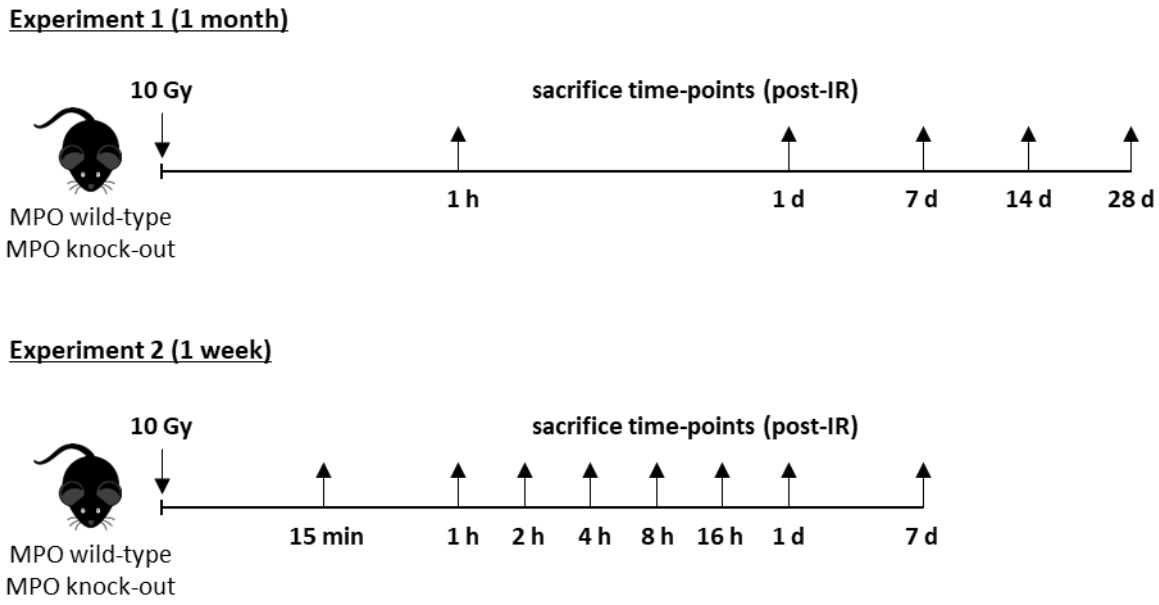


Figure 4.6. Experimental design for evaluation of early effects of whole-thorax radiation in myeloperoxidase (MPO) knock-out mice. Two independent experiments were performed to evaluate the early effects of MPO absence in whole-thorax irradiation responses. MPO wild-type and knock-out C57BL/6J mice were given a single dose of 10 Gy to the whole-thorax and were sacrificed at 1 h, 1 d, 7 d, 14 d and 28 d after radiation (n=3 per time-point). In the second experiment, the same treatment was given and mice were sacrificed at 15 minutes, 1 h, 2 h, 4 h, 8 h, 16 h, 1 d and 7 d post-IR (n=2 per time-point). Left lungs were fixed in formalin for further histological analysis, right lungs were snap frozen and blood was collected for plasma extraction.

As previously shown, in MPO WT C57B6 mice KC plasma levels peaked at 1 h after whole-thorax irradiation. In contrast, in the first experiment conducted in MPO KO mice, no increase in KC levels was observed (Figure 4.7. A). Nevertheless, when a second experiment with a more detailed time course was performed, a significant increase in KC levels in both MPO KO and MPO WT mice was noted from 1 h to 4 h post-irradiation, peaking at 2 h in both strains, compared to unirradiated controls. One day post-irradiation, a second increase was seen only in the MPO KO mice (Figure 4.7 B). When performing statistical analysis to compare MPO WT and MPO KO mice, KC levels where significantly higher in MPO WT compared to MPO KO at 1 h ($p=0.008$, Figure 4.7. A).

A similar profile was observed for IL-6; nevertheless, statistical analysis was not performed because there were no biological replicates for the plasma samples of MPO WT mice. For the MPO KO mice, a significant increase was seen at 1 d post-treatment compared to unirradiated control in both experiments (Figure 4.7. C). In experiment two, MPO WT mice showed a significant increase in IL-6 levels at 2 h when compared to unirradiated control. MPO KO mice showed an increase at 1 h, 2 h and 1 d post-irradiation when compared to unirradiated control (Figure 4.7. D).

Neutrophil recruitment was also compared between MPO WT and MPO KO mice. In the first experiment MPO WT mice showed an increase in recruitment at 1 h post-irradiation (Figure 4.7. E). Similarly to what was observed for the cytokine levels, when samples from the more detailed experiment were analysed, we also observed an increase in recruitment for MPO KO mice, at 4 h post-irradiation (Figure 4.7. F). The recruitment of neutrophils was significantly decreased when comparing MPO KO and MPO WT overall responses in the second experiment ($p=0.007$, Figure 4.7. F).

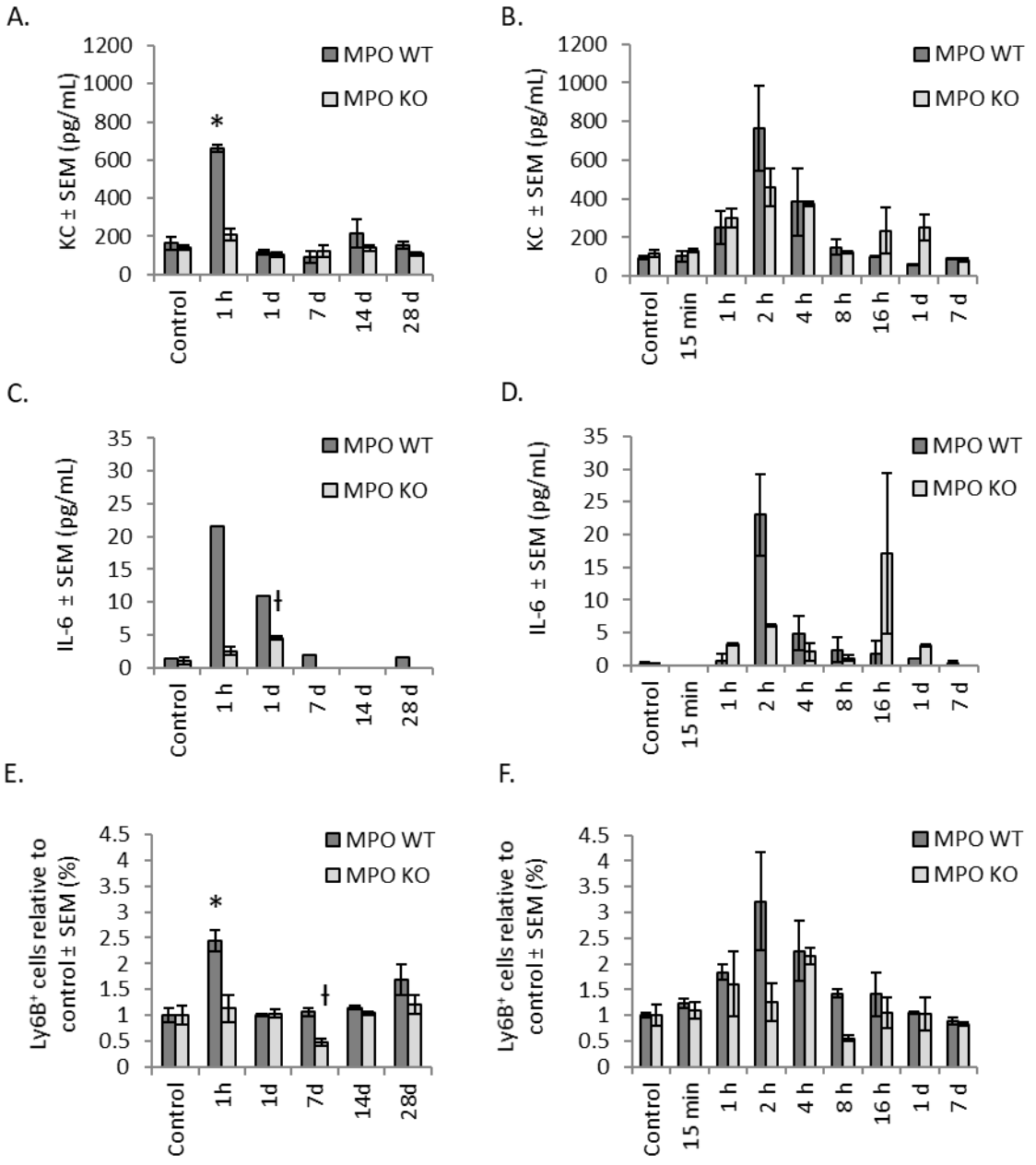


Figure 4.7. MPO knock-out mice showed altered radiation-induced inflammation and decreased neutrophil recruitment to the lung. MPO absence impacted plasma levels of KC (A and B) and IL-6 (B and C) as assessed by ELISA. In addition, MPO absence decreased the recruitment of Ly6B-positive cells to the lung after irradiation as assessed by immunohistochemistry (E and F, Ly6B - marker for neutrophils). WT: wild-type, KO: knock-out; graph bars represent the average in the group (n=2 per group, except for graph E in which n=3 per group) and error bars represent the SEM (MPO WT series in IL-6 graph in the left does not have error bars as samples were pooled together); *$p<0.05$ compared to WT control, ǂ $p<0.05$ compared to KO control (t-test, one-tailed distribution, two-sample equal variance). MPO WT data was reproduced from Figure 3.2.

Regarding DNA damage, MPO KO mice showed fewer γH2AX-positive cells after radiation in comparison to MPO WT mice (Figure 4.8. A). This effect was observed throughout the time points analysed and was maintained for at least 7 days after radiation (Figure 4.8. B).

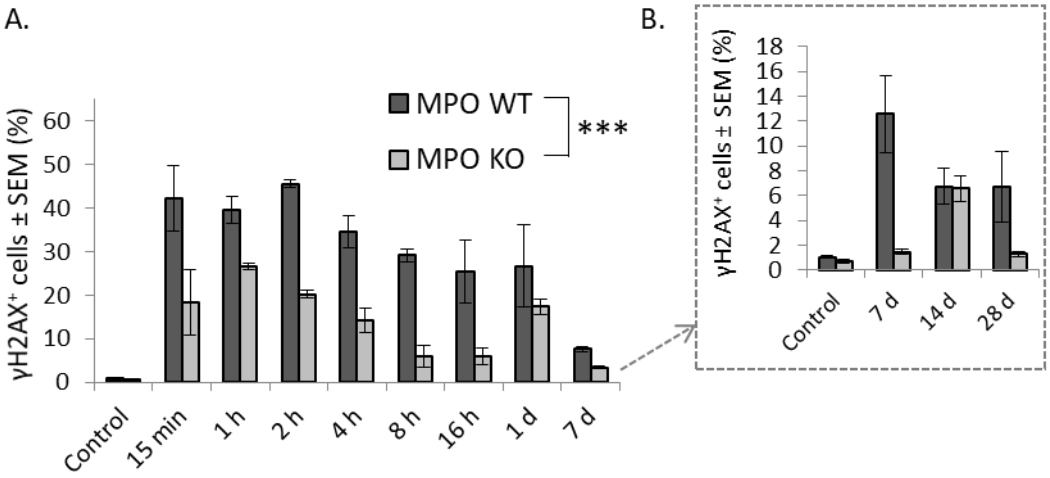


Figure 4.8. MPO absence reduces radiation-induced DNA damage response in the lung cells. γH2AX-positive cell count in the lung of MPO knock-out mice is lower compared to wild-type controls as assessed by immunohistochemistry. WT: wild-type, KO: knock-out; graph bars represent the average in the group and error bars represent the SEM; *p<0.05 and **p<0.005 comparing wild-type and knock-out (t-test, one-tailed distribution, two-sample equal variance). MPO WT data was reproduced from Figure 3.3. A: n=2 per group; B: n=3 per group.

Considering that following radiation MPO KO mice had a blunted inflammatory response with decreased neutrophil recruitment and reduced levels of DNA damage, we next tested whether the absence of MPO also impacted the late toxicity of whole-thorax irradiation. MPO WT and MPO KO C57BL/6J mice were given 3 different schedules of fractionated whole-thorax irradiation (previously described in chapter 3) and monitored for 27 weeks (Figure 3.5).

At 18 weeks post-irradiation, MPO KO mice treated with 25 Gy did not show adverse clinical signs, in contrast to what was observed in MPO WT (as shown in chapter 3). In addition, MPO KO mice treated with 20 or 22.5 Gy also did not show any adverse effects until the scheduled end-point of the experiment (27 weeks post-irradiation), in contrast to MPO WT mice. A

compilation of the number of mice showing adverse effects following radiation is presented in Table 4.1.

Table 4.1. Myeloperoxidase (MPO) knock-out was associated with decreased adverse effects (AE) in mice receiving fractionated whole-thorax irradiation. Adverse side effects observed were >10 % weight loss, abnormal breathing and premature death; n=5 mice per group.

Total dose	Fractionation	Number of mice showing AE	
		MPO wild-type	MPO knock-out
20 Gy	4 x 5 Gy [1]	1	0
22.5 Gy	4 x 5 Gy + 1 x 2.5 Gy [1]	1	0
25 Gy	5 x 5 Gy [2]	2	0

[1] sacrificed at 27 weeks post-irradiation; [2] sacrificed at 18 weeks post-irradiation

For the 25 Gy treatment group, unrestrained plethysmography prior to sacrifice showed that radiation did not lead to increased breathing rate in MPO KO mice while irradiated MPO WT mice showed increased breathing rate compared to unirradiated controls. Interestingly, MPO KO mice showed higher baseline breathing rate (Figure 4.9. A). CT scan images of two MPO KO mice were performed and no areas of lung attenuation were detected, in contrast to MPO WT mice (Figure 4.9. B). Lung samples stained by Masson's trichrome protocol were scored for fibrosis and both MPO WT and MPO KO mice showed significant increase in fibrosis score compared to the respective unirradiated controls, but no significant difference was observed between MPO WT and MPO KO mice (Figure 4.9. C). The absence of MPO did not show any significant impact in accumulation of collagen as assessed by hydroxyproline assay (Figure 4.9. D).

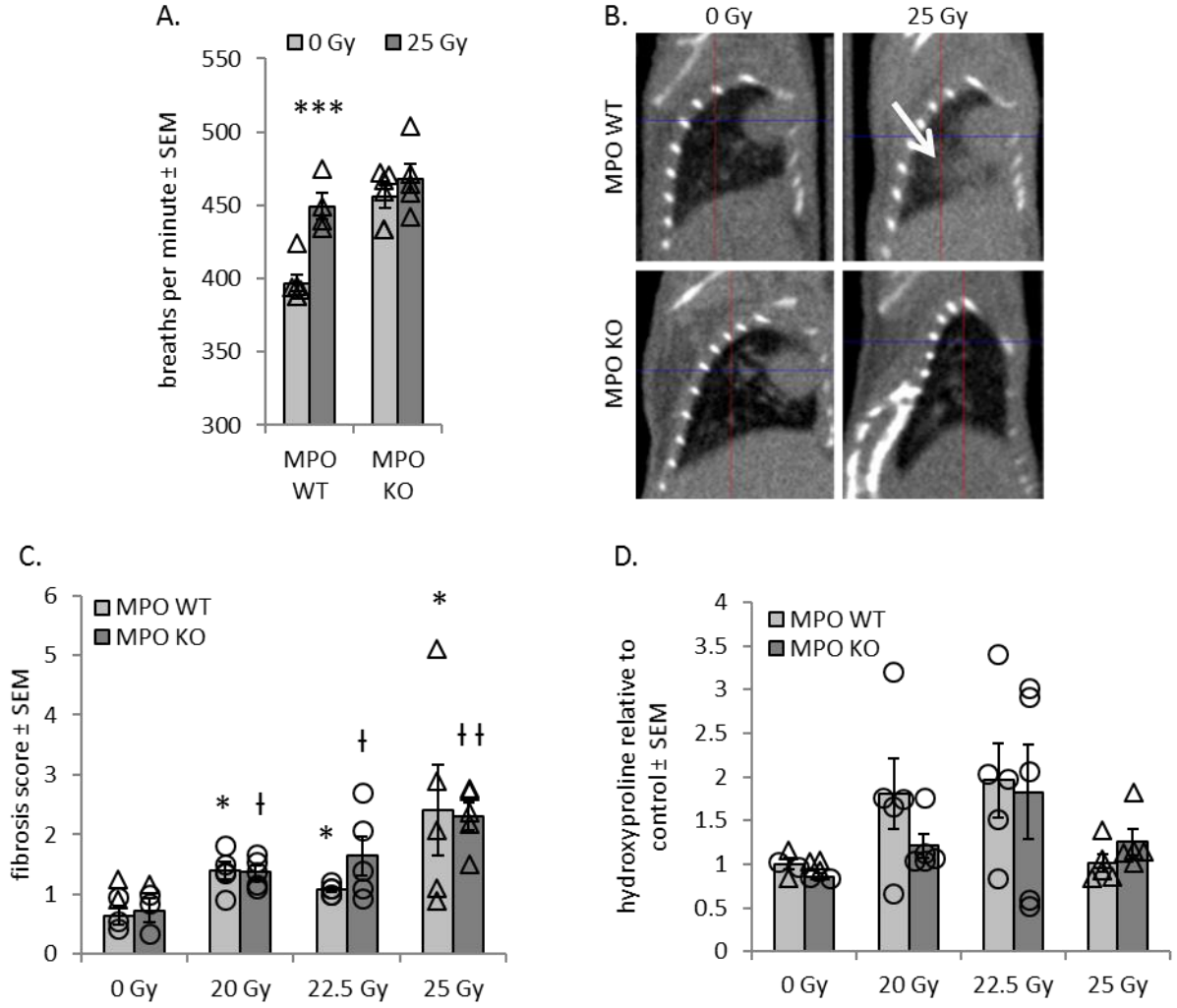


Figure 4.9. Myeloperoxidase knock-out (MPO KO) mice receiving 25 Gy of whole-thorax irradiation showed less lung damage compared to myeloperoxidase wild-type (MPO WT) mice. Mice underwent unrestrained plethysmography and breathing rates were recorded; irradiated MPO KO mice did not show increased breathing rate (A). *In vivo* imaging was performed by CT scan at 18 weeks post-irradiation, showing lung attenuation (arrow) only in irradiated wild-type mice (B). Analysis of lung samples stained by Masson's trichrome protocol revealed increase in fibrosis score in irradiated lungs of MPO WT and MPO KO mice (C). Hydroxyproline levels were not significantly increased in any of the groups (D). In figure C and D, in control group and 20 Gy groups 3 out of 5 MPO mice were males. Graph bars represent the average in the group (n=5 mice per group) and error bars represent the SEM. Open circles represent individual animals sacrificed at 27 weeks post-IR and open triangles represent individual animals sacrificed at 18 weeks post-IR; ***$p<0.0005$ and *$p<0.05$ compared to MPO WT 0 Gy group; ǂ $p<0.05$ and ǂ ǂ $p<0.005$ compared to MPO KO 0 Gy group (t-test, one-tailed distribution, two sample equal variance). MPO WT data was reproduced from Figure 3.5.

4.4. Discussion

Similarly to Haegens et al, we showed that MPO is internalised by lung cells and that it retains its peroxidase activity after internalisation in vitro. In addition, Haegens et al observed an increase in DNA damage in lung cell lines at 20 minutes but not 30 minutes after exposure to MPO (A. Haegens, Vernooy, Heeringa, Mossman, & Wouters, 2008). In our experiments, we only evaluated DNA damage in lung cell lines at 30 minutes of MPO exposure and similarly did not observe any increase in that time-point. These findings suggest that any DNA damage caused by MPO is quickly repaired by lung cells in vitro and is not long lasting - as opposed to radiation-induced damage in vivo. Further analysis (such as immunofluorescence with colocalization of markers) should be performed to determine if MPO is active in the nucleus once internalised or if the MPO generated ROS can reach this organelle and therefore the DNA. Also, regarding the increased ROS levels in cells incubated with MPO, further analysis such as modified comet assays (using enzymatic processing) should be performed to better describe the interaction of MPO generated ROS and the DNA. Our in vitro results were designed to clarify the role of MPO itself on lung cells. To evaluate the interaction of MPO and radiation, we moved to in vivo models that are more complex and account for the other components of radiation responses. Interestingly, when we evaluated the impact of MPO on DNA damage induced by radiation in vivo, we observed higher levels of residual γH2AX-positive cells in MPO WT mice which was sustained for at least a week post-irradiation. Taken together, these findings suggest that MPO knock-out impacts the radiation-induced DNA damage in the lungs of C57BL/6J mice.

In addition, we showed that MPO incubation increased ROS levels in lung cell lines, corroborating a previously reported increase in mRNA levels of the antioxidant heme oxygenase (HO-1) (Haegens et al., 2008). We observed higher levels of DNA DSB markers in MPO WT mice, which can be interpreted as increased damage induction in an environment containing MPO upon radiation. Even though we did not observe induction of DNA damage in vitro when adding MPO to lung cells, it is important to stress that only in vivo the neutrophil respiratory burst would be complete and it has been reported to be related to induction of DNA damage (Knaapen et al., 2006).

The impact of MPO deficiency following asbestos and lipopolysaccharide exposure has been extensively researched by (Haegens et al., 2005, 2009). Similarly to our observations on irradiated mice, they showed that the lack of MPO led to decreased recruitment of neutrophils to the lung and altered cytokine expression after challenge. The two complementary experiments we performed showed that the plasma levels of KC and IL-6 peaked in MPO WT mice a few hours after treatment with radiation in an acute and transient manner, and that this response was less significant in irradiated MPO KO mice compared to MPO WT. It is perhaps challenging to correlate these results with decreased neutrophil recruitment as both cytokines and neutrophils recruitment decrease at the same time post-radiation. This might show that other components of the cytokine cascade might be influencing the recruitment of neutrophils to the lung post-radiation or even potentially that MPO absence affects neutrophil-independent processes. We hypothesise that in the absence of MPO, less oxidative stress led to decreased lung tissue damage (including less DNA damage), culminating in the decreased inflammatory response observed in MPO KO mice. This supports research showing that the use of anti-oxidant therapies may ameliorate radiation-induced pulmonary fibrosis (Lee et al., 2010).

Of note is the difference between the observed peak time of inflammatory cytokines between the two independent experiments that we performed, from 1 h post-irradiation in the first experiment to 2 h in the second for MPO WT mice. This difference may have been technical, for example minor variations in the times of sacrifice and harvesting, but it could also represent an underlying difference in biological responses, perhaps emphasising the importance of performing more detailed time courses for the evaluation of inflammatory responses induced by radiation.

To our knowledge, this is the first report of the effects of whole-thorax irradiation in MPO KO mice. The use of acetylsalicylic acid in the context of whole body irradiation decreased the levels of MPO in rat lungs and decreased radiation-induced lung damage (Demirel et al., 2016). One recent report showed a correlation between the levels of MPO and the severity of radiation-induced mucositis in a rat model (Miyamoto et al., 2015). Other groups have studied the role of neutrophils or other neutrophil-related proteins in the context of bleomycin-induced pulmonary fibrosis. The pathology of fibrosis induced by bleomycin is quite different from fibrosis induced by radiation, as it manifests around 14-21 days post-induction and has been reported to be reversible. It has been observed that neutrophil depletion, inhibition of neutrophil elastase or reduction in neutrophil chemotaxis decreased bleomycin-induced pulmonary fibrosis (Fox, Gordon, & Haston, 2011; Fox & Haston, 2013; Manoury, Nénan, Guénon, Lagente, & Boichot, 2007; Takemasa, Ishii, & Fukuda, 2012). These findings are encouraging, but they may not be directly related to radiation-induced fibrosis due to the different manifestation (and most likely mechanisms) of the disease in bleomycin-treated animals.

Interestingly, no correlation was observed between strain susceptibility to pulmonary fibrosis and neutrophil count in alveolar lavage at 6 h, 1 day or 7 days post-irradiation (Paun, Kunwar,

& Haston, 2015), which suggests that if neutrophils do have an impact on radiation-induced fibrosis, it would be at earlier time-points after radiation. In addition, as already discussed in the previous chapter, our MPO data shows that it is difficult to establish a correlation between radiation-induced pulmonary fibrosis and collagen accumulation in the lung with survival time, as we failed to observe significant differences in hydroxyproline levels or fibrosis score between MPO WT and MPO KO mice despite the difference observed in adverse effects (weight loss, increased breathing rate and lung attenuation). Considering these finding and other studies showing similar disconnection (Down, Laurent, McAnulty, & Steel, 1984; Fox & Haston, 2013; Hallahan, Geng, & Shyr, 2002; Machtay et al., 2006; Puthawala et al., 2008; E. L. Travis, Meistrich, Finch-Neimeyer, Watkins, & Kiss, 1985), we speculate that decreased survival time following whole-thorax irradiation might have other underlying causes in addition to lung fibrosis.

We showed in this chapter that MPO incubation led to increased ROS levels in lung cell lines but did not impact on DNA damage or clonogenic capacity in vitro. In addition, MPO deficiency led to decreased radiation-induced acute inflammation and DNA damage in the lung tissue. Importantly, even though MPO absence did not impact on lung fibrosis, MPO KO mice receiving 25 Gy of whole-thorax radiation showed increased survival time compared to WT controls. As MPO absence impacted on the early induction of DNA damage and on the onset of late adverse effects, we speculate that this early effect induced by radiation could be related to the late effects observed (Figure 4.10). Therefore, in chapter 5 we evaluate the impact of directly modulating early DNA damage on the late effects of radiation by using DNA damage response modulators.

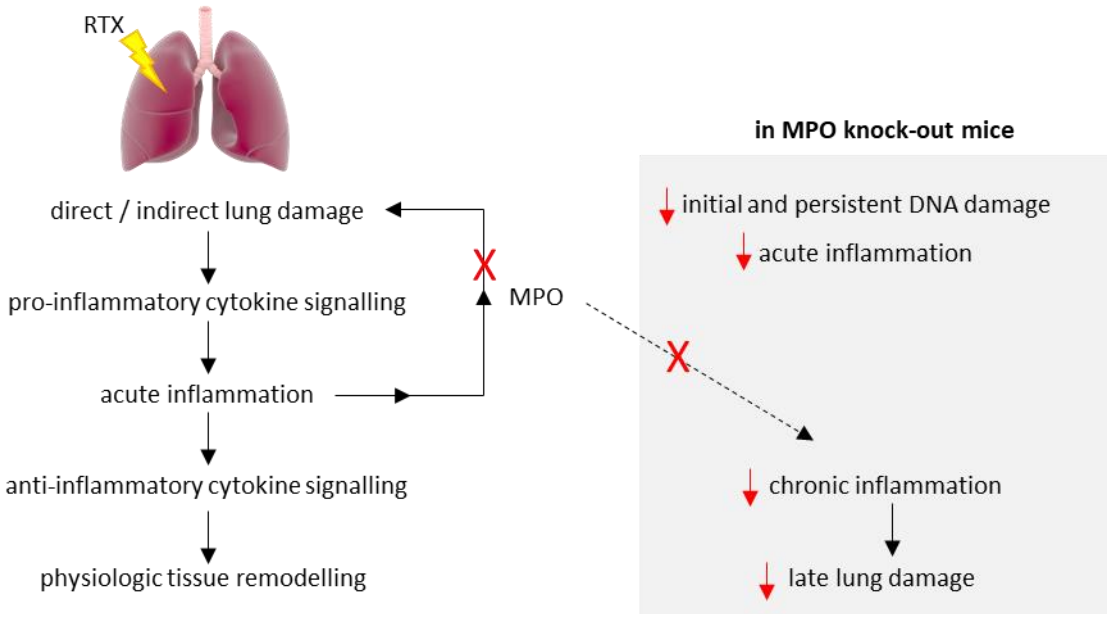


Figure 4.10. MPO contribution to radiation-induced chronic inflammation and late lung damage. Our data showed that in MPO knock-out mice, radiation induced less DNA damage and dampened neutrophil recruitment, which could potentially explain the reduced late effects of thoracic radiation in MPO knock-out compared to MPO wild-type mice.

5. The impact of targeting the DNA damage response induced by whole-thorax irradiation in C57BL/6J mice

5.1. Introduction

The use of DNA damage response modulators has been evaluated as potential cancer therapeutics in the recent years. A rationale for this therapeutic approach is that tumour cells sustain high levels of genomic instability and are more reliant on certain DDR pathways; therefore, impairing such pathways would lead to selective killing of cancer cells and normal tissue sparing (Figure 5.1). Several preclinical experiments and clinical trials have been published and reviewed by several authors (Gavande et al., 2016; Mateo & de Bono, 2017; O'Connor, 2015). In this thesis, focus will be given to ataxia-telangiectasia mutated (ATM), ataxia-telangiectasia and Rad3-related (ATR) and poly(ADP-ribose)-polymerase (PARP) inhibitors, reviewed in (Karnitz & Zou, 2015; Lord & Ashworth, 2017; Sundar, Brown, Ingles Russo, & Yap, 2017; Weber & Ryan, 2015).

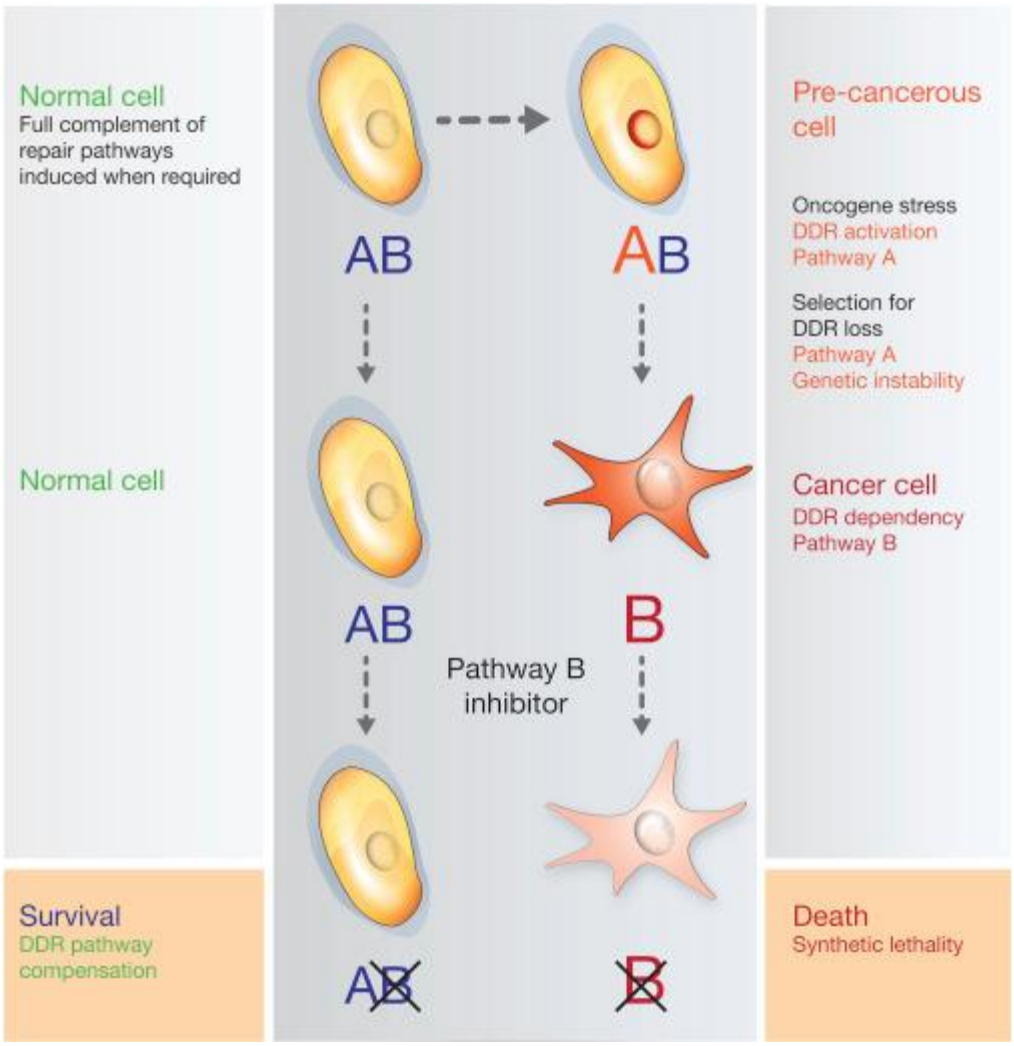


Figure 5.1. The rational for targeting DNA damage repair pathways in cancer treatment. A range of cancer types show defective DNA repair pathways therefore relying on the remaining pathways. By inhibiting the remaining pathways, it would lead to selective killing of tumours cells. Reproduced from (O'Connor, 2015).

Throughout the cell cycle, the main pathway used to repair DNA DSBs is non-homologous end joining (NHEJ). Additionally DNA DSB repair by homologous recombination occurs in S and G2 phases, although NHEJ is still the predominant repair pathway (Mao, Bozzella, Seluanov, & Gorbunova, 2008). Promotion of homologous recombination in the S phase occurs through an increased rate of DNA end resection, as DNA ends extensively processed by the MRN

complex are not recognised by NHEJ effectors. The coordination of end resection and the cell cycle is believed to happen via the cyclin-dependent kinase CDK1. This protein has been shown to be required for homologous recombination by promoting end resection and radiation sensitivity abnormal 51 (RAD51) recruitment (Aylon, Liefshitz, & Kupiec, 2004; Ira et al., 2004). Recently, it has been described that end processing can also occur before NHEJ, but it differs from the processing promoted by MRE11–RAD50–NBS1 (MRN) complex (Biehs et al., 2017).

ATM, a protein of the phosphatidylinositol 3-kinase-related kinases (PIKKs) family, was named after the disease ataxia-telangiectasia (A-T), which presents with progressive loss of neurological function and impaired structure of blood vessels. A-T patients, whose cells lack ATM activity, also present with other symptoms such as immunological disorders, extreme sensitivity to ionising radiation and increased cancer rates. ATM can be classified as a tumour suppressor, and is found to be frequently mutated in a range of human cancers including lung, colorectal, breast and haematopoietic cancers (Bea et al., 2013; Landau et al., 2013; Network, 2012a, 2012b, 2014; The Cancer Genome Atlas Research Network, 2012).

ATM is recruited by the MRN sensor complex upon recognition of DNA DSBs. Interaction of ATM with Nijmegen break syndrome 1 (NBS1) leads to enhanced ATM activity (J.-H. Lee & Paull, 2005). In its inactive state, ATM exists as a noncovalent homodimer and, upon activation, the dimer is dissociated through autophosphorylation of the serine residue 1981 (Bakkenist & Kastan, 2003). Once activated by phosphorylation, ATM phosphorylates downstream targets: more than one thousand proteins have been identified as putative targets of ATM, involved in a range cellular processes, from DNA damage repair to response to oxidative stress (Shiloh & Ziv, 2013). One of the most well studied downstream target of ATM is histone 2AX (H2AX),

a component of the nucleosome cores. Upon DNA damage, active ATM phosphorylates H2AX on serine residue 139 (referred to as γH2AX), which serves as a signal for the assembly of DDR components in the site of damage (Burma, Chen, Murphy, Kurimasa, & Chen, 2001; Paull et al., 2000). Another important role of ATM is controlling the cell cycle, by the direct and indirect (through checkpoint kinase 2, CHK2) phosphorylation of tumour protein 53 (p53), leading to its stabilisation and accumulation, culminating with cell cycle arrest in G1 (Chehab, Malikzay, Appel, & Halazonetis, 2000). ATM-CHK2 have also been shown to control the intra-S phase checkpoint (Falck, Mailand, Syljuasen, Bartek, & Lukas, 2001). Other important downstream targets of ATM are breast cancer type 1/2 susceptibility protein (BRCA1/2) and 53BP1, which are proteins involved in the choice of DNA repair – homologous recombination and non-homologous end joining, respectively (Figure 5.2) (Daley & Sung, 2014).

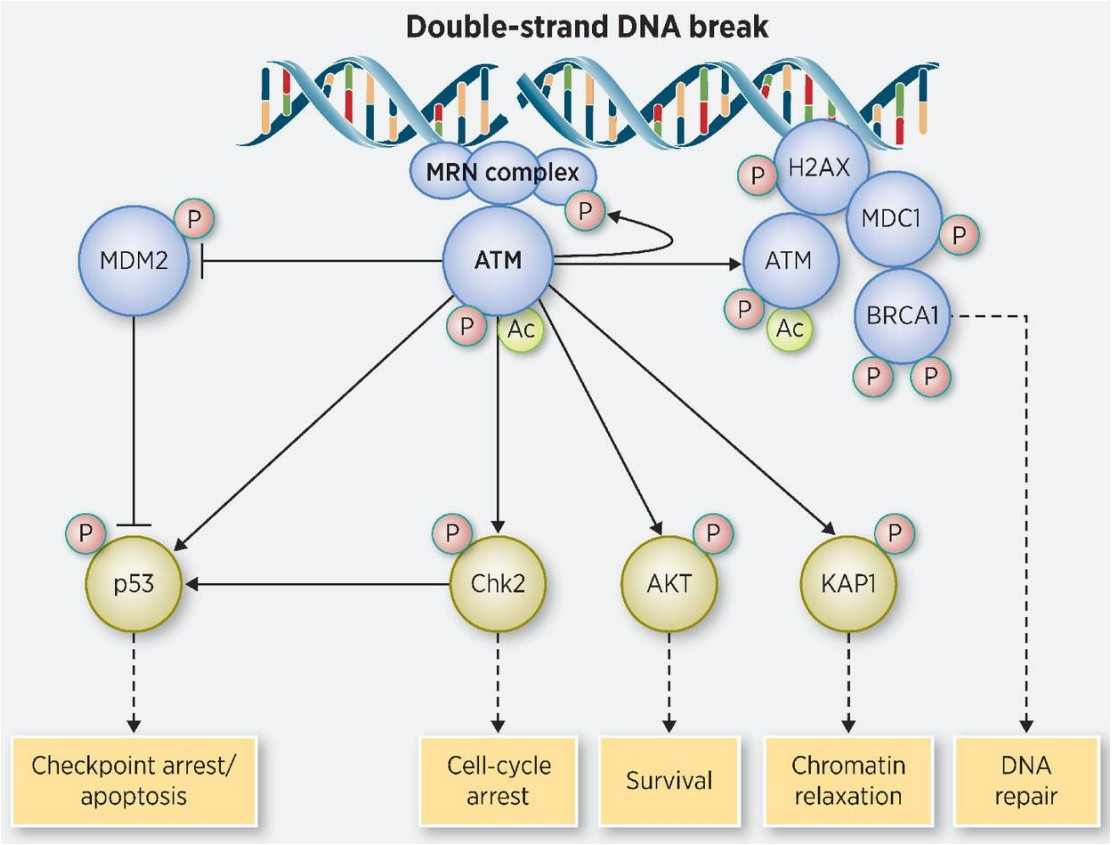


Figure 5.2. ATM signalling upon DNA double strand break. Double strand breaks recognised by the MRN complex lead to the recruitment and activation of ATM which in turn can signal for several responses, including DNA repair, cell cycle arrest, survival and chromatin modification. Reproduced from (M. Choi, Kipps, & Kurzrock, 2016).

Another important player in the DNA damage response and a member of the PIKK family, is the kinase ataxia telangiectasia and Rad3-related (ATR). Interestingly, unlike ATM, ATR is an essential gene and ATR knock-out mouse embryos do not survive (Brown & Baltimore, 2000; de Klein et al., 2000). This is believed to be due to the role of ATR in stabilising DNA replication forks under condition of DNA replication stress; but ATR also has other functions such as DNA DSB repair and response to mechanical and osmotic stresses (Saldivar, Cortez, & Cimprich, 2017). Here we will focus on the role of ATR on replication stress as cancer cells

have elevated levels of replication stress compared to normal cells, and therefore, this was the initial rationale for the use of ATR inhibitors as a cancer therapy.

During replication stress, replication forks can stall and regions of single-stranded DNA (ssDNA) are formed. The canonical pathway of ATR recruitment consists on the recognition of ssDNA by replication protein A (RPA), which is followed by the recruitment of ATR-interacting protein (ATRIP) and ATR (Cortez, Guntuku, Qin, & Elledge, 2001; Zou et al., 2003). The mechanism of activation of ATR is not yet fully described but relies on protein topoisomerase II binding protein 1 (TOPBP1) and Ewing tumour-associated antigen 1 (ETAA1) (Haahr et al., 2016; Mordes, Glick, Zhao, & Cortez, 2008). The range of fork stalling structures and how they can lead to ATR activation have been recently reviewed (Saldivar et al., 2017). ATR signalling promotes cell cycle arrest in S phase through phosphorylation of checkpoint kinase 1 (CHK1) and subsequent degradation of cell division cycle 25 A (CDC25A), which has been shown to be a major mechanism of sensitisation of cells to ATR inhibition (Ruiz et al., 2016). ATR and CHK1 are also linked to control of origin firing, and ATR inhibition can lead to premature firing resulting in fork stalling (Katsuno et al., 2009). Finally, ATR activity stabilises stalled DNA replication forks, decreasing the chance of fork collapse and subsequent DNA DSB formation (Figure 5.3) (Lopes, Cotta-Ramusino, Pellicioli, & Liberi, 2001).

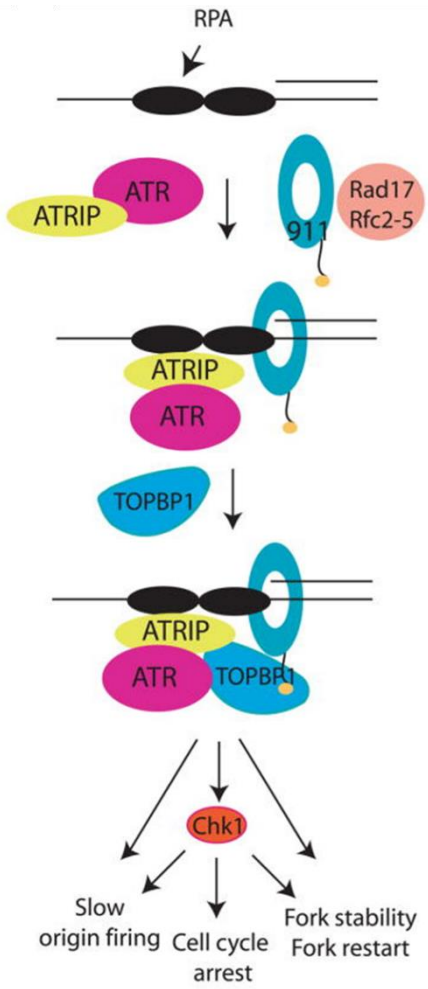


Figure 5.3. ATR activation. Single stranded DNA is recognised by RPA, which leads to the recruitment of ATRIP and ATR. In turn, ATR promotes several processes, including reduction of replication origin firing, cell cycle arrest, fork stability/restart. Reproduced from (Cimprich & Cortez, 2008).

Considering the above, ATM and ATR inhibitors are currently being investigated as cancer treatments as monotherapies and in combination with DNA damaging agents or radiotherapy. Preclinically, several papers have been published so far showing the radiosensitising effects of both targets. Clinical trials are currently underway but so far, no results have been published (NCT02157792, NCT01955668, NCT02223923 and NCT02264678). A recent review from our

group compiles the relevant studies looking at ATM and ATR inhibitors alone or in combination with radiotherapy (Weber & Ryan, 2015).

In contrast to ATM and ATR, PARP has a DNA binding motif and directly recognises DNA strand breaks. Once bound to DNA, PARP cleaves nicotinamide adenine dinucleotide (NAD+) to nicotinamide and ADP-ribose, and adds poly(ADP-ribose) (PAR) to several target proteins related to DNA repair (Figure 5.4). The most well described function of PARP in base excision repair (BER) is by its interaction with XRCC1, which when PARylated, recruits DNA SSB repair machinery (Masson et al., 1998). Also, the role of PARP in restarting stalled replication forks and non-canonical NHEJ pathways has been demonstrated, but detailed mechanistic data is still missing (Bryant et al., 2009; M. Wang et al., 2006).

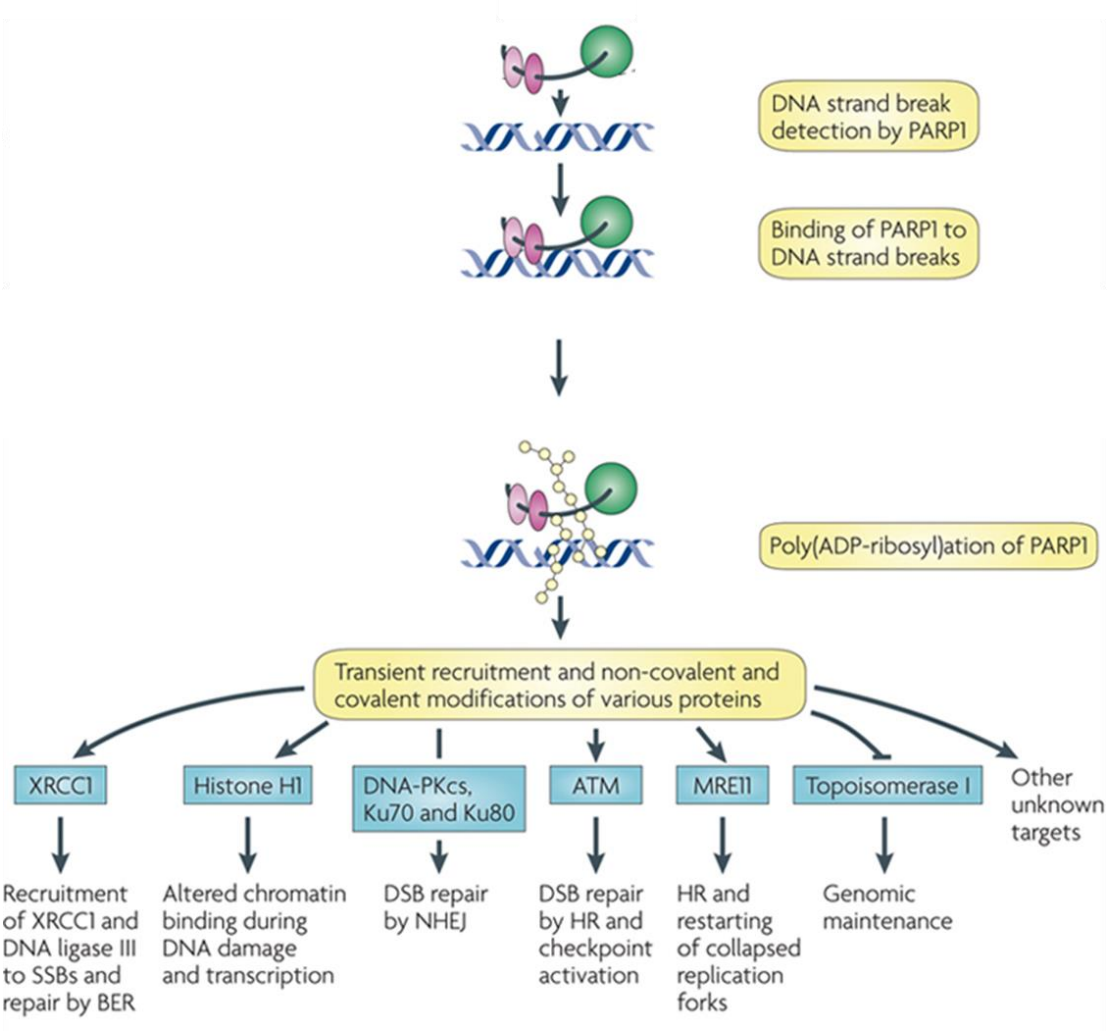


Figure 5.4. PARP activation. PARP directly recognised the DNA break and PARylates (i.e., synthetises poly(ADP) ribose (yellow beads) itself and other targets, notably DNA damage repair proteins, leading to their recruitment to the break site. Reproduced from (Rouleau, Patel, Hendzel, Kaufmann, & Poirier, 2010).

The rational for the use of PARP inhibitors to treat cancer is based on the idea that unrepaired DNA SSBs lead to stalling of replication forks and ultimately fork collapse, culminating in DNA DSBs. Therefore, the use of PARP inhibitors as monotherapy relies on the decreased capacity of cells to deal with the natural occurring DNA damage to which cells are naturally exposed. As tumour cells are highly replicative cells (in contrast to most normal tissue cells), the use of PARP inhibitors would preferably kill tumour cells. Also, in tumour cells mutated

for HR proteins, such as BRCA1/2, the use of PARPi would be even more potent as the DNA DSBs generated after fork collapse can rely only in NHEJ to be repaired. Preclinically, different PARP inhibitors have proven to be efficacious, either in combination with DNA damaging agents or as monotherapy in BRCA1/2 mutant cells and tumours (Calabrese et al., 2004). Clinical data is less conclusive, with one study showing that ovarian but not breast cancer patients benefited from PARPi treatment regardless of their BRCA status (Gelmon et al., 2011). Nevertheless, based on a second phase II trial, The European Medicines Agency approved the use of the PARP inhibitor olaparib as monotherapy for the treatment of ovarian cancer presenting with BRCA mutation (Mullard, 2014). More recently, the United States American Food and Drug Administration (FDA) approved the use of olaparib for treatment of patients with BRCA-mutated advanced ovarian cancer or for maintenance of ovarian cancer patients responsive to platinum-based therapies.

In addition to its use as a monotherapy in patients with defective HR, researchers have proposed the use of PARPi in combination with radiotherapy. The rationale is that radiotherapy would increase the levels of naturally occurring DNA SSBs and base damage, and tumours cells would then have to deal with increased damage in the presence of a PARP inhibitor. Preclinical data has shown efficient radiosensitisation by several PARP inhibitors (Chatterjee et al., 2013; Nowsheen, Bonner, & Yang, 2011; Powell et al., 2010; Senra et al., 2011). Clinical trials are ongoing but efficacy and toxicity data are yet to be reported (M. P. Mehta et al., 2015; Reiss et al., 2014).

As discussed above, the use of DDR modulators has been proposed as a promising way to treat cancer cells and spare normal tissue. More recently, these modulators have been studied in combination with radiotherapy not only preclinically but also in clinical trials, but to our

knowledge preclinical data on the impact of these combination therapies on thoracic normal tissues is lacking. Considering the hypothesised role of DNA damage in the establishment of chronic lung inflammation and fibrosis (Figure 3.10), in this chapter we evaluated the impact of using ATMi, ATRi and PARPi in combination with whole-thorax irradiation on the thoracic normal tissues and the anti-tumour effect of those combination treatments.

5.2. DNA damage response inhibitors show differential normal tissue effects in combination with radiation

As shown in the previous chapter, MPO absence decreased the level of DNA damage induced by radiation in the lung of C57BL/6J and led to decreased late adverse effects. Therefore, we hypothesised that accumulation of DNA damage by inhibition of repair proteins would lead to increased onset of radiation-induced late effects. To test this hypothesis, we used the lowest dose of radiation tested on chapter 3 (20 Gy given in 5 Gy fractions) in combination with two doses of the DNA damage response inhibitors (DDRi) as described in Figure 5.5.

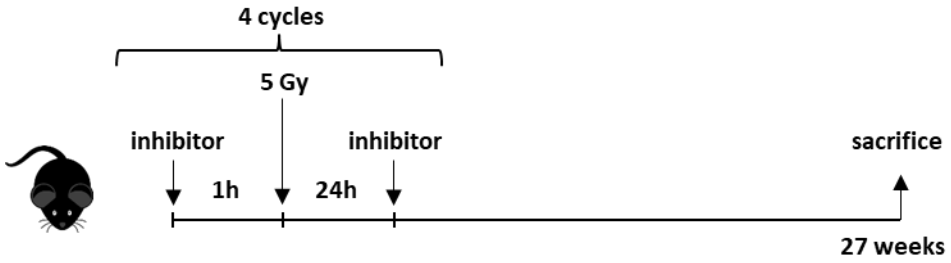


Figure 5.5. Experimental design for evaluation of the impact of ATM, ATR and PARP inhibitors on the late effects of whole-thorax radiation. C57BL/6J mice were given inhibitor 1 h before 5 Gy dose of whole-thorax radiation. Twenty-four hours after radiation, mice were given a second dose of inhibitor. This treatment was repeated 4 times, with 2 days break between radiation doses. Sacrifice was planned for 27 weeks after the first dose of radiation (n=10 per group). Left lungs and oesophagi were fixed in formalin for further histological analysis and right lungs were fresh frozen.

Three compounds were used in this project: BMN673 (PARP inhibitor), AZ31 (ATM inhibitor) and AZD6738 (ATR inhibitor). Their targets, vehicles, doses, normal tissue effects and experiment duration when used in combination with thoracic radiation are described in the methods section 2.4.3 and summarised in Table 5.1. The dose of BMN673 used was previously established in the literature and the doses of AZ31 and AZD6738 were previously assessed in a pharmacodynamics experiment using pKAP1 as a marker of ATM activity and pan-nuclear γH2AX as a marker of ATR activity (Shen et al., 2013).

Table 5.1. Overview of inhibitors tested and the normal tissue effects of combination with whole-thorax radiation in C57BL/6J mice. The number of mice (n) showing significant findings in the combination treatment of the listed compound with radiation is reported.

Compound	Target inhibited	Vehicle[1]	Dose (mg/kg)	Significant findings	n	Sacrifice (weeks)
BMN673	PARP	DMA/solutol HS	0.33	Weight loss	4/10	2
				Oesophagitis	4/10	2
				Dermatitis	6/10	3
AZ31	ATM	Captisol	50	Collagen accumulation	10/10	27
AZD6738	ATR	Poly(ethylene glycol)	50	None	0/10	27

[1] see details in methods section 2.4.3.

All animals receiving ATMi or ATRi in combination with radiation were followed for 27 weeks post-irradiation and did not show any significant clinical signs such as more than 10 % body weight loss (Figure 5.6. A). Four out of 10 animals treated with the combination of PARPi and

radiation (IR + PARPi) showed more than 10 % weight loss at 2 weeks post-irradiation (Figure 5.6. B).

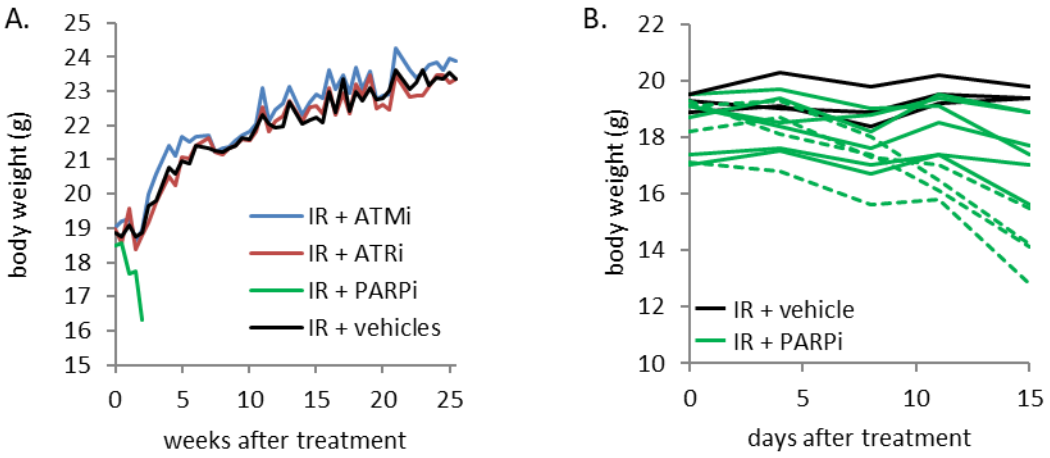


Figure 5.6. PARP inhibition in combination with whole-thorax radiation induced weight loss in C57BL/6J mice. In contrast to animals treated with ATM or ATR inhibitors (ATMi or ATRi) and radiation, mice treated with PARP inhibitor and radiation (IR + PARPi) showed weight loss at 2 weeks after treatment started. Average group weights are shown in graph A. Individual mouse weights are shown in graph B. From 10 animals in IR + PARPi treatment group, 4 showed more than 10 % body weight (dashed lines). 'IR + vehicles' group: n=9 mice.

Animals showing more than 10 % weight loss in the IR + PARPi group were sacrificed at 2 weeks post-treatment. Post-mortem examination and histological analysis indicated that oesophagitis was the most probable cause for weight loss. The oesophagi of mice treated with irradiation in combination with vehicle showed generally normal histology, with a mucosa consisting of keratinised stratified squamous epithelium, lamina propria and a thin muscularis mucosae; followed by a submucosa layer consisting of loose collagenous connective tissue; and an outermost muscularis externa formed by two perpendicular layers of skeletal muscle. In contrast, the oesophagi of mice in the IR + PARPi group showed several abnormalities. Areas with the most severe alterations showed complete denudation of epithelium and marked thickening of the submucosa and lamina propria caused by fibroblastic proliferation, oedema

and infiltration of a mixed population of inflammatory cells. Adjacent to these areas, we observed marked hyperplasia of mucosal epithelium with prominent rete pegs (epithelial extensions projecting into the underlying connective tissue), intercellular oedema and mild parakeratotic hyperkeratosis (Figure 5.7. A).

The remaining 6 mice in this group were followed for another week, when they presented with hair loss, unrecovered skin desquamation and swollen wounds in the field of radiation, and so were then sacrificed (Figure 5.7. B). In these animals, weight loss did not reach 10 % and oesophageal histology appeared normal.

H&E staining of the lungs of all the IR + PARPi treated animals did not show any evident histological changes compared to IR + vehicle sacrificed at the same time point. Nevertheless, those samples were not thoroughly analysed as those animals were sacrificed at an early time point for the development of lung toxicity.

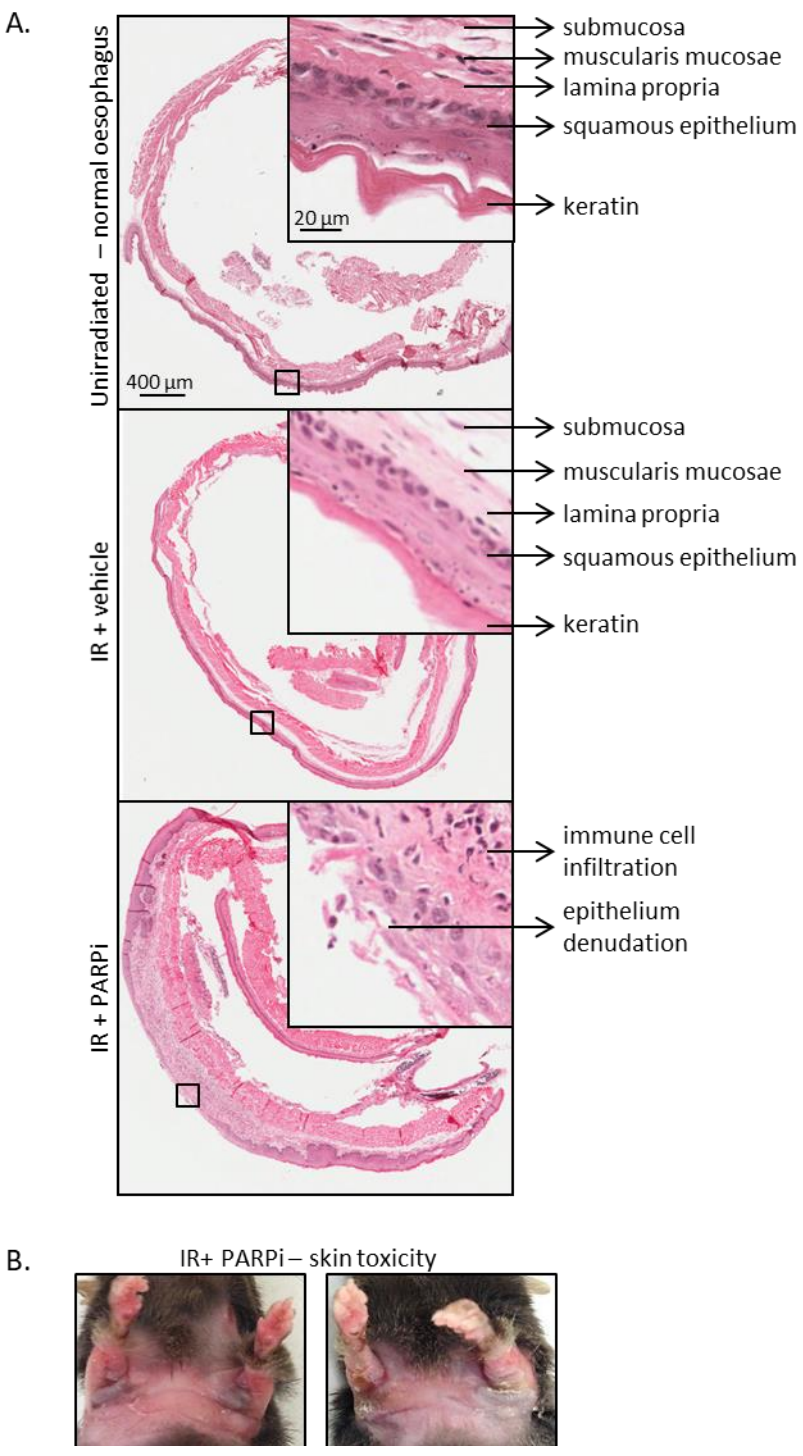


Figure 5.7. PARP inhibition in combination with whole-thorax irradiation induced oesophagitis and dermatitis in C57BL/6J mice. The four mice in the combination treatment of PARP inhibitor and radiation (IR + PARPi) which showed weight loss also presented with oesophagitis as assessed by H&E (A, scale bar represents 400 µm and inset images are a further 20x magnification). The other six mice in the group did not show more than 10 % weight loss but were sacrificed at 3 weeks after treatment due to unresolved skin desquamation (B).

At 27 weeks post-irradiation, animals treated with radiation plus ATMi or ATRi were sacrificed. Lung histology revealed discrete accumulation of collagen around large blood vessels in animals treated with IR + ATMi but no increase in overall fibrosis score was observed in either treatment group when compared to IR + vehicle (Figure 5.8 A and B). However, mice in the IR + ATMi group showed significant increase in hydroxyproline levels (Figure 5.8 C) and in collagen III levels when compared to mice in the IR + vehicle group (Figure 5.8 D and E).

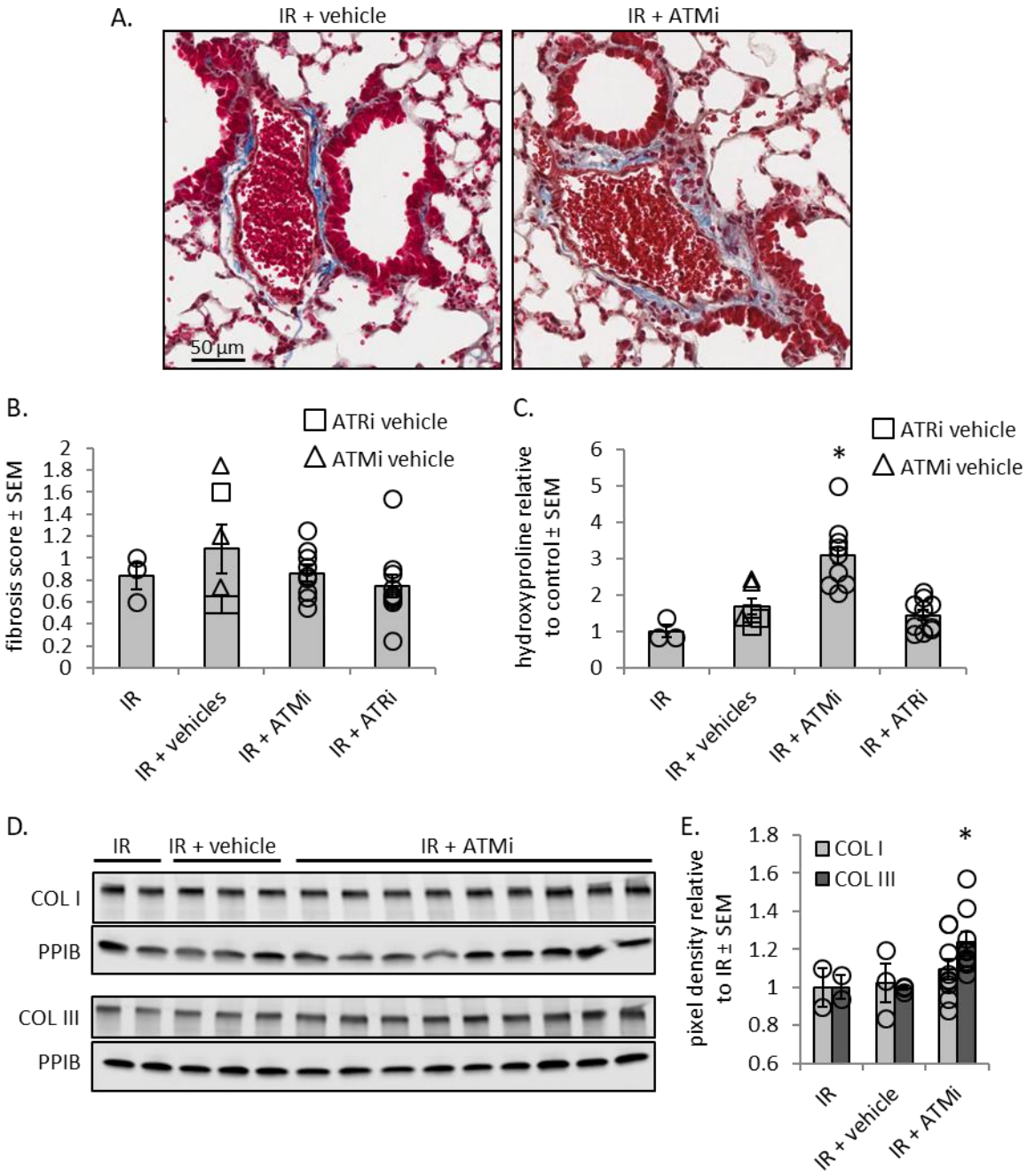


Figure 5.8. ATM inhibition in combination with whole-thorax irradiation induced increased levels of hydroxyproline and accumulation of collagen III in C57BL/6J mice. Analysis of lung samples stained by Masson's trichrome protocol revealed accumulation of collagen around large blood vessels (A) but no increase in the overall fibrosis score (B) in combination treatment of ATM inhibitor and radiation (IR + ATMi). This treatment led to increased levels of hydroxyproline (C) and collagen (COL) I and III, as measured by western blot of lung protein extracts (D). For western blot analysis 1 µL of individual animal protein extracts were loaded into each well and PPIB was used as loading control and bands were quantified (D). IR group: n=3; IR + vehicles: n=6; IR + ATMi: n=3; IR + ATRi: n=3. Graph bars represent the average in the group, error bars represent the SEM; open circles represent individual animals; *$p<0.05$ compared to IR + vehicles group (t-test, one-tailed distribution, two-sample equal variance).

In conclusion, our data showed that inhibition of different DNA damage response proteins have different effects on normal tissues in the field of radiation. PARP inhibition affected the oesophagus and the skin, which are highly proliferative tissues. In contrast, ATM inhibition affected the lung, which consists of low proliferative tissue (Rawlins & Hogan, 2006). As the rate of proliferation may have been an important factor in the outcome of the treatments tested in normal tissues, we then evaluated those treatments in a mouse model of human lung tumour.

5.3. The differential impact of targeting radiation-induced DNA damage in tumours compared to normal tissue: the need for a new model

To evaluate tumour tissue responses to combination treatments with radiotherapy, we injected Calu6 cells subcutaneously in the back of CD1 nude mice and performed local tumour irradiation once the tumours had reached 100 mm^3. The same radiation schedule and compound doses used to evaluate normal tissue responses were tested (Table 5.1). DDRi were given orally 1 h before and 24 h after each dose of radiation. Mice were sacrificed at 42 days after treatment or once tumours reached 400 mm^3 (Figure 5.9).

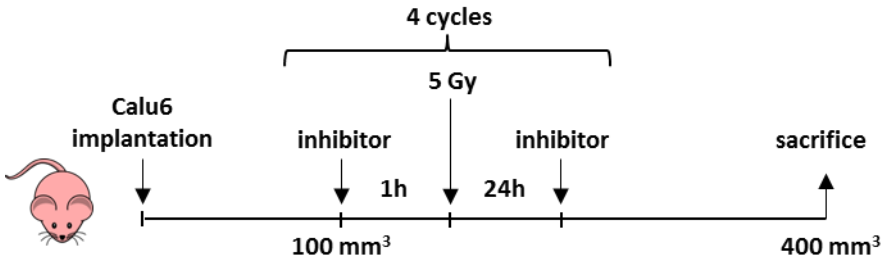


Figure 5.9. Experimental design for evaluating the impact of ATM, ATR or PARP inhibition on the radiation response of Calu6 xenograft tumours. Calu6 cells (5 x 10^6) were subcutaneously injected in the back of CD1 nude mice. Once tumours reached 100 mm^3, mice were given inhibitor (n=6 per group). One hour after treatment, tumours were locally irradiated (5 Gy). Twenty-four hours after radiation, mice were given a second dose of inhibitor. This treatment was repeated 4 times, with 2 days break between radiation doses. Animals were sacrificed at 42 days after treatment start or once tumours reached 400 mm^3. Tumours were measured 3 times per week.

Tumour measurements showed that all 3 inhibitors were radiosensitisers. The most pronounced decrease in tumour size was observed between 20-25 days post-treatment for all inhibitors. ATM inhibition was the most effective radiosensitiser, controlling tumour size until the end of experiment. PARP and ATR inhibitors showed similar responses, leading to a delay in tumour growth compared to IR + vehicles group (Figure 5.10).

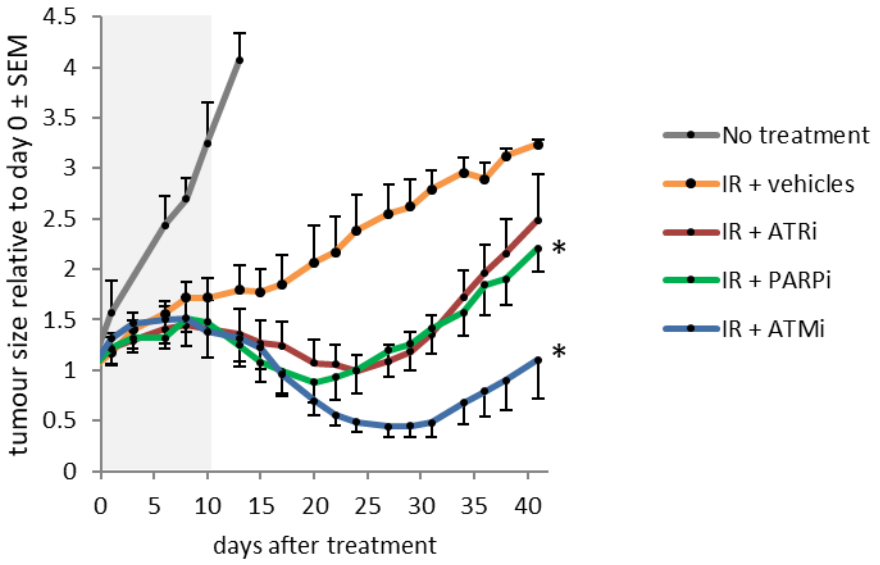


Figure 5.10. ATM, ATR or PARP inhibition radiosensitised Calu6 xenograft tumours. Graph lines represent the average of tumour volume measurements relative to size at the start of experiment. Grey shading represents treatment duration. No treatment: n=2; IR + vehicles, IR + ATMi, IR + ATRi: n= 5 per group; IR + PARPi: n=4. Error bars represent the SEM; *p<0.00005 last day measurement compared to IR + vehicle group (t-test, one-tailed distribution, two-sample equal variance).

5.4. Discussion

Our data showed that tumour tissues and thoracic normal tissues have different sensitivities to DDR modulators when used in combination with radiation. PARPi and ATMi induced normal tissue effects when used in combination with radiotherapy whilst ATRi showed no apparent effect. In contrast, human tumour xenografts responded similarly to ATRi and PARPi, and the biggest radiosensitisation was observed when using ATMi.

Within the first three weeks post-irradiation, PARP inhibition induced oesophagitis and dermatitis in C57BL/6J mice treated with whole-thorax irradiation. Both side effects are common following thoracic radiation in the clinic and no systemic therapies have been proved to be effective in their prevention (Baker & Fairchild, 2016). C57BL/6J mice have been reported

to be resistant to radiation-induced oesophagitis, even to fractionated schedules as high as 5 x 15 Gy of thoracic irradiation (Kim et al., 2016). Therefore, our findings may have direct clinical relevance and suggest that the addition of PARPi (BMN673) to 4 x 5 Gy dose may be equivalent to a substantial increase in the effect of radiation alone.

Acute dermatitis has also been reported for patients receiving thoracic radiotherapy (Bronsart et al., 2017). Interestingly, the DDR capacity of patients has been suggested to play a role in the development of radiation-induced skin toxicity (Pinar et al., 2007). Radiation-induced dermatitis in mice has been less reported in general, though one paper reported that C56BL6 mice developed skin toxicity at 3-7 weeks after receiving a single dose of 17.5 Gy or 5 fractions of 6 Gy given to the whole-thorax (Citrin et al., 2013). Again, our findings suggest that the clinical use of PARP inhibitors in combination with radiotherapy should progress cautiously. Importantly, the inhibitor used in this work (BMN673) has been reported to trap PARP molecules to the site of DNA damage, therefore impeding the resolution of damage through other repair pathway (Murai et al., 2014). This means that the toxicity observed here might not be observed with other PARP inhibitor that do not have the same inhibition mechanism. Due to early sacrifice of animals treated with IR + PARPi, the impact of this drug combination to the lung tissue was not assessed as the toxicity in this organ usually develops months post-irradiation. Using a radiation delivery technique that spares the oesophagus and topic creams to decrease skin toxicity might be an experimental approach to enable longer survival and evaluation of late responses.

The use of PARP inhibitors as a radiosensitiser has being proposed due to its role in DNA SSB repair [the most common DNA lesion caused by radiation (Cadet, Douki, & Ravanat, 2008)], which if left unrepaired in replicating cells can cause fork stalling and potentially develop into

DNA DSBs. Similarly to others reports, our data confirmed the radiosensitising effect of this combination on tumour xenografts (Dungey, Löser, & Chalmers, 2008; Noel et al., 2006). Therefore, we hypothesised that the high proliferative rate of normal cells in the oesophagus and the skin may explain the observed oesophagitis and dermatitis. Supporting this hypothesis, we observed denudation of the oesophageal epithelium, which is the most replicative component of this organ. Of note, a final report on a phase I clinical trial on fallopian and ovarian tumours showed encouraging preliminary efficacy results of treatment with PARPi veliparib and low-dose fractionated whole abdominal radiation therapy but authors did not recommend this combination for a phase II study due to decreased quality of life (Reiss et al., 2017). We conclude that combining PARP inhibitors and radiotherapy is promising, but careful planning should be conducted, especially to spare highly replicative normal tissue.

More challenging to understand was the responses observed in the IR + ATRi treatment. This combination showed similar or greater level of tumour radiosensitisation as PARPi but did not lead to oesophagitis or dermatitis. ATR is mostly involved in DNA repair after replication fork stalling, but also in the repair of single strand DNA structures at resected ends of DSBs and strand cross links (Cimprich & Cortez, 2008; Karnitz & Zou, 2015; Maréchal & Zou, 2013; Weber & Ryan, 2015). Therefore, ATR is especially important to replicating cells, as it is responsible for repairing stalled replication forks controlling the S/G2 check point. ATR inhibition has been shown to radiosensitise lung cancer xenografts in vivo, by abrogating the S/G2 check point and decreasing homologous recombination (Dillon et al., 2017). Therefore, like PARP inhibitors, ATR inhibitors should be particularly effective targeting replicating cells.

Additionally to their role in DNA SSB repair, PARP and ATR have been reported to be involved in the repair of DNA DSBs: PARP through a non-classical end-joining pathway and ATR

through homologous recombination (Jazayeri et al., 2006; Wang et al., 2006). Our data suggest that the combination IR + PARPi is more toxic than IR + ATRi, possibly due to PARP involvement in the detection and repair of SSBs in all phases of the cell cycle, while ATR would primarily affect the cells that were replicating during treatment. Also, ATR has been shown to be especially radiosensitising in hypoxic conditions, and Calu6 xenografts show hypoxic cores (Delgado-SanMartin, Hare, Davies, & Yates, 2017; Pires et al., 2012). Our findings agree with another study recently published, showing that ATR inhibition (AZD6738) in combination with radiation does not lead to increase in pulmonary fibrosis, although this study used a different radiation schedule and a different dose of ATR inhibitor than in our studies (Dunne et al., 2017). Thus, these finding suggests that combining ATRi with radiotherapy may be an attractive approach for the treatment of tumours located close to highly replicative tissues.

Even though ATR and PARP inhibitors showed promising tumour radiosensitising effects, the most effective combination tested was IR + ATMi. Considering its key role in DNA DSB repair and the plethora of other pathways this kinase is involved in, including SSB repair and cell cycle control, this finding was perhaps not surprising. In addition, these experiments were performed with Calu6 cells, which lack p53, and it has been previously shown that ATM inhibition selectively radiosensitised tumours with mutant p53 (Biddlestone-Thorpe et al., 2013).

Not only was ATMi a potent tumour radiosensitiser, it also led to collagen accumulation in the lung of C57BL/6J mice treated with thoracic radiation. Based on the known roles of ATM in DDR, we did not anticipate that combining ATMi with radiation would lead to toxicity in a low proliferative normal tissue such as the lung. In the literature, a few examples of the effect of this combination (or ATM deletion) in normal cells could be found. Of note, ATM deletion has been shown to have a different impact in general when compared to ATM inhibition (Barlow et al.,

1996; Daniel et al., 2012). ATM deletion radiosensitises proliferating tumour-associated endothelial cells but not quiescent heart endothelial cells (Moding et al., 2014). Also, ATM inhibitor given in combination with radiation has been reported to induce gastrointestinal syndrome in C57BL/6J mice and lead to reduced survival time (8 days post 9.25 Gy of total body radiation) (Vendetti et al., 2017). The authors suggested that this effect could be due to direct impediment of DNA DSB repair and impairment of cell cycle arrest in highly proliferative gastrointestinal cells, leading to cell death. Therefore, both studies showed that this combination is toxic to highly proliferative normal tissue/cells, which is expected considering the role of ATM in DNA DSBs repair. On the contrary, it is perhaps surprising that we did not see evidence of oesophageal toxicity in our experiments. One possible explanation for this inconsistency is that different highly proliferative tissues may have different dependencies on ATM activity.

ATMi in combination with radiation lead to accumulation of collagen (hydroxyproline assay and western blot) in the lungs of C57BL/6J, but did not lead to an increase in fibrosis scoring. In contrast, in the MPO experiments, absence of MPO led to decrease in fibrosis score, but not in hydroxyproline levels. Also, by histology, we could not detect an increase in the number of focal fibrotic lesions comparing IR + ATM and radiation alone. We believe that the accumulation of collagen may have occurred in a diffuse manner across the lung tissue or in areas already rich in collagen such as the periphery of blood vessels and therefore accounting for this accumulation by scoring was not possible.

Considering the above, we suggest that the impact of ATM inhibition in combination with radiation cannot be explained solely by the proliferative capacity of tissues as the combination treatment affected both highly proliferative tumour tissue and slowly proliferative normal lung tissue. Interestingly, ATM is also known to be activated by DNA damage independent events

(Paull, 2015). For instance, it has been shown that ATM is directly activated by oxidative stress in the absence of DNA damage (Guo, Kozlov, Lavin, Person, & Paull, 2010). We hypothesise that this function of ATM may be especially important in the lung tissue, which is exposed to high levels of ROS due to respiration. Upon radiation, the high baseline level of oxidative stress within lung cells would be further increased due to its oxidation effect. Therefore, we speculate that inhibition of ATM led to abrogation of an important anti-oxidative response in the lung; and, upon radiation treatment, the extent of oxidative stress was increased, leading to increased lung damage and subsequent collagen accumulation in the lung of mice treated with IR + ATMi.

The numerous roles of ATM make it challenging to identify the specific mechanism that explains our findings. For instance, in a model of skin fibrosis, ATM signalling triggered by oxidative DNA damage was shown to directly induce fibroblast to produce collagen through the Wnt/beta-catenin pathway (Svegliati et al., 2014). Also, ATM seems to be especially important for endothelial cell homeostasis. In a diabetic mouse model of endothelial damage, ATM activity was shown to be responsible for the oxidative stress-induced senescence in endothelial cells (Zhan, Suzuki, Aizawa, Miyagawa, & Nagai, 2010). In addition, ATM is especially required to repair DNA DSBs in heterochromatin; with cells lacking ATM accumulating lesions following radiation (Goodarzi et al., 2008). ATM has also been implicated in the repair of persistent DNA DSBs induced by transcription (Clouaire, Marnef, & Legube, 2017). This role could be important in the repair of the persistent DNA DSBs that we observed in the lung tissue post-irradiation and described in chapter 2. In Figure 5.11, we summarise our hypothesis for role of ATM inhibition in the context of thoracic irradiation.

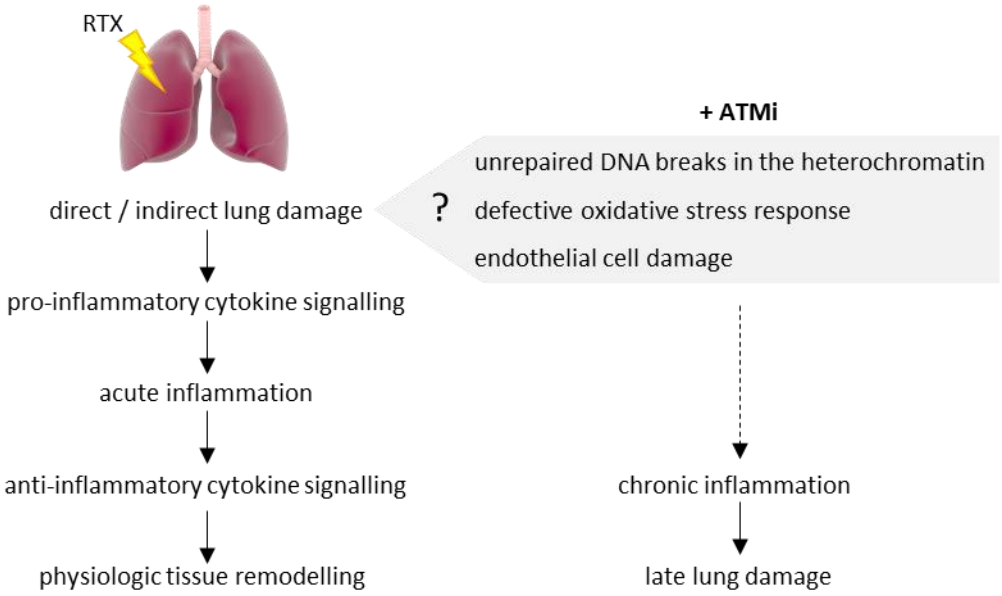


Figure 5.11. The impact of ATM inhibition on the normal lung tissue response to radiation. We hypothesise that the tissue damage induced by radiation is intensified by ATM inhibition, potentially by DNA breaks in the heterochromatin remaining unrepaired, impairment of the oxidative response and damaging of endothelial cells.

Altogether the findings from this chapter show that the effects of combining DDRi with radiation – especially when it comes to normal tissue - are difficult to predict, as they may be related to several components such as cell division, cell cycle control and non-DNA repair related functions of DDR proteins. Therefore, there is a need to evaluate not only tumour responses but also normal tissue responses of IR + DDRi combination treatments preclinically to better understand the potential impact of these combinations in patients.

In this chapter, we used two separate models: C57BL/6J mice for normal tissue responses and CD1 nude mice for tumour responses. Nevertheless, we observed several drawbacks from using two separate models. First, normal tissue responses happened over a period of weeks (oesophagitis and dermatitis) to months (lung fibrosis) in the C57BL/6J model, while tumour responses happened in few weeks in the CD1 nude model. Also, in the xenograft model, tumours were not in the thorax, which left normal tissues of interest outside the field of irradiation. And

finally, nude mice are immunocompromised which may play an important role in the response to treatment (for instance, no skin toxicity was observed in the IR + PARPi xenograft experiment in contrast to the C57BL/6J model). Therefore, using a mouse strain with lung tumours that could develop thoracic side effects of radiation would be an important step forward.

One potential solution to this issue, would be to induce lung tumours in C57BL/6J mice. In the literature, the Cre recombinase model induced by intratracheal delivery of viral particle has been used but the tumour burden is generally very high and therefore difficult to follow (DuPage, Dooley, & Jacks, 2009). Another alternative would be the use of genetically engineered C57BL/6J mice but their low mutational burden might not be a good representation of human tumours (McFadden, Politi, & Bhutkar, 2016). Lung tumour models through intravenous or orthotopic injection of syngeneic lung tumour cells were also tested, but mice had to be sacrificed within days post-irradiation due to fast tumour growth, which therefore did not allow for evaluation of late fibrotic responses (Machtay et al., 2006; Yamaura, Doki, Murakami, & Saiki, 1999). Considering the drawbacks of the models described above, in chapter 6 we propose a novel mouse model for evaluation of therapeutic margin in the treatment of lung cancer.

6. A mouse model for simultaneously evaluating the effect of new therapies in combination with radiation on lung damage and tumour response

6.1. Introduction

As discussed in the previous chapter, there is an unmet need in the field for a mouse model that allows for the evaluation of the therapeutic index of combination treatments with radiation. In this chapter, we tested whether the A/J mouse strain would be suitable to fill this gap. This strain is well known to be susceptible to the carcinogen induction of lung tumours but its response to whole-thorax radiation has not been well characterised.

A known carcinogen used to induce lung tumours in the A/J mouse strain is ethyl carbamate (EC), also known as urethane. This compound was also reported to induce tumours in a variety of tissues, including the skin, liver, mammary gland, and lymphoid tissue. Nevertheless, most studies using urethane focus on the induction of lung tumours, as they can be detected within weeks, as opposed to other sites where there is at least one-year latency period before tumour detection. One possible explanation for the lungs to be the primary organ of tumour induction resides on the differential metabolism of urethane, as evidenced by in vitro incubation of urethane and microsomes from several organs. A study showed a preferential metabolisation of urethane by lung microsomes compared to microsomes derived from other organs (Gupta & Dani, 1989). Also, other species such as rats, hamsters and monkeys have shown to be susceptible to the carcinogenic effect of urethane.

Upon administration, EC is oxidised in a two-step reaction by the membrane protein cytochrome P450 enzyme (CYP2E1), firstly to vinyl carbamate (VC) and secondly to vinyl carbamate epoxide (VCO), the final carcinogenic molecule (Figure 6.1). This carcinogen covalently binds to the DNA forming adducts that lead to misincorporation of nucleotides in the following S-phase, culminating with point mutations. The mutational effect of VC reaches a plateau between weeks 3 and 4 post-injection, as quantified by the induced mutant frequency in experiments with F_1 of A/J X BigBlue strains (Hernandez & Forkert, 2007). Interestingly, different mouse strains show different susceptibility to urethane tumour induction; C57BL/6J is a resistant strain and A/J is a susceptible strain. At least in part, the susceptibility of different mouse strains may be explained by the activity of CYP2E1, A/J mice having 40% more activity than C57BL/6J mice (Titis & Forkert, 2001).

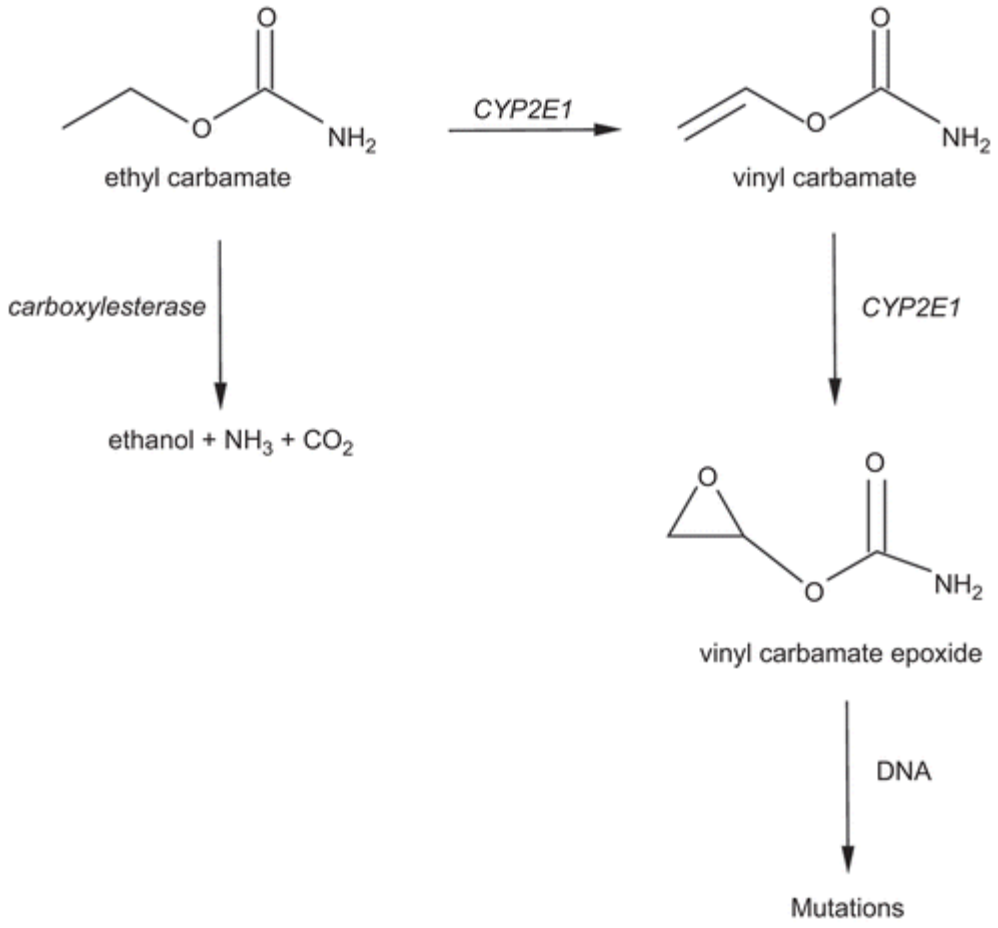


Figure 6.1. Urethane metabolisation. Urethane, or ethyl carbamate is oxidised in a two-step reaction by CYP2E1, firstly into vinyl carbamate and then vinyl carbamate epoxide. This product interacts with the DNA leading to mutations. Reproduced from (Hernandez & Forkert, 2007).

Previously, another study looking at differences between the susceptibility of different mouse strains to urethane-induced lung tumours identified three loci, which were called 'pulmonary adenoma susceptibility' (Pas1, 2 and 3), that accounted for the differences in lung tumour susceptibility between A/J and C57BL/6J (Malkinson, Nesbitt, & Skamene, 1985). Later on, Pas1 locus was shown to be located at the distal region of mouse chromosome 6 and to be composed of two genes, namely Las1 (lung adenoma susceptibility 1) and Kras2 (Kirsten rat sarcoma oncogene 2), the latter contributing for 60% of the variation between C57BL/6J and

A/J (Festing, Yang, & Malkinson, 1994; Gariboldi et al., 1993; Z. Zhang et al., 2003). Eventually, it was shown that sequence differences in the second intron of Kras in A/J mice was responsible for the high susceptibility in this strain (B. Chen, Johanson, Wiest, Anderson, & You, 1994). Other loci have been proposed to play a role in the susceptibility of different strains to lung tumour induction (Devereux et al., 1994).

Considering its role in susceptibility to tumour induction, Kras, not surprisingly, was reported to be mutated in urethane-induced tumours (Ryan, Barker, Nesbitt, & Ruddle, 1987). Kras is mutated in approximately 1/3 of lung adenocarcinomas and has been linked to be a mechanism of resistance arising in EGFR-mutated tumours in patients treated with gefitinib (Network, 2014; Pao et al., 2005). Recent data obtained from whole genome sequencing also showed that urethane-induced tumours have more single nucleotide variants (SNVs) compared to tumour arising from genetically modified Kras mice. The levels of SNVs is similar to that observed in humans when comparing lung tumours from smokers versus never-smokers (Govindan et al., 2012; Westcott et al., 2015). Also, a correlation was identified in which urethane-induced adenomas harbour a Kras Q61L mutation and urethane-induced adenocarcinomas harbour a Kras Q61R mutation. Interestingly, SNVs were also reported in other genes, such as Akt1, Atm, Rnf43, Notch1, Ret, and Rb1, occurring at positions homologous to mutations in human cancers (Westcott et al., 2015). Those findings indicate that urethane-induced tumours bear several similarities to smoking-induced human lung tumours and, therefore, is potentially a promising preclinical model for the study of antitumour therapies.

Historically, urethane-induced lung tumours are classified in two different histological types, namely papillary and solid (Thaete, Gunning, Stoner, & Malkinson, 1987). Nevertheless, a recent paper compared the histological type of tumours induced by two different carcinogens

and reported that N-methyl-N-nitrosourea induced a 2:1:1 proportion of solid, mixed and papillary and urethane induced 9:1 proportion of papillary and mixed in A/J mice at 32 weeks post-induction (Westcott et al., 2015). In our experiments, at 27 weeks post-induction, most tumours were of the mixed type. Of note is the interaction between tumour cells and the surrounding normal tissue, which might represent different stages of invasiveness capacity (Figure 6.2).

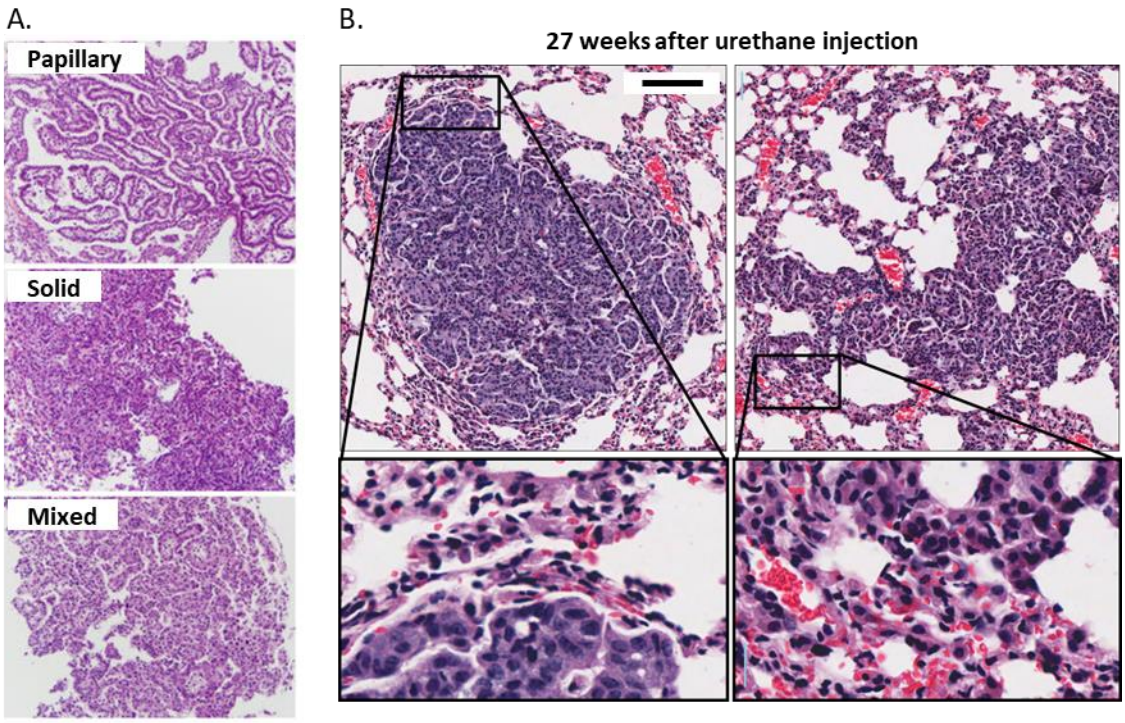


Figure 6.2. Urethane-induced lung tumours. Representative histological images of papillary, solid, and mixed tumours [A; reproduced from (Westcott et al., 2015) ; 200x magnification]. Examples of mixed type tumours at 27 weeks post-induction from the present work (B; bar represents 100 µm and insets are a further 4x magnification).

The two histological types are believed to arrive from different cell types, but this is still controversial. Some studies propose that papillary tumours arise from non-ciliated Clara cells and the solid tumours arise from alveolar type II cells based on morphological and histochemical features (S L Kauffman, Alexander, & Sass, 1979; Thaete & Malkinson, 1991). Work by

Kauffman showed that chronic exposure to urethane in drinking water led to increase cell cycle duration in alveolar type II (AEII) cells for the first week, followed by induction of cell death on the third week and hyperplasia peaking at 6 weeks, which contributed to the hypothesis that AEII cells were the precursor of urethane-induced tumours (Kauffman, 1972; Kauffman, 1976). More recent papers show that both tumour types arise from AEII cells and that the histological differences represent different stages of neoplastic transformation (Malanga et al., 2016; Mason, Kalina, Nielsen, Malkinson, & Shannon, 2000). The inconclusiveness of this matter lays on the fact that both Clara cells and AEII cells have proliferative capacity and on the difficulties in establishing definite markers; therefore, more data is needed to better define the cell of origin of urethane-induced tumours (Adamson & Bowden, 1974; Giangreco, Reynolds, & Stripp, 2002).

Urethane-induced tumours have been extensively used to study carcinogenesis and much less so to study tumour response to cancer therapies. This is probably because tumour establishment in this model requires a long period when compared to other models such as mouse xenografts, which take ~2 weeks to develop large (100 mm^3) tumours. In fact, to the best of our knowledge, no studies have been conducted looking at the radioresponse of urethane-induced tumours. In addition, scarce literature in general can be found on the radiation responses of normal lung tissue of A/J mice. A few reports have been published and their findings are reviewed below.

A study from 1989 showed that a dose of 13 Gy given to the thorax of A/J mice did not lead to lung fibrosis at 28 weeks post-irradiation, although 5-15% of acini were obstructed mostly by cellular infiltrate which was not enough to cause respiratory distress. In the same study, mice sacrificed beyond 36 weeks after radiation doses ranging from 12 to 16 Gy showed 16-19% of acini obstructed by fibrosis (Sharplin & Franko, 1989). A more recent paper reported that a

single dose of 15 Gy induced 50% lethality within 22.5 weeks post-irradiation and 'pneumonitis (alveolitis), with abundant infiltrates of mononuclear cells and alveolar macrophages, interstitial and intra-alveolar oedema and lymphocytic perivascular cuffing' (Jackson, Vujaskovic, & Down, 2011). These findings led to the classification of A/J mice as a pneumonitis-prone strain as opposed to C57BL/6J mice which are considered fibrosis-prone. Nevertheless, due to the scarce data available, we considered that the susceptibility of A/J mice to pulmonary fibrosis was not established.

Considering the above and the differential tissue responses between single and fractionated doses of radiation, we set up experiments to evaluate the responses of normal lung tissue and urethane-induced lung tumours to a fractionated schedule of whole-thorax irradiation in A/J mice. The aims of this chapter are: (i) to establish the susceptibility of A/J mice to radiation-induced lung fibrosis, (ii) to test whether normal and tumour lung tissue responses to radiation could be assessed simultaneously in this model and (iii) to evaluate the radiosensitivity of urethane-induced lung tumours.

6.2. Radiation induced weight loss and collagen accumulation in the lungs of A/J mice

To test whether the A/J strain would be susceptible to clinically relevant side effects induced by thoracic radiation, mice were irradiated with 5 doses of 5 Gy given to the whole-thorax followed by sacrifice at 19 weeks post-irradiation (Figure 6.3). This initial experiment was designed based on the early toxicity (at 18 weeks post-irradiation) observed in C57BL/6J using

this same radiation fractionation schedule (described in chapter 3). For this experiment, urethane injection for tumour induction was not performed as the aim was to evaluate normal tissue responses only.

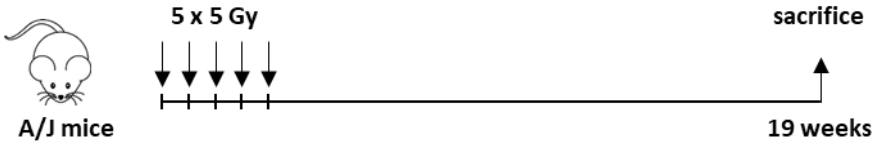


Figure 6.3. Experimental design for preliminary evaluation of late effects of whole-thorax radiation in A/J mice. Mice were given 5 doses of 5 Gy to the whole-thorax (2 days break between radiation doses) and sacrificed at 19 weeks after radiation (n=5 per group). Left lungs were fixed in formalin for further histological analysis and right lungs were fresh frozen.

This initial experiment showed that, as opposed to what was observed with C57BL/6J mice, A/J mice did not lose weight when treated with this radiation dose. Also, we did not observe a significant increase in total hydroxyproline levels, but levels of collagen I and III were significantly higher in irradiated mice when compared to controls (Figure 6.4).

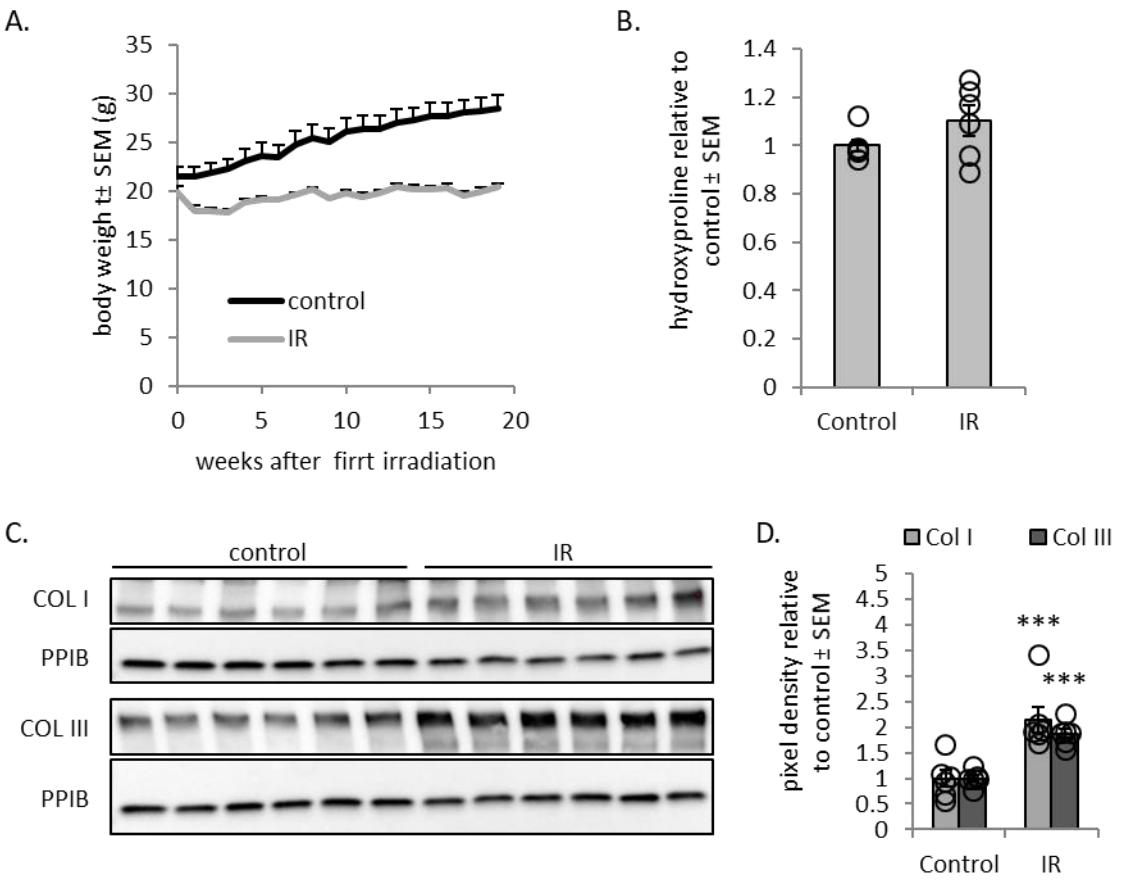


Figure 6.4. Whole-thorax irradiation led to increased collagen I and III in the lungs of A/J mice. Irradiated mice did not show body weight loss (A). Hydroxyproline level increase in the irradiated lungs was not significant (B). Western blot analysis of lung protein extracts revealed collagen (COL) I and III accumulation in irradiated lungs (C; 1 µL of individual animal protein extracts were loaded into each well and PPIB was used as loading control; D, blot quantification). Control: unirradiated mice (n=5), IR: irradiated mice (n=5); graph bars represent the average in the group, error bars represent the SEM and circles represent individual animals. ***$p<0.0005$ compared to control group (t-test, one-tailed distribution, two-sample equal variance).

As the initial study showed it was safe to proceed using this radiation schedule in A/J mice, a second experiment was performed with a time-course more appropriate for the development of fibrosis. We also evaluated if urethane injection (which is used for inducing lung tumours) in combination with radiotherapy would be tolerated in this strain. As urethane induces DNA damage, we wanted to evaluate if it would increase the toxicity of radiation. To test if the combination of urethane and radiation would be tolerated we injected mice with urethane and 3

days later proceeded with whole-thorax irradiation (5 doses of 5 Gy) followed by sacrifice at 24 weeks post-irradiation (Figure 6.5).

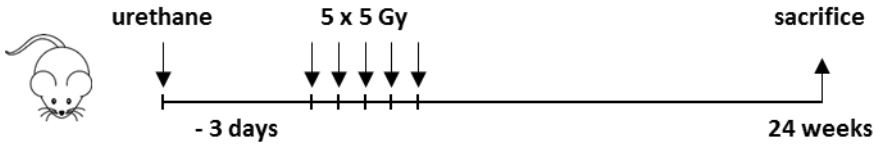


Figure 6.5. Experimental design for evaluation of late effects of whole-thorax irradiation in A/J mice. All mice were intraperitoneally injected with 10 % urethane. After 3 days, animals were given 5 doses of 5 Gy to the whole-thorax (2 days break between radiation doses) and sacrificed at 24 weeks after radiation (n=2 for unirradiated control group and n=10 for irradiated group). Left lungs were fixed in formalin for further histological analysis and right lungs were fresh frozen.

Interestingly, when following mice for a longer period, 5 x 5 Gy treatment eventually led to body weight loss in A/J mice (Figure 6.6). At 22 weeks post-irradiation, one animal (LL476) showed significant weight loss and was sacrificed. Two weeks later, another mouse (LL472) showed significant weight loss and the experiment was ended. In addition, at time of sacrifice, LL476, LL472 and other 2 mice showed evident pleural effusions.

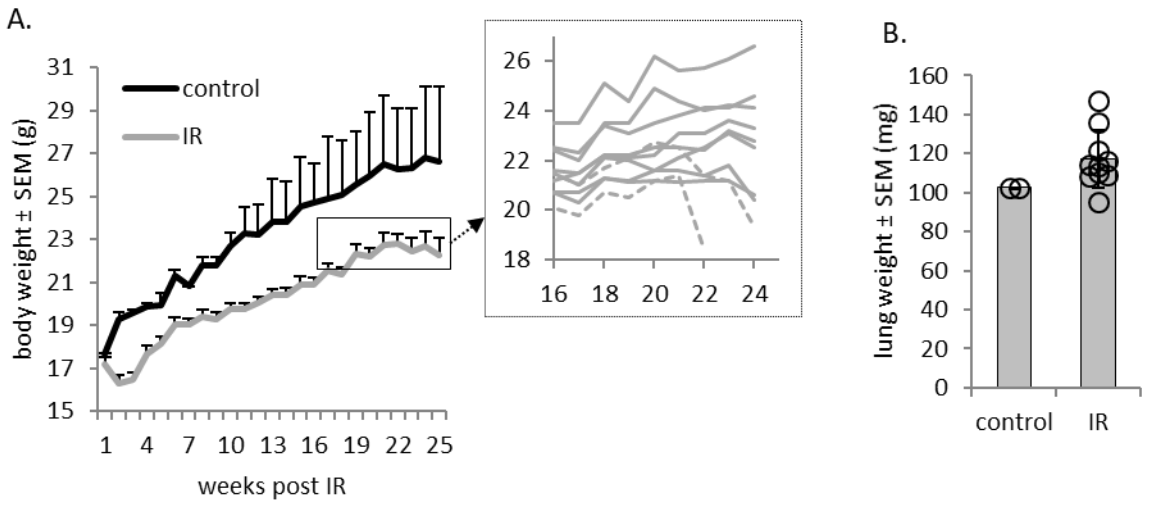


Figure 6.6. Whole-thorax irradiation induced body weight loss in A/J mice. Two out of 10 mice in the irradiated group (IR) showed weight loss. Graph lines represent the average body weight in control (n=2) and irradiated mice (n=10); error bars represent the SEM. Inset graph shows individual animal weights; red lines indicate animals with more than 10 % weight loss.

Lung samples from the 24-week study were scored for fibrosis and an increase in the average grade of fibrosis was observed when comparing irradiated mice with unirradiated controls (Figure 6.7 A). Interestingly, fibrosis scores of irradiated A/J mice were similar, indicating that the response in this strain showed less variability than the response in C57BL/6J mice (Figure 3.6 D). Hydroxyproline levels were increased after radiation (Figure 6.7 B). In contrast, collagen III levels were increased, and animal LL476 showed the highest levels of both collagen I and III (Figure 6.7 C and D).

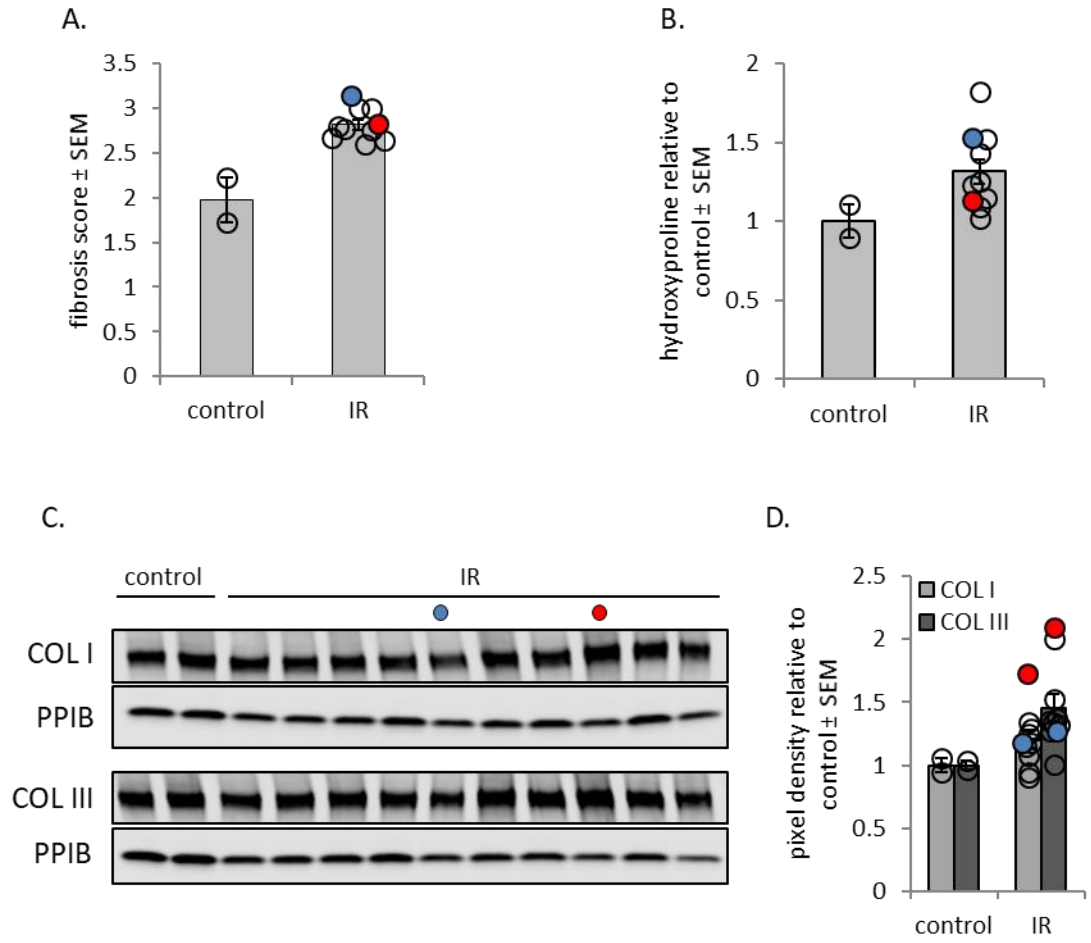


Figure 6.7. Whole-thorax radiation led to increased fibrosis score and collagen III accumulation in the lungs of A/J mice. Analysis of lung samples stained by Masson's trichrome protocol revealed increased fibrosis score of irradiated samples (A). Hydroxyproline level increase in the irradiated lungs was not significant (B). Western blot analysis of lung protein extracts revealed collagen (COL) I accumulation in irradiated lungs (C; individual animal extracts were loaded into each well and PPIB was used as loading control; D, blot quantification). Control: urethane injected and unirradiated (n=2), IR: urethane injected and irradiated (n=10); graph bars represent the average in the group, error bars represent the SEM and circles represent individual animals; red circle (LL476), blue circle (LL472).

Masson's trichrome staining was performed on lung slices from both experiments (19 and 24 weeks long). For the shorter experiment, it revealed marked accumulation of foamy macrophages, especially at the surface of irradiated lungs (Figure 6.8 panel 3). Furthermore, thickening of alveolar walls by collagen accumulation was observed (Figure 6.8 panel 4).

Foamy macrophages were also noticeable at 24 weeks post-irradiation; it was common to observe regions of sparsely distributed foamy macrophages associated with areas of disrupted alveolar walls usually enriched in collagen (Figure 6.8 panel 5). In addition, dense fibrotic lesions were present in irradiated A/J mice at 24 weeks post-irradiation but, in contrast to C57BL/6J, those lesions were not exclusively located at the lung surface (Figure 6.8 panel 6). Interestingly, the presence of foamy macrophages in the fibrotic lesions was varied, but it was noticed in some samples. All 10 lung samples analysed showed positivity for foamy macrophages, thickening of alveolar walls and collagen accumulation; nevertheless, not all samples showed fibrotic lesions. The presence of fibrotic lesions was not exclusive to the animals presenting with weight loss.

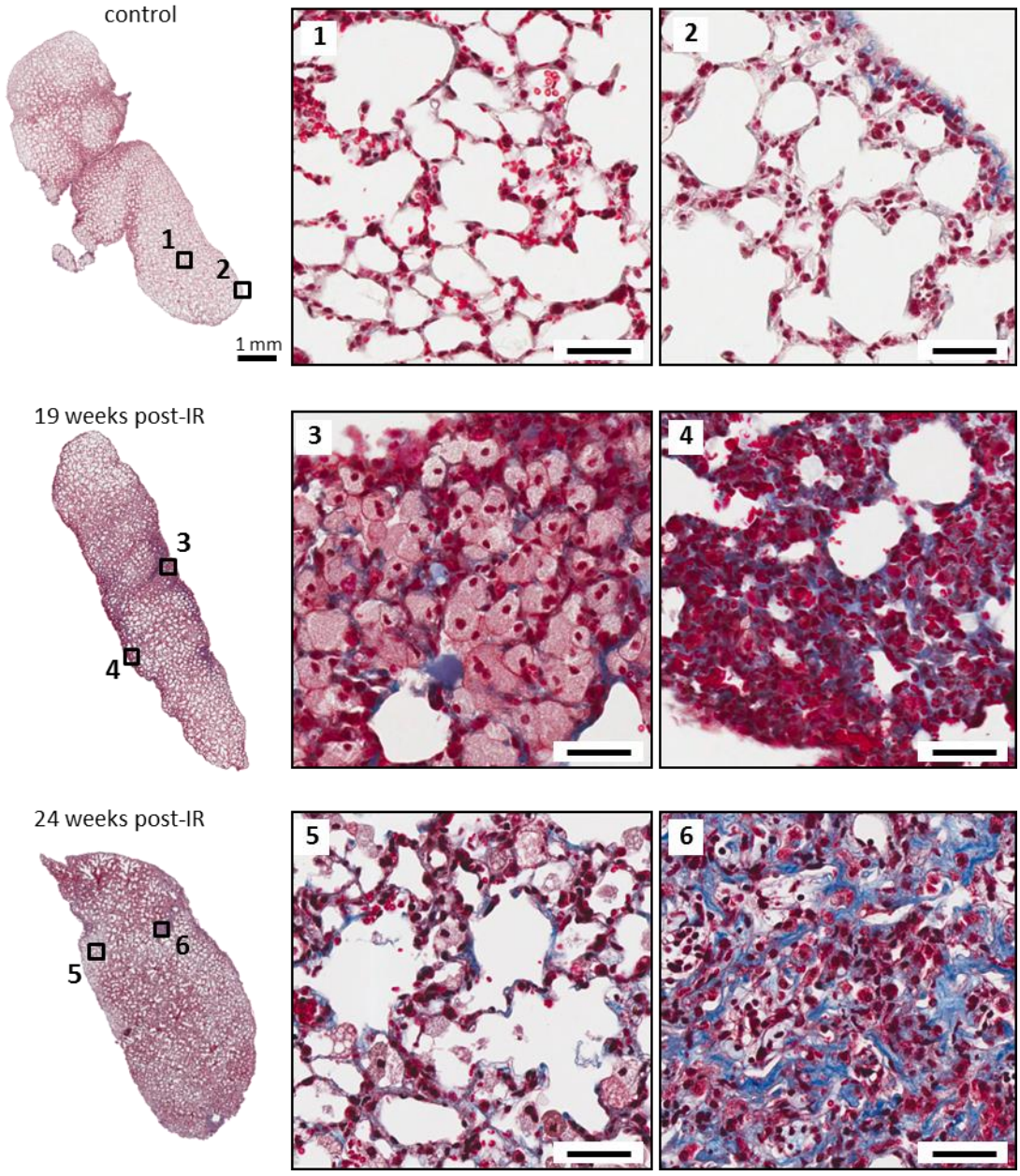


Figure 6.8. Whole-thorax radiation induced foamy macrophage infiltrate and fibrosis in the lung of A/J mice. At 19 weeks after radiation (IR), Masson's trichrome staining of the lungs revealed agglomeration of foamy macrophages and mild collagen accumulation. At 24 weeks, foamy macrophages were less evident and focal fibrotic lesions were detectable. Control group: n=7, '19 weeks' group: n=5; '24 weeks' group: n=10.

Another important finding from this second experiment was that giving radiation at 3 days after urethane injection led to marked decrease in the number of tumours. The two control animals

that received urethane but not radiation, developed lung tumours (4 tumours per lung slice and 1 tumour per lung slice), while out of the 10 animals that received urethane and radiation only 1 lung tumour was detected in one animal by histology. Therefore, we have established for future experiments that it is necessary to let urethane-induced lung tumours develop before giving radiation treatment.

6.3. Normal and tumour tissues show differential DNA repair kinetics

As our previous data suggested, early DNA damage induced by whole-thorax irradiation could be related to the development of pulmonary fibrosis. In addition, radiation is believed to be effective as a cancer treatment mostly due to the induction of DNA damage. Therefore, we assessed if the A/J strain was suitable for evaluating the early induction of DNA damage simultaneously in tumour and normal lung tissue. According to previous experiments in the lab, it was known that at 12 weeks post-urethane injection middle sized (400 μm diameter) lung tumours were present. Therefore, we induced lung tumours by injecting mice with urethane and 12 weeks after induction, mice received a single dose of 5 Gy to the whole thorax. Mice were sacrificed at 2 h, 24 h or 7 days post-irradiation (Figure 6.9).

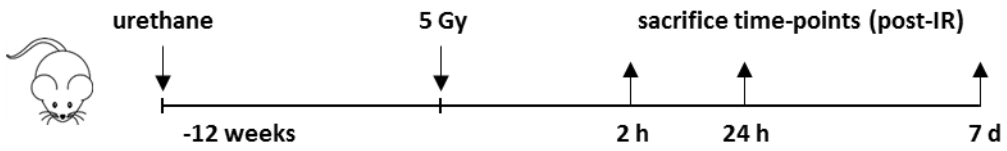


Figure 6.9. Experimental design for evaluation of early DNA damage induced by whole-thorax radiation in A/J mice. Animals were intraperitoneally injected with 10 % urethane. After 12 weeks, mice received a single dose of 5 Gy to the whole-thorax and were sacrificed at 2 h, 24 h or 7 days after radiation (n=3 per group). Left lungs were fixed in formalin for further histological analysis, right lungs were fresh frozen and blood was collected for plasma extraction.

We used γH2AX to evaluate the induction and repair of DNA damage on normal and tumour lung tissue after radiation. Interestingly, we observed a significantly higher induction of γH2AX in the tumour tissue compared to the normal tissue at 2 h post-IR ($p<0.00001$). This difference was not observed at 7 days post-irradiation ($p=0.06$) and as only one tumour was detected in the 24 h histology slice, no statistical analysis was performed for this time point. In both tissues, the number of γH2AX-positive cells was significantly higher at 7 days post-irradiation compared to unirradiated samples ($p<0.005$) (Figure 6.10).

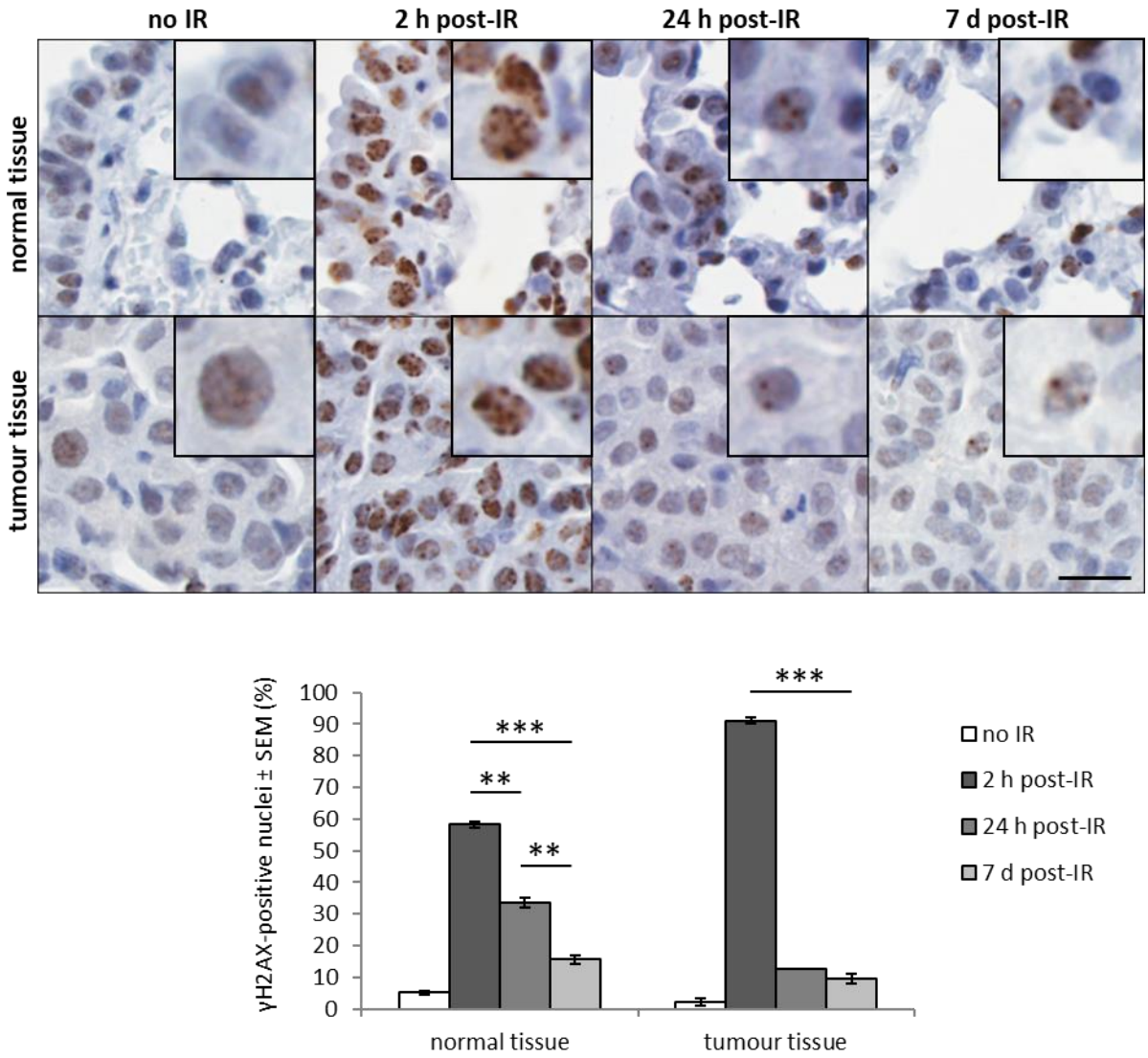


Figure 6.10. Normal and tumour lung tissues showed differential kinetics of γH2AX resolution after whole-thorax radiation. Lung samples were processed for immunohistochemistry and γH2AX-positive cells were quantified. Number of tumours quantified per time point: 5 (2 h), 1 (24 h) and 8 (7 d). For the normal tissue, lungs of 3 animals per group were analysed. Graph bars represent the average in the group and error bars represent the SEM; **p<0.005 and ***p<0.005 (t-test, one-tailed distribution, two-sample equal variance). Scale bar represents 10 µm; insets images are a further 2x magnification.

As positivity for γH2AX could also be indicative of apoptosis (as discussed in chapter 2), we also evaluated positivity for 53BP1 foci as a more specific marker of DSB induction and repair. In contrast to what was observed for γH2AX, the number of positive cells in the normal tissue remained the same from 2 h until 7 days post-IR. The number of cells positive for 53BP1 foci

was significantly higher in the tumour tissue compared to normal tissue at 2 h ($p=0.0004$) and lower at 7 days post-IR ($p=0.02$). In both tissues, the number of cells positive for 53BP1 foci was significantly higher at 7 days post-irradiation compared to unirradiated samples ($p<0.05$) (Figure 6.11).

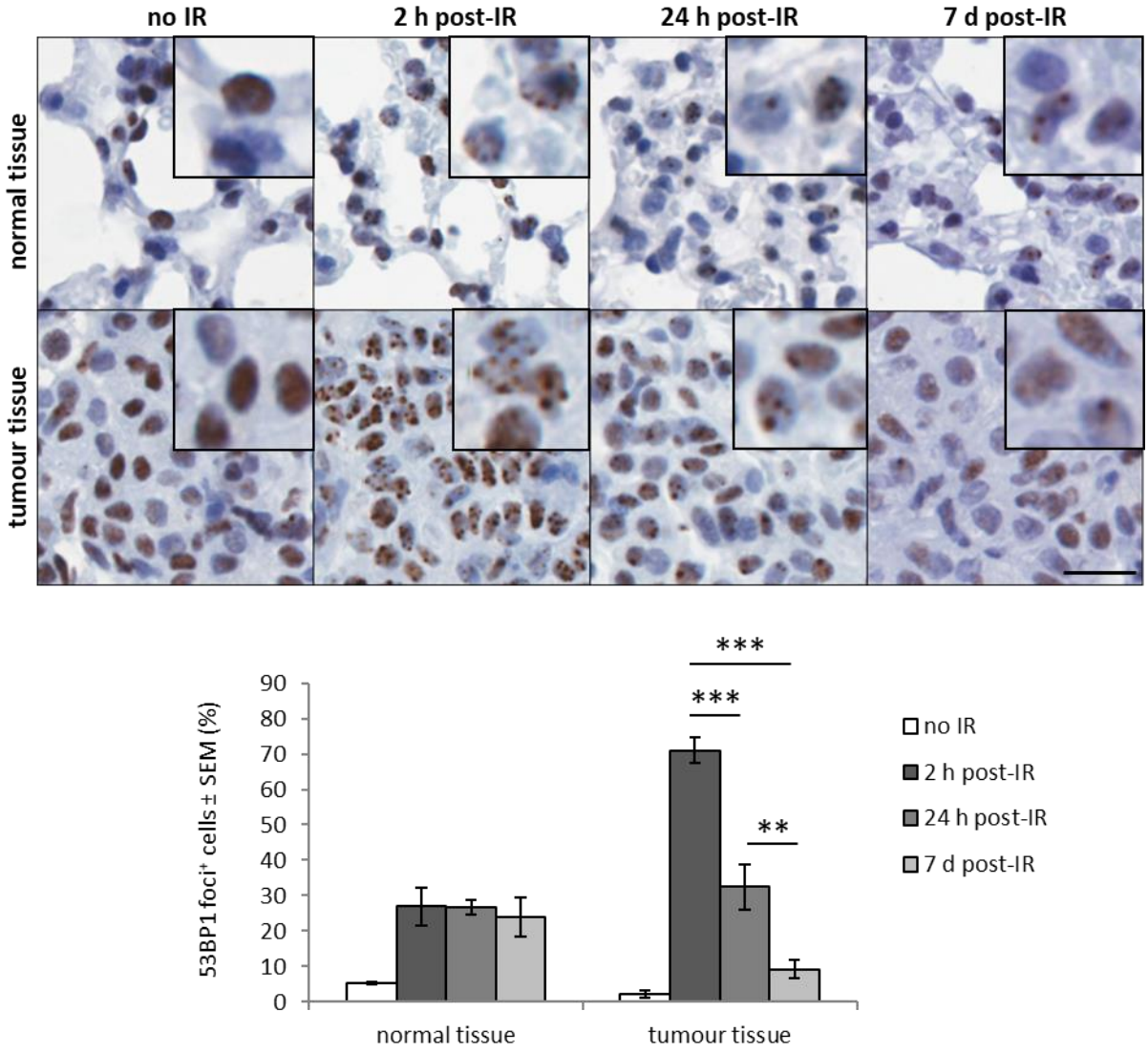


Figure 6.11. Normal and tumour lung tissues showed differential 53BP1 foci resolution after whole-thorax radiation. Lung samples were processed for immunohistochemistry and 53BP1 foci-positive cells were quantified. Number of tumours quantified per time point: 5 (2 h), 2 (24 h) and 6 (7 d). For the normal tissue, lungs of 3 animals per group were analysed. Graph bars represent the average in the group and error bars represent the SEM; **$p<0.005$ and ***$p<0.0005$ (t-test, one-tailed distribution, two-sample equal variance). Scale bar represents 10 µm; insets images are a further 2x magnification.

6.4. Radiation treatment decreased tumour burden in urethane-treated A/J mice

To evaluate the long-term response of urethane-induced tumours to radiation, A/J mice were injected intraperitoneally with urethane and followed for 8 weeks for tumour establishment. According to previous experiments in the lab, it was known that at 6 weeks post-urethane injection it was possible to visualise lung tumours by histology. At that point, mice received whole-thorax radiation (5 doses of 5 Gy) and were followed for 17 weeks for evaluation of tumour response (Figure 6.12).

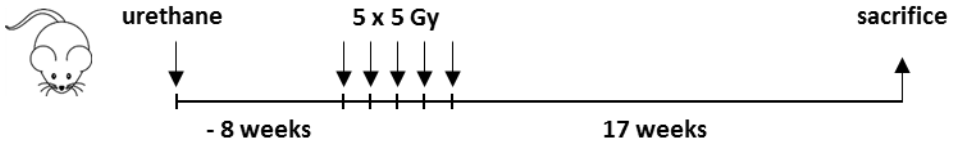


Figure 6.12. Experimental design for evaluation of whole-thorax radiation effect on urethane-induced lung tumours. A/J mice were intraperitoneally injected with 10 % urethane. After 8 weeks, animals were given 5 doses of 5 Gy to the whole-thorax (2 days break between radiation doses) and sacrificed 17 weeks after radiation (n=6 per group). Left lungs were fixed in formalin for further histological analysis.

The number and size of urethane-induced tumours were decreased in the irradiated mice as observed by magnetic resonance imaging, superficial tumour count and histology (Figure 6.13). Most tumours were localised at the lung surface, but internal tumours were also observed. In conclusion, radiation reduces tumour burden in urethane-treated mice.

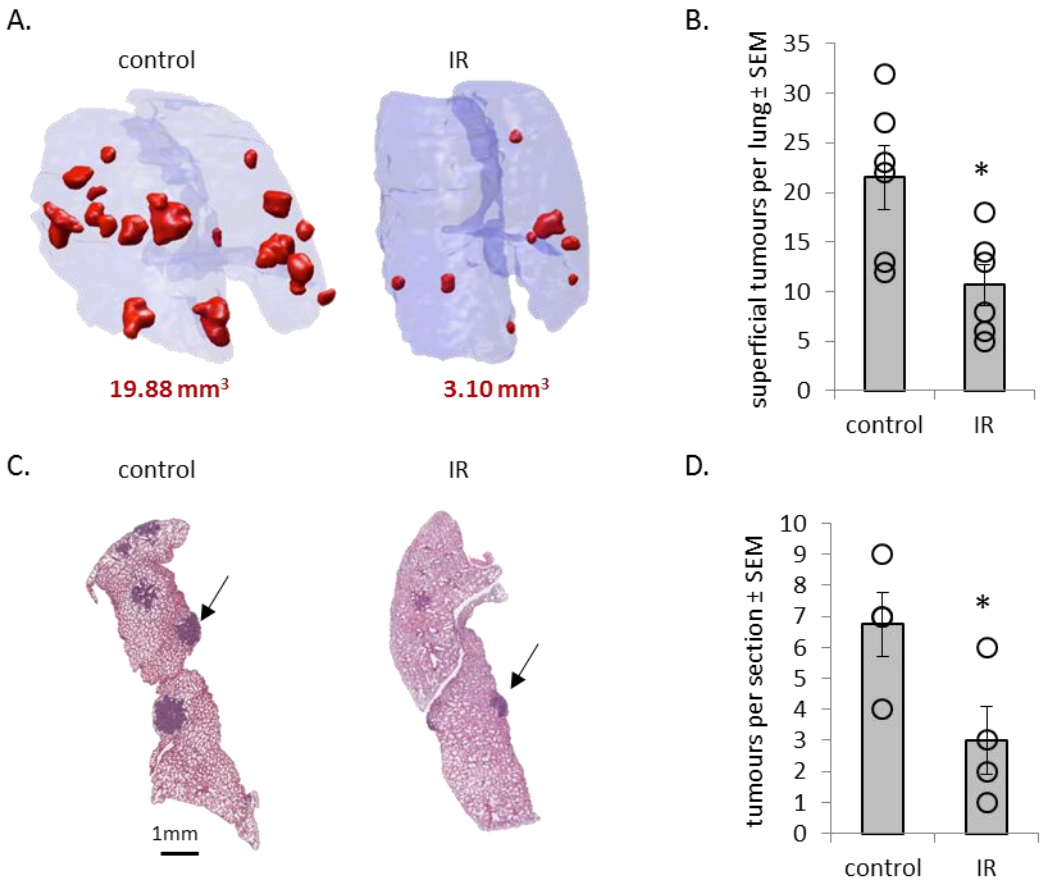


Figure 6.13. Whole-thorax radiation decreased the number of urethane-induced lung tumours. Total tumour burden was assessed by magnetic resonance imaging (A; blue: normal lung, red: tumours; numbers refer to total tumour volume). The number of superficial tumours was decreased in the irradiated (IR) lungs compared to mock irradiation control (B; sum of tumours in right and left lungs; 6 mice per group). H&E images of left lungs (C) were used to quantify tumours (arrows) and revealed less tumours per section in the irradiated lungs (D; 3 animals per group). Graph bars represent the average in the group, error bars represent the SEM and open circles represent individual animals; *$p<0.05$ compared to control group (t-test, one-tailed distribution, two-sample equal variance).

6.5. Discussion

We have identified a lack in the literature of an appropriate preclinical model for the evaluation of the therapeutic index of radiotherapy and combination therapies to treat lung cancer. The main challenge when searching for such a model is the contrast between the long time required

for the development of radiation-induced late effects and the rapid tumour growth observed in most of mouse models of cancer.

One strategy to tackle this problem would be inducing lung tumours in a strain known to develop radiation-induced lung damage such as C57BL/6J mice. Chen et. al. used C57BL/6J mice subcutaneously injected with 3LL cells in the armpit to evaluate pulmonary fibrosis in a tumour bearing model. The experiment was ended at 3 weeks post-irradiation, which is too early for the evaluation of fibrotic responses. The authors did not disclose why this time point was chosen but we speculate it was due to fast growing of the tumours (Chen et al., 2016). In another study, two separate experiments were performed, one looking at the fibrotic responses (4 months duration post-irradiation) and a second one with intravenous injection of LLC cells to evaluate tumour responses (1 week duration post-irradiation), both in C57BL/6J mice (Machtay et al., 2006). In this case, the authors failed to simultaneously evaluate the normal tissue and the tumour response in the same animal. Therefore, we concluded that C57BL/6J mice were not the ideal strain for a model of therapeutic index due to the rapid development of tumours. We chose to test a different strategy and evaluate if another mouse strain - known for the slow development of lung tumours instead of being fibrosis-prone - would develop radiation-induced lung damage.

There are a few reports in the literature that explore different mouse strains in their ability to develop radiation-induced lung damage (Jackson et al., 2010, 2011; Paun & Haston, 2012). The main challenge faced by researchers in the field of radiation-induced normal tissue toxicity is finding a preclinical model that develops similar symptoms when compared to humans. In a recent review, the authors concluded that the use of C57BL/6J as a standard model of radiation-induced lung damage might not be ideal as this is a fibrosis-prone strain and mostly pneumonitis

not pulmonary fibrosis is the primary clinical concern after radiotherapy (Dabjan et al., 2016). In addition, Jackson et. al. refer to clinical observations published in the 1970s describing the histopathology of patients succumbing to radiation-induced pneumonitis: 'epithelial cell hyperplasia, thrombosis and oedema, accumulation of foamy, lipid-laden macrophages and mononuclear cellular infiltrates, increased alveolar septa thickness, hyaline membranes, and increased connective tissue density' (Gross, 1977; Jackson et al., 2012). Therefore, it seems like the human disease is mixed, presenting with features of both pneumonitis and fibrosis. The description above is similar to what we observed in A/J mice, namely prominent pneumonitis with progressive fibrosis. This differences in the development of pneumonitis/fibrosis in the two studied strains might hinder the use of non-invasive imaging such as MRI to follow up on these side effects, as they might not present enough resolution to differentiate between the two distinct pathologies. Effort should be undertaken to improve imaging techniques as they could be performed longitudinally during the experiment and therefore decrease the number of animals used in a given experiment.

In addition, worth of note is the difference observed when using single doses and fractionated schedules of radiation in A/J mice. In the literature, two studies using single doses of whole-thorax irradiation (15 and 18 Gy) reported that A/J mice developed pneumonitis and pleural effusions but not fibrosis (Jackson et al., 2011; Paun & Haston, 2012). Interestingly, our data showed that A/J mice irradiated with fractionated doses developed pulmonary fibrosis. This finding illustrates the importance of testing radiation schedules that are more similar to the ones used in the clinic when establishing a preclinical model.

When analysing the radiation-induced DDR, our data showed similar biological responses in the normal lung tissue of both A/J and C57BL/6J mice. At 24 h, approximately 1/3 of lung cells

maintained positivity for DNA DSB markers and, interestingly, long lasting γH2AX-positive cells were present at 7 days post-irradiation in both strains. 53BP1 foci-positive cells were also present at 7 days post-irradiation. These findings suggest that DDR is active for several days in lung cells upon irradiation which could lead to induction of senescence and chronic inflammation which, as discussed previously, have been shown to be related to the late toxic effects of radiation (Kang et al., 2015). Considering both strains showed long lasting DNA DSBs and developed fibrosis, this finding supports the hypothesis for a link between unresolved long-lasting DNA damage and late term side effects in the irradiated lung tissue.

In addition, using the A/J model, it was possible to simultaneously compare the radiation-induced DDR in both normal and tumour cells. Interestingly, we observed that the fraction of γH2AX-positive cells was significantly larger in the irradiated tumour tissue compared to the normal tissue at 2 h post-irradiation. Two possible explanations for this finding are related to repair kinetics and replication fork stalling. It has been reported that the repair kinetics of DNA DSBs in cells in vitro reached the slowest rate in cells arrested in the G1 phase (Metzger & Iliakis, 1991). Also, in replicating cells such as tumour cells DNA DSBs can arise from replication fork stalling and ultimately collapse in response to DNA SSBs. In addition, the open structure of chromatin during replication render it more susceptible to damage (Sak, M. Stuschke, R. Wurm, V. Budac, 2000). Therefore, even before the development of DNA DSBs due to replication stress, ATR may be phosphorylating H2AX in the tumour cells (I. M. Ward & Chen, 2001). In contrast, in the normal lung tissue where most cells are in G1, γH2AX phosphorylation would primarily happen due to ATM and DNA-PK activity in response to directly induced DNA DSBs (H. Wang, Wang, Wang, Böcker, & Iliakis, 2005). Another possible explanation is the previously reported increased rate of γH2AX dephosphorylation in

tumours by the overexpression of the wild-type p53-induced phosphatase 1 (WIP-1) (Cha et al., 2010).

Interestingly, positivity for 53BP1 foci was also higher in the irradiated tumour tissue compared to the normal tissue at 2 h post-irradiation. Again, this might be an effect of the differential replicative rates between tumour and normal tissue. As a downstream factor of 53BP1 foci positivity, one possible explanation is that ATM is more active in the irradiated tumour tissue compared to the normal tissue. As discussed previously, the MRN complex is responsible for ATM activation through the promotion of DNA end resection upon DNA DSB recognition. The MRN complex activity is regulated by CDK and is predominantly active during S and G2 phases. Consequently, DNA end resection is more frequent in S and G2 phases of the cell cycle in comparison to G1, therefore it is expected to be more prominent in the tumour tissue compared to the normal tissue (Symington & Gautier, 2011). It is believed that as cycling cells have the error-free option of DNA repair (HR), the aforementioned mechanism might have evolved to direct DNA DSBs to be repaired through this pathway via ATM signalling. Nevertheless, Feng et. al. showed that ATM-dependent 53BP1 phosphorylation is restricted to the G1 phase of the cell cycle (Feng et al., 2015). Considering that tumour cells are highly proliferative and that we found that 70.95 ± 3.63 % of cells in the tumours are positive for 53BP1 foci at 2 h post-irradiation, our data suggests that either this is overridden in tumours, or that tumours cells arrest in G1 upon radiation or that 53BP1 foci formation was largely ATM-independent (as discussed in the following chapter). Double staining approaches should be performed to confirm in which phase of the cell cycle those cells positive for 53BP1 foci are as well as assessing more time-points after radiation as we could have missed a signalling peak between 2 h and 24 h post-irradiation.

Intriguingly, we observed the opposite trend at 7 days post-irradiation, i.e. fewer cells positive for 53BP1 foci in the tumours compared to the normal tissue. It is known that, downstream of ATM, one of two opposing repair pathways can take place. If 53BP1 is recruited to the DNA DSB, non-homologous end joining is promoted; in contrast, if BRCA1 accesses the DNA DSBs, homologous recombination is favoured (Bouwman et al., 2010; Daley & Sung, 2014; Escribano-Díaz et al., 2013; Tang et al., 2013; Zimmermann & de Lange, 2014). Most normal lung cells are non-proliferative and therefore do not have the option of engaging in homologous recombination. Therefore, the lower level of 53BP1 foci at 7 days post-irradiation in tumours does not necessarily imply that there is less damage accumulated when compared to normal tissue, but perhaps that a non-53BP1 DNA repair pathway has been chosen. Our findings suggest that 53BP1-related non-homologous end joining is highly activated in tumours in response to radiation and therefore could be an interesting therapeutic target.

In addition to the early effects of radiation on DDR and the normal tissue late effects, our data showed that urethane-induced tumours are radiosensitive. We showed a decrease in the number of tumours in the irradiated mice, both by counting superficial tumours and by histology. This measurement of tumour burden by histology was performed in a single lung slice and therefore to increase accuracy we propose that quantification of multiple lung sections should be performed. Considering the data presented in this chapter, this model may represent patients diagnosed with early or locally advanced disease (stages I-III), before the onset of metastasis. In the clinic, radiotherapy (usually in combination with chemotherapy) is an effective treatment for patients with inoperable stage I-III disease (Postmus et al., 2017). Therefore, due to the responsiveness of urethane-induced tumours to radiotherapy and also the reported normal lung tissue responses, the A/J mouse model may represent a clinically relevant model of early stage

lung cancer for testing the radiosensitising effects of new combination therapies (Barnett et al., 2009). To investigate this as a potential model of therapeutic index, in chapter 7 we tested the effects of combining an ATM inhibitor with radiotherapy on the normal lung tissue as well as lung tumours.

7. The value of using a therapeutic index model: evaluation of ATM inhibition in combination with radiation as a treatment for lung cancer

7.1. Introduction

In the previous chapter, we have established a novel mouse model for evaluating the therapeutic index of therapies in combination with radiation. In chapter 5, we showed that ATM inhibition radiosensitised tumour cells in a xenograft mouse model and that it led to increased accumulation of collagen in the lung of C57BL/6J mice, a fibrosis-prone strain. In this chapter, based on our previous results, we used the ATM inhibitor to evaluate if the A/J model would be a useful tool to assess the effect of combination therapy on the normal and tumour tissues simultaneously.

Our results with Calu6 xenograft tumours showed tumour shrinkage at 20-25 days post-treatment with ATMi in combination with radiotherapy, and then tumour growth was re-established. This is a very unrealistic time course compared to what happens in the clinic; therefore; we expected to obtain more relevant information using the A/J model. In this model, tumours take longer to growth and treatment effect will be evaluated for a longer period as mice will not have to be sacrificed due to oversized tumours. Also, more than one tumour will be present in the lungs, which can give information on the response of potentially genetically diverse tumours.

It has been suggested that the use of DDR modulators is a good strategy to treat cancer mainly due to three differences between normal and tumour cells. Firstly, cancer cells may have lost one or more DDR pathways. Secondly, they are more proliferative therefore are under increased replication stress. Lastly, cancer cells are exposed to higher levels of endogenous DNA damage. Therefore adding more damage by radiotherapy would selectively target cancer cells (O'Connor, 2015).

An important aspect of this model is the potential to evaluate both normal and tumour responses simultaneously. As discussed before, the early changes induced by radiation might be related to the long-term effect of this therapy, so understanding the impact of ATM in the initial DDR in both normal and tumour tissue can bring insights to treatment improvement. Also, as ATM has been shown to be responsible for many other cell processes apart from DDR, other responses can be evaluated, such as the impact of ATM inhibition on radiation-induced acute inflammation.

A/J mice showed similar late and early effects of thoracic radiation compared to C57BL/6J mice, such as weight loss and lung fibrosis. Nevertheless, A/J mice showed prominent pneumonitis (marked foamy macrophage accumulation in the lungs), which was not observed in C57BL/6J. Therefore, it is difficult to predict the impact of combining an ATMi with radiotherapy in A/J mice, as the pathological mechanisms of radiation-induced lung damage in this strain might be different from the ones in C57BL/6J mice. As discussed before, ATM plays a role in several cellular pathways, so the impact of its inhibition could for instance affect the prominent pneumonitis observed.

7.2. ATM inhibition impacts early inflammation induced by thoracic radiation in A/J mice

To evaluate the early effects of ATM inhibition in combination with thoracic radiation in a model of therapeutic index, we treated A/J mice bearing urethane-induced lung tumours with ATMi and irradiated the whole-thorax with a single dose of 5 Gy one hour after treatment. According to previous experiments in the lab, it was known that at 12 weeks post-urethane injection middle sized (400 µm diameter) lung tumours were present. Mice were sacrificed at 2 h, 24 h and 7 days post-irradiation (Figure 7.1).

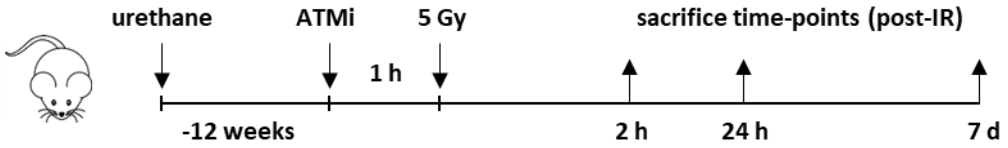


Figure 7.1. Experimental design for evaluation of early effects of whole-thorax irradiation and ATM inhibitor in A/J mice. Animals were intraperitoneally injected with 10 % urethane. After 12 weeks, animals were given 50 mg/kg of ATM inhibitor (ATMi) orally. One hour after treatment, mice received a dose of 5 Gy to the whole-thorax and were sacrificed at 2 h, 24 h or 7 days after radiation (n=3 per group). Left lungs were fixed in formalin for further histological analysis, right lungs were fresh frozen and blood was collected for plasma extraction.

We did not observe a significant increase in KC or IL-6 plasma levels in A/J mice treated with vehicle plus a 5 Gy dose of radiation compared to unirradiated mice. Animals treated with ATMi in combination with radiation, however, showed a significant increase in KC plasma levels at 24 h when compared to animals treated with vehicle plus radiation at the same time-point (Figure 7.2 A). IL-6 was only detectable in plasma samples collected from the unirradiated and 2 h post-irradiation mice. In addition, animals treated with vehicle plus radiation did not show

a significant increase in IL-6 levels or neutrophil (Ly6C/G-positive) count in the lung compared to unirradiated mice, but animals treated with radiation plus ATMi did at 2 h post-irradiation did (Figure 7.2 B and C).

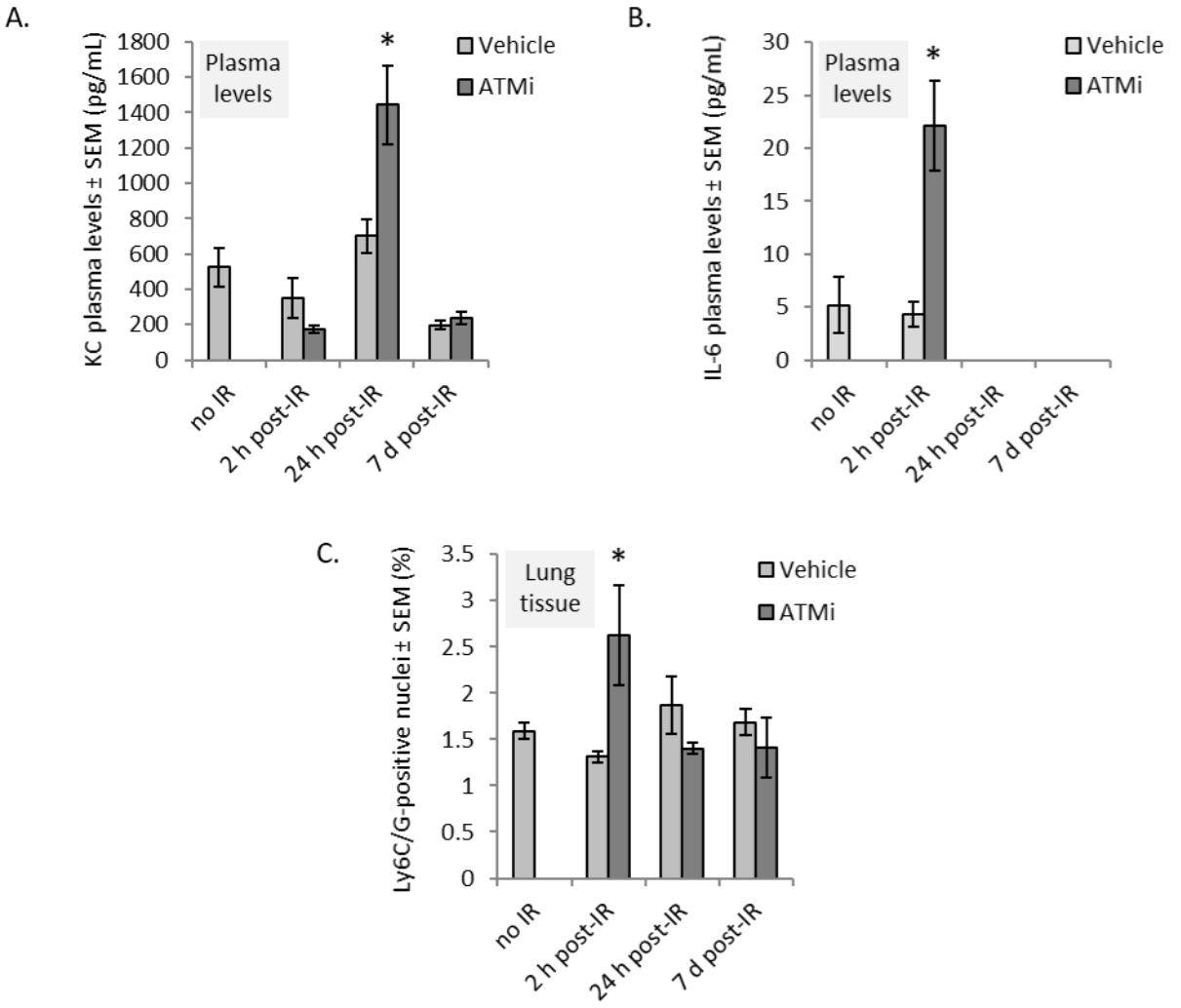


Figure 7.2. ATM inhibition impacted whole-thorax irradiation-induced systemic inflammation and neutrophil recruitment to the lung of A/J mice. Plasma levels of KC (A) and IL-6 (B) were affected early after radiation in animals treated with ATM inhibitor as assessed by ELISA. Neutrophil count in the lung was increased at 2 h after radiation in the ATMi group as assessed by immunohistochemistry (C, Ly6C/G - marker for neutrophils). Graph bars represent the average in the group (n=3 mice per group) and error bars represent the SEM; *$p<0.05$ compared to respective vehicle group (t-test, one-tailed distribution, two sample equal variance).

7.3. ATM inhibition impacted early DNA damage response induced by thoracic radiation on normal and tumour lung tissue in A/J mice

To assess the DNA damage response by radiation in the presence of an ATMi on both normal and tumour lung tissue, we evaluated the downstream targets pKAP1 (ser824), γH2AX and 53BP1 foci positivity in the lung samples obtained from this experiment (Figure 7.3, Figure 7.4 and Figure 7.5).

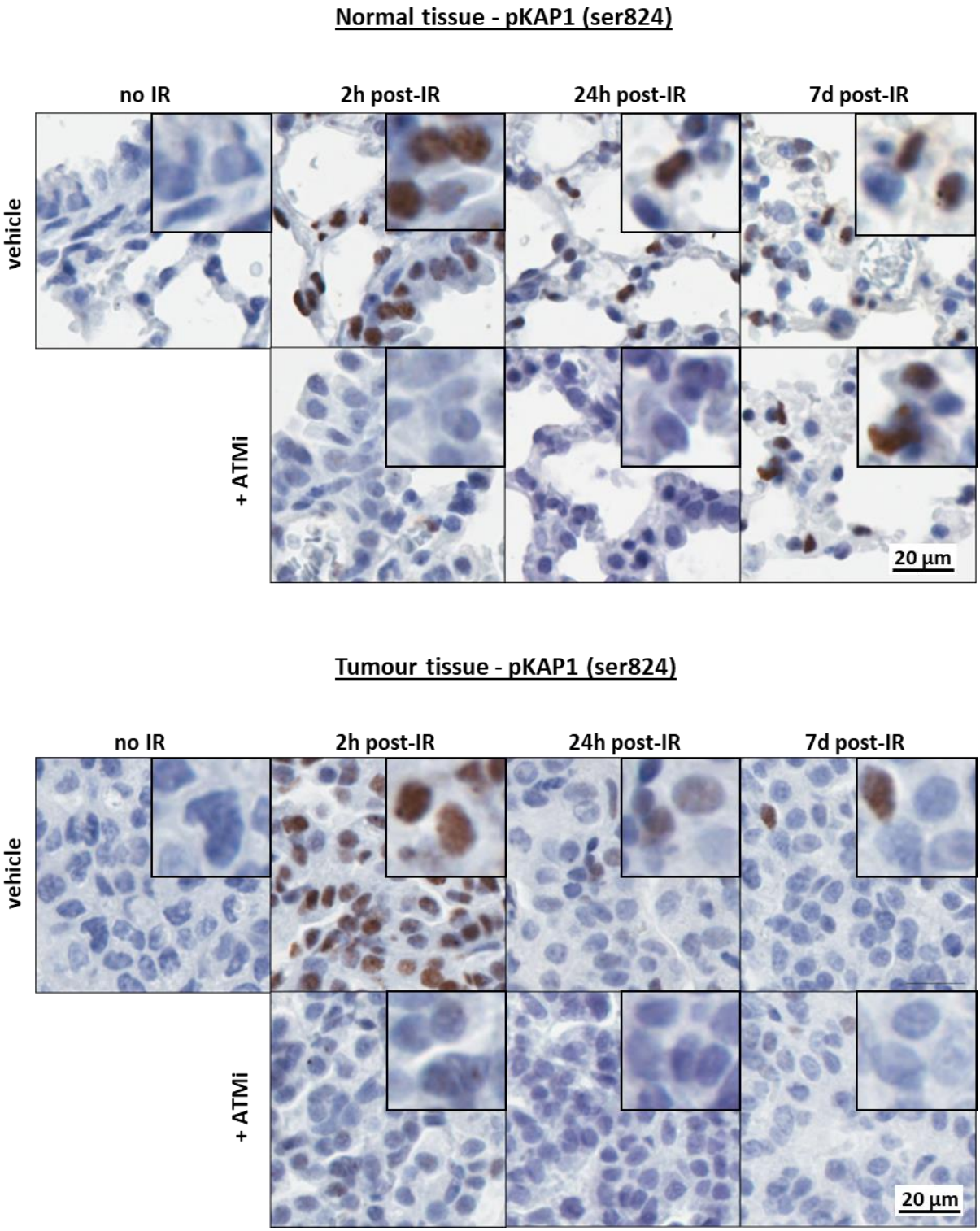


Figure 7.3. Differential normal and tumour lung tissue responses positivity for pKAP1 (ser824) with or without treatment with ATM inhibitor before whole-thorax irradiation. Immunohistochemistry was performed in lung samples from mice treated with ATM inhibitor (ATMi) or vehicle 1 h before receiving a dose of 5 Gy to the whole-thorax. Mice were sacrificed at 2 h, 24 h or 7 days after radiation.

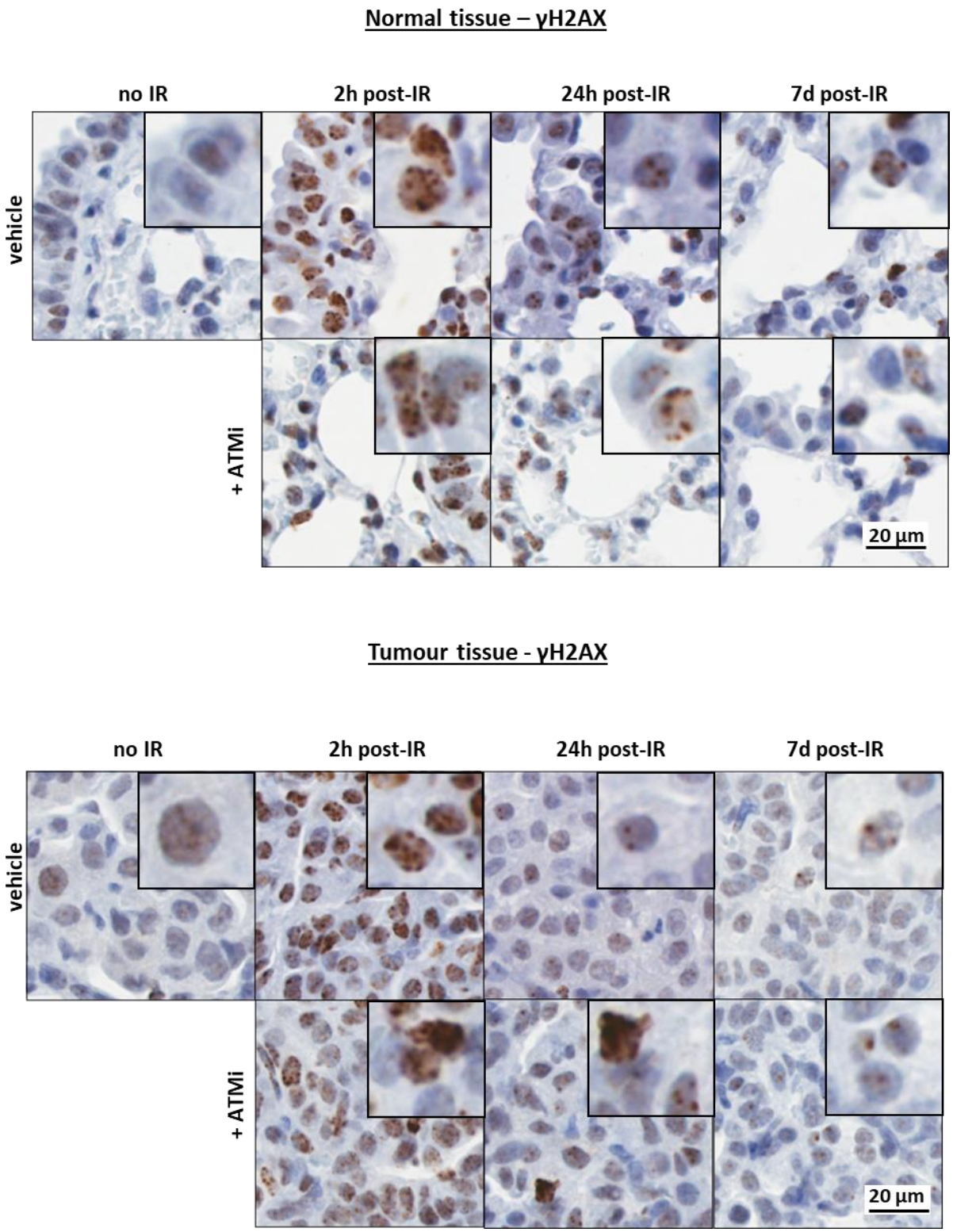


Figure 7.4. Differential normal and tumour lung tissue responses positivity for γH2AX with or without treatment with ATM inhibitor before whole-thorax irradiation. Immunohistochemistry was performed in lung samples from mice treated with ATM inhibitor (ATMi) or vehicle 1 h before receiving a dose of 5 Gy to the whole-thorax. Mice were sacrificed at 2 h, 24 h or 7 days after radiation.

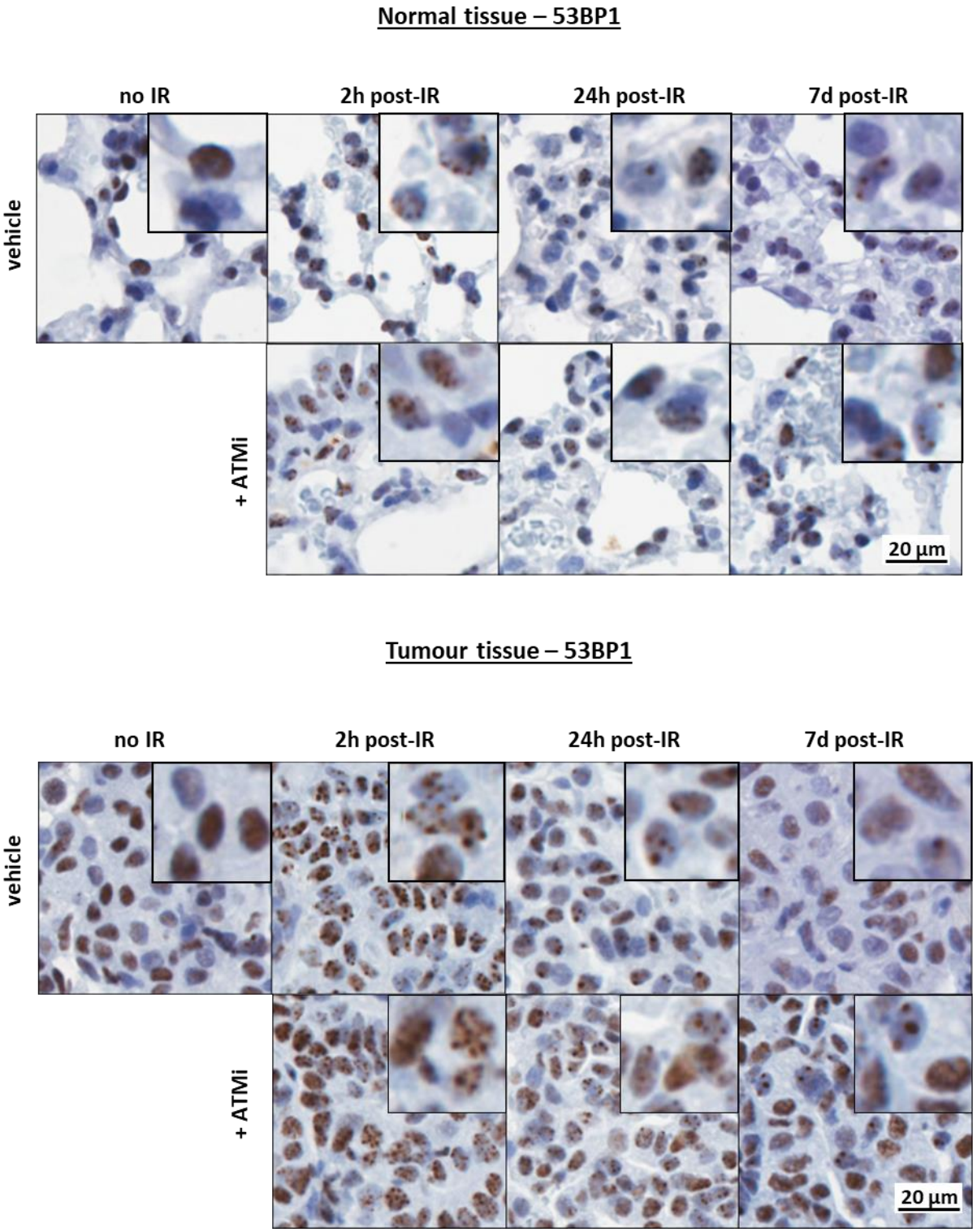


Figure 7.5. Differential normal and tumour lung tissue responses positivity for 53BP1 foci with or without treatment with ATM inhibitor before whole-thorax irradiation. Immunohistochemistry was performed in lung samples from mice treated with ATM inhibitor (ATMi) or vehicle 1 h before receiving a dose of 5 Gy to the whole-thorax. Mice were sacrificed at 2 h, 24 h or 7 days after radiation.

In the normal lung tissue of animals treated with ATMi in combination with radiation, we observed that at 2 h and 24 h post-irradiation ATM inhibition led to a marked decrease in the fraction of cells positive for pKAP1 and γH2AX (known downstream targets of ATM) when compared to animals treated with vehicle plus radiation at the respective time-points ($p<0.0005$ and 0.005, respectively). At 7 days, ATM inhibition did not affect the number of cells positive for γH2AX, but a significant increase was observed for pKAP1-positive cells compared to vehicle plus radiation at the same time-point. In contrast, the fraction of cells positive for 53BP1 foci was not affected by ATMi treatment at any of the time points evaluated compared to vehicle plus radiation (Figure 7.6 graphs on the left).

We also evaluated the tumours present in the lungs obtained in this experiment. As not all treatment groups had more than 1 tumour per lung slice, statistical analysis was not performed and therefore the results described hereafter only suggest the trends observed. Similarly to what was observed for the normal tissue, ATM inhibition led to a marked decrease in the number of cells positive for pKAP1 at 2 h and 24 h post-IR. Interestingly, as opposed to the normal tissue, we did not observe an increase in the fraction of cells positive for pKAP1 at 7 days post-irradiation. In addition, γH2AX did not decrease at 2 h and 24 h post-irradiation when compared to vehicle plus radiation treatment. A similar trend was observed for 53BP1 foci positivity. At 7 days post-irradiation, no differences were observed for the 3 markers compared to samples in the vehicle plus radiation group (Figure 7.6 graphs on the right).

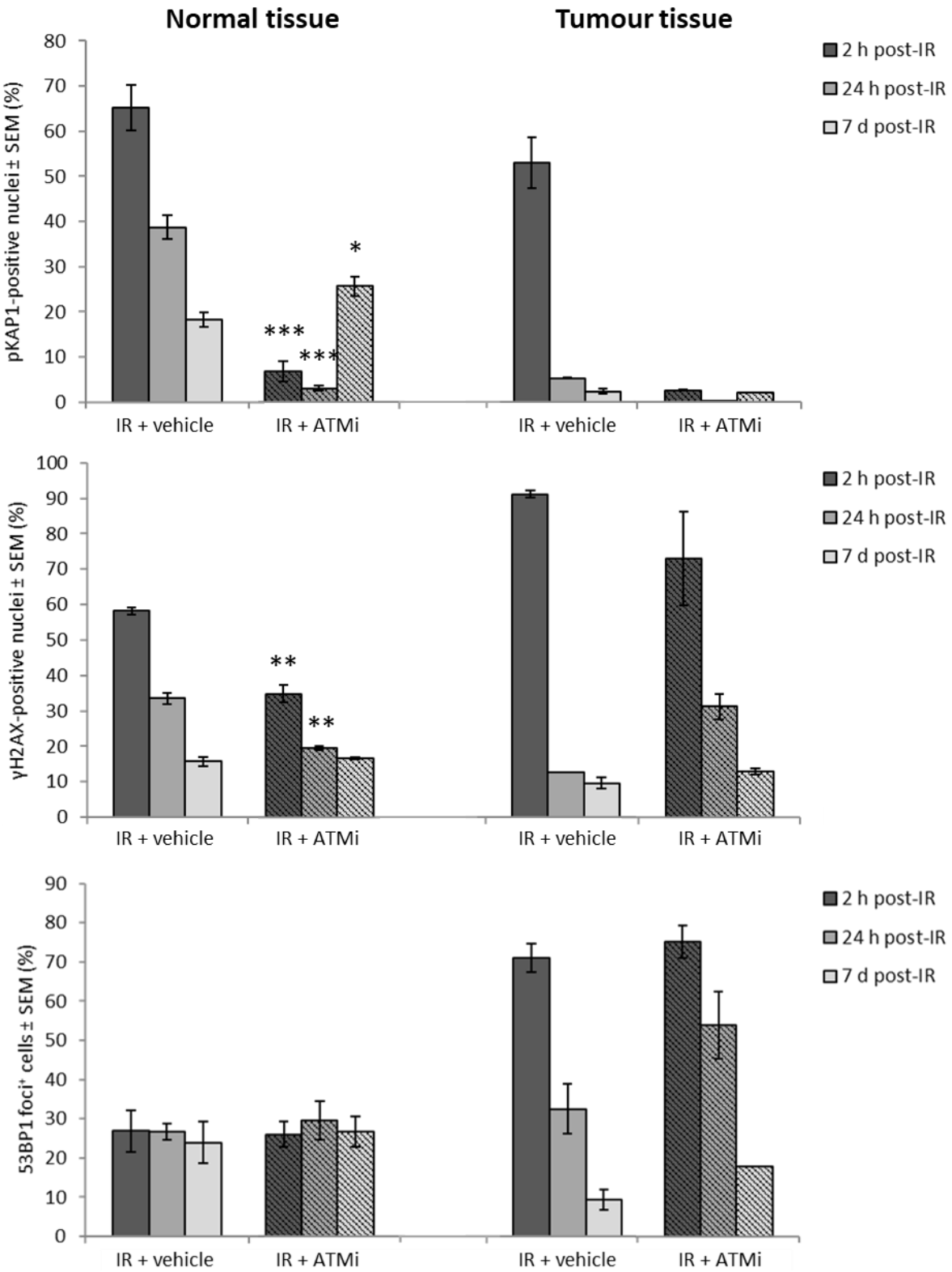


Figure 7.6. ATM inhibition showed differential impact on the radiation-induced DNA damage response of normal and tumour lung tissue. Immunohistochemistry of pKAP1 (ser824), γH2AX and 53BP1 was performed and quantified. Graph bars represent the average in the group and error bars represent the SEM; *p<0.05, **p<0.005 and ***p<0.0005 compared to respective 'IR + vehicle' group (t-test, one-tailed distribution, two sample equal variance).

7.4. ATM inhibition in combination with radiation led to weight loss, pulmonary haemorrhage and impairment of alveolar structure in A/J mice

To evaluate the impact of ATM inhibition on the late effects of thoracic radiation on normal and tumour lung tissue simultaneously, we injected A/J mice with urethane and waited for the development of tumours for 8 weeks (all mice in this experiment received urethane). According to previous experiments in the lab, it was known that at 6 weeks post-urethane injection it was possible to visualise lung tumours by histology. Mice were then treated with ATMi and 1 h after treatment mice were irradiated with a dose of 5 Gy given to the whole-thorax. Another dose of ATMi was given 24 h post-irradiation. This treatment was repeated 5 times. Sacrifice was planned to be conducted at 24 weeks post-treatment but instead the experiment was terminated at 17 weeks post-irradiation due to the manifestation of adverse effects described below (Figure 7.7).

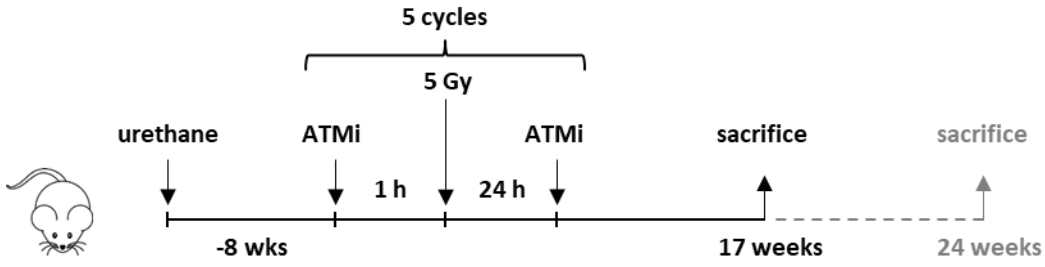


Figure 7.7. Experimental design for evaluation of ATM inhibition on whole-thorax irradiation-induced late effects in A/J mice. Animals were intraperitoneally injected with 10 % urethane. After 8 weeks, animals were given 50 mg/kg of ATM inhibitor (ATMi) orally. One hour after treatment, mice received a 5 Gy dose of radiation to the whole-thorax. Twenty-four hours after radiation, mice were given a second dose of ATMi. This treatment was repeated 5 times, with 2 days break between radiation doses (n=3 for radiation alone and vehicle groups and n=6 for ATMi groups). Sacrifice was planned at 24 weeks after treatment start but performed at 17 weeks due to weight loss. Left lungs were fixed in formalin for further histological analysis and right lungs were fresh frozen.

At 14 weeks post-treatment, one mouse treated with ATMi in combination with radiation showed more than 10 % body weight loss and was sacrificed (LL563). At 17 weeks, another 2 animals (LL564 and LL567) in the combination group showed more than 10 % body weight loss and all the animals in the experiment were sacrificed. Animals treated with vehicle, radiation or ATMi alone did not show weight loss (Figure 7.8).

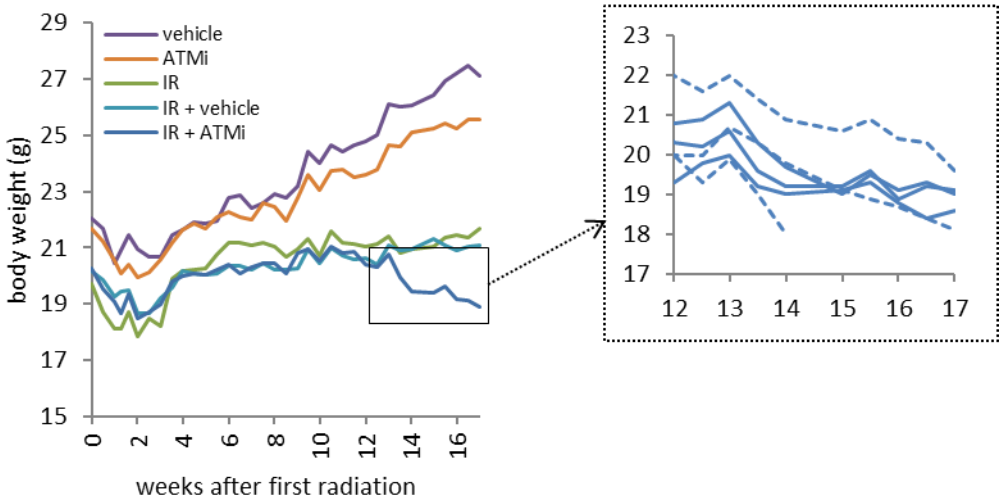


Figure 7.8. ATM inhibition in combination with whole-thorax irradiation induced body weight loss in A/J mice. At 14 weeks post-irradiation one animal in the combination group showed more than 10 % weight loss and was sacrificed. Three weeks later, two other mice in this treatment group showed more than 10 % body weight loss and the experiment was ended (n=3 for radiation alone and vehicle groups and n=6 for ATMi groups; graph lines represent the average in each group; inset graph lines show individual animal weights, dashed lines show animals which presented more than 10 % body weight loss).

Left lungs were processed for histological analysis and fibrosis scoring. ATMi treatment alone did not lead to increase in the fibrosis score or any obvious histological changes in the analysed lungs. Radiation-treated animals showed a significant increase in the average fibrosis score in comparison to unirradiated controls and the combination with ATMi did not lead to a further increase. Of note, animal LL563 (sacrificed at 14 weeks due to weight loss) showed the highest fibrosis score. Interestingly, Masson's trichrome staining revealed areas of lung haemorrhage

and dense fibrotic lesions which were more evident in animals receiving the combination treatment (Figure 7.9).

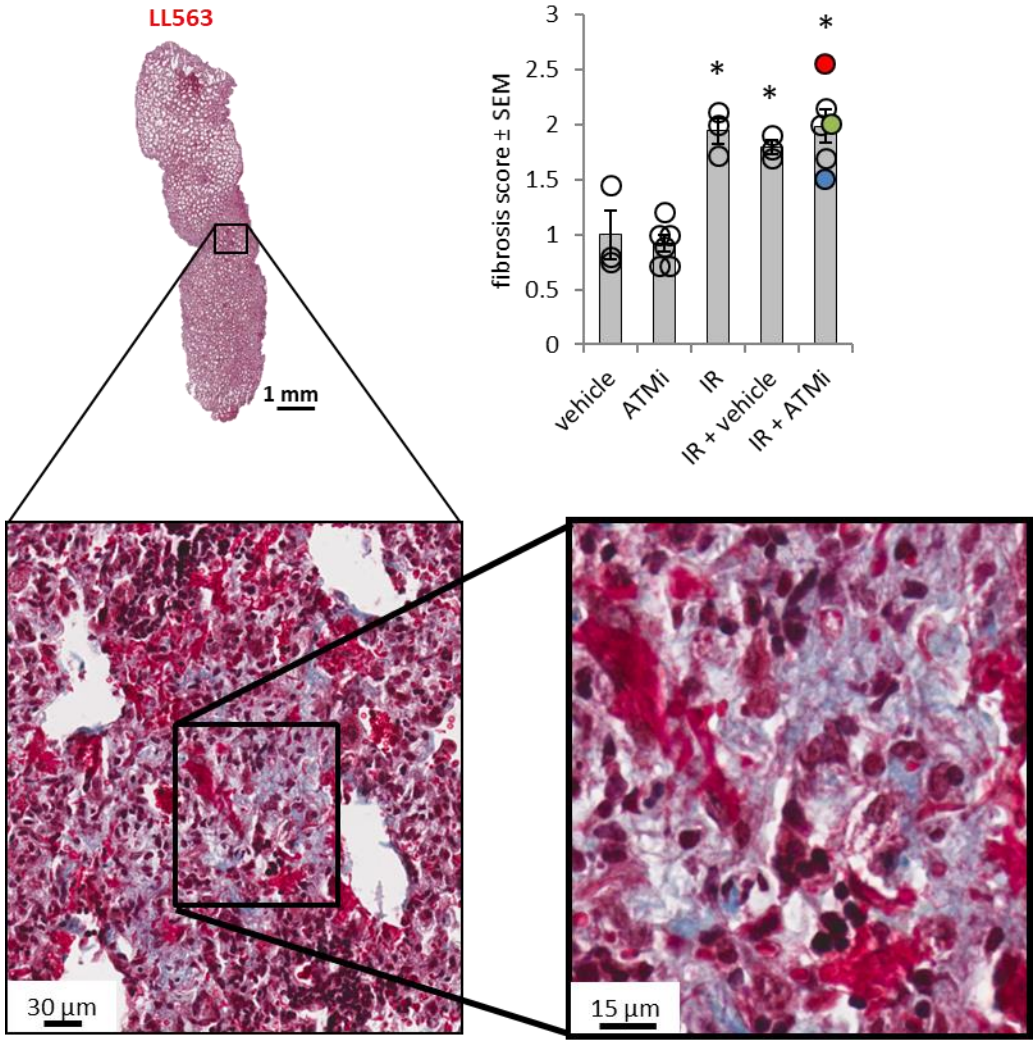


Figure 7.9. Inhibition of ATM in combination with whole-thorax irradiation did not lead to further increase in fibrosis in the lungs of A/J mice. Analysis of lung samples stained by Masson's trichrome protocol revealed no increase in fibrosis in combination treatment (IR+ ATMi) samples compared to radiation alone (IR). Insets show areas of lung haemorrhage and dense fibrotic lesion in animal LL563. Graph bars represent the average in the group; n=3 for radiation alone and vehicle groups and n=6 for ATMi groups; error bars represent the SEM and circles represent individual animals; LL563 (red), LL564 (blue) and LL567 (green); *p<0.05 compared to unirradiated vehicle-treated group (t-test, one-tailed distribution, two sample equal variance).

Right lungs were homogenised and processed for hydroxyproline assay and western blotting. ATMi treatment alone did not lead to increase in collagen accumulation in the lung. Radiation alone led to increased hydroxyproline, collagen I and III protein levels, and combination with ATM inhibition did not lead to a further increase in collagen. Interestingly, the animals that were sacrificed due to weight loss did not show the highest levels of collagen/hydroxyproline in the lungs (Figure 7.10).

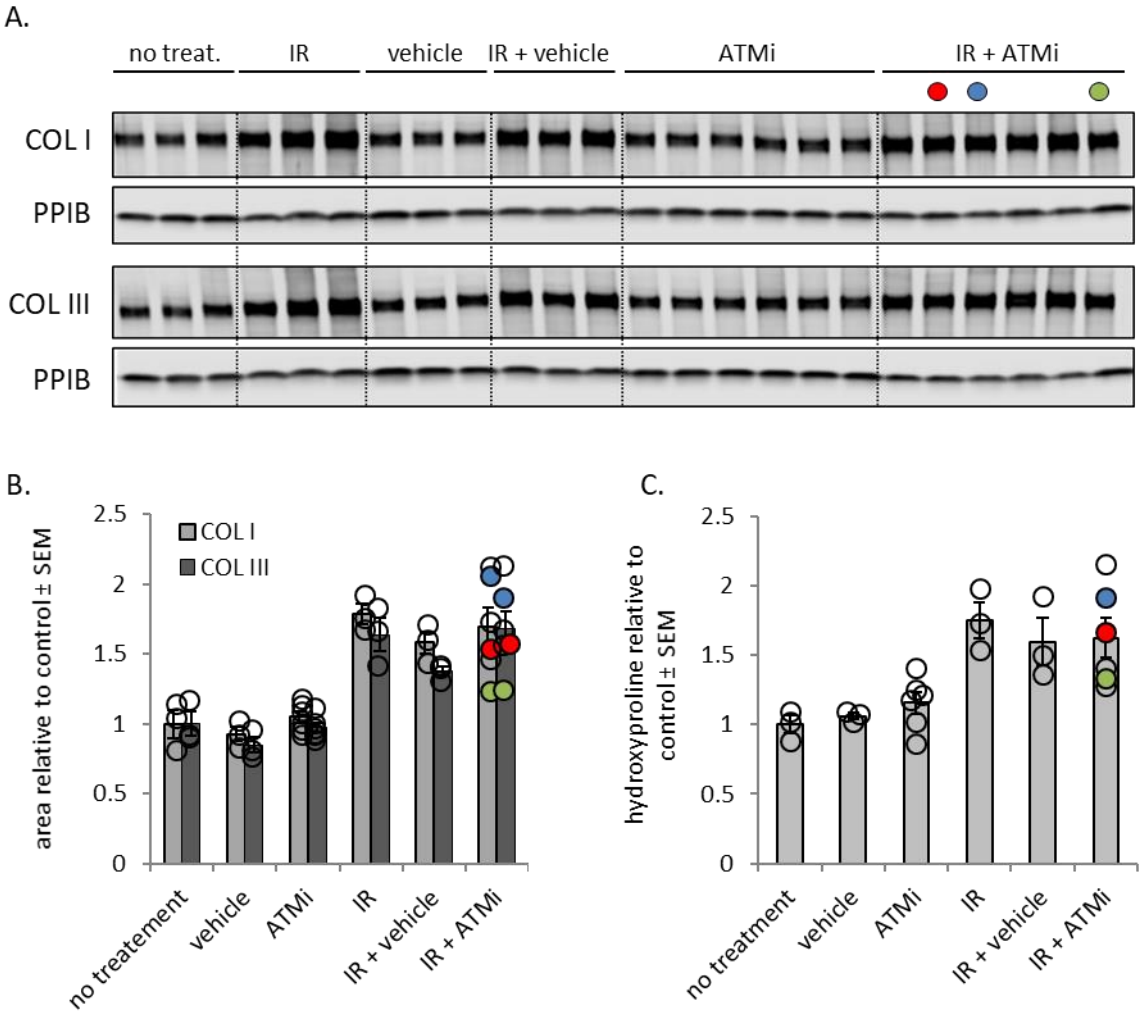


Figure 7.10. ATM inhibition in combination with whole-thorax irradiation did not lead to a further increase in the levels of collagen I, collagen III or hydroxyproline in the lungs of A/J mice. Collagen (COL) I and III were measured by western blot of lung protein extracts, showing no further increase in collagen I or III in the IR + ATMi group compared to IR alone (A, individual animal extracts were loaded into each well and PPIB was used as loading control; B, blot quantification). The same was observed when performing hydroxyproline assay (C). No treatment: n=3, injected with urethane, not treated with radiation or drug. Graph bars represent the average in the group; n=3 for radiation alone and vehicle groups and n=6 for ATMi groups; error bars represent the SEM and circles represent individual animals; LL563 (red), LL564 (blue) and LL567 (green); *$p<0.05$ compared to unirradiated vehicle-treated group (t-test, one-tailed distribution, two sample equal variance).

7.5. ATM inhibition radiosensitised urethane-induced lung tumours

To assess the effect of ATM inhibition on the radiation response of urethane-induced lung tumours in A/J mice, superficial tumours were counted at the time of sacrifice and tumours were counted on lung slices stained by H&E (samples from experiment described on Figure 7.7). ATM inhibition alone did not affect the number of urethane-induced lung tumours, but radiation alone led to a decrease in both superficial tumour count and histology assessed tumours. Interestingly, the combination treatment (IR + ATMi) led to a further decrease in the number of lung tumours in this model (Figure 7.11).

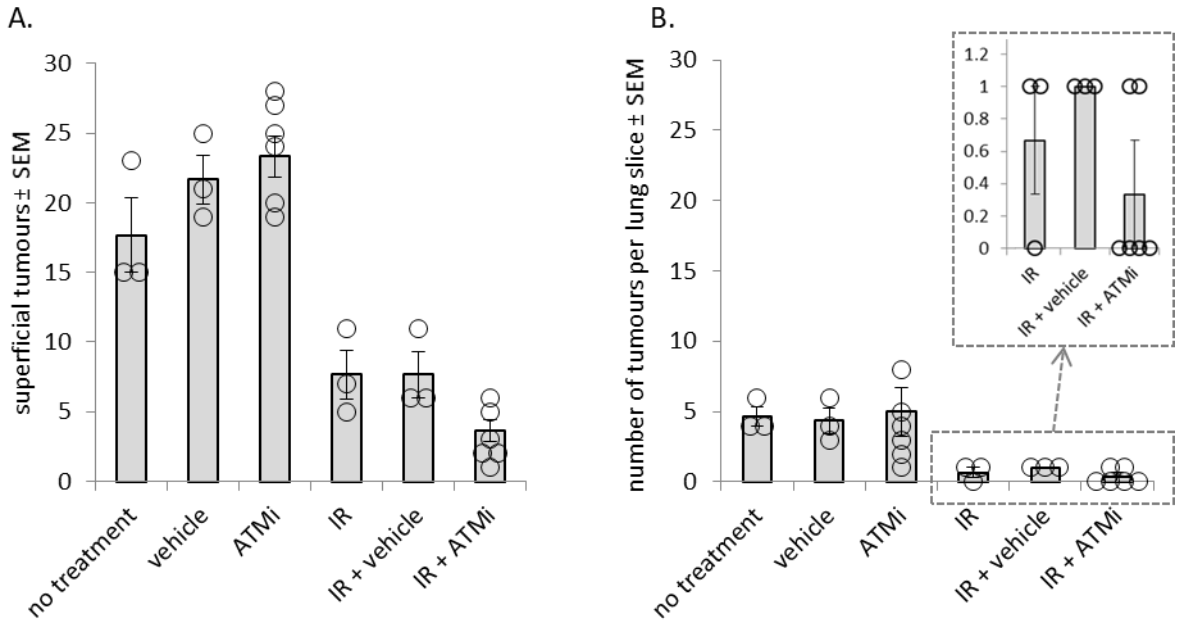


Figure 7.11. ATM inhibition radiosensitised urethane-induced lung tumours. The number of superficial tumours was further decreased in the combination treatment (IR + ATMi) compared to radiation alone (A; sum of superficial tumours in right and left lungs). H&E images were used to quantify tumours and revealed a further decrease in the number of tumours per section in the combination group (B). No treatment: n=3, injected with urethane, not treated with radiation or drug. Graph bars represent the average in the group; n=3 for radiation alone and vehicle groups and n=6 for ATMi groups; error bars represent the SEM and open circles represent individual animals.

7.6. Discussion

Previously, we showed that C57BL/6J mice treated with 10 Gy whole-thorax irradiation had an increase in KC and IL-6 plasma levels as well as neutrophil count in the lung, peaking at 1-2 hours post-irradiation. A 5 Gy dose did not have the same effect on A/J mice, which could be due to the use of a lower dose of radiation or could represent a differential response in the two mouse strains. Also, as observed before, cytokine plasma level increases are usually acute and transient, therefore we could have missed a peak that fell between the time points evaluated. Interestingly, our data showed that, when combining ATMi with whole-thorax irradiation, KC and IL-6 plasma levels and neutrophil recruitment to the lung were increased in A/J mice compared to radiation plus vehicle treatment. This finding indicates that ATM inhibition in the context of radiation impacts the early inflammatory response in the lung. This could be through a direct effect or through an indirect ATM role, i.e. DDR or oxidative stress. More experiments should be performed to determine the precise mechanism by which ATM affects these responses after radiation.

Importantly, our DNA damage response data showed that pKAP1 (ser824) can be used as a marker for ATM activity in vivo (Ziv et al., 2006). The ATMi used was efficient in inhibiting its target in both normal and tumour lung tissue for the first 24 h after radiation treatment, according to pKAP1 positivity. γH2AX can also be used as a marker for ATM activity, but not as a specific marker as upon inhibition of ATM a significant portion of γH2AX-positive cells was present in response to radiation [probably by activity of other kinases such as DNA-dependent protein kinase (DNA-PK) and ATR].

When comparing the effect of ATM inhibition between normal and tumour tissue, the main difference observed was in pKAP1 positivity at 7 days post-irradiation, when a significant fraction of cells was positive in the normal tissue but not in the tumour tissue. Interestingly, it has been reported that when irradiating G1-phase cells treated with ATM inhibitor, persistent DNA DSBs localise to regions of heterochromatin (Goodarzi et al., 2008). This effect was shown to be related to phosphorylation of KAP1 by ATM, which is responsible for relaxation of heterochromatin, making it accessible to repair proteins. In the absence of ATM, KAP1 is not phosphorylated, the break is less accessible to repair and therefore may remain unrepaired. Considering this proposed role of ATM in the repair of heterochromatin DNA DSBs, we speculate that once ATM inhibition subsides in our studies, the radiation-induced DNA DSBs that remained inaccessible in the heterochromatin of normal lung cells are then recognised, leading to the 'delayed' increase in pKAP1 observed at 7 days post-irradiation. As in the tumour tissue cells are replicating, the heterochromatin may eventually become relaxed during DNA replication, allowing for the repair of DSBs by ATM-independent pathways (or leading to cell death due to accumulation of damage).

Increased levels of γH2AX and 53BP1 foci in the tumours at 24 h post-irradiation in the presence of ATMi suggest that DNA damage induced by radiation is not being properly repaired and this might explain the radiosensitising effect of ATMi observed in this model. Similarly to pKAP1, 53BP1 has been reported to play a role in the repair of persistent DSBs in the heterochromatin (Noon et al., 2010). Others have shown that ATM is not required for heterochromatin relaxation after damage, but it is required for repair (Jakob et al., 2011). To further evaluate this, more experiments are needed, especially looking at time points between 24 h and 7 days post-treatment. Furthermore, increased levels of γH2AX in tumours 24 h after

ATMi treatment suggest that other PPIKs such as DNA-PK and ATR act in the absence of ATM and phosphorylated H2AX (Stiff et al., 2004; I. M. Ward & Chen, 2001).

In contrast, ATM inhibition did not have the same effect on γH2AX and 53BP1 foci levels in the normal tissue. In fact, it had the opposite effect on γH2AX at 24 h post-irradiation. Decreased levels of γH2AX in the normal tissue could mean that – in contrast to tumours – other PPIKs were not activated and radiation-induced damaged was not repaired, which could potentially explain the toxicity observed in the combination treatment. Surprisingly, others have shown that in the lung of $ATM^{-/+}$ heterozygous mice, the number of γH2AX foci per cell increased at 24 h post-irradiation compared to $ATM^{+/+}$ wild-type mice (Rübe et al., 2010b). This shows that the effect of transient inhibition of ATM in the context of radiation-responses cannot be directly extrapolated from models of constitutive ATM function absence, such as cells from A-T patients. Surprisingly, the number of cells positive for 53BP1 foci in the normal tissue was not affected by ATM inhibition. The ATM-independent roles of 53BP1 are yet to be understood but have already been reported by others (Rybanska-Spaeder et al., 2013).

In chapter 5, we hypothesised that chronic lung inflammation and fibrosis could be due to persistent DNA breaks in the heterochromatin, which are mainly repaired by ATM. Importantly, we did not observe differences between the number of γH2AX and 53BP1 foci positive cells in the normal tissue when comparing IR alone and IR + ATMi during the first 7 days post-irradiation, even though persistent breaks were present in both groups. More experiments should be conducted to determine if there is a difference in the repair of those persistent breaks after 7 days between IR alone and IR + ATMi.

In addition, DDR-independent roles of ATM could be responsible for the induction of late term toxicity. Especially the role of ATM in the oxidative stress response should be further evaluated in the context of radiation as others have shown that lung damage is related to the induction of oxidative stress (Andersson-Sjöland, Karlsson, & Rydell-Törmänen, 2016; Sprung et al., 2015; Y. Zhang, Zhang, Rabbani, Jackson, & Vujaskovic, 2012). Interestingly, a recent report showed that ATM inhibition protected neuronal cells from oxidative stress, suggesting that, due to the various roles of ATM, its inhibition may lead to opposing effects (Chwastek, Jantas, & Lasoń, 2017). Also, the effect of ATM absence/loss of activity may affect different cell types differently, which shows the need for further understanding of the roles of different lung cell types in the development of radiation-induced damage (Moding et al., 2014). Another important consideration is the genetic differences between C57BL6 and A/J mice, as this might help understand the differences in the late effects observed. For instance, A/J mice have a mutation in the dysferlin gene, which could be associated with the vascular damage observed after IR + ATMi treatment in this strain but not in C57BL6 mice.

Our data showed that there is a potential for the use of ATM inhibitors in combination with radiation to treat lung tumours, but this combination treatment has also the potential to increase normal tissue damage and therefore caution should be exercised when tests reach the clinic. We showed that normal tissue effects of ATMi in combination with radiation were observed in two different preclinical models of radiation-induced lung damage, C57BL/6J and A/J mice. Further experiments should be performed to evaluate the dose response of this combination to potentially identify a treatment schedule that maintains antitumour effect but does not induce normal tissue toxicity. Also, more work should be performed to identify the mechanisms behind the effects observed, for instance, investigating other DDR downstream targets of ATM and/or

other ATM-dependent pathways. Finally, we demonstrated that the therapeutic model evaluated in this work is sensitive to increases in normal tissue damage induced by thoracic radiation and is also useful for the assessment of the tumour radiosensitising effects of new lung cancer therapies.

8. General discussion and conclusion

In this work, we have characterised the initial induction of DNA damage and subsequent repair, as well as the systemic and local induction of inflammation by thoracic irradiation in vivo using mouse models. We also showed that modulation of these initial processes can affect the late lung damage induced by thoracic irradiation. Finally, we have established a novel mouse model to simultaneously evaluate normal and tumour lung tissue responses to radiation. In this section, we highlight the future work that should be undertaken to further understand the mentioned tissue responses.

To the best of our knowledge, we have shown for the first time in vivo that the recognition of DNA damage happens within minutes after irradiation in the lung tissue. Most of the DNA damage repair happens within the first 24 h post-irradiation; nevertheless, a small but potentially important fraction of cells have unrepaired DNA DSBs at 14 days post-irradiation (or at least repair machinery organised in foci). We hypothesised that this persistent damage signal could be responsible for the development of chronic inflammation, culminating in late lung damage. Another interesting finding is that the pro-inflammatory response induced by thoracic radiation can be detected systemically, suggesting the triggering of a potent amplification cascade. This might explain the difficulties of finding a therapy to stop the side effects of thoracic radiation by targeting only one component of this complex inflammatory network. In addition, it is important to note the steep dose-response curve for onset of pulmonary fibrosis when comparing different fractionation schedules of radiation. This finding suggests that even relatively small modulation of these responses may be effective in decreasing the incidence of side effects.

In addition, we showed that the DDR and early inflammatory responses as well as late lung damage were lower in MPO knock-out mice compared with MPO wild-type mice. The observed effect on lung damage was relatively small and dose dependent, but could potentially be increased if used in combination with other mitigating therapies, such as interleukin inhibitors targeting other components of the immune system than neutrophils. Nonetheless, more work is needed to understand the mechanisms behind the observed effects seen in MPO knock-out mice. MPO inhibitors have entered clinical development and may be good tools to further test the potential of this approach in order to reduce the side effects of thoracic radiation in preclinical models (Lazarevic-Pasti, Leskovac, & Vasic, 2015).

We have also evaluated another strategy to potentially increase the therapeutic index of thoracic radiotherapy: the combination with DDR modulators. Our data showed that a range of DDR inhibitors markedly radiosensitised subcutaneous tumour xenografts, but induced differential normal tissue responses when combined with thoracic radiation. We believe that these findings highlight the importance of evaluating normal tissue responses to novel therapies combined with radiation, before proceeding into clinical studies. For instance, we observed different side effects with a PARP inhibitor and with an ATM inhibitor in combination with radiation, potentially illustrating that different normal tissues have different dependencies on specific biological pathways. Data from ongoing clinical trials will allow for validation of the effects that we observed in mouse models, but based on our data we would predict that PARP inhibitors will likely potentiate radiation-induced oesophagitis. In addition, future work should be done looking at other schedules of radiation combinations, as altering the timing of target inhibition and radiation treatment may have profoundly different effects.

Several therapeutic approaches have been tested to reduce the onset of radiation-induced lung damage, including but not restricted to antioxidants, statins and modulators of cytokines, growth factors and metalloproteinases [reviewed by (Graves, Siddiqui, Anscher, & Movsas, 2010)]. Numerous reviews have been written on radiation-induced lung injury and despite the invaluable increase in mechanistic understanding of the pathogenesis of the disease, still no effective therapy is available to patients.

To date, two main approaches have been investigated to manage radiation-induced lung toxicity: ROS scavengers and anti-inflammatory agents. The aim of using ROS scavengers is to target water molecules oxidised by radiation leading to a decrease in the oxidative damage caused by them. Therefore, this approach does not affect the damage directly caused by radiation through the interaction between high energy photons (in the case of X-rays) and biomolecules such as the DNA. The second approach, the anti-inflammatory agents, aims to target the downstream immune cascade that results as a response to the initial damage induced by radiation. As reviewed by many, the inflammatory cascade is a particularly complex network involving different cell types and cytokines. We propose that targeting the downstream inflammatory response may not be an efficient approach as the signal is amplified, and therefore research focusing on decreasing the initial damage would be more effective than targeting the downstream inflammatory cascade.

As discussed previously, the initial damage caused by radiation can be divided into direct and indirect, accounting for 30-40% and 60-70% of damage respectively (Nikjoo, O'Neill, Wilson, & Goodhead, 2001; Ward, 1988). The direct damage is caused by direct oxidation of biomolecules by the ionising photon; in contrast, the indirect damage is caused by ROS generated by water molecules ionised by radiation. The direct damage caused to the DNA is

more complex and difficult to repair due to the clustering of damage along the track of radiation (Lomax, Folkes, & O'Neill, 2013). Due to its high reactivity, ROS interact with molecules in close proximity and generate isolated and generally simpler lesions. In addition, as shown by others, the long lasting DNA DSBs in the normal tissue may localise to the heterochromatin (Goodarzi et al., 2008). We speculate that due to the condensed structure of heterochromatin, DNA DSBs occurring in this part of the genome are mostly formed by direct interaction of radiation with DNA, therefore the use of ROS scavengers could not prevent them. Facilitating the repair of this specific type of damage, for instance, by administration of agents such as histone deacetylases (HDAC) inhibitors that promote the relaxation of chromatin during the period of post-irradiation repair, could be an interesting strategy to investigate the mitigation of radiation-induced lung damage (Figure 8.1).

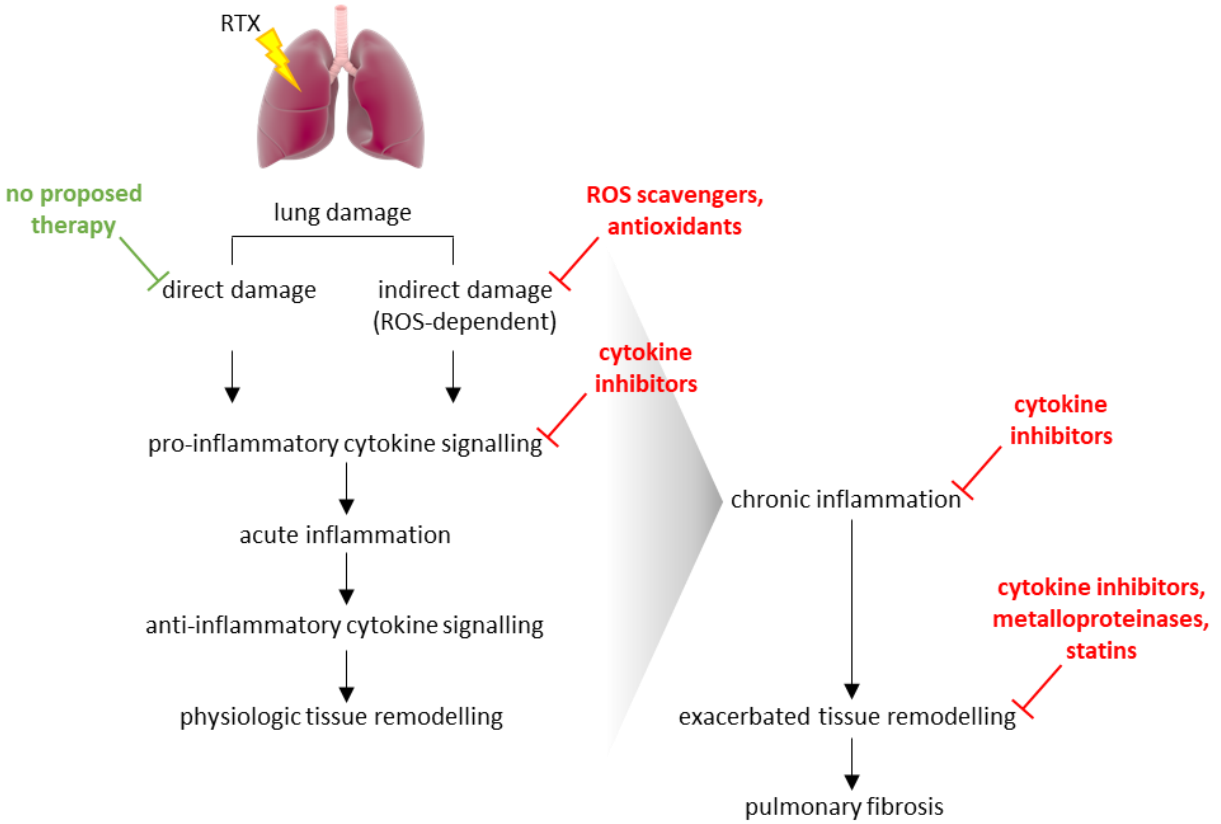


Figure 8.1. Therapeutic strategies for treating radiation-induced pulmonary fibrosis. In red, current approaches that have failed to show efficacy. In green, the initial step of the disease, where we propose should be the target of study for new therapies.

In addition, we believe that developing a therapy that is radiosensitising to the tumour tissue but not to normal tissue will require an understanding of the responses of both tissue types. Therefore, we established a novel mouse model for the study of the therapeutic index of thoracic radiation, described in chapter 6. The model was developed in the A/J strain, which is known to be susceptible to urethane-induced lung tumours and radiation-induced pneumonitis. To our knowledge, we were the first to show that this strain is also susceptible to radiation-induced fibrosis and, importantly, that the timing of lung tumour growth and development of pneumonitis and fibrosis were compatible and therefore allowed the evaluation of both normal and tumour tissue responses simultaneously. Of note, the A/J strain is less sensitive to fibrosis

than the C57BL/6J strain, and future work should be performed to understand the mechanisms behind those differences, not only in the lung tissue but also in other organs at risk, such as the oesophagus. Also, another potentially equivalent model, such as tumour bearing fibrosis-prone C57BL/6J mice, could be developed and then compared to our proposed model so the most clinically relevant model could be established. Another important aspect of the A/J model that needs further investigation is a more detailed understanding of the response of urethane-induced tumours to radiation treatment. For example, an understanding of the immune components and immune-responsiveness of A/J lung tumours, as well as the impact of Kras and other mutations is still required. Also, the response of these tumour to chemoradiotherapy is unknown and should be characterised.

Importantly, the hypothesis behind the treatment rationale proposed in Figure 8.1 suggests that the use of DDR modulators must be carefully studied before being translated to the clinic, especially for targets involved in the repair of heterochromatin (such as ATM). As indicated by data form our A/J model, the repair mechanisms used by normal lung tissue and tumour lung tissue in response to radiation may not be entirely overlapping, therefore there is an opportunity to find appropriate targets for therapy that affects tumour tissue but spares normal lung tissue. In that sense, having a model to study both responses simultaneously such as the A/J model is extremely necessary. Also, the improvement of radiation delivery in order to avoid irradiation of the normal tissue should be encouraged.

Finally, our study with ATMi in the A/J model resulted in some interesting findings that could help opening new strategies for mitigation of radiation-induced lung damage. The combination treatment increased tumour killing and lung toxicity, therefore future work should be done to explore a range of doses (radiation and/or inhibitor) to find an ideal treatment regimen that

would sensitise the tumour but not damage the normal tissue. Also, evaluation of early responses of normal and tumour tissue to radiation in combination with other DDR modulators should be further performed potentially to understand the late effects observed. In conclusion, we believe that finding radiation-induced pathways that differ in normal and tumour tissues is paramount and should be undertaken by future work to develop original strategies to increase the therapeutic index of thoracic radiotherapy.

9. References

Abid, S. H., Malhotra, V., & Perry, M. C. (2001). Radiation-induced and chemotherapy-induced pulmonary injury. *Current Opinion in Oncology*, *13*, 242–248. https://doi.org/10.1097/00001622-200107000-00006

Adamson, I., & Bowden, D. (1974). The type 2 cell as progenitor of alveolar epithelial regeneration. A cytodynamic study in mice after exposure to oxygen. *Lab Invest*, *30*, 35–42. Retrieved from http://ci.nii.ac.jp/naid/10018730507/

Almeida, C., Nagarajan, D., Tian, J., Leal, S. W., Wheeler, K., Munley, M., … Simon, R. (2013). The Role of Alveolar Epithelium in Radiation-Induced Lung Injury. *PLoS ONE*, *8*(1), e53628. https://doi.org/10.1371/journal.pone.0053628

Altmann, C., Andres-Hernando, A., McMahan, R. H., Ahuja, N., He, Z., Rivard, C. J., … Faubel, S. (2012, February). Macrophages mediate lung inflammation in a mouse model of ischemic acute kidney injury. *American Journal of Physiology - Renal Physiology*. Bethesda, MD. https://doi.org/10.1152/ajprenal.00559.2010

Andersson-Sjöland, A., Karlsson, J. C., & Rydell-Törmänen, K. (2016). ROS-induced endothelial stress contributes to pulmonary fibrosis through pericytes and Wnt signaling. *Laboratory Investigation*, *96100*, 206–217. https://doi.org/10.1038/labinvest.2015.100

Antonia, S. J., Villegas, A., Daniel, D., Vicente, D., Murakami, S., Hui, R., … Ozguroglu, M. (2017). Durvalumab after Chemoradiotherapy in Stage III Non-Small-Cell Lung Cancer. *The New England Journal of Medicine*. https://doi.org/10.1056/NEJMoa1709937

Ao, X., Zhao, L., Davis, M. A., Lubman, D. M., Lawrence, T. S., & Kong, F.-M. (2009). Radiation produces differential changes in cytokine profiles in radiation lung fibrosis sensitive and resistant mice. *Journal of Hematology & Oncology*, *2*, 6. https://doi.org/10.1186/1756-8722-2-6

Aylon, Y., Liefshitz, B., & Kupiec, M. (2004). The CDK regulates repair of double-strand breaks by homologous recombination during the cell cycle. *The EMBO Journal*, *23*(24), 4868–4875. https://doi.org/10.1038/sj.emboj.7600469

B. Marks, M. Fan, R. Clough, M. Mun, L. (2000). Radiation-induced pulmonary injury: symptomatic versus subclinical endpoints. *International Journal of Radiation Biology*, *76*(4), 469–475. https://doi.org/10.1080/095530000138466

Babior, B. M. (2000). Phagocytes and oxidative stress. *The American Journal of Medicine*, *109*(1), 33–44. https://doi.org/10.1016/S0002-9343(00)00481-2

Baker, S., Dahele, M., Lagerwaard, F. J., & Senan, S. (2016). A critical review of recent developments in radiotherapy for non-small cell lung cancer. *Radiation Oncology*, *11*(1), 115. https://doi.org/10.1186/s13014-016-0693-8

Baker, S., & Fairchild, A. (2016). Radiation-induced esophagitis in lung cancer. *Lung Cancer (Auckland, N.Z.)*, *7*, 119–127. https://doi.org/10.2147/LCTT.S96443

Bakkenist, C. J., & Kastan, M. B. (2003). DNA damage activates ATM through intermolecular autophosphorylation and dimer dissociation. *Nature*, *421*(6922), 499–506. https://doi.org/10.1038/nature01368

Banáth, J. P., MacPhail, S. H., & Olive, P. L. (2004). Radiation Sensitivity, H2AX Phosphorylation, and Kinetics of Repair of DNA Strand Breaks in Irradiated Cervical Cancer Cell Lines. *Cancer Research*, *64*(19). Retrieved from http://cancerres.aacrjournals.org/content/64/19/7144.short

Barlic, J., Andrews, J. D., Kelvin, A. A., Bosinger, S. E., DeVries, M. E., Xu, L., … Kelvin, D. J. (2000). Regulation

of tyrosine kinase activation and granule release through beta-arrestin by CXCRI. *Nature Immunology*, *1*(3), 227–233. https://doi.org/10.1038/79767

Barlow, C., Hirotsune, S., Paylor, R., Liyanage, M., Eckhaus, M., Collins, F., … Wynshaw-Boris, A. (1996). Atm-Deficient Mice: A Paradigm of Ataxia Telangiectasia. *Cell*, *86*(1), 159–171. https://doi.org/10.1016/S0092-8674(00)80086-0

Barnett, G. C., West, C. M. L., Dunning, A. M., Elliott, R. M., Coles, C. E., Pharoah, P. D. P., & Burnet, N. G. (2009). Normal tissue reactions to radiotherapy: towards tailoring treatment dose by genotype. *Nature Reviews. Cancer*, *9*(2), 134–42. https://doi.org/10.1038/nrc2587

Barriger, R. B., Forquer, J. A., Brabham, J. G., Andolino, D. L., Shapiro, R. H., Henderson, M. A., … Fakiris, A. J. (2012). A dose-volume analysis of radiation pneumonitis in non-small cell lung cancer patients treated with stereotactic body radiation therapy. *International Journal of Radiation Oncology, Biology, Physics*, *82*(1), 457–462. https://doi.org/10.1016/j.ijrobp.2010.08.056

Bea, S., Valdes-Mas, R., Navarro, A., Salaverria, I., Martin-Garcia, D., Jares, P., … Campo, E. (2013). Landscape of somatic mutations and clonal evolution in mantle cell lymphoma. *Proceedings of the National Academy of Sciences of the United States of America*, *110*(45), 18250–18255. https://doi.org/10.1073/pnas.1314608110

Begg, A. C., Stewart, F. A., & Vens, C. (2011). Strategies to improve radiotherapy with targeted drugs. *Nature Reviews. Cancer*, *11*(4), 239–253. https://doi.org/10.1038/nrc3007

Bentwood, B. J., & Henson, P. M. (1980). The sequential release of granule constitutents from human neutrophils. *The Journal of Immunology*, *124*(2). Retrieved from http://www.jimmunol.org/content/124/2/855.short

Bentzen, S. M. (2006). Preventing or reducing late side effects of radiation therapy: radiobiology meets molecular pathology. *Nature Reviews. Cancer*, *6*(9), 702–713. https://doi.org/10.1038/nrc1950

Beucher, A., Birraux, J., Tchouandong, L., Barton, O., Shibata, A., Conrad, S., … Löbrich, M. (2009, November). ATM and Artemis promote homologous recombination of radiation-induced DNA double-strand breaks in G2. *The EMBO Journal*. https://doi.org/10.1038/emboj.2009.276

Biddlestone-Thorpe, L., Sajjad, M., Rosenberg, E., Beckta, J. M., Valerie, N. C. K., Tokarz, M., … Valerie, K. (2013). ATM Kinase Inhibition Preferentially Sensitizes p53-Mutant Glioma to Ionizing Radiation. *Clinical Cancer Research*, *19*(12). Retrieved from http://clincancerres.aacrjournals.org/content/19/12/3189.short

Biehs, R., Steinlage, M., Barton, O., Juhász, S., Künzel, J., Spies, J., … Löbrich, M. (2017). DNA Double-Strand Break Resection Occurs during Non-homologous End Joining in G1 but Is Distinct from Resection during Homologous Recombination. *Molecular Cell*, *65*(4), 671–684.e5. https://doi.org/10.1016/j.molcel.2016.12.016

Bolderston, A., Lloyd, N. S., Wong, R. K. S., Holden, L., Robb-Blenderman, L., & Care, and the S. C. G. G. of C. C. O. P. in E. (2006). The prevention and management of acute skin reactions related to radiation therapy: a systematic review and practice guideline. *Supportive Care in Cancer*, *14*(8), 802–817. https://doi.org/10.1007/s00520-006-0063-4

Bouwman, P., Aly, A., Escandell, J. M., Pieterse, M., Bartkova, J., van der Gulden, H., … Jonkers, J. (2010). 53BP1 loss rescues BRCA1 deficiency and is associated with triple-negative and BRCA-mutated breast cancers. *Nat Struct Mol Biol*, *17*(6), 688–695. Retrieved from http://dx.doi.org/10.1038/nsmb.1831

Brennan, M. L., Anderson, M. M., Shih, D. M., Qu, X. D., Wang, X., Mehta, A. C., … Lusis, A. J. (2001). Increased atherosclerosis in myeloperoxidase-deficient mice. *The Journal of Clinical Investigation*, *107*(4), 419–30. https://doi.org/10.1172/JCI8797

Bronsart, E., Dureau, S., Xu, H. P., Bazire, L., Chilles, A., Costa, E., … Kirova, Y. M. (2017). Whole breast radiotherapy in the lateral isocentric lateral decubitus position: Long-term efficacy and toxicity results.

Radiotherapy and Oncology, *124*(2), 214–219. https://doi.org/10.1016/j.radonc.2017.07.001

Brown, E. J., & Baltimore, D. (2000). ATR disruption leads to chromosomal fragmentation and early embryonic lethality. *Genes & Development*, *14*(4), 397–402. Retrieved from http://www.ncbi.nlm.nih.gov/pubmed/10691732

Bryant, H. E., Petermann, E., Schultz, N., Jemth, A., Loseva, O., Issaeva, N., … Helleday, T. (2009). PARP is activated at stalled forks to mediate Mre11-dependent replication restart and recombination. *The EMBO Journal*, *28*(17), 2601–2615.

Burma, S., Chen, B. P., Murphy, M., Kurimasa, A., & Chen, D. J. (2001). ATM phosphorylates histone H2AX in response to DNA double-strand breaks. *The Journal of Biological Chemistry*, *276*(45), 42462–7. https://doi.org/10.1074/jbc.C100466200

Caamano, J., Ruggeri, B., Momiki, S., Sickler, A., Zhang, S. Y., & Klein-Szanto, A. J. (1991). Detection of p53 in primary lung tumors and nonsmall cell lung carcinoma cell lines. *The American Journal of Pathology*, *139*(4), 839–45. Retrieved from http://www.ncbi.nlm.nih.gov/pubmed/1656762

Cadet, J., Douki, T., & Ravanat, J.-L. (2008). Oxidatively Generated Damage to the Guanine Moiety of DNA: Mechanistic Aspects and Formation in Cells. *Accounts of Chemical Research*, *41*(8), 1075–1083. https://doi.org/10.1021/ar700245e

Calabrese, C. R., Almassy, R., Barton, S., Batey, M. A., Calvert, A. H., Canan-Koch, S., … Curtin, N. J. (2004). Anticancer Chemosensitization and Radiosensitization by the Novel Poly(ADP-ribose) Polymerase-1 Inhibitor AG14361. *JNCI Journal of the National Cancer Institute*, *96*(1), 56–67. https://doi.org/10.1093/jnci/djh005

Cancer Research UK. (2014a). Incidence by stage at diagnosis. Retrieved September 20, 2017, from http://www.cancerresearchuk.org/health-professional/cancer-statistics/statistics-by-cancer-type/lung-cancer/incidence#heading-Three

Cancer Research UK. (2014b). Lung Cancer Survival by stage at diagnosis. Retrieved September 20, 2017, from http://www.cancerresearchuk.org/health-professional/cancer-statistics/statistics-by-cancer-type/lung-cancer/survival#heading-Three

Cancer Research UK. (2014c). One year survival for lung cancer. Retrieved August 14, 2017, from http://www.cancerresearchuk.org/health-professional/cancer-statistics/statistics-by-cancer-type/lung-cancer/survival#heading-Zero

Cappuccini, F., Eldh, T., Bruder, D., Gereke, M., Jastrow, H., Schulze-Osthoff, K., … Jendrossek, V. (2011). New insights into the molecular pathology of radiation-induced pneumopathy. *Radiotherapy and Oncology*, *101*(1), 86–92. https://doi.org/10.1016/j.radonc.2011.05.064

Carver, J. R., Shapiro, C. L., Ng, A., Jacobs, L., Schwartz, C., Virgo, K. S., … ASCO Cancer Survivorship Expert Panel. (2007). American Society of Clinical Oncology clinical evidence review on the ongoing care of adult cancer survivors: cardiac and pulmonary late effects. *Journal of Clinical Oncology : Official Journal of the American Society of Clinical Oncology*, *25*(25), 3991–4008. https://doi.org/10.1200/JCO.2007.10.9777

Cauwe, B., Martens, E., Proost, P., & Opdenakker, G. (2009). Multidimensional degradomics identifies systemic autoantigens and intracellular matrix proteins as novel gelatinase B/MMP-9 substrates. *Integrative Biology*, *1*(5–6), 404. https://doi.org/10.1039/b904701h

Cha, H., Lowe, J. M., Li, H., Lee, J.-S., Belova, G. I., Bulavin, D. V., & Fornace, A. J. (2010). Wip1 Directly Dephosphorylates γ-H2AX and Attenuates the DNA Damage Response. *Cancer Research*, *70*(10). Retrieved from http://cancerres.aacrjournals.org/content/70/10/4112.short

Chatterjee, P., Choudhary, G. S., Sharma, A., Singh, K., Heston, W. D., Ciezki, J., … Almasan, A. (2013). PARP Inhibition Sensitizes to Low Dose-Rate Radiation TMPRSS2-ERG Fusion Gene-Expressing and PTEN-

Deficient Prostate Cancer Cells. *PLoS ONE*, *8*(4), e60408. https://doi.org/10.1371/journal.pone.0060408

Chehab, N. H., Malikzay, A., Appel, M., & Halazonetis, T. D. (2000). Chk2/hCds1 functions as a DNA damage checkpoint in G(1) by stabilizing p53. *Genes & Development*, *14*(3), 278–88. https://doi.org/10.1101/GAD.14.3.278

Chen, B., Johanson, L., Wiest, J. S., Anderson, M. W., & You, M. (1994). The second intron of the K-ras gene contains regulatory elements associated with mouse lung tumor susceptibility. *Proceedings of the National Academy of Sciences of the United States of America*, *91*(4), 1589–93. https://doi.org/10.1073/PNAS.91.4.1589

Chen, G. Y., & Nuñez, G. (2010). Sterile inflammation: sensing and reacting to damage. *Nature Reviews. Immunology*, *10*(12), 826–37. https://doi.org/10.1038/nri2873

Chen, J., Wang, Y., Mei, Z., Zhang, S., Yang, J., Li, X., … Xie, C. (2016). Radiation-induced lung fibrosis in a tumor-bearing mouse model is associated with enhanced Type-2 immunity. *Journal of Radiation Research*, *57*(2), 133–141. https://doi.org/10.1093/jrr/rrv077

Cheung, P., Faria, S., Ahmed, S., Chabot, P., Greenland, J., Kurien, E., … O'Callaghan, C. (2014). Phase II Study of Accelerated Hypofractionated Three-Dimensional Conformal Radiotherapy for Stage T1-3 N0 M0 Non-Small Cell Lung Cancer: NCIC CTG BR.25. *JNCI Journal of the National Cancer Institute*, *106*(8), dju164-dju164. https://doi.org/10.1093/jnci/dju164

Chinnadurai, M., Chidambaram, S., Ganesan, V., Baraneedharan, U., Sundaram, L., Paul, S. F. D., & Venkatachalam, P. (2011). Bleomycin, neocarzinostatin and ionising radiation-induced bystander effects in normal diploid human lung fibroblasts, bone marrow mesenchymal stem cells, lung adenocarcinoma cells and peripheral blood lymphocytes. *International Journal of Radiation Biology*, *87*(7), 673–682. https://doi.org/10.3109/09553002.2010.549536

Choi, D.-K., Pennathur, S., Perier, C., Tieu, K., Teismann, P., Wu, D.-C., … Przedborski, S. (2005). Ablation of the Inflammatory Enzyme Myeloperoxidase Mitigates Features of Parkinson's Disease in Mice. *Journal of Neuroscience*, *25*(28). Retrieved from http://www.jneurosci.org/content/25/28/6594.short

Choi, M., Kipps, T., & Kurzrock, R. (2016). ATM Mutations in Cancer: Therapeutic Implications. *Molecular Cancer Therapeutics*, *15*(8), 1781–1791. https://doi.org/10.1158/1535-7163.MCT-15-0945

Chotirmall, S. H., Low, T. B., Murphy, P., & O'Neill, S. J. (2008). Delayed radiotherapy-related effusions: Malignant or not malignant, that is the question? *Respirology*, *13*(5), 754–754. https://doi.org/10.1111/j.1440-1843.2008.01316.x

Christodoulou, M., Bayman, N., McCloskey, P., Rowbottom, C., & Faivre-Finn, C. (2014). New radiotherapy approaches in locally advanced non-small cell lung cancer. *European Journal of Cancer (Oxford, England : 1990)*, *50*(3), 525–534. https://doi.org/10.1016/j.ejca.2013.11.027

Chung, S. I., Horton, J. A., Ramalingam, T. R., White, A. O., Chung, E. J., Hudak, K. E., … Citrin, D. E. (2016). IL-13 is a therapeutic target in radiation lung injury. *Scientific Reports*, *6*, 39714. https://doi.org/10.1038/srep39714

Chwastek, J., Jantas, D., & Lasoń, W. (2017). The ATM kinase inhibitor KU-55933 provides neuroprotection against hydrogen peroxide-induced cell damage via a γH2AX/p-p53/caspase-3-independent mechanism: Inhibition of calpain and cathepsin D. *The International Journal of Biochemistry & Cell Biology*, *87*, 38–53. https://doi.org/10.1016/j.biocel.2017.03.015

Cimprich, K. A., & Cortez, D. (2008). ATR: an essential regulator of genome integrity. *Nature Reviews. Molecular Cell Biology*, *9*(8), 616–27. https://doi.org/10.1038/nrm2450

Citrin, D. E., Shankavaram, U., Horton, J. A., Shield, W., Zhao, S., Asano, H., … Chung, E. J. (2013). Role of Type II Pneumocyte Senescence in Radiation-Induced Lung Fibrosis. *JNCI: Journal of the National Cancer*

Institute, *105*(19), 1474–1484. https://doi.org/10.1093/jnci/djt212

Clouaire, T., Marnef, A., & Legube, G. (2017). Taming Tricky DSBs: ATM on duty. *DNA Repair*, *56*, 84–91. https://doi.org/10.1016/j.dnarep.2017.06.010

Collins, J. F., Johanson, W. G., McCullough, B., Jones, M. A., & Waugh, H. J. (1978). Effects of compensatory lung growth in irradiation-induced regional pulmonary fibrosis in the baboon. *The American Review of Respiratory Disease*, *117*(6), 1079–89. https://doi.org/10.1164/arrd.1978.117.6.1079

Condliffe, A. M., Kitchen, E., & Chilvers, E. R. (1998). Neutrophil Priming: Pathophysiological Consequences and Underlying Mechanisms. *Clinical Science*, *94*(5). Retrieved from http://www.clinsci.org/content/94/5/461

Coppé, J.-P., Desprez, P.-Y., Krtolica, A., & Campisi, J. (2010). The Senescence-Associated Secretory Phenotype: The Dark Side of Tumor Suppression. *Annual Review of Pathology: Mechanisms of Disease*, *5*(1), 99–118. https://doi.org/10.1146/annurev-pathol-121808-102144

Cortez, D., Guntuku, S., Qin, J., & Elledge, S. J. (2001). ATR and ATRIP: Partners in Checkpoint Signaling. *Science*, *294*(5547). Retrieved from http://science.sciencemag.org/content/294/5547/1713

Cui, Y., Wilder, J., Rietz, C., Gigliotti, A., Tang, X., Shi, Y., … El-Chemaly, S. (2014). Radiation-Induced Impairment in Lung Lymphatic Vasculature. *Lymphatic Research and Biology*, *12*(4), 238–250. https://doi.org/10.1089/lrb.2014.0012

Dabjan, M. B., Buck, C. M., Jackson, I. L., Vujaskovic, Z., Marples, B., & Down, J. D. (2016). A survey of changing trends in modelling radiation lung injury in mice: bringing out the good, the bad, and the uncertain. *Laboratory Investigation*, *96*(9), 936–949. https://doi.org/10.1038/labinvest.2016.76

Dahele, M., Palma, D., Lagerwaard, F., Slotman, B., & Senan, S. (2011). Radiological Changes After Stereotactic Radiotherapy for Stage I Lung Cancer. *Journal of Thoracic Oncology*, *6*(7), 1221–1228. https://doi.org/10.1097/JTO.0b013e318219aac5

Dahlgren, C., & Karlsson, A. (1999). Respiratory burst in human neutrophils. *Journal of Immunological Methods*, *232*(1–2), 3–14. https://doi.org/10.1016/S0022-1759(99)00146-5

Daley, J. M., & Sung, P. (2014). 53BP1, BRCA1, and the choice between recombination and end joining at DNA double-strand breaks. *Molecular and Cellular Biology*, *34*(8), 1380–8. https://doi.org/10.1128/MCB.01639-13

Daniel, J. A., Pellegrini, M., Lee, B.-S., Guo, Z., Filsuf, D., Belkina, N. V., … Nussenzweig, A. (2012). Loss of ATM kinase activity leads to embryonic lethality in mice. *The Journal of Cell Biology*, *198*(3). Retrieved from http://jcb.rupress.org/content/198/3/295.short

de Klein, A., Muijtjens, M., van Os, R., Verhoeven, Y., Smit, B., Carr, A. M., … Hoeijmakers, J. H. J. (2000). Targeted disruption of the cell-cycle checkpoint gene ATR leads to early embryonic lethality in mice. *Current Biology*, *10*(8), 479–482. https://doi.org/10.1016/S0960-9822(00)00447-4

Degorce, S. L., Barlaam, B., Cadogan, E., Dishington, A., Ducray, R., Glossop, S. C., … Thomason, A. G. (2016). Discovery of Novel 3-Quinoline Carboxamides as Potent, Selective, and Orally Bioavailable Inhibitors of Ataxia Telangiectasia Mutated (ATM) Kinase. *Journal of Medicinal Chemistry*, *59*(13), 6281–6292. https://doi.org/10.1021/acs.jmedchem.6b00519

Delgado-SanMartin, J. A., Hare, J. I., Davies, E. J., & Yates, J. W. T. (2017). Multiscalar cellular automaton simulates in-vivo tumour-stroma patterns calibrated from in-vitro assay data. *BMC Medical Informatics and Decision Making*, *17*(1), 70. https://doi.org/10.1186/s12911-017-0461-1

Demirel, C., Kilciksiz, S. C., Gurgul, S., Erdal, N., Yigit, S., Tamer, L., & Ayaz, L. (2016). Inhibition of Radiation-Induced Oxidative Damage in the Lung Tissue: May Acetylsalicylic Acid Have a Positive Role?

Inflammation, *39*(1), 158–165. https://doi.org/10.1007/s10753-015-0234-x

Deng, G., Liang, N., Xie, J., Luo, H., Qiao, L., Zhang, J., … Zhang, J. (2017). Pulmonary toxicity generated from radiotherapeutic treatment of thoracic malignancies (Review). *Oncology Letters*. https://doi.org/10.3892/ol.2017.6268

Devereux, T. R., Wiseman, R. W., Kaplan, N., Garren, S., Foley, J. F., White, C. M., … Anderson, M. W. (1994). Assignment of a locus for mouse lung tumor susceptibility to proximal Chromosome 19. *Mammalian Genome*, *5*(12), 749–755. https://doi.org/10.1007/BF00292007

Devine, A., & Marignol, L. (2016). Potential of Amifostine for Chemoradiotherapy and Radiotherapy-associated Toxicity Reduction in Advanced NSCLC: A Meta-Analysis. *Anticancer Research*, *36*(1), 5–12. Retrieved from http://www.ncbi.nlm.nih.gov/pubmed/26722022

Di Maggio, F., Minafra, L., Forte, G., Cammarata, F., Lio, D., Messa, C., … Bravatà, V. (2015). Portrait of inflammatory response to ionizing radiation treatment. *Journal of Inflammation*, *12*(1), 14. https://doi.org/10.1186/s12950-015-0058-3

Dillon, M. T., Barker, H. E., Pedersen, M., Hafsi, H., Bhide, S. A., Newbold, K. L., … Harrington, K. J. (2017). Radiosensitization by the ATR Inhibitor AZD6738 through Generation of Acentric Micronuclei. *Molecular Cancer Therapeutics*, *16*(1). Retrieved from http://mct.aacrjournals.org/content/16/1/25

Ding, N.-H., Li, J. J., San, L.-Q., & Sun, L.-Q. (2014). Molecular Mechanisms and Treatment of Radiation-Induced Lung Fibrosis, *14*(11), 1347–1356. Retrieved from http://www.ingentaconnect.com/content/ben/cdt/2013/00000014/00000011/art00013

Down, J. D., Laurent, G. J., McAnulty, R. J., & Steel, G. G. (1984). Oxygen-dependent Protection of Radiation Lung Damage in Mice by WR 2721. *International Journal of Radiation Biology and Related Studies in Physics, Chemistry and Medicine*, *46*(5), 597–607. https://doi.org/10.1080/09553008414551791

Dungey, F. A., Löser, D. A., & Chalmers, A. J. (2008). Replication-Dependent Radiosensitization of Human Glioma Cells by Inhibition of Poly(ADP-Ribose) Polymerase: Mechanisms and Therapeutic Potential. *International Journal of Radiation Oncology*Biology*Physics*, *72*(4), 1188–1197. https://doi.org/10.1016/j.ijrobp.2008.07.031

Dunne, V., Ghita, M., Small, D. M., Coffey, C. B. M., Weldon, S., Taggart, C. C., … Butterworth, K. T. (2017). Inhibition of ataxia telangiectasia related-3 (ATR) improves therapeutic index in preclinical models of non-small cell lung cancer (NSCLC) radiotherapy. *Radiotherapy and Oncology*. https://doi.org/10.1016/j.radonc.2017.06.025

DuPage, M., Dooley, A. L., & Jacks, T. (2009). Conditional mouse lung cancer models using adenoviral or lentiviral delivery of Cre recombinase. *Nature Protocols*, *4*(8), 1064–1072. https://doi.org/10.1038/nprot.2009.95

Edge, S., Byrd, D., & Compton, C. (2010). *AJCC Cancer Staging Handbook* (7th ed.). New York: Springer.

Escribano-Díaz, C., Orthwein, A., Fradet-Turcotte, A., Xing, M., Young, J. T. F., Tkáč, J., … Durocher, D. (2013). A Cell Cycle-Dependent Regulatory Circuit Composed of 53BP1-RIF1 and BRCA1-CtIP Controls DNA Repair Pathway Choice. *Molecular Cell*, *49*(5), 872–883. https://doi.org/10.1016/j.molcel.2013.01.001

Falck, J., Mailand, N., Syljuasen, R. G., Bartek, J., & Lukas, J. (2001). The ATM-Chk2-Cdc25A checkpoint pathway guards against radioresistant DNA synthesis. *Nature*, *410*(6830), 842.

Feng, L., Li, N., Li, Y., Wang, J., Gao, M., Wang, W., & Chen, J. (2015). Cell cycle-dependent inhibition of 53BP1 signaling by BRCA1. *Cell Discovery*, *1*, 15019. https://doi.org/10.1038/celldisc.2015.19

Fenwick, J. D., Nahum, A. E., Malik, Z. I., Eswar, C. V, Hatton, M. Q., Laurence, V. M., … Landau, D. B. (2009). Escalation and intensification of radiotherapy for stage III non-small cell lung cancer: opportunities for

treatment improvement. *Clinical Oncology (Royal College of Radiologists (Great Britain))*, *21*(4), 343–360. https://doi.org/10.1016/j.clon.2008.12.011

Ferlay, J., Soerjomataram, I., Dikshit, R., Eser, S., Mathers, C., Rebelo, M., … Bray, F. (2015). Cancer incidence and mortality worldwide: Sources, methods and major patterns in GLOBOCAN 2012. *International Journal of Cancer*, *136*(5), E359–E386. https://doi.org/10.1002/ijc.29210

Festing, M. F. W., Yang, A., & Malkinson, A. M. (1994). At least four genes and sex are associated with susceptibility to urethane-induced pulmonary adenomas in mice. *Genetical Research*, *64*(2), 99. https://doi.org/10.1017/S0016672300032705

Fiedler, T. J., Davey, C. A., & Fenna, R. E. (2000). X-ray crystal structure and characterization of halide-binding sites of human myeloperoxidase at 1.8 A resolution. *The Journal of Biological Chemistry*, *275*(16), 11964–11971.

Formenti, S. C., & Demaria, S. (2009, July). Systemic effects of local radiotherapy. *The Lancet Oncology*. https://doi.org/10.1016/S1470-2045(09)70082-8

Fournier, B. M., & Parkos, C. A. (2012). The role of neutrophils during intestinal inflammation. *Mucosal Immunology*, *5*(4), 354–366. https://doi.org/10.1038/mi.2012.24

Fox, J., Gordon, J. R., & Haston, C. K. (2011). Combined CXCR1/CXCR2 Antagonism Decreases Radiation-Induced Alveolitis in the Mouse. *Radiation Research*, *175*(5), 657–664. https://doi.org/10.1667/RR2449.1

Fox, J., & Haston, C. K. (2013). CXC Receptor 1 and 2 and Neutrophil Elastase Inhibitors Alter Radiation-induced Lung Disease in the Mouse. *International Journal of Radiation Oncology*Biology*Physics*, *85*(1), 215–222. https://doi.org/10.1016/j.ijrobp.2012.02.024

Gariboldi, M., Manenti, G., Canzian, F., Falvella, F. S., Radice, M. T., Pierotti, M. A., … Dragani, T. A. (1993). A major susceptibility locus to murine lung carcinogenesis maps on chromosome 6. *Nature Genetics*, *3*(2), 132–136. https://doi.org/10.1038/ng0293-132

Garofalo, M., Bennett, A., Farese, A. M., Ward, A., Taylor-Howell, C., Cui, W., … MacVittie, T. J. (2014). The Delayed Pulmonary Syndrome Following Acute High-dose Irradiation. *Health Physics*, *106*(1), 56–72. https://doi.org/10.1097/HP.0b013e3182a32b3f

Gavande, N. S., VanderVere-Carozza, P. S., Hinshaw, H. D., Jalal, S. I., Sears, C. R., Pawelczak, K. S., & Turchi, J. J. (2016). DNA repair targeted therapy: The past or future of cancer treatment? *Pharmacology & Therapeutics*, *160*, 65–83. https://doi.org/10.1016/j.pharmthera.2016.02.003

Gelmon, K. A., Tischkowitz, M., Mackay, H., Swenerton, K., Robidoux, A., Tonkin, K., … Oza, A. (2011). Olaparib in patients with recurrent high-grade serous or poorly differentiated ovarian carcinoma or triple-negative breast cancer: a phase 2, multicentre, open-label, non-randomised study. *The Lancet Oncology*, *12*(9), 852–861. https://doi.org/10.1016/S1470-2045(11)70214-5

Ghafoori, B. P., Marks, L. B., Vujaskovic, Z., & Kelsey, C. R. (2008). Radiation-Induced Lung Injury: Assessment, Management, and Prevention. *Oncology*, *22*, 37–47.

Giangreco, A., Reynolds, S. D., & Stripp, B. R. (2002). Terminal Bronchioles Harbor a Unique Airway Stem Cell Population That Localizes to the Bronchoalveolar Duct Junction. *The American Journal of Pathology*, *161*(1), 173–182. https://doi.org/10.1016/S0002-9440(10)64169-7

Gong, Y., & Koh, D.-R. (2010). Neutrophils promote inflammatory angiogenesis via release of preformed VEGF in an in vivo corneal model. *Cell and Tissue Research*, *339*(2), 437–448. https://doi.org/10.1007/s00441-009-0908-5

Good, J. S., & Harrington, K. J. (2013). The Hallmarks of Cancer and the Radiation Oncologist: Updating the 5Rs of Radiobiology. *Clinical Oncology*, *25*(10), 569–577. https://doi.org/10.1016/j.clon.2013.06.009

Goodarzi, A. A., Noon, A. T., Deckbar, D., Ziv, Y., Shiloh, Y., Löbrich, M., & Jeggo, P. A. (2008). ATM Signaling Facilitates Repair of DNA Double-Strand Breaks Associated with Heterochromatin. *Molecular Cell*, *31*(2), 167–177. https://doi.org/10.1016/j.molcel.2008.05.017

Govindan, R., Ding, L., Griffith, M., Subramanian, J., Dees, N. D., Kanchi, K. L., … Wilson, R. K. (2012). Genomic Landscape of Non-Small Cell Lung Cancer in Smokers and Never-Smokers. *Cell*, *150*(6), 1121–1134. https://doi.org/10.1016/j.cell.2012.08.024

Graves, P. R., Siddiqui, F., Anscher, M. S., & Movsas, B. (2010). Radiation Pulmonary Toxicity: From Mechanisms to Management. *Seminars in Radiation Oncology*, *20*(3), 201–207. https://doi.org/10.1016/j.semradonc.2010.01.010

Gross, N. J. (1977). Pulmonary effects of radiation therapy. *Annals of Internal Medicine*, *86*(1), 81–92. Retrieved from http://www.ncbi.nlm.nih.gov/pubmed/319723

Guo, Z., Kozlov, S., Lavin, M. F., Person, M. D., & Paull, T. T. (2010). ATM Activation by Oxidative Stress. *Science*, *330*(6003). Retrieved from http://science.sciencemag.org/content/330/6003/517

Gupta, R., & Dani, H. M. (1989). In vitro formation of organ-specific ultimate carcinogens of 4-dimethylaminoazobenzene and urethan by microsomes. *Toxicology Letters*, *45*(1), 49–54. https://doi.org/10.1016/0378-4274(89)90158-6

Haahr, P., Hoffmann, S., Tollenaere, M. A. X., Ho, T., Toledo, L. I., Mann, M., … Mailand, N. (2016). Activation of the ATR kinase by the RPA-binding protein ETAA1. *Nature Cell Biology*, *18*(11), 1196–1207.

Haegens, A., Heeringa, P., van Suylen, R. J., Steele, C., Aratani, Y., O'Donoghue, R. J. J., … Vernooy, J. H. J. (2009). Myeloperoxidase Deficiency Attenuates Lipopolysaccharide-Induced Acute Lung Inflammation and Subsequent Cytokine and Chemokine Production. *The Journal of Immunology*, *182*(12). Retrieved from http://www.jimmunol.org/content/182/12/7990.short

Haegens, A., van der Vliet, A., Butnor, K. J., Heintz, N., Taatjes, D., Hemenway, D., … Mossman, B. T. (2005). Asbestos-Induced Lung Inflammation and Epithelial Cell Proliferation Are Altered in Myeloperoxidase-Null Mice. *Cancer Research*, *65*(21). Retrieved from http://cancerres.aacrjournals.org/content/65/21/9670.short

Haegens, A., Vernooy, J. H. J., Heeringa, P., Mossman, B. T., & Wouters, E. F. M. (2008). Myeloperoxidase modulates lung epithelial responses to pro-inflammatory agents. *European Respiratory Journal*, *31*(2). Retrieved from http://erj.ersjournals.com/content/31/2/252.short

Hallahan, D. E., Geng, L., & Shyr, Y. (2002). Effects of Intercellular Adhesion Molecule 1 (ICAM-1) Null Mutation on Radiation-Induced Pulmonary Fibrosis and Respiratory Insufficiency in Mice. *CancerSpectrum Knowledge Environment*, *94*(10), 733–741. https://doi.org/10.1093/jnci/94.10.733

Halpenny, D., Ridge, C. A., Hayes, S., Zheng, J., Moskowitz, C. S., Rimner, A., & Ginsberg, M. S. (2015). Computed tomographic features predictive of local recurrence in patients with early stage lung cancer treated with stereotactic body radiation therapy. *Clinical Imaging*, *39*(2), 254–258. https://doi.org/10.1016/j.clinimag.2014.12.005

Harris, R., Probst, H., Beardmore, C., James, S., Dumbleton, C., Bolderston, A., … Southgate, E. (2012). Radiotherapy skin care: A survey of practice in the UK. *Radiography*, *18*(1), 21–27. https://doi.org/10.1016/j.radi.2011.10.040

Hartsell, W. F., Scott, C. B., Dundas, G. S., Mohiuddin, M., Meredith, R. F., Rubin, P., & Weigensberg, I. J. (2007). Can Serum Markers Be Used to Predict Acute and Late Toxicity in Patients With Lung Cancer? *American Journal of Clinical Oncology*, *30*(4), 368–376. https://doi.org/10.1097/01.coc.0000260950.44761.74

Hasegawa, T., Malle, E., Farhood, A., & Jaeschke, H. (2005). Generation of hypochlorite-modified proteins by neutrophils during ischemia-reperfusion injury in rat liver: attenuation by ischemic preconditioning. *American Journal of Physiology - Gastrointestinal and Liver Physiology*, *289*(4). Retrieved from

http://ajpgi.physiology.org/content/289/4/G760.short

Haseltine, J. M., Rimner, A., Gelblum, D. Y., Modh, A., Rosenzweig, K. E., Jackson, A., … Wu, A. J. (2016). Fatal complications after stereotactic body radiation therapy for central lung tumors abutting the proximal bronchial tree. *Practical Radiation Oncology*, *6*(2), e27-33. https://doi.org/10.1016/j.prro.2015.09.012

Hellevik, T., & Martinez-Zubiaurre, I. (2014). Radiotherapy and the tumor stroma: the importance of dose and fractionation. *Frontiers in Oncology*, *4*, 1. https://doi.org/10.3389/fonc.2014.00001

Hernandez, L. G., & Forkert, P.-G. (2007). *In vivo* mutagenicity of vinyl carbamate and ethyl carbamate in lung and small intestine of F $_1$ (Big Blue® × A/J) transgenic mice. *International Journal of Cancer*, *120*(7), 1426–1433. https://doi.org/10.1002/ijc.22502

Hogg, J. C., & Doerschuk, C. M. (1995). LEUKOCYTE TRAFFIC IN THE LUNG. *Annu. Rev. Physiol*, *57*, 97–114. Retrieved from http://www.annualreviews.org/doi/pdf/10.1146/annurev.ph.57.030195.000525

Hornsey, S., Kutsutanl, Y., & Field, S. B. (1975). Damage to Mouse Lung with Fractionated Neutrons and X Rays. *Radiology*, *116*(1), 171–174. https://doi.org/10.1148/116.1.171

Huang, K., Dahele, M., Senan, S., Guckenberger, M., Rodrigues, G. B., Ward, A., … Palma, D. A. (2012). Radiographic changes after lung stereotactic ablative radiotherapy (SABR) – Can we distinguish recurrence from fibrosis? A systematic review of the literature. *Radiotherapy and Oncology*, *102*(3), 335–342. https://doi.org/10.1016/j.radonc.2011.12.018

Hübner, R. H., Gitter, W., El Mokhtari, N. E., Mathiak, M., Both, M., Bolte, H., … Bewig, B. (2008). Standardized quantification of pulmonary fibrosis in histological samples. *BioTechniques*, *44*(4), 507–517. https://doi.org/10.2144/000112729

Ira, G., Pellicioli, A., Balijja, A., Wang, X., Fiorani, S., Carotenuto, W., … Foiani, M. (2004). DNA end resection, homologous recombination and DNA damage checkpoint activation require CDK1. *Nature*, *431*(7011), 1011–7. https://doi.org/10.1038/nature02964

Jackson, I. L., Vujaskovic, Z., & Down, J. D. (2010). Revisiting Strain-Related Differences in Radiation Sensitivity of the Mouse Lung: Recognizing and Avoiding the Confounding Effects of Pleural Effusions. *Radiation Research*, *173*(1), 10–20. https://doi.org/10.1667/RR1911.1

Jackson, I. L., Vujaskovic, Z., & Down, J. D. (2011). A Further Comparison of Pathologies after Thoracic Irradiation among Different Mouse Strains: Finding the Best Preclinical Model for Evaluating Therapies Directed Against Radiation-Induced Lung Damage. *Radiation Research*, *175*(4), 510–518. https://doi.org/10.1667/RR2421.1

Jackson, I., Xu, P., Hadley, C., Katz, B., McGurk, R., Down, J., & Vujaskovic, Z. (2012). A preclinical rodent model of radiation-induced lung injury for medical countermeasure screening in accordance with the FDA animal rule. *Health Physics*, *103*(4), 463–73. https://doi.org/10.1097/HP.0b013e31826386ef

Jackson, S. P., & Bartek, J. (2009). The DNA-damage response in human biology and disease. *Nature*, *461*(7267), 1071–8. https://doi.org/10.1038/nature08467

Jakob, B., Splinter, J., Conrad, S., Voss, K.-O., Zink, D., Durante, M., … Taucher-Scholz, G. (2011). DNA double-strand breaks in heterochromatin elicit fast repair protein recruitment, histone H2AX phosphorylation and relocation to euchromatin. *Nucleic Acids Research*, *39*(15), 6489–6499. https://doi.org/10.1093/nar/gkr230

Jazayeri, A., Falck, J., Lukas, C., Bartek, J., Smith, G. C. M., Lukas, J., & Jackson, S. P. (2006). ATM-and cell cycle-dependent regulation of ATR in response to DNA double-strand breaks. *NATURE CELL BIOLOGY*, *8*(1). https://doi.org/10.1038/ncb1337

Jeong, H., Bok, S., Hong, B.-J., Choi, H.-S., Ahn, G.-O., & Lord, E. (2016). Radiation-induced immune responses: mechanisms and therapeutic perspectives. *Blood Research*, *51*(3), 157.

https://doi.org/10.5045/br.2016.51.3.157

Jin, H., Jeon, S., Kang, G.-Y., Lee, H.-J., Cho, J., & Lee, Y.-S. (2017). Identification of radiation response genes and proteins from mouse pulmonary tissues after high-dose per fraction irradiation of limited lung volumes. *International Journal of Radiation Biology*, *93*(2), 184–193. https://doi.org/10.1080/09553002.2017.1235297

Kainthola, A., Haritwal, T., Tiwari, M., Gupta, N., Parvez, S., Tiwari, M., … Agrawala, P. K. (2017). Immunological Aspect of Radiation-Induced Pneumonitis, Current Treatment Strategies, and Future Prospects. *Frontiers in Immunology*, *8*, 506. https://doi.org/10.3389/fimmu.2017.00506

Kang, C., Xu, Q., Martin, T. D., Li, M. Z., Demaria, M., Aron, L., … Elledge, S. J. (2015). The DNA damage response induces inflammation and senescence by inhibiting autophagy of GATA4. *Science*, *349*(6255). Retrieved from http://science.sciencemag.org/content/349/6255/aaa5612

Karnitz, L. M., & Zou, L. (2015). Molecular Pathways: Targeting ATR in Cancer Therapy. *Clinical Cancer Research*, *21*(21). Retrieved from http://clincancerres.aacrjournals.org/content/21/21/4780.short

Katsuno, Y., Suzuki, A., Sugimura, K., Okumura, K., Zineldeen, D. H., Shimada, M., … Nakanishi, M. (2009). Cyclin A-Cdk1 regulates the origin firing program in mammalian cells. *Proceedings of the National Academy of Sciences of the United States of America*, *106*(9), 3184–9. https://doi.org/10.1073/pnas.0809350106

Kauffman, S. L. (1972). Alterations in cell proliferation in mouse lung following urethane exposure. 3. Effects of chronic exposure on type 2 alveolar epithelial cell. *The American Journal of Pathology*, *68*(2), 317–26. Retrieved from http://www.ncbi.nlm.nih.gov/pubmed/5049428

Kauffman, S. L. (1976). AUTORADIOGRAPHIC STUDY OF TYPE II-CELL HYPERPLASIA IN LUNGS OF MICE CHRONICALL EXPOSED TO URETHANE. *Cell Proliferation*, *9*(5), 489–497. https://doi.org/10.1111/j.1365-2184.1976.tb01299.x

Kauffman, S. L., Alexander, L., & Sass, L. (1979). Histologic and ultrastructural features of the clara cell adenoma of the mouse lung. *Laboratory Investigation; a Journal of Technical Methods and Pathology*, *40*(6), 708–16. Retrieved from http://www.ncbi.nlm.nih.gov/pubmed/449277

Kesava Reddy, G., & Enwemeka, C. S. (1996). A simplified method for the analysis of hydroxyproline in biological tissues. *Clinical Biochemistry*, *29*(3), 225–229. https://doi.org/10.1016/0009-9120(96)00003-6

Kim, K. S., Jeon, S.-U., Lee, C.-J., Kim, Y.-E., Bok, S., Hong, B.-J., … Kim, H. J. (2016). Radiation-Induced Esophagitis In Vivo and In Vitro Reveals That Epidermal Growth Factor Is a Potential Candidate for Therapeutic Intervention Strategy. *International Journal of Radiation Oncology*Biology*Physics*, *95*(3), 1032–1041. https://doi.org/10.1016/j.ijrobp.2016.02.051

Kishimoto, T., Akira, S., Narazaki, M., & Taga, T. (1995). Interleukin-6 family of cytokines and gp130. *Blood*, *86*(4), 1243–1254.

Klammer, H., Mladenov, E., Li, F., & Iliakis, G. (2015). Bystander effects as manifestation of intercellular communication of DNA damage and of the cellular oxidative status. *Cancer Letters*, *356*(1), 58–71. https://doi.org/10.1016/j.canlet.2013.12.017

Klebanoff, S. J. (2005). Myeloperoxidase: friend and foe. *Journal of Leukocyte Biology*, *77*(5), 598–625. https://doi.org/10.1189/jlb.1204697

Klyubin, I. V, Kirpichnikova, K. M., & Gamaley, I. A. (1996). Hydrogen peroxide-induced chemotaxis of mouse peritoneal neutrophils. *European Journal of Cell Biology*, *70*(4), 347–51. Retrieved from http://www.ncbi.nlm.nih.gov/pubmed/8864663

Knaapen, A. M., Gu, N., Borm, P. J. A., & Schooten, F. J. Van. (2006). Neutrophils and respiratory tract DNA damage and mutagenesis : a review. *Mutagenesis*, *21*(4), 225–236. https://doi.org/10.1093/mutage/gel032

Kouvaris, J. R., Kouloulias, V. E., & Vlahos, L. J. (2007). Amifostine: the first selective-target and broad-spectrum radioprotector. *The Oncologist*, *12*(6), 738–747. https://doi.org/10.1634/theoncologist.12-6-738

Kreisel, D., Nava, R. G., Li, W., Zinselmeyer, B. H., Wang, B., Lai, J., … Miller, M. J. (2010). In vivo two-photon imaging reveals monocyte-dependent neutrophil extravasation during pulmonary inflammation. *Proceedings of the National Academy of Sciences of the United States of America*, *107*(42), 18073–8. https://doi.org/10.1073/pnas.1008737107

Kunwar, A., & Haston, C. K. (2015). DNA damage at respiratory distress, but not acute time-points, correlates with tissue fibrosis following thoracic radiation exposure in mice. *International Journal of Radiation Biology*, *91*(4), 360–367. https://doi.org/10.3109/09553002.2015.997897

Lacy, P. (2006). Mechanisms of Degranulation in Neutrophils. *Allergy, Asthma, and Clinical Immunology : Official Journal of the Canadian Society of Allergy and Clinical Immunology*. https://doi.org/10.1186/1710-1492-2-3-98

Landau, D. A., Wu, C. J., Put, N., Bontemps, F., Neste, E. Van Den, Heuberger, M., … Haussler, D. (2013). Chronic lymphocytic leukemia: molecular heterogeneity revealed by high-throughput genomics. *Genome Medicine*, *5*(5), 47. https://doi.org/10.1186/gm451

Law, M. P. (1985). Vascular permeability and late radiation fibrosis in mouse lung. *Radiation Research*, *103*(1), 60–76. Retrieved from http://www.ncbi.nlm.nih.gov/pubmed/4070560

Law, M. P., Hornsey, S., & Field, S. B. (1976). Collagen content of lungs of mice after x-ray irradiation. *Radiation Research*, *65*(1), 60–70. Retrieved from http://www.ncbi.nlm.nih.gov/pubmed/1246570

Lazarevic-Pasti, T., Leskovac, A., & Vasic, V. (2015). Myeloperoxidase Inhibitors as Potential Drugs. *Current Drug Metabolism*, *16*(3), 168–190.

Lee, J.-H., & Paull, T. T. (2005). ATM activation by DNA double-strand breaks through the Mre11-Rad50-Nbs1 complex. *Science (New York, N.Y.)*, *308*(5721), 551–554. https://doi.org/10.1126/science.1108297

Lee, J. C., Kinniry, P. A., Arguiri, E., Serota, M., Kanterakis, S., Chatterjee, S., … Christofidou-Solomidou, M. (2010). Dietary Curcumin Increases Antioxidant Defenses in Lung, Ameliorates Radiation-Induced Pulmonary Fibrosis, and Improves Survival in Mice. *Radiation Research*, *173*(5), 590–601. https://doi.org/10.1667/RR1522.1

Lloyd, R. V., Hanna, P. M., & Mason, R. P. (1997). The Origin of the Hydroxyl Radical Oxygen in the Fenton Reaction. *Free Radical Biology and Medicine*, *22*(5), 885–888. https://doi.org/10.1016/S0891-5849(96)00432-7

Lomax, M. E., Folkes, L. K., & O'Neill, P. (2013). Biological Consequences of Radiation-induced DNA Damage: Relevance to Radiotherapy. *Clinical Oncology*, *25*(10), 578–585. https://doi.org/10.1016/j.clon.2013.06.007

London Cancer. (2013). Lung Radiotherapy Guidelines. Retrieved September 20, 2017, from http://www.londoncancer.org/media/84334/london-cancer-lung-radiotherapy-guidelines-2013-v1-0.pdf

Lopes, M., Cotta-Ramusino, C., Pellicioli, A., & Liberi, G. (2001). The DNA replication checkpoint response stabilizes stalled replication forks. *Nature*, *412*(6846), 557.

Lord, C. J., & Ashworth, A. (2012). The DNA damage response and cancer therapy. *Nature*, *481*(7381), 287–294. https://doi.org/10.1038/nature10760

Lord, C. J., & Ashworth, A. (2017). PARP inhibitors: Synthetic lethality in the clinic. *Science*, *355*(6330). Retrieved from http://science.sciencemag.org/content/355/6330/1152

Machtay, M., Scherpereel, A., Santiago, J., Lee, J., McDonough, J., Kinniry, P., … Christofidou-Solomidou, M. (2006). Systemic polyethylene glycol-modified (PEGylated) superoxide dismutase and catalase mixture

attenuates radiation pulmonary fibrosis in the C57/bl6 mouse. *Radiotherapy and Oncology*, *81*(2), 196–205. https://doi.org/10.1016/j.radonc.2006.09.013

Malanga, D., Belmonte, S., Colelli, F., Scarfò, M., De Marco, C., Oliveira, D. M., … Viglietto, G. (2016). AKT1E17K Is Oncogenic in Mouse Lung and Cooperates with Chemical Carcinogens in Inducing Lung Cancer. *PLOS ONE*, *11*(2), e0147334. https://doi.org/10.1371/journal.pone.0147334

Malkinson, A. M., Nesbitt, M. N., & Skamene, E. (1985). Susceptibility to Urethan-Induced Pulmonary Adenomas Between A/J and C57BL/6J Mice: Use of AXB and BXA Recombinant Inbred Lines Indicating a Three-Locus Genetic Model234. *JNCI: Journal of the National Cancer Institute*, *75*(5), 971–974. https://doi.org/10.1093/jnci/75.5.971

Malle, E., Furtmüller, P. G., Sattler, W., & Obinger, C. (2007). Myeloperoxidase: a target for new drug development? *British Journal of Pharmacology*, *152*(6), 838–854. https://doi.org/10.1038/sj.bjp.0707358

Malle, E., Waeg, G., Schreiber, R., Gröne, E. F., Sattler, W., & Gröne, H.-J. (2000). Immunohistochemical evidence for the myeloperoxidase/H2O2/halide system in human atherosclerotic lesions. *European Journal of Biochemistry*, *267*(14), 4495–4503. https://doi.org/10.1046/j.1432-1327.2000.01498.x

Manoury, B., Nénan, S., Guénon, I., Lagente, V., & Boichot, E. (2007). Influence of early neutrophil depletion on MMPs/TIMP-1 balance in bleomycin-induced lung fibrosis. *International Immunopharmacology*, *7*(7), 900–911. https://doi.org/10.1016/j.intimp.2007.02.009

Mao, Z., Bozzella, M., Seluanov, A., & Gorbunova, V. (2008). DNA repair by nonhomologous end joining and homologous recombination during cell cycle in human cells. *Cell Cycle*, *7*(18), 2902–2906. https://doi.org/10.4161/cc.7.18.6679

Marcu, L. G. (2010). Altered fractionation in radiotherapy: From radiobiological rationale to therapeutic gain. *Cancer Treatment Reviews*, *36*(8), 606–614. https://doi.org/10.1016/j.ctrv.2010.04.004

Maréchal, A., & Zou, L. (2013). DNA damage sensing by the ATM and ATR kinases. *Cold Spring Harbor Perspectives in Biology*, *5*(9), a012716. https://doi.org/10.1101/cshperspect.a012716

Marks, L., Yu, X., Vujaskovic, Z., Small, W., Folz, R., & Anscher, M. (2003). Radiation-induced lung injury. *Seminars in Radiation Oncology*, *13*(3), 333–345. https://doi.org/10.1016/S1053-4296(03)00034-1

Marnett, L. J. (2000). Oxyradicals and DNA damage. *Carcinogenesis*, *21*(3), 361–370. https://doi.org/10.1093/carcin/21.3.361

Mason, R. J., Kalina, M., Nielsen, L. D., Malkinson, A. M., & Shannon, J. M. (2000). Surfactant Protein C Expression in Urethane-Induced Murine Pulmonary Tumors. *The American Journal of Pathology*, *156*(1), 175–182. https://doi.org/10.1016/S0002-9440(10)64717-7

Massena, S., Christoffersson, G., Hjertström, E., Zcharia, E., Vlodavsky, I., Ausmees, N., … Phillipson, M. (2010). A chemotactic gradient sequestered on endothelial heparan sulfate induces directional intraluminal crawling of neutrophils. *Blood*, *116*(11). Retrieved from http://www.bloodjournal.org/content/116/11/1924.short?sso-checked=true

Masson, M., Niedergang, C., Schreiber, V., Muller, S., Menissier-de Murcia, J., & de Murcia, G. (1998). XRCC1 is specifically associated with poly(ADP-ribose) polymerase and negatively regulates its activity following DNA damage. *Molecular and Cellular Biology*, *18*(6), 3563–71. https://doi.org/10.1128/MCB.18.6.3563

Mateo, J., & de Bono, J. S. (2017). Targeting DNA damage response systems to impact cancer care. *Current Problems in Cancer*, *41*(4), 247–250. https://doi.org/10.1016/j.currproblcancer.2017.04.001

Mattonen, S. A., Huang, K., Ward, A. D., Senan, S., & Palma, D. A. (2014). New techniques for assessing response after hypofractionated radiotherapy for lung cancer. *Journal of Thoracic Disease*, *6*(4), 375–386. https://doi.org/10.3978/j.issn.2072-1439.2013.11.09

Mauguen, A., Le Péchoux, C., Saunders, M. I., Schild, S. E., Turrisi, A. T., Baumann, M., … Pignon, J.-P. (2012). Hyperfractionated or accelerated radiotherapy in lung cancer: an individual patient data meta-analysis. *Journal of Clinical Oncology : Official Journal of the American Society of Clinical Oncology*, *30*(22), 2788–97. https://doi.org/10.1200/JCO.2012.41.6677

Mazeron, R., Etienne-Mastroianni, B., Pérol, D., Arpin, D., Vincent, M., Falchero, L., … Claude, L. (2010). Predictive Factors of Late Radiation Fibrosis: A Prospective Study in Non–Small Cell Lung Cancer. *International Journal of Radiation Oncology*Biology*Physics*, *77*(1), 38–43. https://doi.org/10.1016/j.ijrobp.2009.04.019

McCord, J. M., & Fridovich, I. (1969). Superoxide dismutase. An enzymic function for erythrocuprein (hemocuprein). *The Journal of Biological Chemistry*, *244*(22), 6049–6055.

McDonald, B., Pittman, K., Menezes, G. B., Hirota, S. A., Slaba, I., Waterhouse, C. C. M., … Kubes, P. (2010). Intravascular Danger Signals Guide Neutrophils to Sites of Sterile Inflammation. *Science*, *330*(6002). Retrieved from http://science.sciencemag.org/content/330/6002/362

McFadden, D., Politi, K., & Bhutkar, A. (2016). Mutational landscape of EGFR-, MYC-, and Kras-driven genetically engineered mouse models of lung adenocarcinoma. *Proceedings of the*. Retrieved from http://www.pnas.org/content/early/2016/10/03/1613601113.short

Mehta, M. P., Wang, D., Wang, F., Kleinberg, L., Brade, A., Robins, H. I., … Curran, W. J. (2015). Veliparib in combination with whole brain radiation therapy in patients with brain metastases: results of a phase 1 study. *Journal of Neuro-Oncology*, *122*(2), 409–417. https://doi.org/10.1007/s11060-015-1733-1

Mehta, V. (2005). Radiation pneumonitis and pulmonary fibrosis in non–small-cell lung cancer: Pulmonary function, prediction, and prevention. *International Journal of Radiation Oncology*Biology*Physics*, *63*(1), 5–24. https://doi.org/10.1016/j.ijrobp.2005.03.047

Metzger, L., & Iliakis, G. (1991). Kinetics of DNA Double-strand Break Repair Throughout the Cell Cycle as Assayed by Pulsed Field Gel Electrophoresis in CHO Cells. *International Journal of Radiation Biology*, *59*(6), 1325–1339. https://doi.org/10.1080/09553009114551201

Miyamoto, H., Kanayama, T., Horii, K., Kawai, T., Tsuchimochi, T., Shigetomi, T., … Shibuya, Y. (2015). The relationship between the severity of radiation-induced oral mucositis and the myeloperoxidase levels in rats. *Oral Surgery, Oral Medicine, Oral Pathology and Oral Radiology*, *120*(3), 329–336. https://doi.org/10.1016/j.oooo.2015.04.012

Moding, E. J., Lee, C.-L., Castle, K. D., Oh, P., Mao, L., Zha, S., … Kirsch, D. G. (2014). Atm deletion with dual recombinase technology preferentially radiosensitizes tumor endothelium. *The Journal of Clinical Investigation*, *124*(8), 3325–38. https://doi.org/10.1172/JCI73932

Moolenbeek, C., & Ruitenberg, E. J. (1981). The "Swiss roll": a simple technique for histological studies of the rodent intestine. *Laboratory Animals*, *15*(1), 57–60. https://doi.org/10.1258/002367781780958577

Mordes, D. A., Glick, G. G., Zhao, R., & Cortez, D. (2008). TopBP1 activates ATR through ATRIP and a PIKK regulatory domain. *Genes & Development*, *22*(11), 1478–89. https://doi.org/10.1101/gad.1666208

Morrone, N., Gama e Silva Volpe, V. L., Dourado, A. M., Mitre, F., & Coletta, E. N. (1993). Bilateral pleural effusion due to mediastinal fibrosis induced by radiotherapy. *Chest*, *104*(4), 1276–8. Retrieved from http://www.ncbi.nlm.nih.gov/pubmed/8404208

Movsas, B., Moughan, J., Sarna, L., Langer, C., Werner-Wasik, M., Nicolaou, N., … Bruner, D. W. (2009). Quality of life supersedes the classic prognosticators for long-term survival in locally advanced non-small-cell lung cancer: an analysis of RTOG 9801. *Journal of Clinical Oncology : Official Journal of the American Society of Clinical Oncology*, *27*(34), 5816–5822. https://doi.org/10.1200/JCO.2009.23.7420

Movsas, B., Raffin, T. A., Epstein, A. H., & Link, C. J. (1997). Pulmonary radiation injury. *Chest*.

https://doi.org/10.1378/chest.111.4.1061

Movsas, B., Scott, C., Langer, C., Werner-Wasik, M., Nicolaou, N., Komaki, R., … Byhardt, R. (2005). Randomized trial of amifostine in locally advanced non-small-cell lung cancer patients receiving chemotherapy and hyperfractionated radiation: radiation therapy oncology group trial 98-01. *Journal of Clinical Oncology : Official Journal of the American Society of Clinical Oncology*, *23*(10), 2145–54. https://doi.org/10.1200/JCO.2005.07.167

Mullard, A. (2014). European regulators approve first PARP inhibitor. *Nature Reviews Drug Discovery*, *13*(12), 877–877. https://doi.org/10.1038/nrd4508

Multhoff, G., & Radons, J. (2012). Radiation, inflammation, and immune responses in cancer. *Frontiers in Oncology*, *2*, 58. https://doi.org/10.3389/fonc.2012.00058

Muñoz-Espín, D., & Serrano, M. (2014). Cellular senescence: from physiology to pathology. *Nature Reviews Molecular Cell Biology*, *15*(7), 482–496. https://doi.org/10.1038/nrm3823

Murai, J., Huang, S.-Y. N., Renaud, A., Zhang, Y., Ji, J., Takeda, S., … Pommier, Y. (2014). Stereospecific PARP trapping by BMN 673 and comparison with olaparib and rucaparib. *Molecular Cancer Therapeutics*, *13*(2), 433–443. https://doi.org/10.1158/1535-7163.MCT-13-0803

Nakad, R., & Schumacher, B. (2016). DNA Damage Response and Immune Defense: Links and Mechanisms. *Frontiers in Genetics*, *7*, 147. https://doi.org/10.3389/fgene.2016.00147

Network, T. C. G. A. R. (2012a). Comprehensive genomic characterization of squamous cell lung cancers. *Nature*, *489*(7417), 519–525. https://doi.org/10.1038/nature11404

Network, T. C. G. A. R. (2012b). Comprehensive molecular characterization of human colon and rectal cancer. *Nature*, *487*(7407), 330–337. Retrieved from http://dx.doi.org/10.1038/nature11252

Network, T. C. G. A. R. (2014). Comprehensive molecular profiling of lung adenocarcinoma. *Nature*, *511*(7511), 543–550. Retrieved from http://dx.doi.org/10.1038/nature13385

Nikjoo, H., O'Neill, P., Wilson, W. E., & Goodhead, D. T. (2001). Computational Approach for Determining the Spectrum of DNA Damage Induced by Ionizing Radiation. *Radiation Research*, *156*(5), 577–583. https://doi.org/10.1667/0033-7587(2001)156[0577:CAFDTS]2.0.CO;2

Noel, G., Godon, C., Fernet, M., Giocanti, N., Megnin-Chanet, F., & Favaudon, V. (2006). Radiosensitization by the poly(ADP-ribose) polymerase inhibitor 4-amino-1,8-naphthalimide is specific of the S phase of the cell cycle and involves arrest of DNA synthesis. *Molecular Cancer Therapeutics*, *5*(3), 564–574. https://doi.org/10.1158/1535-7163.MCT-05-0418

Noon, A. T., Shibata, A., Rief, N., Löbrich, M., Stewart, G. S., Jeggo, P. A., & Goodarzi, A. A. (2010). 53BP1-dependent robust localized KAP-1 phosphorylation is essential for heterochromatic DNA double-strand break repair. *Nature Cell Biology*, *12*(2). https://doi.org/10.1038/ncb2017

Novello, S., Barlesi, F., Califano, R., Cufer, T., Ekman, S., Levra, M. G., … Peters, S. (2016). Metastatic non-small-cell lung cancer: ESMO Clinical Practice Guidelines for diagnosis, treatment and follow-up†. *Annals of Oncology*, *27*(suppl_5), v1–v27. Retrieved from http://dx.doi.org/10.1093/annonc/mdw326

Nowsheen, S., Bonner, J. A., & Yang, E. S. (2011). The poly(ADP-Ribose) polymerase inhibitor ABT-888 reduces radiation-induced nuclear EGFR and augments head and neck tumor response to radiotherapy. *Radiotherapy and Oncology*, *99*(3), 331–338. https://doi.org/10.1016/j.radonc.2011.05.084

O'Connor, M. J. (2015). Targeting the DNA Damage Response in Cancer. *Molecular Cell*, *60*(4), 547–560. https://doi.org/10.1016/j.molcel.2015.10.040

Olive, P. L. (2011). Retention of γH2AX foci as an indication of lethal DNA damage. *Radiotherapy and Oncology*,

101(1), 18–23. https://doi.org/10.1016/j.radonc.2011.05.055

Otani, K., Nishiyama, K., Ito, Y., Kawaguchi, Y., & Inaji, H. (2014). Steroid treatment increases the recurrence of radiation-induced organizing pneumonia after breast-conserving therapy. *Cancer Medicine*, *3*(4), 947–953. https://doi.org/10.1002/cam4.255

Palma, D. A., van Sornsen de Koste, J., Verbakel, W. F. A. R., Vincent, A., & Senan, S. (2011). Lung density changes after stereotactic radiotherapy: a quantitative analysis in 50 patients. *International Journal of Radiation Oncology, Biology, Physics*, *81*(4), 974–978. https://doi.org/10.1016/j.ijrobp.2010.07.025

Pálmai-Pallag, T., & Bachrati, C. Z. (2014). Inflammation-induced DNA damage and damage-induced inflammation: a vicious cycle. *Microbes and Infection*, *16*(10), 822–832. https://doi.org/10.1016/j.micinf.2014.10.001

Pan, J., Li, D., Xu, Y., Zhang, J., Wang, Y., Chen, M., … Meng, A. (2017). Inhibition of Bcl-2/xl With ABT-263 Selectively Kills Senescent Type II Pneumocytes and Reverses Persistent Pulmonary Fibrosis Induced by Ionizing Radiation in Mice. *International Journal of Radiation Oncology*Biology*Physics*, *99*(2), 353–361. https://doi.org/10.1016/j.ijrobp.2017.02.216

Pao, W., Wang, T. Y., Riely, G. J., Miller, V. A., Pan, Q., Ladanyi, M., … Varmus, H. E. (2005). KRAS mutations and primary resistance of lung adenocarcinomas to gefitinib or erlotinib. *PLoS Medicine*, *2*(1), e17. https://doi.org/10.1371/journal.pmed.0020017

Parkin, D. M., Bray, F., Ferlay, J., & Pisani, P. (2005). Global cancer statistics, 2002. *CA: A Cancer Journal for Clinicians*, *55*(2), 74–108.

Paull, T. T. (2015). Mechanisms of ATM Activation. *Annual Review of Biochemistry*, *84*(1), 711–738. https://doi.org/10.1146/annurev-biochem-060614-034335

Paull, T. T., Rogakou, E. P., Yamazaki, V., Kirchgessner, C. U., Gellert, M., & Bonner, W. M. (2000). A critical role for histone H2AX in recruitment of repair factors to nuclear foci after DNA damage. *Current Biology*, *10*(15), 886–895. https://doi.org/10.1016/S0960-9822(00)00610-2

Paun, A., & Haston, C. K. (2012). Genomic and genome-wide association of susceptibility to radiation-induced fibrotic lung disease in mice. *Radiotherapy and Oncology*, *105*(3), 350–357. https://doi.org/10.1016/j.radonc.2012.08.004

Paun, A., Kunwar, A., & Haston, C. K. (2015). Acute adaptive immune response correlates with late radiation-induced pulmonary fibrosis in mice, 1–11. https://doi.org/10.1186/s13014-015-0359-y

Penney, D. P., Sieman, D. W., Rubin, P., & Maltby, K. (1994). Morphological correlates of fractionated radiation of the mouse lung: Early and late effects. *International Journal of Radiation Oncology*Biology*Physics*, *29*(4), 789–804. https://doi.org/10.1016/0360-3016(94)90568-1

Peters, A. M. (1998). Just how big is the pulmonary granulocyte pool? *Clinical Science (London, England : 1979)*, *94*(1), 7–19. https://doi.org/10.1042/CS0940007

Pinar, B., Lara, P. C., Lloret, M., Bordón, E., Núñez, M. I., Villalobos, M., … Ruiz de Almodóvar, J. M. (2007). Radiation-Induced DNA Damage as a Predictor of Long-Term Toxicity in Locally Advanced Breast Cancer Patients Treated with High-Dose Hyperfractionated Radical Radiotherapy. *Radiation Research*, *168*(4), 415–422. https://doi.org/10.1667/RR0746.1

Pires, I. M., Olcina, M. M., Anbalagan, S., Pollard, J. R., Reaper, P. M., Charlton, P. A., … Hammond, E. M. (2012). Targeting radiation-resistant hypoxic tumour cells through ATR inhibition. *British Journal of Cancer*, *107*(2), 291–9. https://doi.org/10.1038/bjc.2012.265

Pojda, Z., & Tsuboi, A. (1990). In vivo effects of human recombinant interleukin 6 on hemopoietic stem and progenitor cells and circulating blood cells in normal mice. *Experimental Hematology*, *18*(9), 1034–7.

Retrieved from http://www.ncbi.nlm.nih.gov/pubmed/2397750

Postmus, P. E., Kerr, K. M., Oudkerk, M., Senan, S., Waller, D. A., Vansteenkiste, J., … Peters, S. (2017). Early and locally advanced non-small-cell lung cancer (NSCLC): ESMO Clinical Practice Guidelines for diagnosis, treatment and follow-up†. *Annals of Oncology*, *28*(suppl_4), iv1-iv21. https://doi.org/10.1093/annonc/mdx222

Powell, C., Mikropoulos, C., Kaye, S. B., Nutting, C. M., Bhide, S. A., Newbold, K., & Harrington, K. J. (2010). Pre-clinical and clinical evaluation of PARP inhibitors as tumour-specific radiosensitisers. *Cancer Treatment Reviews*, *36*(7), 566–575. https://doi.org/10.1016/j.ctrv.2010.03.003

Puthawala, K., Hadjiangelis, N., Jacoby, S. C., Bayongan, E., Zhao, Z., Yang, Z., … Munger, J. S. (2008). Inhibition of Integrin αvβ6, an Activator of Latent Transforming Growth Factor-β, Prevents Radiation-induced Lung Fibrosis. *American Journal of Respiratory and Critical Care Medicine*, *177*(1), 82–90. https://doi.org/10.1164/rccm.200706-806OC

Rajan Radha, R., & Chandrasekharan, G. (2017). Pulmonary injury associated with radiation therapy – Assessment, complications and therapeutic targets. *Biomedicine & Pharmacotherapy*, *89*, 1092–1104. https://doi.org/10.1016/j.biopha.2017.02.106

Ramroth, J., Cutter, D. J., Darby, S. C., Higgins, G. S., McGale, P., Partridge, M., & Taylor, C. W. (2016). Dose and Fractionation in Radiation Therapy of Curative Intent for Non-Small Cell Lung Cancer: Meta-Analysis of Randomized Trials. *International Journal of Radiation Oncology, Biology, Physics*, *96*(4), 736–747. https://doi.org/10.1016/j.ijrobp.2016.07.022

Rawlins, E. L., & Hogan, B. L. M. (2006). Epithelial stem cells of the lung: privileged few or opportunities for many? *Development*, *133*(13). Retrieved from http://dev.biologists.org/content/133/13/2455.short

Reiss, K. A., Herman, J. M., Armstrong, D., Zahurak, M., Fyles, A., Brade, A., … Azad, N. S. (2017). A final report of a phase I study of veliparib (ABT-888) in combination with low-dose fractionated whole abdominal radiation therapy (LDFWAR) in patients with advanced solid malignancies and peritoneal carcinomatosis with a dose escalation in ovarian and fallopian tube cancers. *Gynecologic Oncology*, *144*(3), 486–490. https://doi.org/10.1016/j.ygyno.2017.01.016

Reiss, K. A., Herman, J. M., Zahurak, M. L., Brade, A., Dawson, L., Scardina, A., … Azad, N. A. (2014). A Phase I study of veliparib (ABT-888) in combination with low-dose fractionated whole abdominal radiation therapy in patients with advanced solid malignancies and peritoneal carcinomatosis. *Clinical Cancer Research*. Retrieved from http://clincancerres.aacrjournals.org/content/early/2014/10/29/1078-0432.CCR-14-1552.short

Rock, J. R., Barkauskas, C. E., Cronce, M. J., Xue, Y., Harris, J. R., Liang, J., … Hogan, B. L. M. (2011). Multiple stromal populations contribute to pulmonary fibrosis without evidence for epithelial to mesenchymal transition. *Proceedings of the National Academy of Sciences of the United States of America*, *108*(52), E1475-83. https://doi.org/10.1073/pnas.1117988108

Rödel, F., Frey, B., Multhoff, G., & Gaipl, U. (2015). Contribution of the immune system to bystander and non-targeted effects of ionizing radiation. *Cancer Letters*, *356*(1), 105–113. https://doi.org/10.1016/j.canlet.2013.09.015

Rodríguez-García, J. L., Fraile, G., Moreno, M. A., Sánchez-Corral, J. A., & Peñalver, R. (1991). Recurrent massive pleural effusion as a late complication of radiotherapy in Hodgkin's disease. *Chest*, *100*(4), 1165–6. Retrieved from http://www.ncbi.nlm.nih.gov/pubmed/1914584

Roos, J. E., McAdams, H. P., Kaushik, S. S., & Driehuys, B. (2015). Hyperpolarized Gas MR Imaging: Technique and Applications. *Magnetic Resonance Imaging Clinics of North America*, *23*(2), 217–29. https://doi.org/10.1016/j.mric.2015.01.003

Rouleau, M., Patel, A., Hendzel, M. J., Kaufmann, S. H., & Poirier, G. G. (2010). PARP inhibition: PARP1 and

beyond. *Nature Reviews. Cancer*, *10*(4), 293–301. https://doi.org/10.1038/nrc2812

Rübe, C. E., Fricke, A., Wendorf, J., Stützel, A., Kühne, M., Ong, M. F., … Rübe, C. (2010a). Accumulation of DNA Double-Strand Breaks in Normal Tissues After Fractionated Irradiation. *International Journal of Radiation Oncology*Biology*Physics*, *76*(4), 1206–1213. https://doi.org/10.1016/j.ijrobp.2009.10.009

Rübe, C. E., Fricke, A., Wendorf, J., Stützel, A., Kühne, M., Ong, M. F., … Rübe, C. (2010b). Accumulation of DNA Double-Strand Breaks in Normal Tissues After Fractionated Irradiation. *International Journal of Radiation Oncology*Biology*Physics*, *76*(4), 1206–1213. https://doi.org/10.1016/j.ijrobp.2009.10.009

Rübe, C. E., Palm, J., Erren, M., Fleckenstein, J., König, J., Remberger, K., & Rübe, C. (2008). Cytokine Plasma Levels: Reliable Predictors for Radiation Pneumonitis? *PLoS ONE*, *3*(8), e2898. https://doi.org/10.1371/journal.pone.0002898

Rubin, P., Johnston, C. J., Williams, J. P., McDonald, S., & Finkelstein, J. N. (1995). A perpetual cascade of cytokines postirradiation leads to pulmonary fibrosis. *International Journal of Radiation Oncology*Biology*Physics*, *33*(1), 99–109. https://doi.org/10.1016/0360-3016(95)00095-G

Ruebe, C., Uthe, D., Wilfert, F., Ludwig, D., Yang, K., Koenig, J., … Ruebe, C. (2004). The bronchiolar epithelium as a prominent source of pro-inflammatory cytokines after lung irradiation. *International Journal of Radiation Oncology*Biology*Physics*, *60*(1), S349. https://doi.org/10.1016/j.ijrobp.2004.07.180

Ruiz, S., Mayor-Ruiz, C., Lafarga, V., Murga, M., Vega-Sendino, M., Ortega, S., & Fernandez-Capetillo, O. (2016). A Genome-wide CRISPR Screen Identifies CDC25A as a Determinant of Sensitivity to ATR Inhibitors. *Molecular Cell*, *62*(2), 307–313. https://doi.org/10.1016/j.molcel.2016.03.006

Ryan, J., Barker, P. E., Nesbitt, M. N., & Ruddle, F. H. (1987). KRAS2 as a genetic marker for lung tumor susceptibility in inbred mice. *Journal of the National Cancer Institute*, *79*(6), 1351–7. Retrieved from http://www.ncbi.nlm.nih.gov/pubmed/2891865

Rybanska-Spaeder, I., Reynolds, T. L., Chou, J., Prakash, M., Jefferson, T., Huso, D. L., … Franco, S. (2013). 53BP1 is limiting for NHEJ repair in ATM-deficient model systems that are subjected to oncogenic stress or radiation. *Molecular Cancer Research : MCR*, *11*(10), 1223–1234. https://doi.org/10.1158/1541-7786.MCR-13-0252-T

Sak, M. Stuschke, R. Wurm, V. Budac, A. (2000). Protection of DNA from radiation-induced double-strand breaks: influence of replication and nuclear proteins. *International Journal of Radiation Biology*, *76*(6), 749–756. https://doi.org/10.1080/09553000050028896

Saldivar, J. C., Cortez, D., & Cimprich, K. A. (2017). The essential kinase ATR: ensuring faithful duplication of a challenging genome. *Nat Rev Mol Cell Biol*, *advance on*. Retrieved from http://dx.doi.org/10.1038/nrm.2017.67

Santivasi, W. L., & Xia, F. (2014). Ionizing Radiation-Induced DNA Damage, Response, and Repair. *Antioxidants & Redox Signaling*, *21*(2), 251–259. https://doi.org/10.1089/ars.2013.5668

Schaue, D., Kachikwu, E. L., & McBride, W. H. (2012). Cytokines in Radiobiological Responses: A Review. *Radiation Research*, *178*(6), 505–523. https://doi.org/10.1667/RR3031.1

Schaue, D., & Mcbride, W. H. (2015). Opportunities and challenges of radiotherapy for treating cancer. *Nat. Rev. Clin. Oncol*, *12*, 527–540. https://doi.org/10.1038/nrclinonc.2015.120

Sekine, I., Sumi, M., Ito, Y., Nokihara, H., Yamamoto, N., Kunitoh, H., … Tamura, T. (2006). Retrospective analysis of steroid therapy for radiation-induced lung injury in lung cancer patients. *Radiotherapy and Oncology : Journal of the European Society for Therapeutic Radiology and Oncology*, *80*(1), 93–97. https://doi.org/10.1016/j.radonc.2006.06.007

Sengeløv, H., Kjeldsen, L., & Borregaard, N. (1993). Control of exocytosis in early neutrophil activation. *The*

Journal of Immunology, *150*(4). Retrieved from http://www.jimmunol.org/content/150/4/1535.short

Senra, J. M., Telfer, B. A., Cherry, K. E., McCrudden, C. M., Hirst, D. G., O'Connor, M. J., … Stratford, I. J. (2011). Inhibition of PARP-1 by olaparib (AZD2281) increases the radiosensitivity of a lung tumor xenograft. *Molecular Cancer Therapeutics*, *10*(10), 1949–1958. https://doi.org/10.1158/1535-7163.MCT-11-0278

Serhan, C. N. (2010). Novel Lipid Mediators and Resolution Mechanisms in Acute Inflammation. *The American Journal of Pathology*, *177*(4), 1576–1591. https://doi.org/10.2353/ajpath.2010.100322

Sharplin, J., & Franko, A. J. (1989). A Quantitative Histological Study of Strain-Dependent Differences in the Effects of Irradiation on Mouse Lung during the Early Phase. *Radiation Research*, *119*(1), 1. https://doi.org/10.2307/3577363

Shen, Y., Rehman, F. L., Feng, Y., Boshuizen, J., Bajrami, I., Elliott, R., … Ashworth, A. (2013). BMN 673, a Novel and Highly Potent PARP1/2 Inhibitor for the Treatment of Human Cancers with DNA Repair Deficiency. *Clinical Cancer Research*, *19*(18). Retrieved from http://clincancerres.aacrjournals.org/content/19/18/5003.short

Shibamoto, Y., Miyakawa, A., Otsuka, S., & Iwata, H. (2016). Radiobiology of hypofractionated stereotactic radiotherapy: what are the optimal fractionation schedules? *Journal of Radiation Research*, *57*(S1), i76–i82. https://doi.org/10.1093/jrr/rrw015

Shiloh, Y., & Ziv, Y. (2013). The ATM protein kinase: regulating the cellular response to genotoxic stress, and more. *Nature Reviews. Molecular Cell Biology*, *14*(4), 197–210. https://doi.org/10.1038/nrm3546

Shirai, K., Tamaki, Y., Kitamoto, Y., Murata, K., Satoh, Y., Higuchi, K., … Nakano, T. (2011). Dose–Volume Histogram Parameters and Clinical Factors Associated With Pleural Effusion After Chemoradiotherapy in Esophageal Cancer Patients. *International Journal of Radiation Oncology*Biology*Physics*, *80*(4), 1002–1007. https://doi.org/10.1016/j.ijrobp.2010.03.046

Siva, S., Lobachevsky, P., MacManus, M. P., Kron, T., Möller, A., Lobb, R. J., … Martin, O. A. (2016). Radiotherapy for Non–Small Cell Lung Cancer Induces DNA Damage Response in Both Irradiated and Out-of-field Normal Tissues. *Clinical Cancer Research*, *22*(19). Retrieved from http://clincancerres.aacrjournals.org/content/22/19/4817

Siva, S., MacManus, M., Kron, T., Best, N., Smith, J., Lobachevsky, P., … Martin, O. (2014). A Pattern of Early Radiation-Induced Inflammatory Cytokine Expression Is Associated with Lung Toxicity in Patients with Non-Small Cell Lung Cancer. *PLoS ONE*, *9*(10), e109560. https://doi.org/10.1371/journal.pone.0109560

Sprung, C. N., Ivashkevich, A., Forrester, H. B., Redon, C. E., Georgakilas, A., & Martin, O. A. (2015). Oxidative DNA damage caused by inflammation may link to stress-induced non-targeted effects. *Cancer Letters*, *356*(1), 72–81. https://doi.org/10.1016/j.canlet.2013.09.008

Stenmark, M. H., Cai, X., Vuong, H., Wang, L., Hayman, J. A., Yuan, S., … Kong, F. M. (2017). Plasma Cytokine Profile during Radiotherapy may Predict Symptomatic Radiation-induced Lung Toxicity in Patients with Non–small-cell Lung Cancer. *International Journal of Radiation Oncology • Biology • Physics*, *75*(3), S109. https://doi.org/10.1016/j.ijrobp.2009.07.264

Stiff, T., O'Driscoll, M., Rief, N., Iwabuchi, K., Löbrich, M., & Jeggo, P. A. (2004). ATM and DNA-PK Function Redundantly to Phosphorylate H2AX after Exposure to Ionizing Radiation. *Cancer Research*, *64*(7). Retrieved from http://cancerres.aacrjournals.org/content/64/7/2390.short

Sugamata, R., Dobashi, H., Nagao, T., Yamamoto, K., Nakajima, N., Sato, Y., … Suzuki, K. (2012). Contribution of neutrophil-derived myeloperoxidase in the early phase of fulminant acute respiratory distress syndrome induced by influenza virus infection. *Microbiology and Immunology*, *56*(3), 171–182. https://doi.org/10.1111/j.1348-0421.2011.00424.x

Summers, C., Rankin, S. M., Condliffe, A. M., Singh, N., Peters, A. M., & Chilvers, E. R. (2010). Neutrophil kinetics in health and disease. *Trends in Immunology*, *31*(8), 318–324. https://doi.org/10.1016/j.it.2010.05.006

Summers, C., Singh, N. R., White, J. F., Mackenzie, I. M., Johnston, A., Solanki, C., … Chilvers, E. R. (2014). Pulmonary retention of primed neutrophils: a novel protective host response, which is impaired in the acute respiratory distress syndrome. *Thorax*, *69*, 623–629. https://doi.org/10.1136/thoraxjnl-2013-204742

Sundar, R., Brown, J., Ingles Russo, A., & Yap, T. A. (2017). Targeting ATR in cancer medicine. *Current Problems in Cancer*, *41*(4), 302–315. https://doi.org/10.1016/j.currproblcancer.2017.05.002

Svegliati, S., Marrone, G., Pezone, A., Spadoni, T., Grieco, A., Moroncini, G., … Avvedimento, E. V. (2014). Oxidative DNA damage induces the ATM-mediated transcriptional suppression of the Wnt inhibitor WIF-1 in systemic sclerosis and fibrosis. *Science Signaling*, *7*(341). Retrieved from http://stke.sciencemag.org/content/7/341/ra84.short

Symington, L. S., & Gautier, J. (2011). Double-Strand Break End Resection and Repair Pathway Choice. *Annual Review of Genetics*, *45*(1), 247–271. https://doi.org/10.1146/annurev-genet-110410-132435

Takemasa, A., Ishii, Y., & Fukuda, T. (2012). A neutrophil elastase inhibitor prevents bleomycin-induced pulmonary fibrosis in mice. *The European Respiratory Journal*, *40*(6), 1475–1482. https://doi.org/10.1183/09031936.00127011

Tang, J., Cho, N. W., Cui, G., Manion, E. M., Shanbhag, N. M., Botuyan, M. V., … Greenberg, R. A. (2013). Acetylation limits 53BP1 association with damaged chromatin to promote homologous recombination. *Nat Struct Mol Biol*, *20*(3), 317–325. Retrieved from http://dx.doi.org/10.1038/nsmb.2499

Tekatli, H., Haasbeek, N., Dahele, M., De Haan, P., Verbakel, W., Bongers, E., … Senan, S. (2016). Outcomes of Hypofractionated High-Dose Radiotherapy in Poor-Risk Patients with "Ultracentral" Non–Small Cell Lung Cancer. *Journal of Thoracic Oncology*, *11*(7), 1081–1089. https://doi.org/10.1016/j.jtho.2016.03.008

Tekatli, H., Senan, S., Dahele, M., Slotman, B. J., & Verbakel, W. F. A. R. (2015). Stereotactic ablative radiotherapy (SABR) for central lung tumors: Plan quality and long-term clinical outcomes. *Radiotherapy and Oncology*, *117*(1), 64–70. https://doi.org/10.1016/j.radonc.2015.09.028

Thaete, L. G., Gunning, W. T., Stoner, G. D., & Malkinson, A. M. (1987). Cellular Derivation of Lung Tumors in Sensitive and Resistant Strains of Mice: Results at 28 and 56 Weeks After Urethan Treatment<xref ref-type="fn" rid="FN2">2</xref><xref ref-type="fn" rid="FN3">3</xref> *JNCI: Journal of the National Cancer Institute*, *78*(4), 743–749. https://doi.org/10.1093/jnci/78.4.743

Thaete, L. G., & Malkinson, A. M. (1991). Cells of Origin of Primary Pulmonary Neoplasms in Mice: Morphologic and Histochemical Studies. *Experimental Lung Research*, *17*(2), 219–228. https://doi.org/10.3109/01902149109064413

The Cancer Genome Atlas Research Network. (2012). Comprehensive molecular portraits of human breast tumours. *Nature*, *490*(7418), 61–70. https://doi.org/10.1038/nature11412

Timmerman, R., McGarry, R., Yiannoutsos, C., Papiez, L., Tudor, K., DeLuca, J., … Fletcher, J. (2006). Excessive toxicity when treating central tumors in a phase II study of stereotactic body radiation therapy for medically inoperable early-stage lung cancer. *Journal of Clinical Oncology : Official Journal of the American Society of Clinical Oncology*, *24*(30), 4833–4839. https://doi.org/10.1200/JCO.2006.07.5937

Timmerman, R., Papiez, L., McGarry, R., Likes, L., DesRosiers, C., Frost, S., & Williams, M. (2003). Extracranial stereotactic radioablation: results of a phase I study in medically inoperable stage I non-small cell lung cancer. *Chest*, *124*(5), 1946–1955.

Titis, A. P., & Forkert, P.-G. (2001). Strain-Related Differences in Bioactivation of Vinyl Carbamate and

Formation of DNA Adducts in Lungs of A/J, CD-1, and C57BL/6 Mice. *Toxicological Sciences*, *59*(1), 82–91. https://doi.org/10.1093/toxsci/59.1.82

Travis, E. L., Meistrich, M. L., Finch-Neimeyer, M. V., Watkins, T. L., & Kiss, I. (1985). Late Functional and Biochemical Changes in Mouse Lung after Irradiation: Differential Effects of WR-2721. *Radiation Research*, *103*(2), 219. https://doi.org/10.2307/3576576

Travis, E. L., Rachakonda, G., Zhou, X., Korhonen, K., Sekhar, K. R., Biswas, S., & Freeman, M. L. (2011). NRF2 deficiency reduces life span of mice administered thoracic irradiation. *Free Radical Biology and Medicine*, *51*(6), 1175–1183. https://doi.org/10.1016/j.freeradbiomed.2011.05.038

Travis, E. L., Thames, H. D., Watkins, T. L., & Kiss, I. (1987). The Kinetics of Repair in Mouse Lung after Fractionated Irradiation. *International Journal of Radiation Biology and Related Studies in Physics, Chemistry and Medicine*, *52*(6), 903–919. https://doi.org/10.1080/09553008714552491

Tsoutsou, P. G., & Koukourakis, M. I. (2006). Radiation pneumonitis and fibrosis: Mechanisms underlying its pathogenesis and implications for future research. *International Journal of Radiation Oncology*Biology*Physics*, *66*(5), 1281–1293. https://doi.org/10.1016/j.ijrobp.2006.08.058

Tsujino, K., Hirota, S., Endo, M., Obayashi, K., Kotani, Y., Satouchi, M., … Takada, Y. (2003). Predictive value of dose-volume histogram parameters for predicting radiation pneumonitis after concurrent chemoradiation for lung cancer. *International Journal of Radiation Oncology*Biology*Physics*, *55*(1), 110–115. https://doi.org/10.1016/S0360-3016(02)03807-5

Valdiglesias, V., Giunta, S., Fenech, M., Neri, M., & Bonassi, S. (2013). γH2AX as a marker of DNA double strand breaks and genomic instability in human population studies. *Mutation Research/Reviews in Mutation Research*, *753*(1), 24–40. https://doi.org/10.1016/j.mrrev.2013.02.001

Van Renterghem, D. M., & Pauwels, R. A. (1995). Chylothorax and pleural effusion as late complications of thoracic irradiation. *Chest*, *108*(3), 886–7. Retrieved from http://www.ncbi.nlm.nih.gov/pubmed/7656656

Vendetti, F. P., Lau, A., Schamus, S., Conrads, T. P., O'Connor, M. J., & Bakkenist, C. J. (2015). The orally active and bioavailable ATR kinase inhibitor AZD6738 potentiates the anti-tumor effects of cisplatin to resolve ATM-deficient non-small cell lung cancer in vivo. *Oncotarget*, *6*(42), 44289–44305. https://doi.org/10.18632/oncotarget.6247

Vendetti, F. P., Leibowitz, B. J., Barnes, J., Schamus, S., Kiesel, B. F., Abberbock, S., … Bakkenist, C. J. (2017). Pharmacologic ATM but not ATR kinase inhibition abrogates p21-dependent G1 arrest and promotes gastrointestinal syndrome after total body irradiation. *Scientific Reports*, *7*, 41892. https://doi.org/10.1038/srep41892

Walker, F., Zhang, H.-H., Matthews, V., Weinstock, J., Nice, E. C., Ernst, M., … Burgess, A. W. (2008). IL6/sIL6R complex contributes to emergency granulopoietic responses in G-CSF- and GM-CSF-deficient mice. *Blood*, *111*(8), 3978–3985. https://doi.org/10.1182/blood-2007-10-119636

Wang, H., Wang, M., Wang, H., Böcker, W., & Iliakis, G. (2005). Complex H2AX phosphorylation patterns by multiple kinases including ATM and DNA-PK in human cells exposed to ionizing radiation and treated with kinase inhibitors. *Journal of Cellular Physiology*, *202*(2), 492–502. https://doi.org/10.1002/jcp.20141

Wang, M., Wu, W., Wu, W., Rosidi, B., Zhang, L., Wang, H., … N., A. (2006). PARP-1 and Ku compete for repair of DNA double strand breaks by distinct NHEJ pathways. *Nucleic Acids Research*, *34*(21), 6170–6182. https://doi.org/10.1093/nar/gkl840

Wang, S., Campbell, J., Stenmark, M. H., Zhao, J., Stanton, P., Matuszak, M. M., … Kong, F.-M. (Spring). (2017). Plasma Levels of IL-8 and TGF-β1 Predict Radiation-Induced Lung Toxicity in Non-Small Cell Lung Cancer: A Validation Study. *International Journal of Radiation Oncology*Biology*Physics*, *98*(3), 615–621. https://doi.org/10.1016/j.ijrobp.2017.03.011

Wang, Y., Boerma, M., & Zhou, D. (2016). Ionizing Radiation-Induced Endothelial Cell Senescence and Cardiovascular Diseases. *Radiation Research*, *186*(2), 153–161. https://doi.org/10.1667/RR14445.1

Ward, I. M., & Chen, J. (2001). Histone H2AX is phosphorylated in an ATR-dependent manner in response to replicational stress. *The Journal of Biological Chemistry*, *276*(51), 47759–62. https://doi.org/10.1074/jbc.C100569200

Ward, J. F. (1988). DNA Damage Produced by Ionizing Radiation in Mammalian Cells: Identities, Mechanisms of Formation, and Reparability (pp. 95–125). https://doi.org/10.1016/S0079-6603(08)60611-X

Weber, A. M., & Ryan, A. J. (2015). ATM and ATR as therapeutic targets in cancer. *Pharmacology & Therapeutics*, *149*, 124–138. https://doi.org/10.1016/j.pharmthera.2014.12.001

Weichselbaum, R. R., Liang, H., Deng, L., & Fu, Y.-X. (2017). Radiotherapy and immunotherapy: a beneficial liaison? *Nature Reviews. Clinical Oncology*, *14*(6), 365–379. https://doi.org/10.1038/nrclinonc.2016.211

Weinberg, J., Misukonis, M., Shami, P., Mason, S., Sauls, D., Dittman, W., … Bachus, K. (1995). Human mononuclear phagocyte inducible nitric oxide synthase (iNOS): analysis of iNOS mRNA, iNOS protein, biopterin, and nitric oxide production by blood monocytes and peritoneal macrophages. *Blood*, *86*(3). Retrieved from http://www.bloodjournal.org/content/86/3/1184.short?sso-checked=true

Werner-Wasik, M., Yorke, E., Deasy, J., Nam, J., & Marks, L. B. (2010). Radiation Dose-Volume Effects in the Esophagus. *International Journal of Radiation Oncology*Biology*Physics*, *76*(3), S86–S93. https://doi.org/10.1016/j.ijrobp.2009.05.070

Westcott, P. M. K., Halliwill, K. D., To, M. D., Rashid, M., Rust, A. G., Keane, T. M., … Balmain, A. (2015). The mutational landscapes of genetic and chemical models of Kras-driven lung cancer. *Nature*, *517*(7535), 489–92. https://doi.org/10.1038/nature13898

Willers, H., Dahm-Daphi, J., & Powell, S. N. (2004). Repair of radiation damage to DNA. *British Journal of Cancer*, *90*(7), 1297–301. https://doi.org/10.1038/sj.bjc.6601729

Williams, J. P., Calvi, L., Chakkalakal, J. V, Finkelstein, J. N., Kerry O 'banion, M., Puzas, E., … Puzas, M. K. (1667). Addressing the Symptoms or Fixing the Problem? Developing Countermeasures against Normal Tissue Radiation Injury REVIEW Addressing the Symptoms or Fixing the Problem? Developing Countermeasures against Normal Tissue Radiation Injury. *Source: Radiation Research RADIATION RESEARCH*, *186*(186), 1–16. https://doi.org/10.1667/RR14473.1

Wood, S. L., Pernemalm, M., Crosbie, P. A., & Whetton, A. D. (2015). Molecular histology of lung cancer: From targets to treatments. *Cancer Treatment Reviews*, *41*(4), 361–375. https://doi.org/10.1016/j.ctrv.2015.02.008

Yamaura, T., Doki, Y., Murakami, K., & Saiki, I. (1999). Model for mediastinal lymph node metastasis produced by orthotopic intrapulmonary implantation of lung cancer cells in mice. *Human Cell*, *12*(4), 197–204. Retrieved from http://www.ncbi.nlm.nih.gov/pubmed/10834106

Yarnold, J., & Vozenin Brotons, M.-C. (2010). Pathogenetic mechanisms in radiation fibrosis. *Radiotherapy and Oncology*, *97*(1), 149–161. https://doi.org/10.1016/j.radonc.2010.09.002

Yushkevich, P. A., Piven, J., Hazlett, H. C., Smith, R. G., Ho, S., Gee, J. C., & Gerig, G. (2006). User-guided 3D active contour segmentation of anatomical structures: significantly improved efficiency and reliability. *NeuroImage*, *31*(3), 1116–1128. https://doi.org/10.1016/j.neuroimage.2006.01.015

Zhan, H., Suzuki, T., Aizawa, K., Miyagawa, K., & Nagai, R. (2010). Ataxia telangiectasia mutated (ATM)-mediated DNA damage response in oxidative stress-induced vascular endothelial cell senescence. *The Journal of Biological Chemistry*, *285*(38), 29662–70. https://doi.org/10.1074/jbc.M110.125138

Zhang, X. W., Liu, Q., Wang, Y., & Thorlacius, H. (2001). CXC chemokines, MIP-2 and KC, induce P-selectin-dependent neutrophil rolling and extravascular migration *in vivo*. *British Journal of Pharmacology*, *133*(3),

413–421. https://doi.org/10.1038/sj.bjp.0704087

Zhang, Y., Zhang, X., Rabbani, Z. N., Jackson, I. L., & Vujaskovic, Z. (2012). Oxidative Stress Mediates Radiation Lung Injury by Inducing Apoptosis. *International Journal of Radiation Oncology*Biology*Physics*, *83*(2), 740–748. https://doi.org/10.1016/j.ijrobp.2011.08.005

Zhang, Z., Futamura, M., Vikis, H. G., Wang, M., Li, J., Wang, Y., … You, M. (2003). Positional cloning of the major quantitative trait locus underlying lung tumor susceptibility in mice. *Proceedings of the National Academy of Sciences of the United States of America*, *100*(22), 12642–7. https://doi.org/10.1073/pnas.2133947100

Zimmermann, M., & de Lange, T. (2014). 53BP1: pro choice in DNA repair. *Trends in Cell Biology*, *24*(2), 108–117. https://doi.org/10.1016/j.tcb.2013.09.003

Ziv, Y., Bielopolski, D., Galanty, Y., Lukas, C., Taya, Y., Schultz, D. C., … Shiloh, Y. (2006). Chromatin relaxation in response to DNA double-strand breaks is modulated by a novel ATM- and KAP-1 dependent pathway. *NATURE CELL BIOLOGY*, *8*(8). https://doi.org/10.1038/ncb1446

Zou, L., Elledge, S. J., Futcher, B., Morrison, C., Hashimoto, M., Utsumi, H., … Takeda, S. (2003). Sensing DNA damage through ATRIP recognition of RPA-ssDNA complexes. *Science (New York, N.Y.)*, *300*(5625), 1542–8. https://doi.org/10.1126/science.1083430

10. Appendix

Supplementary Table 1. Code and descriptions of primary tumour (T), regional lymph nodes (N) and distant metastasis (M). Adapted from (Edge, Byrd, & Compton, 2010).

Code	Description
Primary tumour (T)	
TX	Primary tumour cannot be assessed, or tumour proven by the presence of malignant cells in sputum or bronchial washings but not visualised by imaging or bronchoscopy
T0	No evidence of primary tumour
Tis	Carcinoma *in situ*
T1	Tumour 3 cm or less in greatest dimension, surrounded by lung or visceral pleura, without bronchoscopic evidence of invasion more proximal than the lobar bronchus (i.e. not in the main bronchus)[a]
T1a	Tumour 2 cm or less in greatest dimension
T1b	Tumour >2 cm but 3 cm or less in greatest dimension
T2	Tumour >3 cm but 7 cm or less or tumour with any of the following features (T2 tumours with these features are classified T2a if 5 cm or less); involves main bronchus, 2 cm or more distal to the carina; invades visceral pleura (PL1 or PL2); associated with atelectasis or obstructive pneumonitis that extends to the hilar region but does not involve the entire lung
T2a	Tumour >3 cm but 5 cm or less in greatest dimension
T2b	Tumour >5 cm but 7 cm or less in greatest dimension
T3	Tumour >7 cm or one that directly invades any of the following: parietal pleural (PL3) chest wall (including superior sulcus tumours), diaphragm, phrenic nerve, mediastinal pleura, parietal pericardium or tumour in the main bronchus (<2 cm distal to the carina[a] but without involvement of the carina; or associated atelectasis or obstructive pneumonitis of the entire lung or separate tumour nodule(s) in the same lobe)
T4	Tumour of any size that invades any of the following: mediastinum, heart, great vessels, trachea, recurrent laryngeal nerve, oesophagus, vertebral body, carina, separate tumour nodule(s) in a different ipsilateral lobe
Regional lymph nodes (N)	
NX	Regional lymph nodes cannot be assessed
N0	No regional lymph node metastases
N1	Metastasis in ipsilateral peribronchial and/or ipsilateral hilar lymph nodes and intrapulmonary nodes, including involvement by direct extension
N2	Metastasis in ipsilateral mediastinal and/or subcarinal lymph node(s)
N3	Metastasis in contralateral mediastinal, contralateral hilar, ipsilateral or contralateral scalene, or supraclavicular lymph node(s)

Distant metastasis (M)

M0	No distant metastasis
M1	Distant metastasis
M1a	Separate tumour nodule(s) in a contralateral tumour with pleural nodules or malignant pleural (or pericardial) effusion[b]
M1b	Distant metastasis

[a]The uncommon superficial spreading tumour of any size with its invasive component limited to the bronchial wall, which may extend proximally to the main bronchus, is also classified as T1a.

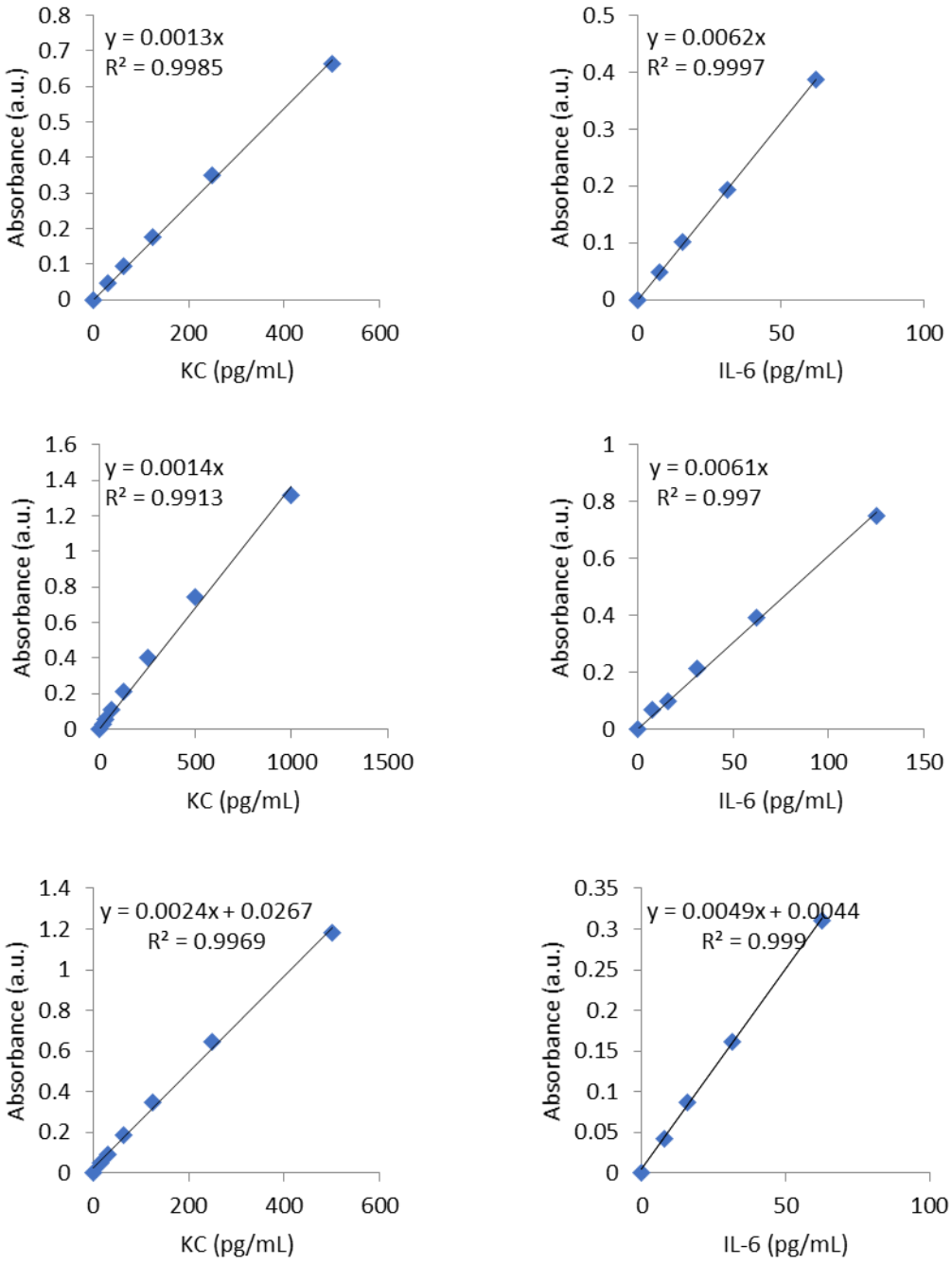
[b]Most pleural (and pericardial) effusions with lung cancer are due to tumour. In a few patients, however, multiple cytopathologic examinations of pleural (pericardial) fluid are negative for tumour, and the fluid is non-bloody and is not an exudate. Where these elements and clinical judgment dictate that the effusion is not related to the tumour, the effusion should be excluded as a staging element and the patient should be classified as M0.

Supplementary Table 2. NSCLC stages according to TNM staging system. Adapted from (Novello et al., 2016)**.**

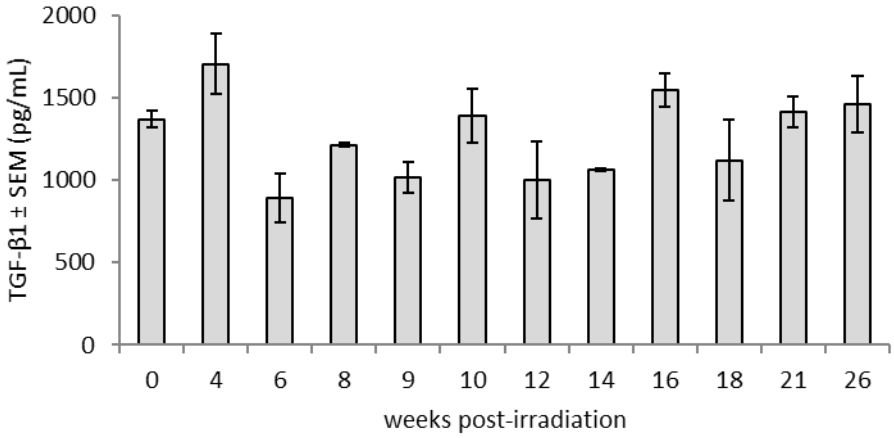
Occult carcinoma	T	N	M
Stage 0	Tis	N0	M0
Stage IA	T1a,b	N0	M0
Stage IB	T2a	N0	M0
Stage IIA	T2b	N0	M0
	T1a,b	N1	M0
	T2a	N1	M0
Stage IIB	T2b	N1	M0
	T3	N0	M0
Stage IIIA	T1a,b, T2a,b	N2	M0
	T3	N1, N2	M0
	T4	N0, N1	M0
Stage IIIB	T4	N2	M0
	Any T	N3	M0
Stage IV	Any T	Any N	M1

Supplementary Table 3. Examples of radiotherapy schedules given to NSCLC patients according to stage. Radiotherapy fractionation schedules are colour coded: conventional (green), accelerated (orange) and stereotactic (red). Modified from (London Cancer, 2013).

Stage	Schedule
Stage I	60 Gy in 30 fractions 66 Gy in 33 fractions 55 Gy in 20 fractions 54 Gy in 36 fractions 54Gy in 3 fractions
Stage II	60 Gy in 30 fractions 66 Gy in 33 fractions 55 Gy in 20 fractions 54 Gy in 36 fractions 54Gy in 3 fractions
Stage IIIA	60 Gy in 30 fractions 66 Gy in 33 fractions 45 Gy in 25 fractions 55 Gy in 20 fractions 54 Gy in 36 fractions 36 Gy in 12 fractions 30 Gy in 10 fractions 20 Gy in 5 fractions 16 Gy in 2 fractions 10 Gy in 1 fraction
Stage IIIB	66 Gy in 30 fractions 66 Gy in 33 fractions 55 Gy in 20 fractions 54 Gy in 36 fractions 36 Gy in 12 fractions 30 Gy in 10 fractions 39 Gy in 13 fractions 20 Gy in 5 fractions 16 Gy in 2 fractions 17 Gy in 2 fractions 10 Gy in 1 fraction
Stage IV	36 Gy in 12 fractions 30 Gy in 10 fractions 39 Gy in 13 fractions 20 Gy in 5 fractions 16 Gy in 2 fractions 17 Gy in 2 fractions 10 Gy in 1 fraction



Supplementary Figure 1. Standard curves for ELISA experiments. (A) curve for experiment presented in Figure 3.3 A and Figure 4.7 B. (B) curve for experiment presented in Figure 3.3 B and Figure 4.7 D. (C) curve for experiment presented in Figure 4.7 A. (D) curve for experiment presented in Figure 4.7 C. (E) curve for experiment presented in Figure 7.2 A. (F) curve for experiment presented in Figure 7.2 B.



Supplementary Figure 2. Whole-thorax irradiation did not increase TGFβ-1 plasma levels in C57BL/6J mice. Mice were irradiated with 4 x 5 Gy schedule and plasma samples were collected at different time points post-irradiation. Levels of TGF-β1 were assessed by ELISA. Graph bars represent the average in the group (n=2 or 3 per group), control unirradiated are labelled as '0 weeks post-irradiation' and error bars represent the SEM.